Markus Joel Benjamin Ristola

# Characterisation of tungsten-doped silicon

## An intermediate band material candidate from ion implantation and nanosecond pulsed laser melting

Master's thesis in Nanotechnology
Supervisor: Turid Worren Reenaas
December 2019

Master's thesis

NTNU
Norwegian University of Science and Technology
Faculty of Natural Sciences
Department of Physics

NTNU
Kunnskap for en bedre verden

Markus Joel Benjamin Ristola

# Characterisation of tungsten-doped silicon

## An intermediate band material candidate from ion implantation and nanosecond pulsed laser melting

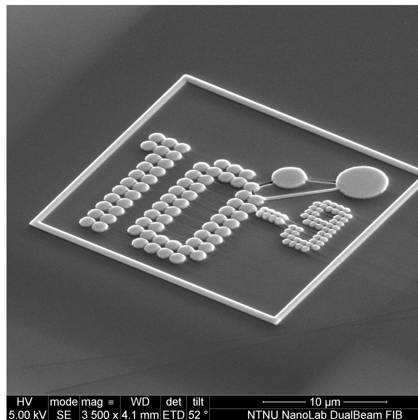


Master's thesis in Nanotechnology
Supervisor: Turid Worren Reenaas
December 2019

Norwegian University of Science and Technology
Faculty of Natural Sciences
Department of Physics

NTNU
Norwegian University of
Science and Technology

# Summary

A shift to renewable energy sources is vital in combatting global warming, and photovoltaic solar cells are becoming one of the most widely adopted solutions, owing to a steady decrease in cost and increase in efficiency. However, the commercially available panels of today are approaching the theoretical limits of the materials and technologies utilised, and new innovations are required for further improvements.

One such innovation is a solar cell of an intermediate band (IB) material, which may be made by heavily doping semiconductors with transition metals. Silver implanted silicon has previously been studied as an IB material candidate at NTNU, and based on the results, tungsten doped silicon was chosen as a new research candidate.

In this thesis, single crystalline silicon was ion implanted with tungsten to achieve concentrations above the equilibrium solubility limit. Nominal tungsten peak concentrations were 2, 1, 0.1 and 0.01 at.%. The ion implantation amorphised the silicon, as shown by Raman spectroscopy, and a crystal was re-grown in the implanted volume via pulsed laser melting (PLM). PLM was done in vacuum by single pulse excimer laser at average fluences of 0.9, 1.4 and 1.8 $J/cm^2$.

The resulting material had its surface properties characterised by optical microscopy, white light interferometry (WLI), scanning electron microscopy (SEM), and atomic force microscopy (AFM). The surface was found to exhibit extensive nanometre-scale cracking, with a correlation between cracking pattern, tungsten content and laser fluence. The edges of the cracks curved upwards, increasing surface roughness, and on a larger scale the wafer pieces curved around the PLM spots.

The crystallinity of the PLM samples was investigated with electron backscatter diffraction (EBSD) and Raman spectroscopy. EBSD revealed highly textured polycrystallinity with a correlation between grain orientation and surface morphology, but grain sizes could not be determined with the available setup. Raman spectroscopy did not detect other crystalline phases than silicon, and showed a lessened long range order compared to unimplanted silicon. Raman spectroscopy also showed residual stresses in the crystals in excess of 1 GPa.

Secondary ion mass spectrometry (SIMS) was used to study the effect of PLM on tungsten distribution. The tungsten remained primarily in the bulk, with local concentration peaks at the sample surfaces plausibly due to cellular breakdown. Unexpected

ion yield behaviour during sputtering prompted further investigation of the SIMS craters with WLI, SEM, and AFM.

The electronic band structure of the PLM samples was investigated with photoluminescence (PL) spectroscopy via hyperspectral imaging. There was a strong sub-band gap response, but due to unfortunate experimental conditions, the signal was too noisy to draw any conclusions.

From previous work, it was suspected that W ion implantation had occurred also outside the designated $1 \times 1$ cm$^2$ squares. Using SIMS and Raman spectroscopy, it was shown that an unknown dose of W had been implanted over large areas of the wafer pieces.

# Sammendrag

En overgang til fornybare energikilder er uunnværlig for å motvirke effektene av global oppvarming, og fotovoltaiske solceller er i ferd med å bli en av de mest anvendte løsningene takket deres stadig synkende kostnader og økende effektivitet. Kommersielt tilgjengelige paneler er dog i ferd med å støte mot de teoretiske begrensningene til dagens materialer og teknologier, og nye innovasjoner kreves for å forbedre effektiviteten ytterligere.

En slik innovasjon er en solcelle av et mellombåndsmateriale, som kan lages ved kraftig doping av halvledere med overgangsmetaller. Silisium implantert med sølv har tidligere blitt forsket på som et potensielt mellombåndsmateriale her ved NTNU, og ut ifra resultatene har silisium implantert med wolfram blitt valgt som en ny forskningskandidat.

I denne avhandlingen har enkrystallinsk silisium blitt ioneimplantert med wolfram for å oppnå en wolframkonsentrasjon over løselighetsgrensen ved likevekt. Nominelle verdier for maksimal konsentrasjon av wolfram er 2, 1, 0.1 og 0.01 atom%. Ioneimplanteringen amorfiserte silisiumet, slik vist ved bruk av Raman-spektroskopi, og en krystallstruktur ble grodd på nytt i det implanterte volumet med pulset lasersmelting (PLM). PLM ble gjennomført i vakuum med enkeltpulser fra en eksimerlaser, der laserpulsene hadde gjennomsnittlige energitettheter på 0.9, 1.4 og 1.8 $J/cm^2$.

Overflateegenskapene til det resulterende materialet ble karakterisert med optisk mikroskopi, hvitlysinterferometri (WLI), skanningelektronmikroskopi (SEM) og atomkraftmikroskopi (AFM). Overflatene var fulle av sprekker med tykkelse på nanometerskalaen, og det var en sammenheng mellom sprekkenes mønsterdannelse, andel wolfram i prøvene og anvendt laserenergi. Kantene til sprekkene krummet oppover, noe som økte overflateruheten, og på en større skala krummet også waferbitene seg om PLM-områdene.

Krystalliniteten til PLM-prøvene ble undersøkt med diffraksjon av tilbakespredte elektroner (EBSD) og Raman-spektroskopi. Fra EBSD så man at det var oppstått en finkornet flerkrystall med sterk retningspreferanse for krystallkornene. Størrelsen på krystallkornene kunne ikke avgjøres, men det var en tydelig sammenheng mellom oppdaget krystallinitet og mønsteret på sprekkdannelsen. Raman-spektroskopi oppdaget ikke krystallfaser fra andre stoffer enn silisium, og viste en større uorden i atomanord-

ningen i krystallen til PLM-prøvene i forhold til uimplantert silisiumwafer. Raman-spektroskopi viste også at det var gjenværende stressmoment på over 1 GPa i PLM-prøvene.

Massespektrometri med sekundærioner (SIMS) ble brukt til å undersøke effekten av PLM på fordelingen av wolfram i hovedmassen til silisiumet. Wolframmen forble hovedsakelig nede i materialet, med lokale konsentrasjonstopper ved overflaten, sannsynligvis på grunn av cellulært sammenbrudd. Uventede variasjoner i ioneutbytte under sputtring av prøvene førte til ytterligere undersøkelse av SIMS-kratrene med WLI, SEM og AFM.

De tillatte energinivåene i PLM-prøvene ble utforsket med fotoluminesensspektroskopi (PL) i form av hyperspektral avbildning. Prøvene viste et sterkt signal under båndgapet til silisium, men på grunn av uheldige eksperimentelle forhold var signalet for støyete til å kunne trekke noen solide konklusjoner.

Fra tidligere arbeid var det mistenkt at implantering av wolframioner hadde skjedd også utenfor de angitte områdene på $1\,\text{cm} \times 1\,\text{cm}$. Ved bruk av SIMS og Raman-spektroskopi ble det vist at en ukjent dose med wolfram var blitt implantert over store områder av waferbitene.

# Preface

This thesis concludes Markus' degree of Master of Science in Nanotechnology at the Norwegian University of Science and Technology. The presented work is based on H. Lysne's Ph.D. project about advanced material characterisation of materials intended for use in intermediate band solar cells. The work was carried out in 2019 at the Department of Physics and Department of Material Science and Engineering at NTNU, NTNU NanoLab, NTNU/SINTEF solar characterisation lab, UiO MiNaLab in Oslo, and at the Faculty of Science and Technology at NMBU in Ås.

The layout of this document was made with the printed book version in mind. Readers of the digital version are therefore encouraged to do so with a two-page view, making sure that the cover page is on its own separate line. A dedicated PDF viewer is recommended, so that internal links are clickable and the vector graphics render correctly.

Høvik, Norway
December 19, 2019

Markus J. B. RISTOLA

# Acknowledgements

First and foremost, I would like to express my sincerest gratitude to my supervisor **Turid Worren Reenaas**, and to my de facto and de jure co-supervisors **Hogne Lysne**, **Marisa Di Sabatino Lundberg**, and **Randi Holmestad**. Your feedback in the weekly meetings has been invaluable to the development of this project. I also want to thank you for the encouragement along the way, and am grateful to have been part of your research group this past year.

I would like to thank **Torbjørn Mehl** at NMBU for welcoming me and Hogne to your university at Ås. It was very nice to borrow both the hyperspectral imaging setup and your knowledge of silicon PVs. Thank you too for preparing the data files for analysis. I would also like to thank **Christoph Seiffert** for receiving us warmly at UiO MiNaLab. You worked hard to help us get through as many samples as possible in the allotted time slot. **Håkon Ånes**, I thank you for your help with the EBSD. Your input has been invaluable, especially concerning the Hough transform. To **Sohaib Dastagir**, thank you for your assistance with the AFM measurements. I could not have done them nearly as fast on my own. I would also like to collectively thank the **staff at NanoLab**. You always respond quickly to enquiries, readily share your knowledge, and are an awesome bunch in general.

Lastly, I want to thank my parents for the never-ending love and support. You have always put your kids first and foremost. Though it is of the smaller things you do, it is nice to always receive a few home-cooked meals with me whenever I leave for Trondheim, to get that taste of home on the busiest of days.

# Table of Contents

**Summary** i

**Sammendrag** iii

**Preface** v

**Acknowledgements** vii

**Table of Contents** xi

**List of Figures** xv

**Abbreviations** xvii

**1 Introduction** 1

**2 Materials and Methods** 5
- 2.1 Material Properties . . . . . . . . . . 6
  - 2.1.1 Intermediate Band Basics . . . . . . . . . . 6
  - 2.1.2 Silicon as Host Material . . . . . . . . . . 7
  - 2.1.3 Tungsten-silicon System . . . . . . . . . . 9
  - 2.1.4 W as a Deep-level Impurity . . . . . . . . . . 10
- 2.2 Material Processing . . . . . . . . . . 11
  - 2.2.1 Ion Implantation . . . . . . . . . . 11
  - 2.2.2 Pulsed Laser Melting (PLM) . . . . . . . . . . 12
  - 2.2.3 Cellular breakdown . . . . . . . . . . 12
- 2.3 Characterisation Techniques . . . . . . . . . . 16
  - 2.3.1 Optical Microscopy . . . . . . . . . . 16
  - 2.3.2 Electron Microscopy Techniques . . . . . . . . . . 16
  - 2.3.3 Raman Spectroscopy . . . . . . . . . . 20
  - 2.3.4 Secondary Ion Mass Spectrometry (SIMS) . . . . . . . . . . 24
  - 2.3.5 Atomic Force Microscopy (AFM) . . . . . . . . . . 25

2.3.6 White Light Interferometry (WLI) . . . . . . . . . . . . . . . . 26
2.3.7 Photoluminescence Spectroscopy (PL) . . . . . . . . . . . . . . 28

**3 Experimental Details 29**
3.1 Sample Preparation . . . . . . . . . . . . . . . . . . . . . . . . . 30
3.1.1 Ion Implantation . . . . . . . . . . . . . . . . . . . . . . . . 30
3.1.2 Pulsed Laser Melting (PLM) . . . . . . . . . . . . . . . . . . 31
3.2 Characterisation Techniques . . . . . . . . . . . . . . . . . . . . . 33
3.2.1 Electron Microscopy . . . . . . . . . . . . . . . . . . . . . . 33
3.2.2 Optical Microscopy . . . . . . . . . . . . . . . . . . . . . . . 36
3.2.3 Raman Spectroscopy . . . . . . . . . . . . . . . . . . . . . . 36
3.2.4 Secondary Ion Mass Spectrometry (SIMS) . . . . . . . . . . . 37
3.2.5 White Light Interferometry (WLI) . . . . . . . . . . . . . . . . 38
3.2.6 Atomic Force Microscopy (AFM) . . . . . . . . . . . . . . . . 38
3.2.7 Photoluminescence Spectroscopy (PL) . . . . . . . . . . . . . . 39

**4 Results 41**
4.1 Overview Images and Nomenclature . . . . . . . . . . . . . . . . . 42
4.2 Surface Properties . . . . . . . . . . . . . . . . . . . . . . . . . . 44
4.2.1 Optical Microscopy . . . . . . . . . . . . . . . . . . . . . . . 44
4.2.2 White Light Interferometry . . . . . . . . . . . . . . . . . . . 52
4.2.3 Atomic Force Microscopy . . . . . . . . . . . . . . . . . . . . 56
4.2.4 Scanning Electron Microscopy . . . . . . . . . . . . . . . . . . 59
4.3 Near-surface Properties . . . . . . . . . . . . . . . . . . . . . . . 62
4.3.1 Electron Backscatter Diffraction . . . . . . . . . . . . . . . . . 62
4.3.2 Raman Spectroscopy . . . . . . . . . . . . . . . . . . . . . . 70
4.3.3 Secondary Ion Mass Spectrometry . . . . . . . . . . . . . . . . 75
4.3.4 Hyperspectral Imaging & photoluminescence . . . . . . . . . . 86

**5 Discussion 93**
5.1 Surface Properties . . . . . . . . . . . . . . . . . . . . . . . . . . 94
5.1.1 Surface Morphology . . . . . . . . . . . . . . . . . . . . . . 94
5.1.2 Crack Investigation Technicalities . . . . . . . . . . . . . . . . 97
5.2 Near-surface Properties . . . . . . . . . . . . . . . . . . . . . . . 99
5.2.1 Raman Spectroscopy . . . . . . . . . . . . . . . . . . . . . . 99
5.2.2 Electron Backscatter Diffraction . . . . . . . . . . . . . . . . . 102
5.2.3 SIMS Craters . . . . . . . . . . . . . . . . . . . . . . . . . . 109
5.2.4 SIMS Depth Profiles . . . . . . . . . . . . . . . . . . . . . . 112
5.2.5 Hyperspectral Imaging & photoluminescence . . . . . . . . . . 116

**6 Conclusions 123**

**7 Future Work** **125**

**A Wafer Shape Investigations** **127**

**B WLI Roughness Measurements** **131**

**C WLI SIMS Crater Measurements** **137**

**D µ-PCD of W-D1** **143**

**E More AFM of PLM Samples** **145**

**F Raman of W-D2-F0.9** **147**

**G MATLAB Code** **149**

**Bibliography** **156**

# List of Figures


1.1 Efficiency-cost relation for 1st, 2nd, and 3rd generation solar cells. . . . . 2

2.1 Schematic: Intermediate band formation. . . . . . . . . . . . . . . . . . . 6
2.2 Theoretical IBSC efficiency vs. IB energy level. . . . . . . . . . . . . . . 7
2.3 Tungsten-silicon system phase diagram. . . . . . . . . . . . . . . . . . . 9
2.4 Cellular breakdown in Ag implanted Si, SEM and TEM views. . . . . . 13
2.5 Schematic: Cellular breakdown in Si. . . . . . . . . . . . . . . . . . . . 13
2.6 SIMS depth profiles of cellular breakdown of Au in Si. . . . . . . . . . 14
2.7 Schematic: Interaction of electrons in matter and generated signals. . . 16
2.8 Schematic: Working principles of EBSD and Bragg scattered electrons. 18
2.9 Different orientations of crystals and observed EBSD pattern rotation. . 19
2.10 Diagram of vibrational transitions and Raman scattering. . . . . . . . . 21
2.11 Phonon dispersion curves in c-Si and related Raman peaks. . . . . . . . 23
2.12 Schematic: Working principles of a SIMS instrument with electromagnetic mass separation. . . . . . . . . . . . . . . . . . . . . . . . . . 24
2.13 Schematic: Working principles of an AFM. . . . . . . . . . . . . . . . 25
2.14 Schematic: Working principles of a WLI instrument. . . . . . . . . . . 26
2.15 Schematic: Hyperspectral camera working principles. . . . . . . . . . . 28

3.1 TRIM simulation of W implantation depth. . . . . . . . . . . . . . . . 30
3.2 Schematic: Pulsed laser melting (PLM) setup. . . . . . . . . . . . . . . 31

4.1 Overview image of wafer piece W-D1- . . . . . . . . . . . . . . . . . . 42
4.2 Overview images of wafer pieces W-D0.1 and W-D2. . . . . . . . . . . 43
4.3 Optical micrograph of W-D0.1-F1.8. . . . . . . . . . . . . . . . . . . . 45
4.4 Optical micrograph of W-D1-F1.8. . . . . . . . . . . . . . . . . . . . . 46
4.5 Optical micrograph of W-D2-F1.8. . . . . . . . . . . . . . . . . . . . . 47
4.6 Optical micrographs of F1.4 samples. . . . . . . . . . . . . . . . . . . 48
4.7 Optical micrographs of F0.9 samples. . . . . . . . . . . . . . . . . . . 49
4.8 Optical micrograph detail of surface holes. . . . . . . . . . . . . . . . . 50
4.9 Optical summary of PLM samples. . . . . . . . . . . . . . . . . . . . . 51

4.10 WLI measurement for straight line surface morphology in W-D2-F1.8. . 52
4.11 WLI measurements for rectangular and polygonal surface morphologies. 53
4.12 WLI measurement from an as-implanted sample and W-D1-F1.8. . . . . 54
4.13 Plots of surface roughness vs. PLM laser fluence. . . . . . . . . . . . . 54
4.14 WLI measurement from a large hole in W-D2-F1.8. . . . . . . . . . . . 55
4.15 AFM across cracks in centre of W-D0.1-F1.8. . . . . . . . . . . . . . . 57
4.16 AFM across cracks at edge of W-D0.1-F1.8. . . . . . . . . . . . . . . . 58
4.17 SEM micrographs of cracks in PLM samples. . . . . . . . . . . . . . . 59
4.18 SEM micrographs shallow and deep SIMS craters in W-D1-F0.9. . . . . 60
4.19 SEM micrographs of SIMS craters in F1.8 samples. . . . . . . . . . . . 61
4.20 Effects of combining IQ and crystal orientation maps in EBSD. . . . . . 63
4.21 SEM micrographs and EBSD crystal orientation maps of F1.8 samples. 65
4.22 SEM micrographs and EBSD crystal orientation maps of F1.4 samples. 67
4.23 SEM micrograph and EBSD crystal orientation map for W-D0.1-F0.9. . 68
4.24 Raman spectrum from Fz-Si. . . . . . . . . . . . . . . . . . . . . . . . 71
4.25 Raman spectra from as-implanted samples and accidental implant. . . . 71
4.26 Raman spectra from "FzSi" on W-D1 and W-D2 wafer pieces. . . . . . 73
4.27 Raman spectra from F1.8 samples. . . . . . . . . . . . . . . . . . . . . 73
4.28 Raman stress mapping of sample W-D2-F1.8. . . . . . . . . . . . . . . 74
4.29 WLI image from SIMS crater in W-d0.1-asImp. . . . . . . . . . . . . . 75
4.30 WLI image from SIMS crater in W-D0.1-F18. . . . . . . . . . . . . . . 76
4.31 WLI image of shallow and deep SIMS craters in W-D1-F0.9. . . . . . . 77
4.32 SIMS yield of Si vs. depth for all samples. . . . . . . . . . . . . . . . . 79
4.33 Data point adjustment for SIMS profiles of F0.9 samples. . . . . . . . . 80
4.34 SIMS depth profiles for as-implanted samples. . . . . . . . . . . . . . . 81
4.35 SIMS depth profiles for F0.9 samples. . . . . . . . . . . . . . . . . . . 82
4.36 SIMS depth profiles for F1.8 samples. . . . . . . . . . . . . . . . . . . 83
4.37 SIMS depth profiles for W from accidentally implanted and "FzSi" regions. 84
4.38 Hyperspectral images and PL spectra of wafer piece W-D2. . . . . . . . 87
4.39 Hyperspectral images and PL spectra of wafer piece W-D1. . . . . . . . 89
4.40 Hyperspectral images and PL spectra of wafer piece W-D0.1. . . . . . . 91

5.1 Comparison between PLM morphology and cracked clay. . . . . . . . . 95
5.2 Schematic: Hole formation through explosive boiling. . . . . . . . . . . 96
5.3 Kikuchi patterns from Fz-Si and F1.8 samples. . . . . . . . . . . . . . 103
5.4 Incorrect EBSP indexing for sample W-D2-F1.8. . . . . . . . . . . . . 105
5.5 Incorrect EBSP indexing for sample W-D0.1-F1.4. . . . . . . . . . . . 106
5.6 SEM micrographs of SIMS rippling by Vajo et al. . . . . . . . . . . . . 110
5.7 Comparison between TRIM predicted and SIMS measured W distribution 112
5.8 PL spectra of D-lines by Arguirov. . . . . . . . . . . . . . . . . . . . . 117

A.1 Topographic map comparison of an Fz-Si wafer piece from WLI and contact profilometry. . . . . . . . . . . . . . . . . . . . . . . . . . . 128
A.2 Topographic map of wafer piece W-D1 from WLI. . . . . . . . . . . . 129
A.3 Topographic maps of wafer pieces W-D1, W-D2, and an Fz-Si piece on which PLM was tested, from WLI. . . . . . . . . . . . . . . . . . . . . 130

B.1 WLI roughness measurements for D2 samples. . . . . . . . . . . . . . 132
B.2 WLI roughness measurements for D1 samples. . . . . . . . . . . . . . 133
B.3 WLI roughness measurements for D0.1 samples. . . . . . . . . . . . . 134

C.1 WLI scans of SIMS craters in F1.8 samples. . . . . . . . . . . . . . . . . 138
C.2 WLI scans of deep SIMS craters in F0.9 samples. . . . . . . . . . . . . 139
C.3 WLI scans of shallow SIMS craters in F0.9 samples . . . . . . . . . . . 140
C.4 WLI scans of SIMS craters in as-implanted samples. . . . . . . . . . . 141

D.1 µ-PCD mapping of wafer piece W-D1 before and after PLM. . . . . . . 144

E.1 AFM from the bottom of the SIMS crater in W-D1-asImp. . . . . . . . 145
E.2 AFM from the centre of all PLM samples on wafer piece W-D1. . . . . 146

F.1 Extended Raman spectrum from sample W-D2-F0.9. . . . . . . . . . . 148

# Abbreviations

| | |
|---|---|
| AFM | Atomic Force Microscope/Microscopy |
| a-Si | Amorphous Silicon |
| BB | Band-to-Band |
| BSE | Backscattered Electron(s) |
| CB | Conduction Band |
| c-Si | Crystalline Silicon |
| EBSD | Electron Backscatter Diffraction |
| EBSP | Electron Backscatter Pattern |
| EOR | End-Of-Range |
| Fz-Si | Float-zone Silicon |
| IB | Intermediate Band |
| IBSC | Intermediate Band Solar Cell |
| LA | Longitudinal Acoustic (phonon) |
| LO | Longitudinal Optical (phonon) |
| PL | Photoluminescence |
| PLM | Pulsed Laser Melting |
| PSI | Phase-Shifting Interferometry |
| PV | Photovoltaic |
| SE | Secondary Electron(s) |
| SEM | Scanning Electron Microscope/Microscopy |
| SIMS | Secondary Ion Mass Spectrometry |
| TEM | Transmission Electron Microscope/Microscopy |
| TA | Transverse Acoustic (phonon) |
| TO | Transverse Optical (phonon) |
| TRIM | Transport of Ions in Matter |
| VB | Valence Band |
| VSI/VXI | Vertical Scanning Interferometry |
| WD | Working Distance |
| WLI | White Light Interferometry |
| μ-PCD | Microwave Photoconductance Decay |

| | |
|---|---|
| $\alpha$ | Absorption coefficient |
| $\lambda$ | Wavelength |
| $\vartheta$ | Bragg angle |

*Knowledge, if it does not determine action,*
*is dead to us.*

Plotinus, 3rd century CE

# 1 Introduction

Between 2008 and 2018, the primary energy consumption[1] of the world grew by 18.5 %. Of the total energy consumption, 88.9 % was covered by non-renewable sources, primarily fossil fuels [1]. Greenhouse gas (GHG) emissions into the atmosphere from the consumption of fossil fuels are already estimated to have raised the average global temperature by 1.0 °C compared to pre-industrial levels [2]. The temperature increase is projected to reach 1.5 °C between 2030 and 2052 if emissions continue to increase at current rates. For a temperature increase of 2 °C rather than 1.5 °C, significantly greater negative impacts on climate and society are predicted [2], meaning that it is of utmost importance to explore every avenue possible to reduce GHG emissions. One such avenue is an increased reliance on solar cells as the primary energy source, as the photovoltaic (PV) conversion of sunlight to electric current does not emit any GHGs.

Recent decades have seen significant advances in solar PV technology in regards to efficiency and production costs. As depicted in figure 1.1, PV technology has been divided into three generations based on their specific working principles and costs [3]. The chart shows the conversion efficiency vs. production cost per unit area for the three generations of solar cells. The first generation (I) is based on crystalline Si (c-Si) and GaAs single-junction devices, and has a typical performance of 20 % for commercial

[1] As physicists,we know that energy is neither consumed nor produced, merely converted from one form to another. 'Consumption', however, is how it is reported in all the statistics, and thus the term that will be used here to denote the source of the energy used to perform useful work, heating etc.

cells, with a record attained laboratory efficiency of 26.7 % for silicon [4, 5]. The second generation (II) is based on thin-film technology, with the aim to reduce the costs by decreasing material needs and production costs, at a drawback in efficiency. The third generation (III) is defined by their ability to overcome the single-band gap Shockley-Queisser limit of 31-41 %, which is the theoretical efficiency limit of a single p-n junction PV with loss only from radiative recombination. Current third generation technologies include multi-layer tandem cells, quantum dot cells, dye-sensitised cells, hot carrier cells and intermediate band single junction cells. Third generation solar cells are a current research topic, and have not yet been commercially applied outside spacecraft (except for tandem cells) despite the theoretical high efficiencies [3, 6].

Commercially, about 95 % of the PV market share is c-Si cells. In terms of price per Watt, they are competitive with fossil fuels and other renewable sources on the European and world markets [5]. A significant drawback, however, is the PV covered area required for a substantial power output, owing to their relatively modest efficiency. The development of more efficient third generation solar cells means less competition for land, which is at a premium in urbanised areas. Additionally, they allow relatively lower installation costs versus power output for small consumers who do not benefit from economies of scale, such as for instance commercial solar farms do. Third generation solar cells are therefore a relevant research topic with societal implications.

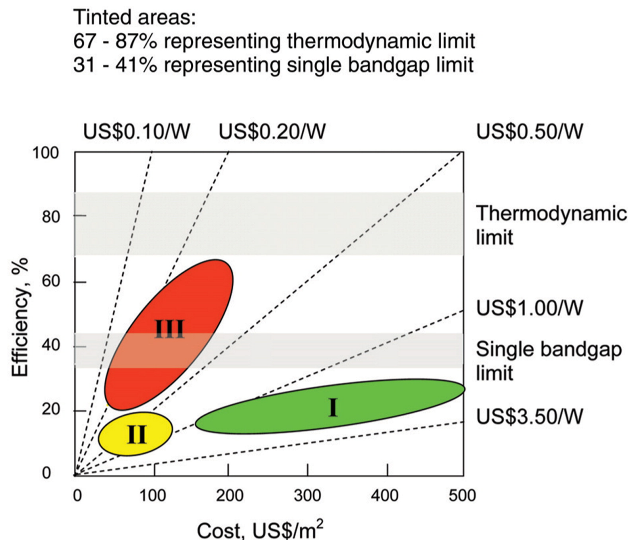


**Figure 1.1:** Efficiency-cost relation for solar cells of the first (I), second (II) and third (III) generations. The shaded area between 31 and 41 % indicates the single band gap ShockleyQueisser limit, while the tinted area between 67 and 87 % indicates the thermodynamic efficiency limit for PV conversion. Figure acquired from [3].

In this thesis, the focus will be on materials for intermediate band (IB) solar cells (IBSC), specifically those based on deep level dopants. IBSCs were conceptualised by Luque and Martí in 1997, and have since gained much interest with multiple proposed approaches to IB formation [7–9]. The deep-level approach is presented in section 2.1.1. Other approaches include arrays of quantum dots, which have been demonstrated with InAs quantum dots in AlGaAs [10], and layering of semiconductors with mismatched electronegativities in 'highly mismatched alloys', such as $ZnTe_{1-X}O_X$ [11].

**At the Norwegian University of Science and Technology** IB materials and IBSCs have been a research topic since 2015. Currently, one studied approach is hyperdoping of float-zone silicon (Fz-Si) wafers via ion implantation, followed by recrystallisation with pulsed laser melting (PLM). Two master's students have previously studied Si implanted with Ag [12, 13]. As expected a large fraction of the silver segregated from the silicon, owing to low solubility and high diffusion rates. The resulting material contained complex structures and local phases of Ag in the bulk of the sample.

In 2017, a new project was therefore initiated with a different dopant - tungsten (W). The working hypothesis is that W should diffuse less in and segregate from the Si, owing to its large size and slow diffusion mechanism. By ion implantation, the peak W concentration can exceed the solubility limit in solid Si. With PLM, it should be possible to recrystallise the ion implanted volume without severe W segregation. The recrystallisation is performed to increase minority carrier lifetime, which is an important metric for real-world performance of solar cells.

In this thesis, the W-implanted and recrystallised Si is investigated. Both bulk and surface properties have been studied, as we know from earlier work that the samples are highly non-uniform. The surface morphology is investigated with optical microscopy, scanning electron microscopy (SEM), white light interferometry (WLI) and atomic force microscopy (AFM). The crystal structure is examined with electron backscatter diffraction (EBSD) and Raman spectroscopy, while the diffusion of W is probed with secondary ion mass spectrometry (SIMS). Electronic properties are investigated with photoluminescence (PL) spectroscopy in the form of hyperspectral imaging.

For a general outline of the thesis, first, relevant theory will be covered for the materials, processing methods and characterisation techniques. A chapter with experimental details for the sample processing and characterisation follows. Next, the results from the materials characterisation are presented. Then, the results are discussed in a separate chapter. Finally, concluding remarks and suggestions for further work are given. Results from some samples on certain instruments will only be presented in the appendices.

*A blind man knows he cannot see, and is glad to be led, though it be by a dog; but he that is blind in his understanding, which is the worst blindness of all, believes he sees as the best, and scorns a guide.*

Samuel Butler

# 2
# Materials and Methods

This chapter will cover the theoretical background for the thesis. The first section will cover the basic principles behind an intermediate band material, the relevant properties of silicon, and the effects of tungsten incorporation into the silicon. The second section will cover the processing techniques used, and some possible effects in silicon with ultra high doping density. The last section will cover the working principles behind the different characterisation methods utilised, namely optical microscopy, white light interferometry, atomic force microscopy, scanning electron microscopy, electron backscatter diffraction, secondary ion mass spectrometry, and hyperspectral photoluminescence imaging.

## 2.1 Material Properties

### 2.1.1 Intermediate Band Basics

While a detailed discussion of IBSCs are outside the scope of this thesis, a basic introduction to the concept will nevertheless be provided. Interested readers are referred to [14] for a more comprehensive review.

As stated in the introduction, the focus in this thesis will be on deep-level IB formation through hyperdoping. By doping a semiconductor with a transition element whose energy states do not overlap with those of the host material, additional states will be introduced within the band gap of the host material. If these states are close to the centre of the band gap, they are termed deep levels, hence the naming. If they are close to the valence or conduction bands, they are termed shallow levels. By increasing the concentration of dopant atoms, the dopant states will increasingly overlap, until they are so dense that the electrons in them become delocalised, and the initially discrete dopant states split into a band of states - the intermediate band. This change in energy level properties is termed the Mott transition, with the critical dopant concentration termed the Mott limit. It is believed that the Mott transition also inhibits non-radiative recombination caused by the deep dopants [15]. The formation of the IB is depicted in figure 2.1.

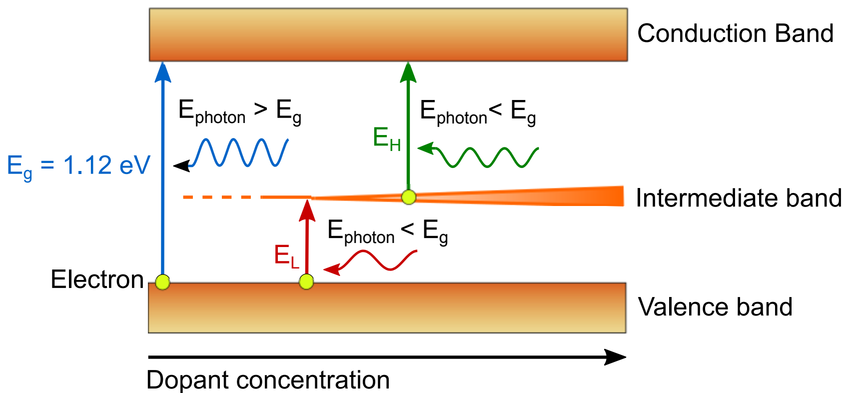


**Figure 2.1:** Schematic representation of the formation of the intermediate band as impurity atom concentration increases. Figure acquired from [16] and slightly modified.

After the formation of the IB the material now has three effective band gaps. Photons with energies below the main band gap may now contribute to the photocurrent of the IBSC by exciting electron-hole pairs across one of the sub-band gaps. Ideally, the IB will be partially filled so that it is able to both receive new electrons and excite existing ones [17]. The properties of the IB would be metallic, allowing the delocalised electrons to transport charge in the material [18].

### 2.1.2 Silicon as Host Material

For this thesis, monocrystalline silicon was chosen as the host material. While the theoretical efficiency limit for an IBSC is 63.2 %, it is for a material with a large band gap of 1.95 eV. Silicon based materials will not be able to match the ideal band gap, with possible silicon-based IBSC efficiencies based on the IB location sketched in figure 2.2, accounting for both overlapping and non-overlapping photon absorption coefficients [19]. When absorption coefficients overlap, a high-energetic photon may cause a low-energetic transition instead of a high-energetic one. As seen in the figure, overlap leads to a degradation in device performance. In theory, an efficiency of 54.8 % is attainable for fully concentrated sunlight (46050 suns), which is a great improvement compared to the ~20 % efficient commercial PVs of today.

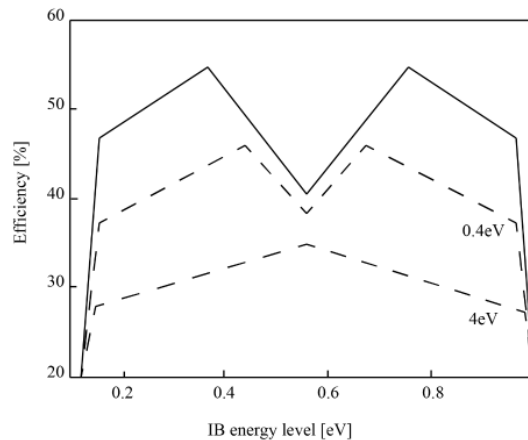


**Figure 2.2:** IBSC theoretical peak efficiency vs IB energy level centre for a Si-based device under fully concentrated sunlight (46050 suns) at 6000 K. The continuous line represents no overlap of photon absorption coefficients, while the dashed lines indicate overlaps of 0.4 eV (top) and 4 eV (bottom). Figure acquired from fig. 2.6 in [12].

From a pure materials processing and manufacturing standpoint, Si has certain redeeming qualities which the III-V materials do not. First, Si is the second most abundant element in the Earth's crust, forming about 27.7 % by weight [20]. Secondly, Si-based solar cells hold about 95 % of the market share, and as such there exists much knowledge about materials processing and manufacturing which may be re-used in IBSC devices [5, 21]. Lastly, solid Si is non-toxic to humans both in elemental form and in silicide compounds, though pulverised silicon compounds do pose health risks [22].

### Light penetration depth

As a number of laser frequencies are employed in this work, it is of interest to know their respective penetration depths into silicon, which is also the depth from which information is obtained. The penetration depth is dependent on the absorption coefficient, which increases as the photon energy approaches the energy of the direct band gap of ~3.4 eV. The penetration depth will therefore decrease for higher laser energies.

The total scattered light intensity from the sample surface to a depth of $d$ is $I_S$, and it is given by the integral

$$I_S = I_0 D \int_0^d e^{-2\alpha x} dx = \frac{I_0 D}{2\alpha}(1 - e^{-2\alpha d}), \tag{2.1}$$

where $I_0$ is the incident laser intensity, $D$ is the scattering cross section, and $\alpha$ the absorption coefficient of Si for a given wavelength. The total scattered light intensity from depth $d$ to infinite depth, $I_D$, is given by the integral

$$I_d = I_0 D \int_d^{\infty} e^{-2\alpha x} dx = \frac{I_0 D}{2\alpha} e^{-2\alpha d}. \tag{2.2}$$

The penetration depth, $d_p$, is now defined as the depth from which 90 % of the scattered light intensity originates, such that the relation

$$I_s = 0.9(I_S + I_d) \tag{2.3}$$

is satisfied. By solving relation 2.3 for $d_p$ using equations 2.1 and 2.2, an expression for the penetration depth is obtained:

$$d_p = \frac{-\ln 0.1}{2\alpha} \tag{2.4}$$

Using eq. 2.4 and values for α from [23], penetration depths for relevant laser wavelengths are calculated and summarised in table 2.1.

**Table 2.1:** Penetration depths and absorption coefficients in silicon for the lasers used in this thesis.

| Laser wavelength [nm] | Penetration depth $d_p$ [nm] | Absorption coefficient α [$cm^-1$] |
|---|---|---|
| 248 | 6.4 | $1.81 \times 10^6$ |
| 532 | 1129 | $1.02 \times 10^4$ |
| 808 | $12.3 \times 10^3$ | $9.37 \times 10^2$ |

### 2.1.3 Tungsten-silicon System

When W is introduced into Si, it is primarily incorporated in a substitutional rather than interstitial manner, owing to the atom's great size. De Luca et. al. [24] reported a solubility limit of 0.15-0.2 at% in the temperature range 837-934 °C. For higher concentrations, it has been reported that clusters of tungsten silicides ($W_xSi_y$) of ~10 nm tend to form after thermal annealing at 900-1100 °C [24, 25], however the exact nature of these clusters could not be determined [24].

In figure 2.3 is shown the equilibrium phase diagram for the tungsten-silicon system for high temperatures. For higher concentrations of W, the melting point is expectedly increased, as W has a higher melting point than Si (3422 °C vs. 1414 °C for the pure metals at atmospheric pressure [26]). During equilibrium cooling, tungsten silicide formation is expected for all concentrations of W. In this thesis, the melting and cooling will not be in equilibrium, so the diagram does not necessarily apply, however the formation of silicides must still be considered a possibility.

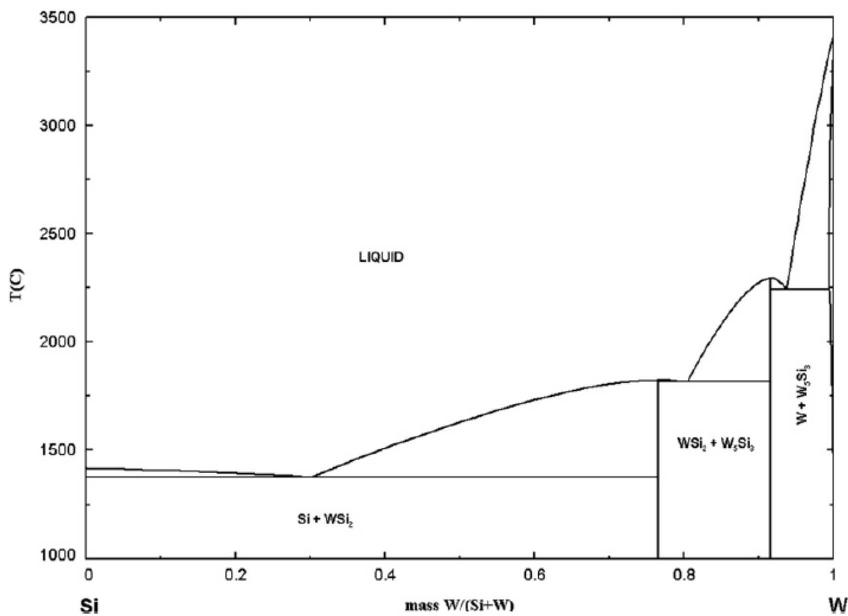


**Figure 2.3:** Equilibrium diagram of the tungsten-silicon system, showing tungsten silicide formation. Figure acquired from fig. 11.3 in [27].

### 2.1.4 W as a Deep-level Impurity

Tungsten is one of the least studied metallic impurities in silicon [24], but has nonetheless been found to introduce deep-level states below the band-gap. There is little consensus on the locations of these energy states, however, and table 2.2 summarises previously reported results. The table gives the energy states relative to the top edge of the valence band ($E_V$) and bottom edge of the conduction band ($E_C$) of Si.

**Table 2.2:** Introduced energy levels of tungsten traps in a silicon host crystal. $E_V$ denotes the top edge of the VB, while $E_C$ is the bottom edge of the CB.

| Type | Energy level [eV] | Year | Reference |
|---|---|---|---|
| Hole trap | $E_V + 0.22$ | 1991 | [28] |
| | $E_V + 0.31$ | 1967 | [29] |
| | $E_V + 0.33$ | 1991 | [28] |
| | $E_V + 0.34$ | 1967 | [29] |
| | $E_V + 0.38$ | 1991 | [30] |
| | $E_V + 0.41$ | 1988/91 | [31, 32] |
| | $E_V + 0.73$[1] | 1983 | [33] |
| Electron trap | $E_C - 0.22$ | 1967/88 | [29, 31] |
| | $E_C - 0.23$[2] | 2014 | [34] |
| | $E_C - 0.25$ | 1977 | [35] |
| | $E_C - 0.28$ | 1977 | [35] |
| | $E_C - 0.30$ | 1967 | [29] |
| | $E_C - 0.37$ | 1967 | [29] |
| | $E_C - 0.59$ | 1991 | [28] |

[1] Only at material interface.
[2] Co-doped with gold.

Due in part to having almost twice the atomic radius of Si, W has a very low diffusion coefficient in the Si matrix [36]. De Luca et. al. [24] found that W exhibited an unusual, linear diffusion profile with a concentration maximum at the sample surface. These findings could not be explained by common models for diffusion of metallic impurities in Si, and they proposed a novel model with simultaneous diffusion of interstitial W-atoms and W-Si atomic pairs. As W occupies mainly substitutional lattice sites, only a small fraction of W atoms are eligible for diffusion under the proposed model, in line with the observed slow kinetics. The diffusion coefficient for W was estimated to be on the same order of magnitude as coefficients for slow-diffusing dopant species such as

As, B, P and Sb, meaning that room temperature diffusion is negligible. Furthermore, higher concentrations of W were associated with cavity formation at the Si surface.

## 2.2 Material Processing

### 2.2.1 Ion Implantation

This section is based primarily on Chapter 7 in [37] by Sze.
To exceed the solubility limit of a dopant in the host matrix, a non-equilibrium process must be used. Ion implantation is such a process, offering precise control over implanted concentrations of various dopant species.

Atoms from the dopant material are ionised, and the ions are accelerated to high velocities. A mass spectrometer is used to select a narrow energy range of ions, and the ions are directed in a focused beam towards a target sample. The beam of focused ions is raster scanned across the surface, with the ions colliding with sufficient energy to penetrate into the bulk.

After entering the material, the ions will transfer energy to the host matrix through elastic and inelastic collisions, until their momentum is depleted and they come to a halt. The incident ions interact with sample atom nuclei, causing scattering of the ions and displacement of lattice atoms with bond breakage and possible defect formation. Also, the electron clouds of the ions interact with those of the sample atoms, leading to host material ionisation and emission of electrons, x-rays and lower energy photons [38]. The ions will eventually come to rest at a certain depth within the material, termed the ion range. The ion range profile may often be approximated by a Gaussian distribution, given in eq. 2.5,

$$n(\chi) = \frac{S}{\sqrt{2\pi\sigma_p}} exp\left[-\frac{(\chi - R_p)^2}{2\sigma_p^2}\right] \tag{2.5}$$

where $S$ is the ion dose per unit area, $R_p$ is the projected ion range, $\sigma_p$ is the standard deviation, and $n$ is the concentration of dopants at depth $\chi$.

The orientation of the ion beam relative to the crystallographic orientation of the sample may also affect the depth distribution of the dopants. If the ion beam is parallel to a high symmetry crystal direction, it is possible for the ions to pass through mostly empty space between the arrays of atoms, penetrating deeper into the material as collisions become infrequent. This effect is known as channelling [39].

The result of the collision events is a degradation and amorphisation of the host material which the ions pass through, giving rise to an amorphous-crystalline (a/c) interface in the bulk below the implanted volume. Below this layer may exist a damaged crystalline region supersaturated with interstitials, known as end-of-range (EOR) defects [40].

### 2.2.2 Pulsed Laser Melting (PLM)

Though amorphous silicon may be utilised for photovoltaics, it is of interest to regain the crystal structure to improve charge transport and reduce non-radiative recombination. Pulsed laser melting (PLM) is a suitable non-equilibrium technique for crystal recovery, being able to rapidly heat and melt the sample. By achieving crystal growth speeds well in excess of dopant diffusion rates, it should be possible to incorporate solute concentrations of W above the solubility limit into the Si lattice [41].

In PLM, one or more pulses from a laser irradiate the implanted sample for short time intervals, commonly in the femto- to nanosecond range. The photons are absorbed, heating the sample, causing it to melt within a few hundred nanoseconds. As the heat is dissipated into the bulk, re-solidification begins as liquid phase epitaxial growth at the liquid-solid-interface [16]. The solidification front achieves velocities on the order of m/s, while the cooling rate may exceed $10^9\,\mathrm{K\,s^{-1}}$ [42]. It has been demonstrated that the partitioning constant increases at high solidification velocities, aiding in dopant incorporation in the crystal matrix of the host material [43, 44].

The nature of the epitaxial re-solidification depends on the ordering of the atoms in the solid phase at the liquid-solid-interface. If the laser has heated the sample sufficiently for the melt to reach the crystal lattice beneath the implanted volume, the lattice may act as a seed and result in single-crystalline recovery of the amorphous region [41, 45]. If the melt does not penetrate the amorphous/crystalline interface before sample cooling, the crystal growth is instead likely to consist of arbitrarily oriented crystal grains [46, 47]. As the boundaries between the grains are associated with increased Gibbs free energy, such systems tend to attempt reduction of this energy by introduction of various defects, such as foreign atoms. Increased dopant segregation is therefore expected for polycrystalline growth. Excessive dopant segregation is likely to lead to a phenomenon termed cellular breakdown.

### 2.2.3 Cellular breakdown

When silicon implanted with low solubility species is recrystallised by PLM, the dopants tend to segregate and form regions of high concentrations. In literature, this is commonly referred to as cellular breakdown [48–54]. Cellular breakdown of silver in silicon is illustrated in figure 2.4, where it appears as a rectangular pattern in a SEM image of the surface (A), and as bright, irregular lines stretching downwards in a TEM image (B). The naming originates from the idea that the bright lines resemble the walls of a plant cell, with a similar separation of silicon and segregated material continuing down into the bulk. This understanding has been shown to be incorrect [54], and the segregation is limited to the near-surface region as seen in the TEM image. While the cellular breakdown of Ag in Si forms squares, calculations by Ma and Plapp predict W to form

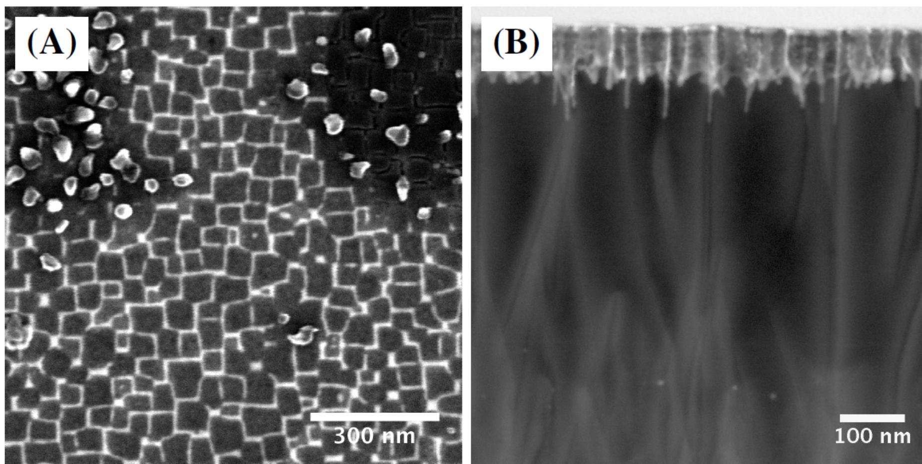


**Figure 2.4:** Cellular breakdown in Si implanted with Ag, showing (a) a surface view acquired with SEM, and (b) a bulk view acquired with STEM. In both images, the bright areas are Ag rich phases. Figure acquired from fig. 2.3 in [13].

hexagonal patterns [55].

Akey et al. [54] studied cellular breakdown of cobalt in silicon with scanning electron microscopy (SEM) and atom probe tomography to investigate the three-dimensional nature of the features. Until then, the assumption was that the cell-like structure continued as walls of dopants into the bulk. Instead, they found that only the top few nm have a cell-like structure, with the structure becoming branched and filamentary in the bulk. A schematic illustration is provided in figure 2.5, showing (a) the rectangular patterning of the surface, from which filamentary structures extend into the bulk, and (b) a digital reconstruction of a single filament based on atom probe tomography.

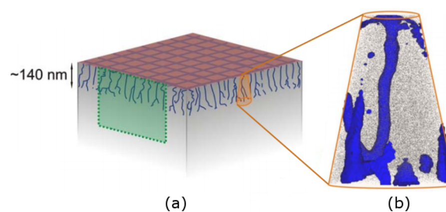


**Figure 2.5:** Schematic illustration of (a) cellular breakdown in silicon implanted with cobalt, with (b) a 3D reconstruction of a filament based on atom probe tomography. While the surface has a square, cellular patterning, the structure in the bulk is filamentary. Figure acquired from [54] and slightly modified.

Cellular breakdown in silicon has been observed for numerous dopants. Recht. et al. [52] studied PLM annealing of Si implanted with Au, Co, Cr, Cu, Fe, Pd, Pt, W

and Zn, and found that all samples displayed either cellular breakdown or severe surface segregation (where the dopants end up on the surface or evaporate). Cellular breakdown has also been studied extensively with regards to incorporation of titanium in silicon [14, 49, 53, 56].

Cellular breakdown has consequences for the resultant dopant concentration depth profile after PLM annealing. Recht et al. [52] doped silicon with gold, and simulated the expected changes in dopant concentration vs. depth in the sample, without taking cellular breakdown into account. The concentration profiles were then measured using secondary ion mass spectrometry (SIMS), with their findings shown in figure 2.6. The initial, as-implanted dopant distribution resembles a Gaussian profile, while the PLM pushes the gold towards the sample surface, where it reaches higher concentrations than simulated in the area where cellular breakdown is observed in the underlaid TEM image. A supersaturated region exists beneath the cellular breakdown.

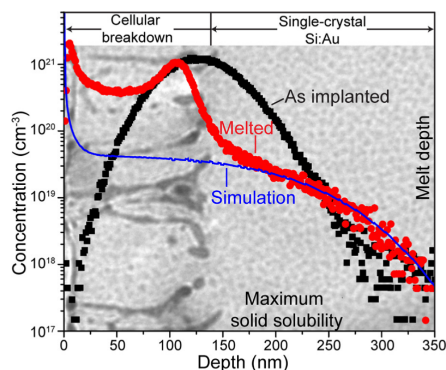


**Figure 2.6:** Concentration profiles of $^{197}$Au in Si obtained with SIMS before and after PLM, as well as a simulated concentration profile which does not take into account cellular breakdown. Graphs are superimposed on a TEM image of the relevant region. Figure acquired from [52].

While the understanding of cellular breakdown formation is not complete, a few concepts are likely to help understand the basic course of events during PLM of highly doped silicon.

Let us regard hyperdoped silicon immediately after absorption of the laser pulse, such that there exists a solid and liquid phase. Generally, a dopant will have a higher solubility in liquid than solid silicon. If the solid phase is supersaturated, the dopant is likely to diffuse across the solid-liquid interface into the liquid phase. As the solidification front moves towards the sample surface, the concentration of the dopant in the liquid phase continues to increase well beyond that of the solid phase [57]. Thus, the dopants are transported towards the sample surface, giving a concentration profile as observed in figure 2.6.

The formation of the filamentary structures inherent to cellular breakdown may be

explained by melting point depression [58], which is a decrease in a material's melting point due to the presence of impurities. Assuming a non-uniform distribution of dopant atoms across the solidification front, the areas with higher dopant concentrations will solidify later than the rest of the crystal. At some point in time, the surface of the material will consist of liquid areas with high dopant concentrations and areas with supersaturated solid phases. Diffusion of the dopants across the solid-liquid interface will continue, amplifying the concentration differences until the temperature is low enough for the dopant-rich areas to solidify as well [54], creating the cellular structure with dopant-rich walls.

## 2.3 Characterisation Techniques

### 2.3.1 Optical Microscopy

This section is based on reference [59].

Optical microscopy is a well-established characterisation technique to view and image samples with visible light, through magnification using a set of lenses. The sample is illuminated with visible light, and a portion of the light is reflected. The reflected light is directed through a set of lenses onto a CCD camera, which generates a micrograph.

### 2.3.2 Electron Microscopy Techniques

#### Scanning Electron Microscopy (SEM)

This section is based primarily on reference [60].

Scanning electron microscopy (SEM) is a microscopy technique used to image a material with electrons, rather than photons, to resolve smaller detail. In SEM, a beam of electrons is accelerated in a magnetic field and focused down to a small point, which is then raster scanned across the surface. The interaction between the beam electrons and the sample gives rise to several different signals of electrons and photons, shown in figure 2.7. The interaction between the beam and the sample may broadly be classified as elastic or inelastic.

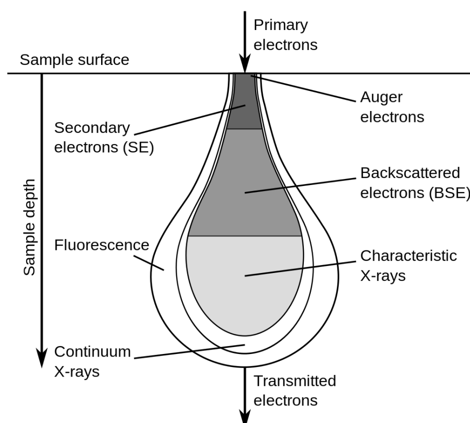


**Figure 2.7:** Different signals generated from the interaction between the primary electron beam and the sample in the SEM. The figure shows roughly the regions from which the signals can be detected; not to scale. Figure from Wikimedia Commons.

In elastic scattering, the beam electrons are deflected with minimal energy loss by sample atom nuclei or outer shell electrons, usually resulting in a wide-angle change in direction. Electrons whose angle is changed by >90° such that they re-emerge from the

sample with almost no energy loss are termed backscattered electrons (BSE). The BSEs may be used to image the top layers of the sample, in which case the presence of atoms of differing atomic numbers will give contrast in the image, as heavier atoms are ore likely to cause backscattering. BSEs may also be used to probe the crystallinity of the material through diffraction, as covered in section 2.3.2.

In inelastic scattering, energy is transferred from beam electrons to atoms in the sample through various interactions. In some cases, ionisation of the sample atoms will cause outer shell electrons to become ejected from the material with low energies (<50 eV). These are termed secondary electrons (SE), and originate from very near the surface (some material dependency, but typically within 3 nm [61, 62]). The SE signal is greatly influences by edge effects, as they increase the effective volume from which the SEs may escape. Thus, contrast for this mode is mainly topographic, with marked intensity increases near edges.

In a different inelastic process, a beam electron may knock out an inner shell electron, leaving a core hole. An outer shell electron relaxing into this core hole may emit its extraneous energy in the form of a photon (characteristic x-ray), or by transferring it to a valence electron which is summarily ejected from the atom (Auger electron). Heavier elements typically relax with photoemission, while lighter elements emit Auger electrons, however in both cases chemically identifying information about the host atom is obtained.

#### Electron Backscatter Diffraction (EBSD)

This section is primarily based on references [60, 63].

Electron backscatter diffraction (EBSD) is a technique used to map the crystallographic orientations of a sample by detecting backscattered electrons. When highly energetic primary electrons from the beam interact with lattice planes in a crystalline material, some of them will become elastically scattered according to Bragg's law, given in equation 2.6.

$$2 \cdot d_{hkl} \cdot sin\theta_{hkl} = n \cdot \lambda \tag{2.6}$$

$d_{hkl}$ is the interplanar spacing, $\theta_{hkl}$ is the Bragg angle, $n$ is the order of reflection, and $\lambda$ is the primary electron beam wavelength. The interplanar spacing and Bragg angle are related to the Miller indices (h k l).

An electron backscatter diffraction pattern (EBSP) is created from the Bragg scattered electrons by capturing them on a flourescent phosphor screen, which is imaged by a camera. During this process, the primary electron beam is stationary relative to the sample. The diffraction pattern on the phosphor screen will appear as a regular arrangement of bright bands, termed Kikuchi bands, on a continuous background of varying intensity. If the lattice planes were extended out of the sample, they would intersect

the screen in the centre between the pairs of lines that form the edges of their related Kikuchi bands, as is visualised in figure 2.8.

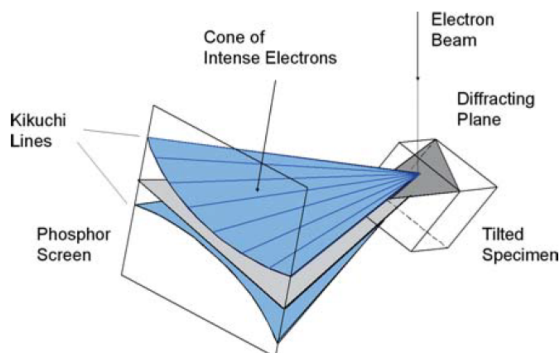


**Figure 2.8:** Schematic representation of EBSD, with the Bragg scattered electrons from the incident primary beam projecting the diffracting atomic plane on the phosphor screen in the form of Kikuchi lines/bands. Acquired from figure 1.2 in[63].

The mechanisms which determine the exact shapes and intensities of the Kikuchi bands are complex, involving i.a. the atomic scattering factor for electrons, the fractional coordinates of the scattering atom in the unit cell, and the orientation of the unit cell. The angular width of the Kikuchi bands is $2\theta_{hkl}$, and is related to the interplanar spacing per equation 2.6, while the angles between projected plane normals correspond to real, interplanar angles.

The act of relating the Kikuchi bands to the crystal structure is termed indexation. As established, the centrelines of the bands correspond to the intersections of the lattice planes with the phosphor screen, and thus each Kikuchi band may be indexed with the Miller indices of the diffracting plane family from which it is formed. Intersections of Kikuchi bands will therefore correspond to the zone axes of the crystal. As the angular width of the bands is $2\theta_{hkl}$, the width (w) on the phosphor screen may through eq. 2.6 be approximated as

$$w \approx l \cdot 2\theta_{hkl} \approx \frac{nl\lambda}{d_{hkl}}$$

where l is the distance between the sample and the screen. Planes with wider spacing will thus give narrower bands. Finally, the orientations of the bands and their relative intensities relate to the orientation of the crystal, as exemplified in figure 2.9. A correct indexation of the EBSP will therefore give the crystal structure and orientation(s) of the sample.

The signal to noise in EBSD is inherently poor, with the background on which the Kikuchi patterns are superimposed having an intensity up to 25 times that of the useful signal. Additionally, a host of factors such as surface stress, surface contamination, local phases, variations in probe current, alignment drift and specimen charging may negatively impact the signal.

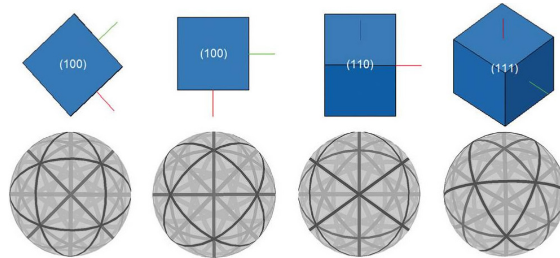


**Figure 2.9:** Different spherical EBSPs generated by rotating a cubic crystal. Depending on the axis of rotation, both the shapes and intensities of the Kikuchi bands may change in an unintuitive manner, because the the pattern is a 2D projection of a 3D structure. Figure acquired from [64].

The spatial resolution of EBSD is governed primarily by the excitation volume, and not only the diameter of the electron beam at the point of impact, typically being an order of magnitude less than the imaging resolution for the same SEM. The excitation volume in this context is understood as the fraction of the interaction volume of the primary electrons from which pattern-forming backscattered electrons leave the sample without further scattering. By tilting the sample steeply to 70°, the excitation volume is limited to approximately 20 nm of depth in the sample, but is greatly increased along the surface in the tilt direction. The excitation volume increases for higher acceleration voltages and lower atomic weight materials. An accurate estimate of actual resolution would require experimental determination for any given sample set. For Al, which directly precedes Si in the periodic table, spatial resolution has been measured to around 1 µm at 20 kV accelerating voltage [65], and may be seen as indicative for our Si samples.

It is important to note that spatial resolution does not depend on the actual magnification of the SEM, as it does not change the beam spot size. Thus, mapping of large specimen areas does not imply any inherent decrease in resolution.

### 2.3.3 Raman Spectroscopy

This section is primarily based on references [66–68].

Raman spectroscopy is a technique based on the inelastic scattering of coherent light to examine the highly specific vibrational fingerprint of a material. It is based on the Raman effect, discovered by Indian physicist Chandrashekhara Venkata Raman in 1928. By probing vibrational stretching and bending modes, information is gained about chemical composition and the short-range order of atoms. Well-defined repetitive structures, such as crystal lattices, will give rise to sharp peaks in the Raman spectra, as the vibrations are coherent also over long-range order. Broad bands indicate large variations in binding configurations, or defects in the case of crystalline solids.

When a photon interacts with matter, it may excite a molecule from a lower electronic state to a higher electronic state, should the photon energy match that of such a real transition within the material. The excited molecule may later relax, emitting a photon with energy equal to that of the incident photon. If the energy of the incident photon does not match a real electronic transition within the material, a scattering event takes place. Scattering may be elastic or inelastic. In the elastic case, the energy (and thus wavelength) of the photon will not change, and the process may be regarded as a brief excitation into a transient virtual intermediate state, followed by relaxation with photon re-emission. In the inelastic case, the photon energy is changed following interaction with a phonon in the lattice or other molecular vibrations. Not all vibrations or phonons may give rise to Raman scattering, as it is also dependent on symmetry and polarisability of the material. Only one in $10^6 - 10^8$ photons will undergo Raman scattering; the rest are scattered elastically.

The elastic and inelastic scattering processes are illustrated with a Jablonski energy diagram in figure 2.10. In the elastic case (a), the frequencies of the incident and re-emitted photons are identical. In the first inelastic case (b), the system relaxes from the virtual state into a vibrationally excited state, and the energy of the emitted photon is less than that of the incident photon ($\hbar\omega_i > \hbar\omega_s$). This is termed a Stokes shift, and the magnitude of the Stokes shift is what is most commonly measured in Raman spectroscopy. In the second inelastic case (c), the system relaxes to a lower vibrational state than it was in upon photon absorption, and the result is a gain in energy for the re-emitted photon ($\hbar\omega_i < \hbar\omega_a s$). This is termed an anti-Stokes shift. It is symmetric to the Stokes shift, with the relative intensities of the Stokes and anti-Stokes shifts governed by the relative populations between vibrational states. At room temperature, the Stokes shift is much stronger.

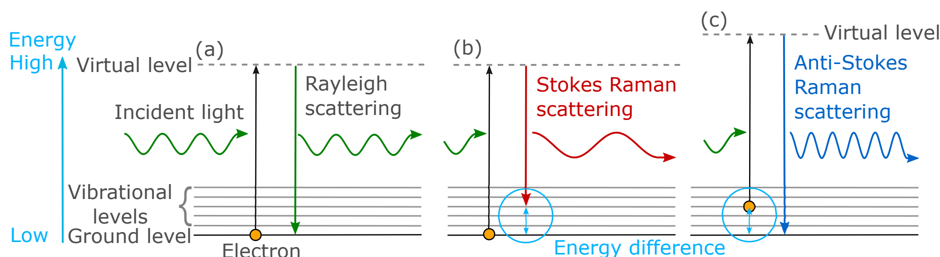


**Figure 2.10:** Jablonski energy diagram of the scattering of light in matter, showing (a) elastic scattering with no change in frequency, (b) inelastic scattering with a loss in frequency (Stokes shift) and (c) inelastic scattering with a gain in frequency (anti-Stokes shift). Figure re-drawn according to fig. 2.6 in [69].

In a crystalline solid, Raman scattering occurs on phonons propagating in the crystal. In the case of a Stokes shift whereby the photon loses energy, the incident radiation may be viewed as transmitting energy to the crystal by creating a phonon. Total energy, momentum, and wave vector are conserved in the creation of the phonon, whose propagation direction depends on the angle of the incident radiation. Due to the momentum transfer from photons being near-negligible, the magnitude of the wave vector of the created phonon will typically be several orders of magnitude lower than for phonons at the first Brillouin zone edge of the crystal. Thus, for first order Raman scattering involving a single phonon, only phonons very close to the Brillouin zone centre will contribute to Raman scattering in a crystal, creating narrow bands in the spectrum. For multi-phonon processes, the shapes of bands may wary greatly, as well as their point of origin in the Brillouin zone.

An amorphous solid may be modelled as a collection of same-formula chemical units, with varying bond lengths and angles. For an amorphous solid, the concept of phonons therefore no longer applies, as there is no long-range symmetry for waves to travel through. However, it is expedient to continue using the term 'phonon' here to describe vibrational excitations in the solid, as the first order bands in the Raman spectrum closely approximates the phonon density of states across the Brillouin zone for the a crystalline solid of the same material [70, 71]. Consequently, the variation of chemical bond lengths and angles manifests itself in the Raman spectrum as very broad bands.

**Raman scattering on silicon.** As the selection rules for Raman active modes are mathematically complex, it is convenient to look only at the expected results for silicon. Because of the cubic symmetry of the silicon lattice, the optical phonon branches are triply degenerate at the Γ-point, as shown in figure 2.11 (a). These phonons give rise to the first order peak in c-Si, located at approximately 521 $cm^{-1}$ at room temperature and under no mechanical stress. This peak, as well as peaks caused by multi-phonon interactions in c-Si, have been identified in figure 2.11 (b). Both transverse (T) and longitudinal (L) phonons in optical (O) and acoustic (A) branches have Raman active modes.

For amorphous silicon, broad bands have been identified centred around 150, 300 and 480 $cm^{-1}$. [72, 73].

**Curve fitting.** To fit curves to Raman peaks, it is conventional to use a Lorentzian function, given by

$$L(x) = \frac{1}{\pi} \frac{\frac{1}{2}\Gamma}{(x - x_0)^2 + (\frac{1}{2}\Gamma)^2}, \tag{2.7}$$

where $x_0$ is the position of the peak, and $\Gamma$ a parameter specifying the width, equal to the peak full width at half maximum (FWHM). For practical purposes, the function is rewritten as

$$L(x) = \frac{A}{1 + (\frac{x - x_0}{\gamma})^2}, \tag{2.8}$$

where $A$ is the amplitude, and $\gamma$ is another width-specifying parameter, equal to the peak half width at half maximum (HWHM).

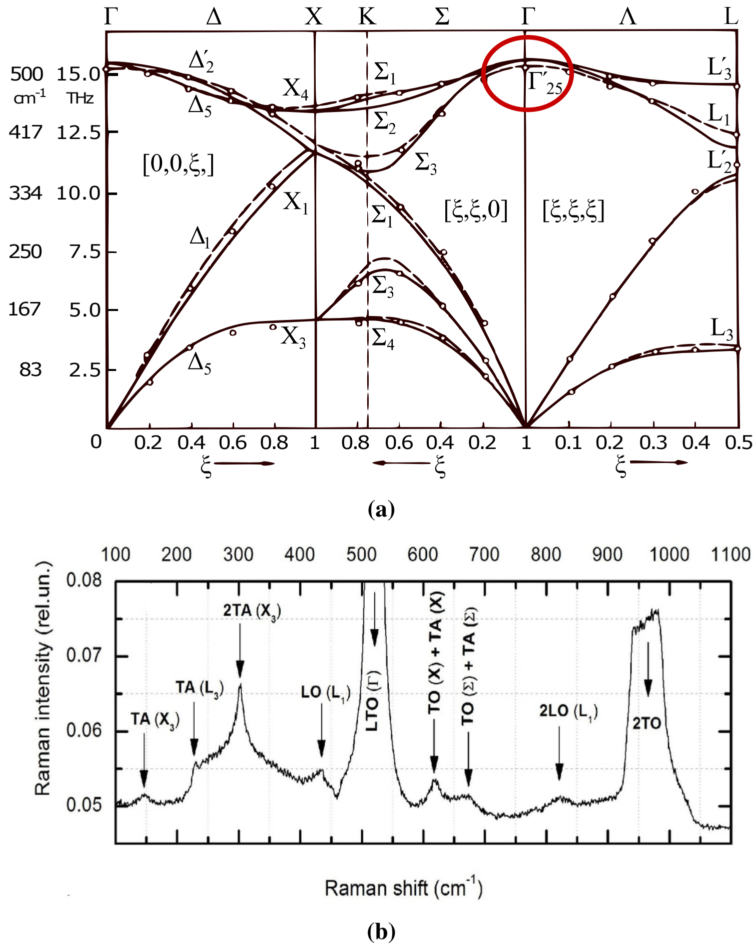


**Figure 2.11:** (a) Phonon dispersion curves and (b) resulting Raman spectrum from crystalline silicon. The red circle in (a) indicates the Γ-point of the phonons on which first order scattering occurs. In (b) are labelled the high-symmetry points on which multi-phonon scattering occurs, with acoustic (A), optical (O), transverse (T) and longitudinal (L) phonons participating. Sub-figure (a) is re-drawn based on [74], while (b) is acquired from [75].

### 2.3.4 Secondary Ion Mass Spectrometry (SIMS)

Section based primarily on reference [76].

Secondary ion mass spectrometry (SIMS) is a destructive method for determining the elemental composition of a sample. In SIMS, a target sample is sputtered with a highly energetic primary ion beam. Transfer of the impact energy causes ejection of microscopic particles from the sample, some of which become ionised (secondary ions). The secondary ions are then accelerated and focused into a mass spectrometer, which is able to determine their chemical species and even specific isotope. The instrument is schematically presented in figure 2.12. To achieve sufficient mean free paths for the atoms, high vacuum is required by this technique. SIMS is highly sensitive, being able to detect concentrations down to $10^{12}$-$10^{16}$ atoms/cm$^3$ (ppm-ppb regime).

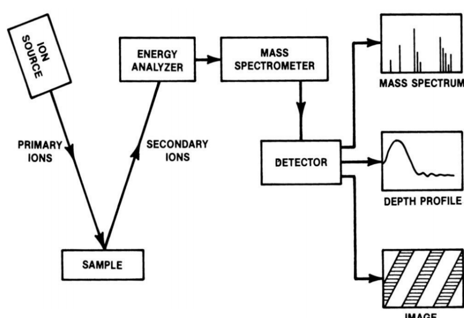


**Figure 2.12:** Schematic representation of SIMS. A target sample is sputtered by a highly energetic primary ion beam, ejecting secondary ions from the sample. The secondary ions are accelerated and passed through a mass spectrometer. Figure acquired from [77].

In the mass spectrometer, mass separation is performed sequentially with electrostatic and magnetic fields, termed sectors. The secondary ions are accelerated to a given potential and directed into the sectors as a focused beam. The electromagnetic forces will deflect the ions, with the magnitude of the deflection depending on their mass and charge state. By passing the beam through a slit, a narrow range of ion masses may be selected, which are then counted by a sensor, e.g. an electron multiplier or a Faraday cup.

SIMS has challenges related to the quantifiability of results, as the yield of secondary ions varies greatly with local chemical conditions (matrix effect), sputter ion energy, sputtering angle, surface roughness, charge transfer effects, relative species concentration, crystal orientation and other conditions. These variations are further impacted by instabilities in the ion beam, mass spectrometer or vacuum conditions, overall creating a complex system where perceived ion yield variations may not correspond to real variations in concentration.

### 2.3.5 Atomic Force Microscopy (AFM)

In atomic force microscopy (AFM), a sharp tip is raster scanned across a surface. Conventionally, the tip is kept in contact with the surface, and the forces generated by the inter-atomic van der Waals interaction between tip and sample surface cause the tip to become displaced in the z-direction. The displacement is recorded, and a topographic map is obtained. By changing the tip material, other interaction mechanisms may be utilised, such as thermal, electric, magnetic etc. The tip is also often tapped up and down, rather than dragged across the surface.

To obtain sub-atomic precision in the z-direction, the tip is mounted at the end of a flexible cantilever, as illustrated in figure 2.13. A laser beam is reflected off the back of the cantilever onto a position-sensitive photodiode, and the deflection of the beam gives the position of the tip. An auto-adjusting feedback loop keeps the laser centred on the detector, such that large, systematic variations in height do not affect the measurements. The use of the cantilever also allows other measurement modes than constant contact, such as rapid tapping.

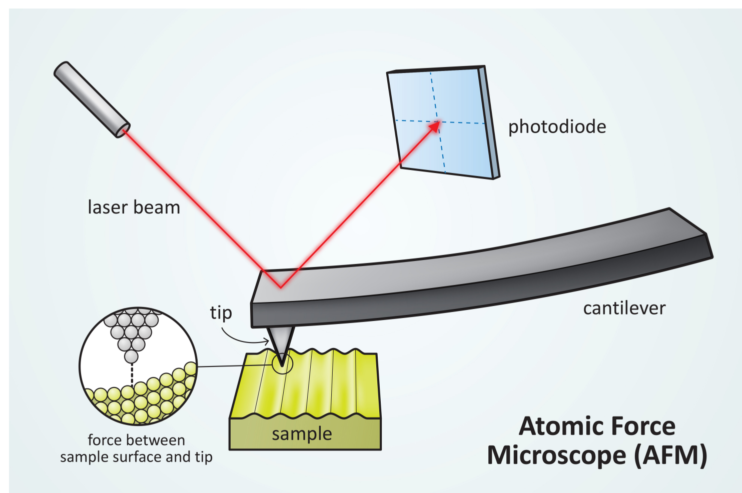


**Figure 2.13:** Schematic presentation of an AFM. A sharp tip is mounted at the end of a flexible cantilever, and the deflection of the cantilever is measured by laser. Figure acquired from [78]

### 2.3.6 White Light Interferometry (WLI)

This section is based primarily on references [79–82].

In interferometry, a beam of light from a single source is divided and recombined. If there exists a phase difference between the beams of light at recombination, an interferogram is formed. By combining multiple patterns, it is possible to determine the difference in path lengths for the two beams. In WLI, multiple wavelengths of light are used simultaneously and analysed separately to increase sensitivity. As the path length is determined from the interferogram, spatial resolution is much smaller than the wavelength of the light used.

A schematic representation of an interferometer is provided in figure 2.14. A beam of light exits the light source, and is split in two by a beam splitter. One beam is reflected off the sample, while the other is reflected off a reference mirror. The two beams are recombined by the beam splitter, and directed through a focusing lens onto a CCD camera, which images the resulting interferogram. For the interferogram to form, it is required that the wavefronts of the two reflected beams not be parallel. This may be accomplished by a tilt of the reference mirror, or more commonly the sample stage.

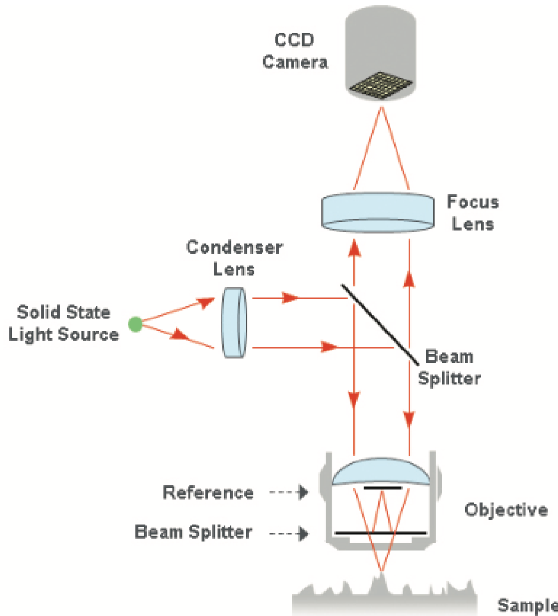


**Figure 2.14:** Schematic representation of a WLI instrument. A beam of light is split, with the reflections from a reference mirror and sample surface recombined to form an interferogram. This configuration of beam splitter and reference mirror is known as a Mirau interferometer. Figure acquired from [83].

The interferogram appears as a set of interference fringes. The spacing between fringes corresponds to a path difference of $\lambda$ between the interfering wavefronts, where $\lambda$ is the wavelength of the light analysed. By varying the distance between the beam splitter and the sample, the lateral position of the fringes will shift, with the magnitude of the shift corresponding to the rate of change of height in the sample. By using white light and splitting it into its spectral components, multiple interferograms may be acquired simultaneously, improving accuracy. The combination of many interferograms gives a topographic map of the sample surface.

In vertical scanning interferometry (VSI), the shift of fringes between interferograms is achieved by moving the objective vertically. Fringes will only appear at sample points in focus, meaning that every point on the sample is always measured at best focus, and the maximum measurable height difference is limited only by the movement range of the objective. Height resolution is limited by objective movement step size. VXI is a form of VSI with different data processing algorithms, reducing artefacts for rough surfaces.

In phase shifting interferometry (PSI), the height of the objective is changed slightly to shift the fringes by only $\lambda/4$. The fringes are then interpreted as a direct topographic map of the surface. For this measurement mode, monochromatic light is used. For flat surfaces, this method provides much greater height resolution compared to VSI/VXI, but the low phase shift limits the measurable height difference between two neighbouring points to $\lambda/4$. In practice, green light of $\lambda$ = 532 nm is often used, giving a practical height limitation between neighbouring features of 130 nm.

### 2.3.7 Photoluminescence Spectroscopy (PL)

This section is primarily based on references [84, 85].

Photoluminescence spectroscopy (PL) is used to probe the electronic structure of a material. It is done by exciting electrons in the target material with a laser, and analysing the re-emitted photons arising from radiative recombination of electron-hole pairs. The emitted photon energies are characteristic of the emitting material, as the frequency relates to the internal electronic states of the material. In an intrinsic semiconductor, the dominant transition would be from the edge of the conduction band to the edge of the valence band. Transitions to states in the band gap introduced by e.g. dopant atoms or lattice defects will also be measurable, granted that they facilitate radiative recombination.

Additionally, a signal is expected from excitons in the material. An exciton is a quasi-particle made up by both an electron and a hole. An exciton may be formed when a photon is absorbed and generates an electron-hole pair, but Coulomb forces keep them spatially bound to one another. The exciton energy is very close to that of the band gap. Upon creation in a semiconductor, the exciton often manifests as a free (Wannier) exciton, with a distance between the electron and hole of several unit cells, and with an ability to move about the lattice. Upon encountering a donor or acceptor impurity, the exciton may become bound to it, eventually annihilating radiatively [86].

In hyperspectral imaging, the spectroscopic capabilities of PL are combined with the spatial imaging properties of a camera. In the image, each pixel contains a complete PL spectrum, relating electronic properties to a physical space on the sample. The working principles of the hyperspectral camera are demonstrated in figure 2.15. The radiation from the sample is separated into its wavelength components with a diffraction grating, and a lens focuses the divergent beam on the 2D detector, recording spatial and spectral information along separate directions.

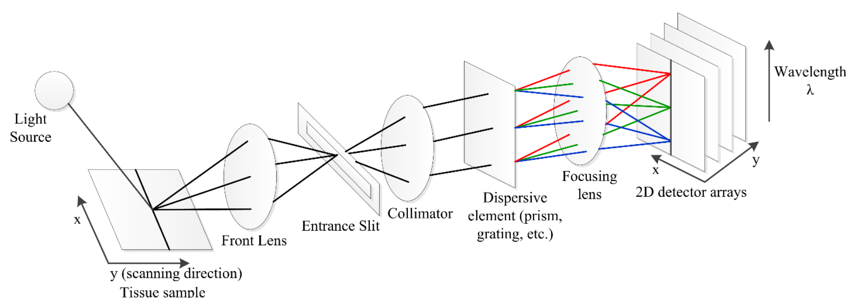


**Figure 2.15:** Schematic representation of a hyperspectral camera. A narrow laser line is scanned across the sample. Re-emitted photons are collimated and split into their wavelength components by a grating. The optics focus the divergent beams on the 2D detector such that spectral and spatial information are recorded simultaneously along separate directions. Figure acquired from [87].

*Remember, kids, the difference between screwing around and science is writing it down.*

Adam Savage, Mythbusters

# 3 Experimental Details

This chapter will cover the experimental details for the practical work in the thesis, and is divided into two parts. The first part covers the details relating to sample preparation, that is, ion implantation and pulsed laser melting. The second part covers sample mounting and experimental parameters for the characterisation techniques used, with enough detail that the experiments may be repeated.

## 3.1 Sample Preparation

### 3.1.1 Ion Implantation

The sample set originates from a single 4 inch wafer of single-crystalline p-type float-zone silicon (Fz-Si), which was cut with scriber and breaker into multiple smaller pieces. Of these pieces, 4 rectangular pieces with approximate dimensions of 2 cm × 3 cm were sent to ion implantation at the University of Surrey Ion beam Centre. On each piece was implanted a single 1 cm × 1 cm square of W, with nominal peak concentrations of 2, 1, 0.1 and 0.01 atomic% at 0.5 µm depth into the sample. Referred to as dosages D2, D1, D0.1 and D0.01, the peak concentrations correspond to $1 \times 10^{21}$, $5 \times 10^{20}$, $5 \times 10^{19}$ and $5 \times 10^{18}$ atoms/cm$^2$, respectively. Ion implantation was performed at an angle of 7° with respect to the wafer surface normal to reduce channelling effects.

The ion implantation profiles were simulated in advance with Transport of Ion in Matter (TRIM) calculations to determine the experimental parameters necessary to achieve the concentration peaks at 0.5 µm of depth. TRIM simulations were performed by H. Lysne [88]. An expected distribution profile from TRIM calculations is shown in figure 3.1, though the simulations do not take into account channelling effects. An ion energy of 1800 keV was used for all implantations to achieve the same implantation profile in every sample.

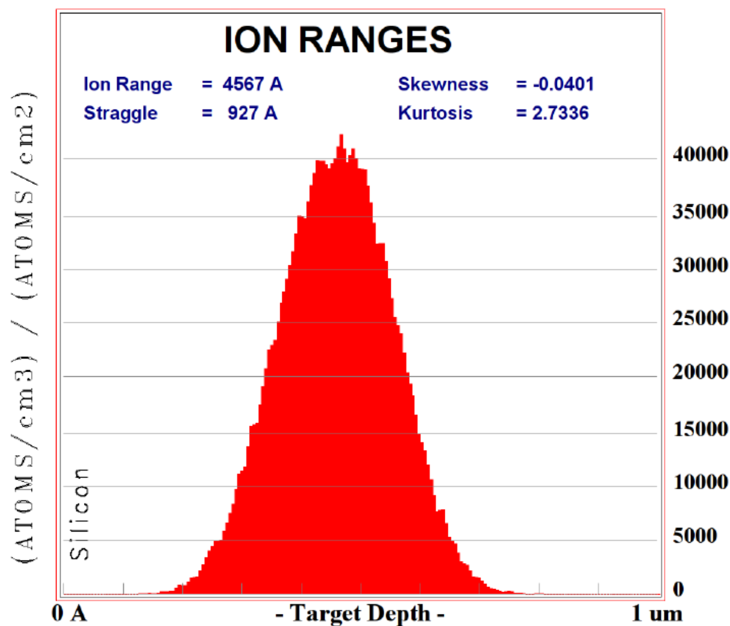


**Figure 3.1:** TRIM simulation of the distribution profile of W in Si achieved through ion implantation. The calculations were performed by Lysne [88].

During implantation, the ion beam flux was monitored by having the samples act as Faraday cups, counting each ion impact on the wafer pieces. Total implantation time was ~14 hours, and the ion source experienced a failure during the procedure. Despite the challenges, instrument logs indicate that the implantation was performed as specified. However, previous work on the samples suggests W implantation outside the $1 \times 1$ cm squares. Also, the designated square of 0.01 at.% W has not been possible to locate through any microscopic or spectroscopic method utilised in this thesis.

### 3.1.2 Pulsed Laser Melting (PLM)

Pulsed laser melting (PLM) was carried out in vacuum to recrystallise ~2x2 $mm^2$ areas on the samples after ion implantation by firing single pulses. PLM was performed with a COMPex Pro ultraviolet KrF excimer laser at 248 nm wavelength from Lambda Physik. The laser pulses have a full width at half maximum (FWHM) duration of 25 ns. The setup is a modified pulsed laser deposition (PLD) system, and is depicted schematically in figure 3.2.

The laser beam is directed through a series of mirrors, a mask and a focusing lens, before entering the vacuum chamber through a window, hitting the sample(s) on the targeting carousel at 45° incidence. The laser mask is a steel plate with a rectangular 9 mm × 13 mm holes, allowing only the central, most homogeneous part of the beam to pass. The positions of the mask and target carousel are fixed, such that the laser will always produce nearly identical, rectangular spots, measured to 0.0363 $cm^2$ (error on the order of $10^{-5}$ cm) by Lysne [88].

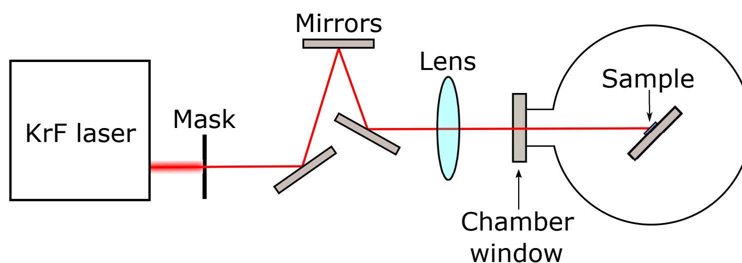


**Figure 3.2:** Schematic illustration of the PLM setup. The KrF excimer laser fires a pulse, which is guided through a set of mirrors into the PLD chamber, where the sample is mounted. Before being focused into the chamber by the lens, the outer parts of the beam are blocked by a mask. Fixed distances between the components ensure that the size of the laser spot will remain unchanged between fluence series.

Before each series of shots at the samples, the laser fluence was recorded with a photometer placed directly in front of the PLD chamber window, as the fluence output is dependent on the fill level of KrF gas in the laser. The target and obtained laser fluences for the three series of shots are given in table 3.1, as calculated by Lysne [88]. The laser fluences were chosen based on COMSOL Multiphysics simulations of heat transfer in Si during PLM [89]. Losses from transmission through the chamber window are taken into account in the calculations.

**Table 3.1:** Target and calculated laser fluences for PLM on W-implanted samples. Calculations were performed by H. Lysne [88].

| Target Fluence [J/cm$^2$] | Calculated fluence [J/cm$^2$] | Fluence error [J/cm$^2$] |
|---|---|---|
| 0.9 | 0.91(8) | 0.06(6) |
| 1.4 | 1.48(1) | 0.10(6) |
| 1.8 | 1.88(8) | 0.13(5) |

# 3.2 Characterisation Techniques

## 3.2.1 Electron Microscopy

### Scanning Electron Microscopy (SEM)

SEM investigations were performed with either a Zeiss Ultra 55 Limited Edition (LE) at the NTNU Department of Materials Science and Engineering, or a FEI SEM Apreo at NTNU NanoLab. Which SEM was used to acquire a specific image will be stated together with the result.

The samples were mounted on a stainless steel holder with spring-loaded, flexible clamps. As the clamp arms were made of a copper-beryllium-alloy, a piece of aluminium foil was placed between the sample(s) and the arms to prevent copper diffusion into the silicon. For the Zeiss Ultra 55 LE, the sample holder was then attached via screw to a base plate, which mounted a socket in the SEM chamber. As the sample holder did not quite lie flat against the base plate due to a mismatch in screw size, a piece of folded aluminium foil was placed in-between the base plate and sample holder to make their surfaces parallel. For the FEI SEM Apreo, the sample holder was inserted into a socket in the motorised stage.

After sample insertion, the chamber was pumped to vacuum, the beam was aligned and corrected for astigmatism, and the sample was brought to focus. Beam alignment and stigmators were re-adjusted after every change in accelerating voltage, to ensure best focus.

If the sample was imaged with the Zeiss Ultra 55 LE, it was done in conjunction with EBSD investigations, and the SEM state would be the same as during EBSD pattern collection, i.e. ~25 mm WD at 70° tilt, 20 kV voltage and high beam current. The imaging signal is SE, however, and not BSE.

Imaging on the FEI SEM Apreo was done over a range of settings. The relevant parameters are included with each presented micrograph. The only common factor is the WD of ~10 mm, as it is optimal for the SE Everhart-Thornley detector.

### Electron Backscatter Diffraction (EBSD)

EBSD investigations were performed with the Zeiss Ultra 55 LE field emission (FE) SEM at the Department of Materials Science and Engineering, NTNU. A fluorescent screen imaged with a CCD camera served as the BSE detector.

The sample mounting was as described above for SEM imaging. Sample tilt was always 70° at approximately 25 mm working distance (WD). Accelerating voltage was set to 20 kV, aperture size to the maximum of 300 µm and probe current to 'high'. After beam alignment and adjustment, the vertical centre of the region of interest (ROI) was brought to focus. Dynamic focus of roughly 5 % was then applied to achieve the best

focus in the ROI as a whole.

The electron backscatter patterns (EBSPs) were collected with Nordif 3 software, for which collection parameters are given in table 3.2. Prior to collection, calibration points were assigned in the ROI. The software did some evaluation of the point, likely an attempted indexation of the pattern in the point, and either accepted or rejected it. Unfortunately, the software was liable to crash upon rejection of a calibration point. As the likelihood of rejection was greater for higher pattern resolutions, varying resolutions were achieved for the different samples, as seen in the table, with none attaining the specified 480 $\times$ 480 px max. resolution of the detector.

Indexing of the acquired EBSPs was done with TSL OIM Data Collection 7. The EBSPs are transformed into Hough space, where the Kikuchi bands are detected as peaks. The input parameters for the Hough transform are given in table 3.3. The software is calibrated via semi-manual assignment of the pattern centre on patterns acquired from calibration spots on the sample. Finally, image quality (IQ) and crystal orientation maps were imaged from the indexed EBSPs with TSL OIM Analysis 7.

**Table 3.3:** Input parameters in TSL OIM Data Collection 7 for indexing of EBSPs obtained from all W-doped samples.

| Parameter | Value |
|---|---|
| Indexing for | Si |
| Binned pattern size [px] | 96 |
| Theta step size [°] | 0.5 |
| Rho fraction [%] | 88 |
| Min. peak count | 3 |
| Max. peak count | 7 |
| Min. peak magnitude | 1 |
| Min. peak distance | 10 |
| Peak symmetry | 0.50 |
| Vertical bias [%] | 0 |

**Table 3.2:** Input parameters in Nordif 3 for EBSD measurements on all W-implanted samples, performed with the Zeiss Ultra 55 LE FE-SEM. Includes specific magnification and working distance per measurement. Aq. and Cal. are shorthand for acquisition and calibration, respectively.

| Sample | **W-D2-F1.8** | | **W-D1-F1.8** | | **W-D1-F1.4** | | **W-D0.1-F1.8** | | **W-D0.1-F1.4** | | **W-D0.1-F0.9** | |
|---|---|---|---|---|---|---|---|---|---|---|---|---|
| Parameter | Cal. | Aq. | Cal. | Aq. | Cal. | Aq. | Cal. | Aq. | Cal. | Aq. | Cal. | Aq. |
| Resolution [px] | 160x160 | 96x96 | 160x160 | 96x96 | 240x240 | 96x96 | 240x240 | 120x120 | 160x160 | 120x120 | 160x160 | 120x120 |
| Exposure time [µs] | 12450 | 3950 | 12450 | 4116 | 19950 | 4495 | 24950 | 4950 | 12450 | 6616 | 16616 | 7642 |
| Frame rate [fps] | 80 | 250 | 80 | 240 | 50 | 220 | 40 | 200 | 40 | 200 | 60 | 130 |
| Gain | 1 | 4 | 1 | 4 | 1 | 4 | 1 | 4 | 1 | 4 | 1 | 4 |
| WD | 25.2 | | 25.0 | | 25.9 | | 24.9 | | 24.9 | | 25.0 | |
| Magnification | 50 | | 45 | | 200 | | 65 | | 65 | | 50 | |

### 3.2.2 Optical Microscopy

Optical microscopy was performed at NTNU NanoLab with a Carl Zeiss AxioScope A1 differential interference contrast (DIC) microscope running bundled AxioVision software. Mounted to the top of the microscope is a 3.3 megapixel CCD camera for micrograph capture.

The samples were placed on standard glass microscopy slides which were mounted on the sample stage. Focus was achieved by adjusting the height of the stage, and contrast was adjusted by adjusting the illumination intensity of the microscope halogen lamp. The software was set to always display the maximal range of greyscale values. Exposure time and white balance were adjusted through the automated features in the software. The DIC feature was not used as the samples are opaque to visible light.

### 3.2.3 Raman Spectroscopy

Micro-Raman Spectroscopy was performed with a Renishaw InVia Reflex Spectrometer System using Renishaw WiRE 4.1 software. The excitation source was a 532 nm Renishaw RL532C100 laser with a maximum power output of 100 mW.

The sample was placed on a standard microscope glass slide, which was mounted to the instrument stage using a clamping mechanism. The sample was brought to focus with the desired objective, and the highest laser power that did not saturate the detector or modify the sample properties was selected. For the Fz-Si and PLM annealed samples, this was 50-100 mW (chapter 5.2.1 that they were barely heated above room temperature at full laser power). For the as-implanted samples, laser powers of $\leq 10$ mW were used, as higher settings were sufficient to locally recrystallise the surface, and also leave burn marks. Exposure time was set so that detector saturation was avoided (min. 1 s), and signal-to-noise ratio was improved through tens to thousands of accumulations. The accumulations were automatically compared to remove spurious lines in the spectra stemming from cosmic rays hitting the detector. For the 532 nm laser, a 2400 $mm^{-1}$ diffraction grating was used.

For line and map measurements, a FocusTrack was set up to adjust the focus for each measurement. The FocusTrack was set to operate with a simple search algorithm, whereby it would step the stage through a range of Z-values to minimise the size of the laser spot, as detected with the CCD camera. The search range was set to 2 µm with steps of 0.1 µm.

### 3.2.4 Secondary Ion Mass Spectrometry (SIMS)

Depth profiles of W concentration in the samples were obtained using Secondary Ion Mass Spectrometry (SIMS). The measurements were performed with a Cameca IMS 7F at MiNaLab, University of Oslo, together with Cristoph Seiffert, who calibrated and operated the instrument. A positive primary beam of $O^+$ at 10 keV was used to sputter the target at 25° of incidence, continually raster scanning square craters between $150 \times 150$ and $200 \times 200$ μm$^2$ in size. The generated secondary ions were extracted at 5 keV and separated in the mass spectrometer using an electrostatic sector and a magnetic sector. The sectors cycled through the specified masses, with a wait time for cycling of 2 s and counting time of 1 s. The secondary ions were detected with an electron multiplier (EM) at $3419 \pm 2$ V with a background level of less than 0.01 count/s. The EM had a saturation threshold of $1.39 \times 10^6$ counts/s, after which a Faraday cup would be used, but saturation was not reached in the presented measurements. Vacuum chamber pressure was 4.4-6.8 $\times 10^{-9}$ mbar during sputtering.

The sample holder was a hollow cylinder with a coarse mesh at one end. The samples were placed upside-down inside the cylinder such that the regions of interest were visible through the mesh. Springs were then placed on the sample backsides, and a plate was added to the other side of the cylinder, so that mechanical tension from the springs would keep the samples pressed against the mesh.

**W signal calibration**

The signal from $^{30}Si_2^+$ was recorded for every depth series and used as a baseline for W signal calibration, based on the assumption that the Si signal would be proportional to the sputtering rate. Thus, by dividing the W signals by the Si signal, effects from sputter speed variations are avoided and any change would presumably result primarily from an actual change in W concentration. Simultaneous capture of the Si signal was possible due to it being within 6 orders of magnitude of the $^{183}W^+$ and $^{184}W^+$ signals of interest, avoiding detector saturation.

To relate the sputtering cycles to depth, all of the SIMS craters were later investigated with a Bruker CountourGT-K 3D Optical Profiler. The experimental details for the acquisitions are given in section 3.2.5. The SIMS craters and surrounding area were imaged using vertical scanning interferometry (VSI), and the built-in step detection algorithm was used to three-dimensionally evaluate the height difference between the surface plane and the bottom plane of the craters. Additionally, manually averaged Z-profiles across the centre of the craters along the X and Y axes were obtained and compared to the results from the step detection algorithm. The step detection and manual results were in good agreement; within a few nm, and the depths reported by the algorithm were used when possible. For PLM samples of fluence 0.9 J/cm$^2$ , the crater bottoms were too rough to be detected by the step algorithm, and an average of the X and Y profiles were

used to determine depth. The depth calibration is presented as a result in section 4.3.3.

### 3.2.5 White Light Interferometry (WLI)

White light interferometry was performed at NTNU NanoLab with a Bruker CountourGT-K 3D Optical Profiler running bundled Vision64 software. The instrument is comprised of a tilting sample stage and a lifting tower housing the light source and interferometer. Samples were placed on the stage, and brought into focus by adjusting the height of the tower such that interference fringes were visible. The stage tilt was then adjusted such that the interference fringes were oriented diagonally on and numbered 3-7 across the features of interest. Light intensity and fine focus were adjusted automatically by the software, which also removed extreme statistical outliers.

For vertical scanning interferometry (VSI/VXI), white light was used with forward and back scan lengths both set to 8 µm. Measurements were averaged over 5-10 scans with a scanning speed of 1 X. For phase shift interferometry (PSI), green light of 532 nm was used with a signal-to-noise threshold of 2 % and averaging over 10-15 scans. For measurements where the total height difference was less than ~50 nm, planar phase unwrapping was used for greater accuracy in the PSI measurements. As the profiler is fitted with 2.5X, 20X and 50X main objectives and 0.55X and 2X zoom objectives, a wide range of magnifications is possible. The actual magnification is stated with each presented result, as well as whether it was measured with VSI/VXI or PSI.

The presented heightmaps were created later with Gwyddion 2.55, and correspond well - but not exactly - to the data in Vision64. The discrepancies are likely to stem from different data levelling algorithms and some information loss in file conversion from Bruker's proprietary .OPD to the open source .SDF. In the main sections of this work, heightmaps are presented as top-down orthographic projections of 3D surface renders with an imposed false-colour map. The introduction of shading makes their understanding more intuitive, but does make the displayed colour value correspond less well to the key in the colourbar. In the appendices, purely 2D colourmaps are presented.

### 3.2.6 Atomic Force Microscopy (AFM)

Atomic force microscopy (AFM) was performed at NTNU NanoLab with a Bruker AFM Dimension Icon running bundled NanoScope software. Measurements were performed together with Sohaib Dastagir, who aligned and operated the instrument. The instrument is comprised of a horizontally moving sample stage and a vertically moving tower where the probe is situated. The probe is mounted at the end of a cantilever, the position of which is measured by two lasers.

Before the sample is loaded, the stage is moved to an adjustment position where the lasers are re-aligned on the cantilever. After sufficient alignment is done, the sample is

placed on the stage, and the probe tower is brought above the sample and lowered close to the surface. Scanning parameters are entered, and the tower is lowered the rest of the way until the probe contacts the surface, initiating the scan. Scanning was performed using the tapping 'ScanAsyst in air' probe mode, with line lengths of 10/25 µm and resolutions of 256/512 px. Positioning of the probe on the sample surface was helped by an optical camera. The limited field of view and poor observed contrast on the sample surfaces made it difficult to land the probe within ~100 µm of the intended spot.

### 3.2.7 Photoluminescence Spectroscopy (PL)

Hyperspectral imaging with photoluminescence (PL) spectroscopy was carried out at the Norwegian University of Life Sciences (NMBU) together with Torbjørn Mehl, who calibrated and operated the instrument. Sample illumination was achieved with a 2 W laser at 808 nm, and the hyperspectral image was recorded with a SWIR Specim near-infrared camera from Spectral Imaging ltd. The camera uses a HgCdTe detector with a lateral resolution of 320 pixels and a spectral resolution of 256 channels, ranging from 0.4899 eV to 1.3344 eV. The spectral resolution is non-uniform, being denser for lower energy values. On the camera lens was mounted a 805 nm low pass filter.

The instrument setup consists of a stationary stage and a movable rig mounted above housing the camera and laser, everything in turn mounted inside a cabinet with shutters to block out ambient light. The sample stage is made of aluminium, and it houses a liquid $N_2$ cooling system with Styrofoam insulation. Evaporated nitrogen from the cooling system escapes from the top, producing some air turbulence above the sample stage. A pane of polycarbonate glass is mounted between the camera and sample stage to lessen the air turbulence contributions from the camera's cooling fans. The temperature of the stage is monitored via thermocouple probe.

Prior to measurement on the samples, the camera lens was focused by scanning on solar cells of known thickness. The stage was then cooled to <90 K with liquid $N_2$, and the height was adjusted to account for thermal compression and the thickness difference between the solar cells and our samples. The samples were then one-by-one placed on the stage and scanned by the laser-camera-rig, with shutters closed. All samples were scanned over three times, and a median was taken to produce the presented measurements. As there was a possibility for the camera to skip recording of individual lines, the data files had to be manually verified and possibly adjusted manually, before further processing. File integrity verification, median calculation and background noise subtraction were performed by Torbjørn Mehl.

It should be noted that the samples immediately developed a thin layer of frost on the surface after coming in contact with the cooled sample stage, as unfortunate weather conditions impacted the humidity in the laboratory. Despite dehumidifiers running at full capacity, they could not keep the humidity within normal levels.

*Measure what is measurable, and make measurable what is not so.*

Galileo Galilei

# 4 Results

The results from the material characterisation are presented in this chapter. The chapter is divided into three main sections. The first section explains the sample nomenclature and presents an overview of the sample set. The second section is focused strictly on the physical surface of the samples. The third section will investigate the crystallographic, compositional and electronic properties of the samples.

The results are presented on a per-instrument basis. The exception is WLI, where measurements of the sample surfaces will be presented first, while measurements from the SIMS craters will be presented together with the SIMS depth calibration and profiles.

## 4.1 Overview Images and Nomenclature

As detailed in the previous section, the sample set consists of pieces of silicon with and without ion implantation, some of which have been recrystallised with PLM. The pieces which have undergone no processing, and were not sent to implantation, are denoted **Fz-Si**. The pieces which have undergone tungsten ion implantation follow nomenclature on the form of **W-D#-F#-suffix**, where the first # denotes peak implanted W concentration in atomic% and the second # denotes the laser fluence used during recrystallisation in J/cm$^2$. Because each wafer piece was only implanted with a given concentration of tungsten, W-D2, W-D1 and W-D0.1 refer to physically separate wafer pieces. An suffix at the end may further restrict the area of interest. For tungsten implanted samples where no PLM has been performed, the F#-parameter is omitted. The sample nomenclature is visualised in figures 4.1 and 4.2.

A practical example with sample W-D1-asImp: 'W-D1' signifies that we are investigating the wafer piece which has been implanted with tungsten at a peak concentration of 1 at.%, while 'asImp' restricts the scope to the as-implanted area. Naturally, PLM annealed spots within the implanted area are excluded here, as they would be referred to as for instance W-D1-F1.8.

Regarding suffixes, in addition to 'asImp', there is '**"FzSi"**', which refers to nominally unimplanted areas on the W-D1 and W-D2 wafer pieces. The areas were assumed to be identical to the unprocessed Fz-Si pieces, but the results show that this is not the case. To prevent confusion with the actual Fz-Si pieces, quotation marks were added and the hyphen was removed. The areas may be referred to as e.g. W-D1-"FzSi".

**Figure 4.1:** Overview image for wafer piece W-D1 from optical stitching. The area with 1 at.% W implantation is indicated with a yellow border and labelled "asImp". The "FzSi" area is indicated with a white border. The PLM spots of fluences 0.9 J/cm$^2$ , 1.4 J/cm$^2$ , and 1.8 J/cm$^2$ are indicated in their respective colours of blue, red, and cyan, and labelled F0.9, F1.4, and F1.8. Purple arrows indicate SIMS sputter craters, while orange ones denote TEM wells.

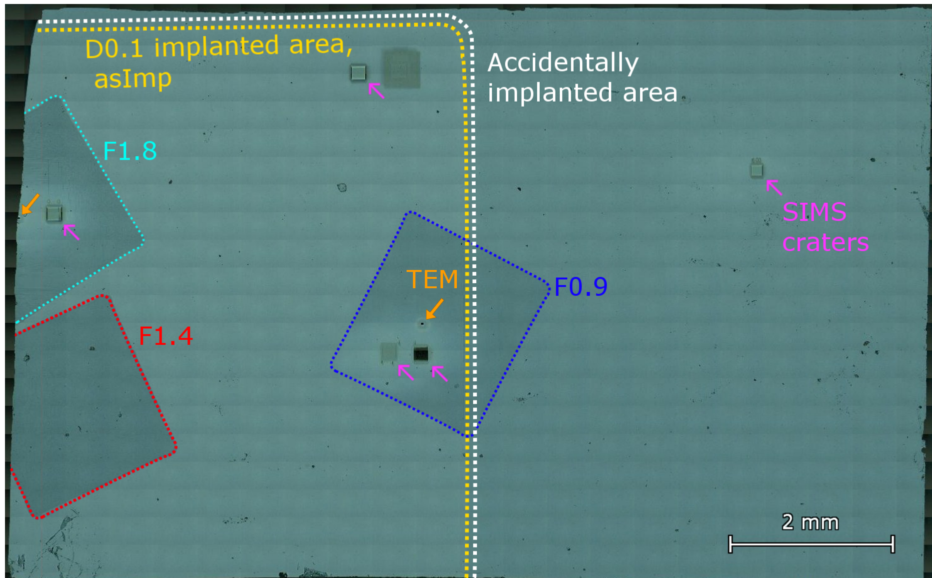


**(a)**

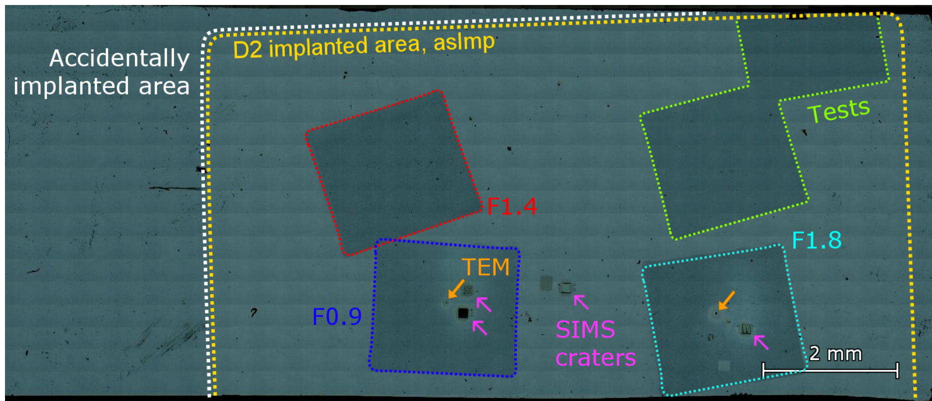


**(b)**

**Figure 4.2:** Overview image for wafer pieces (a) W-D0.1 and (b) W-D2 from optical stitching. The area with respectively 0.1 and 2 at.% W implantation are indicated and labelled "asImp". The PLM spots of fluences 0.9 J/cm$^2$ , 1.4 J/cm$^2$ , and 1.8 J/cm$^2$ are indicated in their respective colours of blue, red, and cyan, and labelled F0.9, F1.4, and F1.8. The green Purple arrows indicate SIMS sputter craters, while orange ones denote TEM wells.

# 4.2 Surface Properties

## 4.2.1 Optical Microscopy

Optical microscopy was performed to assess surface features resulting from the PLM. Optical microscopy was chosen as it provides a good balance between level of detail and field of view, being able to image almost an entire PLM spot at once. The primary focus in this section will be major features and overall morphology. As such, the PLM samples shot with a laser fluence of 1.8 J/cm$^2$ will be given the most attention, as they display the full range of morphologies obtained for all samples. For these samples, full, high-resolution images of the PLM spots will be presented. For PLM samples of laser fluences 1.4 J/cm$^2$ and 0.9 J/cm$^2$, smaller cut-outs showing the change in morphology across the sample centre will be shown instead.

**Sample W-D0.1-F1.8.** An optical micrograph of sample W-D0.1-F1.8 is shown in figure 4.3. The very centre of the sample is dominated by a large, continuous area of even surface, with what appears to be slight, vertically-aligned ripples throughout. Towards the edges, this area is broken by a multitude of straight, near-parallel lines, oriented diagonally with respect to the PLM spot edges. The lines do not cross, and meet at orthogonal angles. Towards the very edge, the scale of features rapidly diminishes, and the lines form rectangles, which increase in irregularity as distance to the edge of the PLM spot decreases. Eventually, the rectangles devolve into a polygon-like structure with random wall orientations. Along the left edge specifically, there is a sharp cut-off from straight lines into polygons.

Other surface features include black circles of varying sizes. By adjusting the focus and zoom, and also from measurements with an optical profiler (section 4.2.2), these are determined to be depressions in the surface, and will henceforth be referred to as holes. The largest circular surface structures are visibly textured, with a black outer rim. These are determined to be protrusions from the surface via similar methodology to hole determination. Outward from some of the holes are extended lines of random orientations, with the number of lines increasing with the size of the feature from which they originate. The square, dark feature near the middle surrounded by a bright halo is a well for TEM samples.

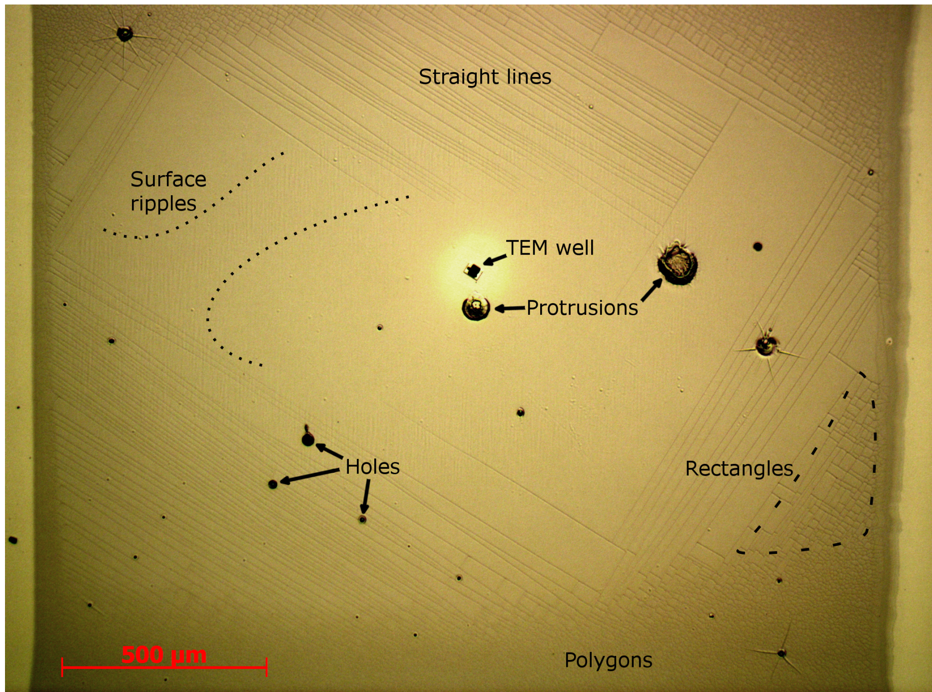


**Figure 4.3:** Optical micrograph of sample W-D0.1-F1.8, showing the overall surface morphology, and its change from straight lines to a polygonal structure. Also present are holes and a TEM sampling well.

**Sample W-D1-F1.8.** An optical micrograph of sample W-D1-F1.8 is displayed in figure 4.4. The central morphology for this sample is quite similar to that of the W-D0.1-F1.8 sample, with large areas of smooth surface broken by straight lines. For this sample, the straight lines are less dense and exhibit a lesser degree of parallelism, though they are more consistently spaced across the surface. Towards the edges, the change in morphology from lines to polygons is abrupt, with a rectangular structure evident only along the bottom left and right edges. The polygonal structure along the edges is larger in scale for this sample compared with the previous sample.

The most prominent surface structure for the W-D1-F1.8 sample is a canyon-like structure at the top right, with curvature such as would be expected from a strand of hair. A multitude of holes of various sizes is present, with some hosting randomly oriented lines. In the very centre is again a square TEM-sample well with surrounding bright area, and down and to the right of it is a square depression with 200 µm sides formed during SIMS sputtering. The two other highly luminous areas, a square and an oval, are similarly results of ion beam damage.

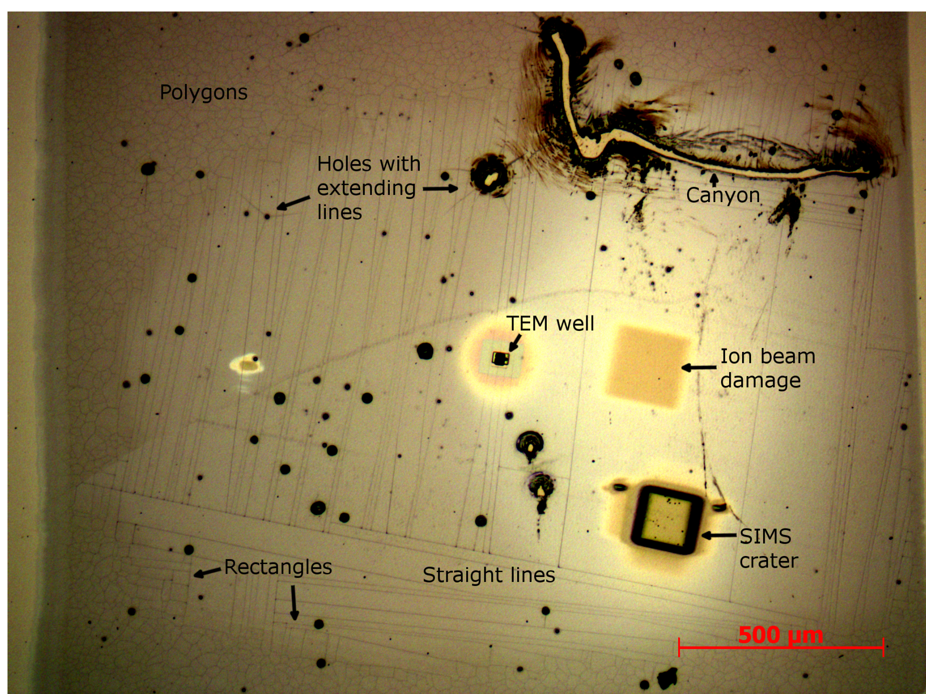


**Figure 4.4:** Optical micrograph of sample W-D1-F1.8, showing the overall surface morphology, and its change from straight lines to a polygonal structure. Also present are features such as holes, a canyon, TEM sampling well and a sputtering crater.

**Sample W-D2-F1.8.** The last sample of fluence 1.8 J/cm$^2$ is W-D2-F1.8, and its micrograph is displayed in figure 4.5. Immediately evident is the great reduction in size of the central area with straight line morphology. The shape of this area is also irregular with respect to the previous samples, resembling a dented oval with a square tail on the right side. The degree of parallelism and density of lines is similar to that of sample W-D1-F1.8. The transition from lines, to rectangles, to polygons is abrupt, though quite uniform along all edges.

This sample, too, exhibits holes of various sizes, many of which have lines extending out from them. The dark squares with highly luminous halos are again wells dug with a focused ion beam for TEM sample preparation.

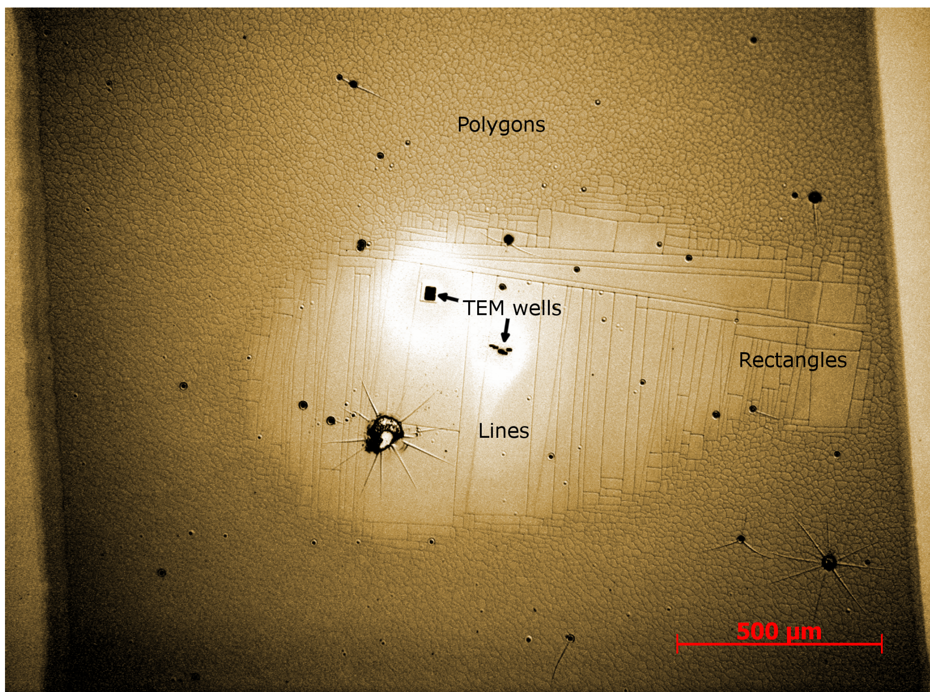


**Figure 4.5:** Optical micrograph of sample W-D2-F1.8, showing the overall surface morphology, and its change from straight lines to a polygonal structure. The area of line-morphology is greatly reduced with respect to samples of similar laser fluence, but lower W concentration.

**Fluence 1.4 J/cm$^2$ samples.** Moving onto samples annealed with lower laser fluences, the edge-to-edge surface morphology for PLM spots with a laser fluence of 1.4 J/cm$^2$ is displayed in figure 4.6, with W concentrations of 0.1 at%, 1 at% and 2 at% at the top, middle and bottom, respectively. For W-D0.1-F1.4, a rectangular morphology is present in the middle, reminiscent of the structures seen for the higher laser fluence F1.8. The scale is smaller, however, and towards the edges it devolves into a polygonal structure of random wall orientation, as seen for the previous samples. Both small and large holes from which lines extends are present. For sample W-D1-F1.4, there is a large-scale polygonal structure with random wall orientations throughout the sample, with intermittent subdivision into smaller-scale structures, with the frequency of the smaller scale structures increasing towards the edges. Holes are present in varying sizes, with the middling ones tending to sport a lesser amount of outwards extending lines than the largest holes. For W-D2-F1.4, the structure of randomly oriented polygons is uniform throughout the sample. Only from the largest holes do lines extend outwards for this laser fluence.

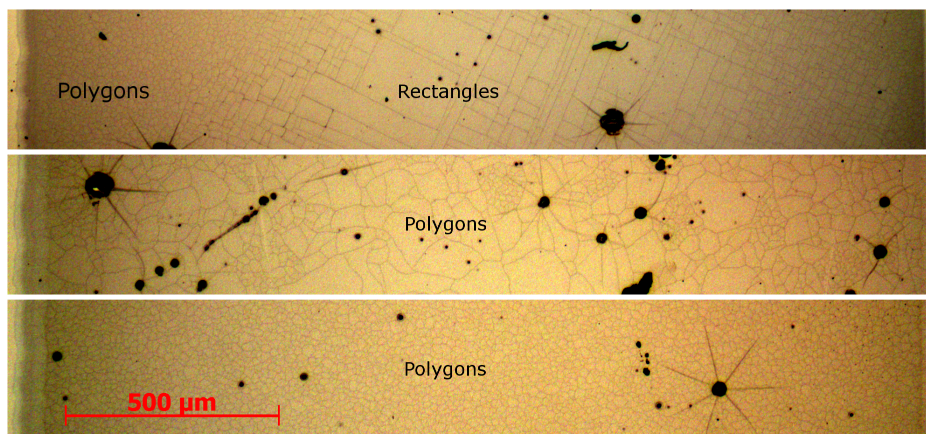


**Figure 4.6:** Optical micrograph cutouts showing representative surface morphologies for (top) W-D0.1-F1.4, (middle) W-D1-F1.4 and (bottom) W-D2-F1.4, from edge to edge through the centre of the samples.

**Fluence 0.9 J/cm$^2$ samples.** Micrograph cutouts across the sample centres for the 0.9 J/cm$^2$ fluence samples are shown in figure 4.7, with W concentrations of 0.1 at%, 1 at% and 2 at% at the top, middle and bottom, respectively. TEM sampling spots and SIMS craters are assumed familiar at this point and will receive no further comment. The W-D0.1-F0.9 sample is devoid of any visible surface texture at this magnification. The only major feature is a diagonal line, which marks the transition between the 0.1 at% W-implanted and accidentally implanted regions, as the laser pulse did not hit entirely within the 0.1 at% implanted area as intended. Mirroring this diagonal closer to the edge is an abrupt change in surface reflectivity. A handful of small holes are present in the surface. Inexplicably, the PLM spot for this sample appears narrower than the others. W-D1-F0.9 and W-D2-F0.9 are similar enough to be grouped in description. Both exhibit the randomly-oriented polygonal pattern, with the size of the polygons being larger for the 2 at% W concentration. Both have holes present, from some of which extend lines as seen before.

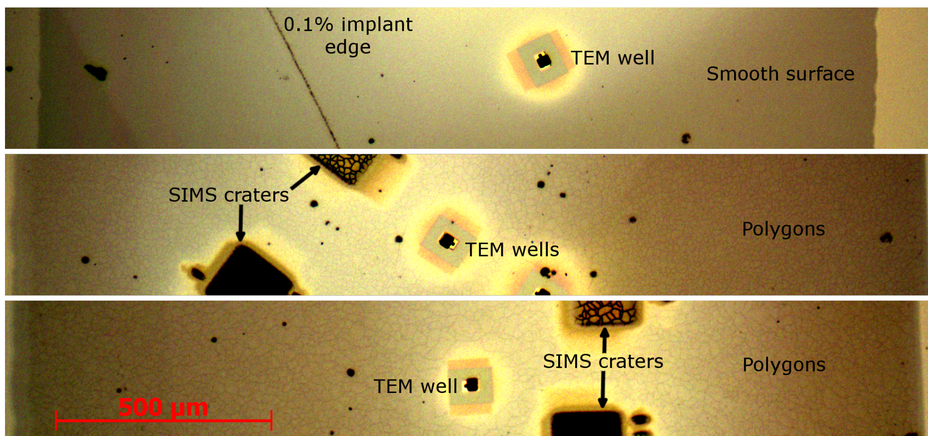


**Figure 4.7:** Optical micrograph cutouts showing representative surface morphologies for (top) W-D0.1-F0.9, (middle) W-D1-F0.9 and (bottom) W-D2-F0.9, from edge to edge through the centre of the samples.

**Surface details.** All of the sample surfaces contained holes in various shapes and sizes. In figure 4.8 are displayed optical micrographs of both small and large holes, from some of which lines extend out radially. There appears to be no relationship between the location of holes and the presence of lines which make up the surface morphology. The holes range in size from <10 µm to almost 100 µm.

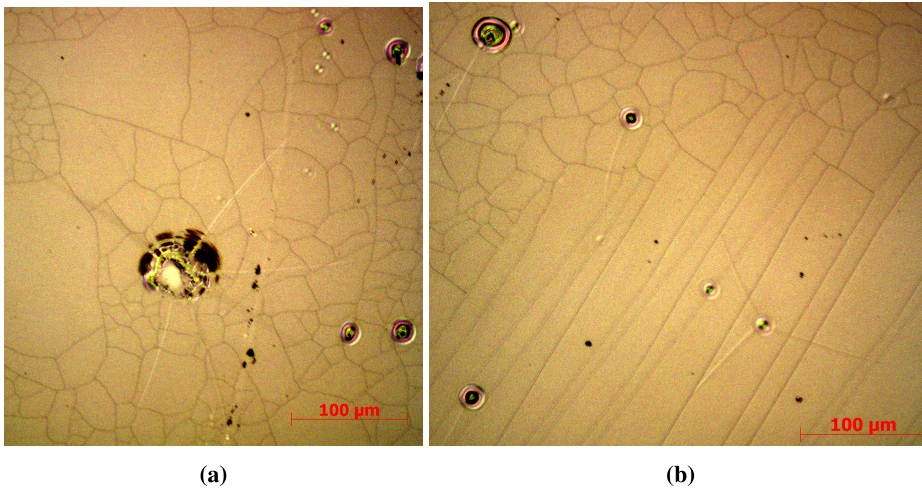


(a) (b)

**Figure 4.8:** Optical micrographs showing both large and small holes, from some of which lines extend out radially. There appears to be no relationship between the location of holes and the presence of lines which make up the surface morphology.

**Visual summary.** For easy comparison between different laser fluences and W dosages, optical micrograph cutouts for all PLM samples are provided in figure 4.9. Taken at the same positions relative to laser spot orientation, the scale and extent of features may be compared directly. When viewed side by side, it is easy to see the transition from straight line morphology for low W dosages and high fluences, to a polygonal structure for high W dosages and low laser fluences.

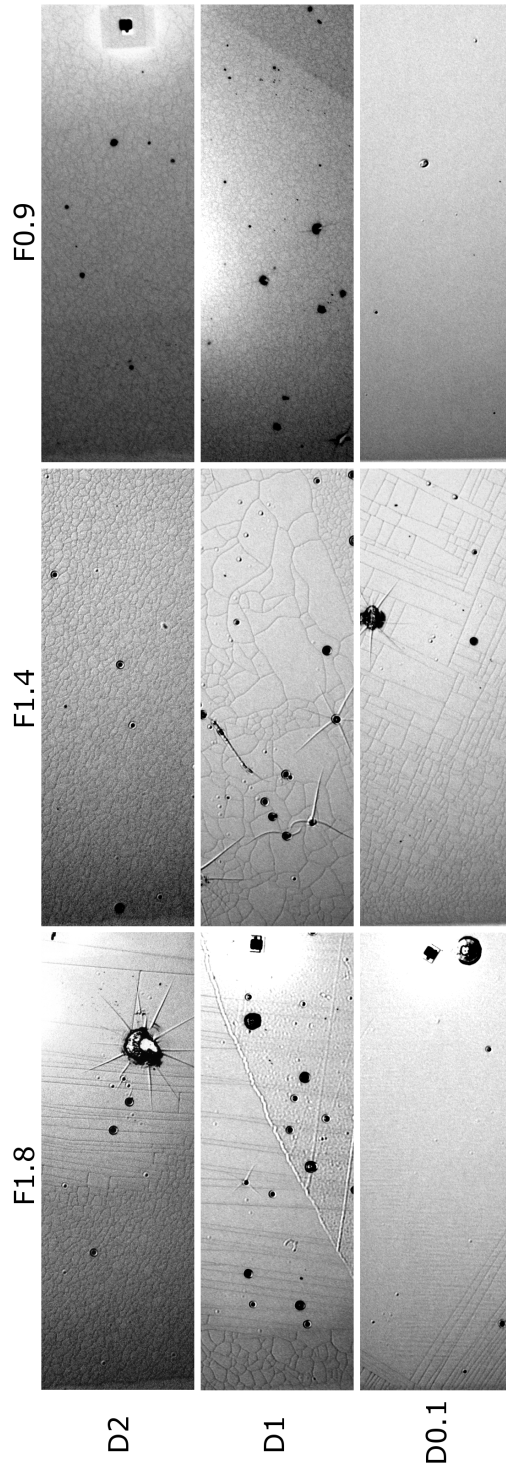


**Figure 4.9:** For all PLM samples, optical micrograph cutouts from the edge to the centre of the PLM spots, at approximately the same position for every sample.

### 4.2.2 White Light Interferometry

In this section, the overarching surface morphology uncovered with optical microscopy will be quantified using white light interferometry. As there are many similarities between the samples, only representative measurements for the different morphologies and features will be covered here, while a comprehensive set of measurements will be given in Appendix B. In this section, only arithmetic mean (Sa) and root mean square (Sq) roughness parameters will be covered, while the appendix contains a table with extended 3-dimensional roughness parameters for all samples. WLI maps of the entire wafer pieces, showing the global changes in curvature, are included in Appendix A.

The reader is reminded that the presented heightmaps are top-down projections of shaded 3D renders of the surfaces. The rendering introduces perspective for a more intuitive understanding of the surface shape, but does mean that the colour tones in the map are slightly darker than those of the colour bar (Sa/Sq not affected).

**Morphology quantification.** The optical investigations uncovered three major surface morphologies in the PLM samples, which are exemplified in figures 4.10 and 4.11. Figure 4.10 shows line morphology, while figure 4.11 shows (a) rectangular morphology and (b) randomly oriented polygons. In each case, the morphology results from raised ridges, with taller ridges for higher laser fluences. The maximal ridge heights are around 50, 35 and 15 nm for long lines, rectangles and polygons, respectively.

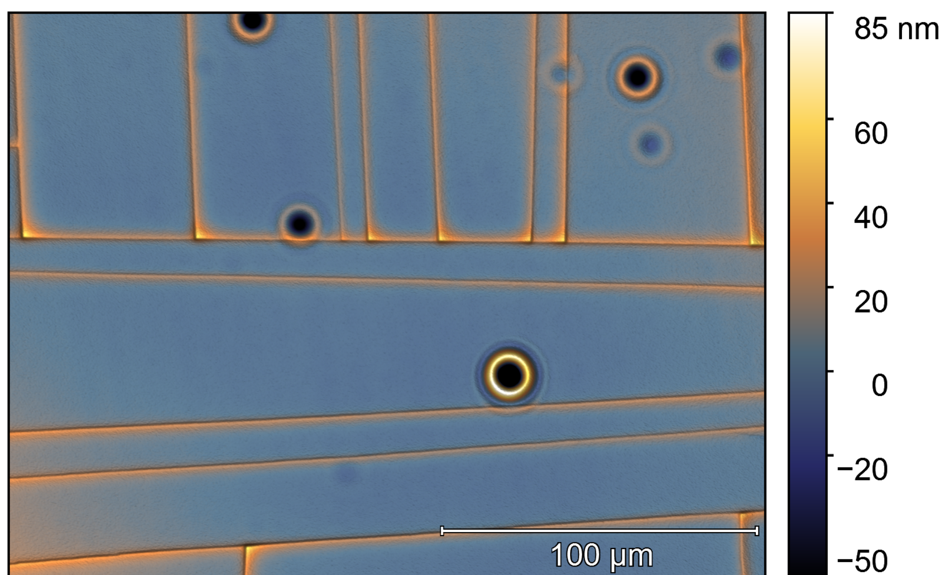


**Figure 4.10:** Representative WLI height measurement for straight line morphology. Acquired with VXI at 20 X magnification from sample W-D2-F1.8.

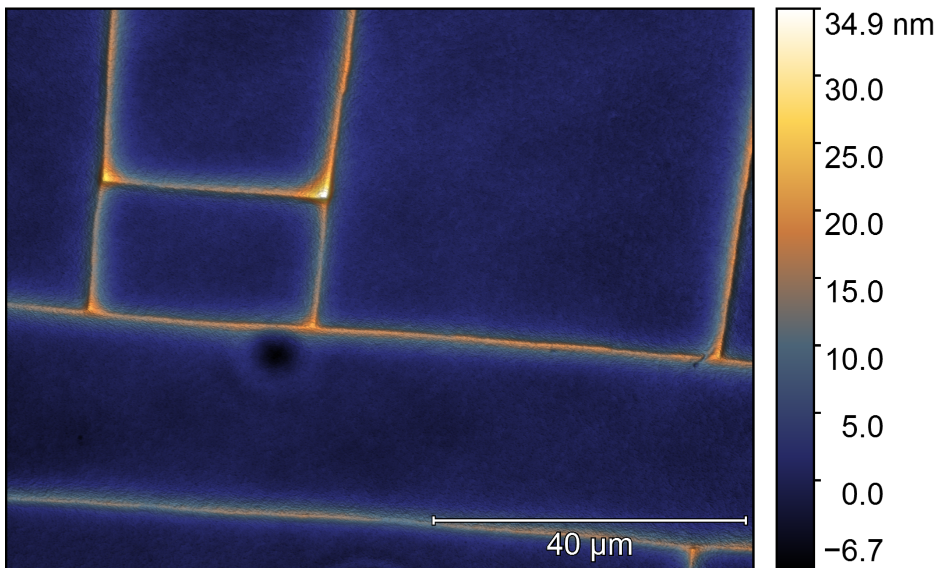


**(a)** W-D0.1-F1.4

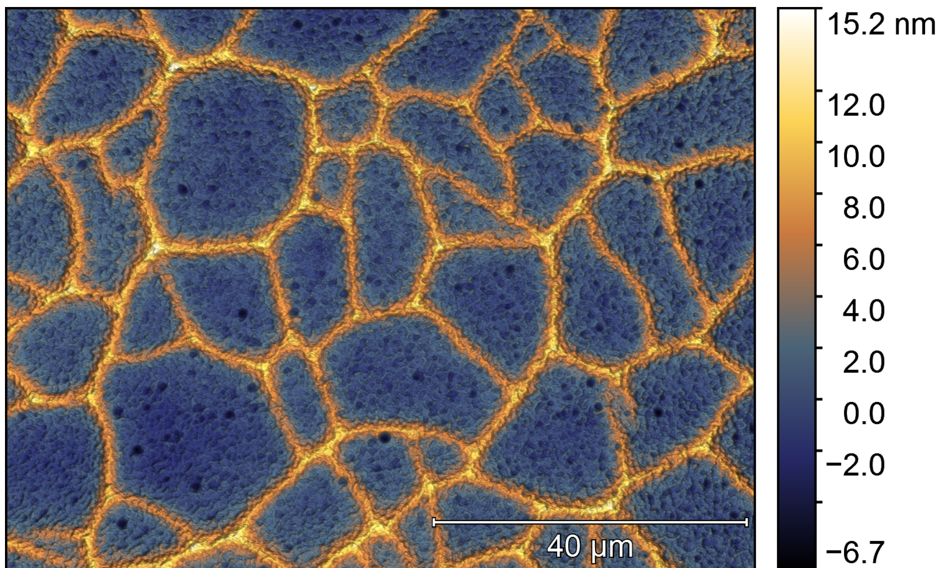


**(b)** W-D1-F0.9

**Figure 4.11:** Representative WLI height measurements for (a) rectangular and (b) polygonal surface morphologies. Acquired with PSI at 50 X magnification

Excepting height differences introduced by the ridges, holes, and other features, the surfaces appear very flat, with variations of <5 nm. The values are similar to those obtained for the as-implanted samples, as shown in the heightmap for sample W-D0.1-asImp in figure 4.12 (a). Samples of fluences 1.8 J/cm$^2$ and 1.4 J/cm$^2$ have no discernible surface patterning, while the fluence 0.9 J/cm$^2$ samples have a porous-like appearance. Additionally, figure 4.12 (b) includes a heightmap from sample W-D1-F1.8, which is unique in having a very wavy surface in one third of the PLM spot.

By evaluating over the entire 95 × 71 micron area, 3D roughness parameters are obtained. The dependence of Sa (a) and Sq (b) on the applied laser fluence is plotted in figure 4.13. The roughness values tend to increase for higher laser fluences, but with only 4 data points per series, it is unjustifiable to make claims about the nature of the relationship.

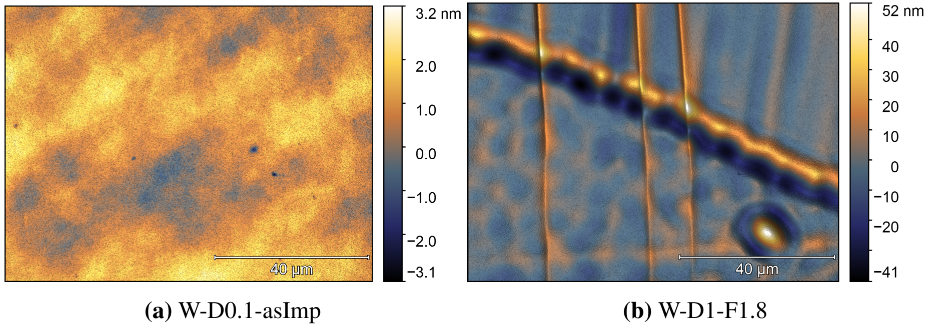


**(a)** W-D0.1-asImp **(b)** W-D1-F1.8

**Figure 4.12:** WLI height measurements of (a) an as-implanted sample and (b) W-D1-F1.8. The as-implanted sample is flatter than what the instrument can reliably measure. Acquired with PSI as 50 X magnification.

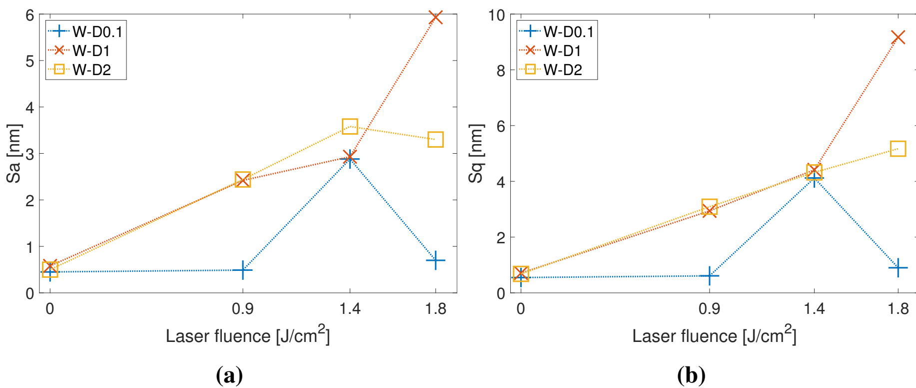


**(a)** **(b)**

**Figure 4.13:** For all PLM samples, plots of (a) average roughness (Sa) and (b) RMS roughness (Sq) against laser fluence.

**Surface details.** In figure 4.14 is presented the height map of a large hole from which lines extended (similar to one seen optically in figure 4.8 page 50). The lines are revealed to be broad grooves in the surface. The overall surface morphology of polygonal ridges extends across the grooves. The centre of the large hole contains a raised plateau, which is almost level with the rest of the surface. The edges of both the large hole and the smaller holes are all raised with respect to the sample surface. There appears to be no relation between the locations of holes and morphology-creating ridges. The surface height in any point is simply a superposition of their respective effects.

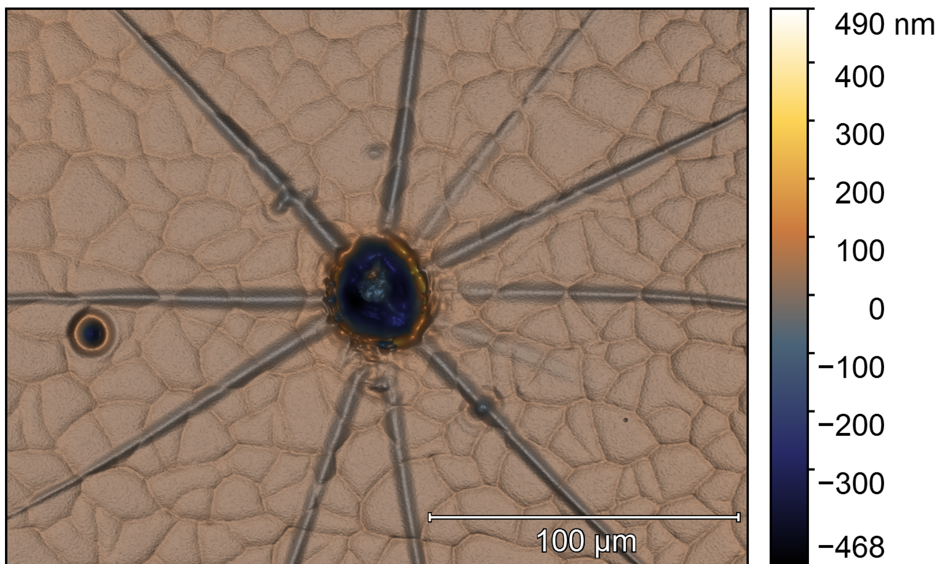


**Figure 4.14:** From sample W-D2-F1.8, a large hole from which grooves extend radially. The centre of the hole contains a plateau which is almost level with the sample surface. The edges of both the big and small hole are raised. Acquired with VXI at 20 X magnification.

### 4.2.3 Atomic Force Microscopy

Atomic force microscopy was performed to investigate the surface morphology at a smaller scale than the lateral resolution of the optical profiler. Of particular interest were the macroscopic lines as observed in the optical microscope, as they appeared as ridges when viewed with the 3D profiler, and cracks when viewed with the SEM. In this section, measurements from sample W-D0.1-F1.8 will be presented, obtained from the centre and near the edge to cover both straight and arbitrarily oriented cracks. Additional measurements from cracks in samples W-D0.1-F1.4 and W-D0.1-F0.9 will be presented in Appendix E, as well as a measurement investigating surface rippling in the SIMS crater in sample W-D1-F1.8.

**Straight lines.** AFM measurements from a central region on sample W-D0.1-F1.8, crossing multiple such ridge lines are presented in figure 4.15 for (a) height map with (b) accompanying peak force error map, (c) zoomed-in height map of the same measurement area and (d) accompanying peak force error map. In height map (a), there are clear slopes forming ridge lines, both in vertical and horizontal directions. At the top of the near-horizontal ridges, the height seems to decrease drastically by over 100 nm for a few pixels, before resuming either a slope or flat area. For the pixels with large, negative height values, the peak error map is greatly impacted, so this data alone is inconclusive, and receives corroboration in section 5.1.2 in the discussion. The central area of the map appears flat, which is in agreement with the higher resolution height map provided figure 4.15 (c). The surface structure appears columnar with a total height difference of 12 nm; there are no significant peak force errors as seen in (d). Obtained roughness parameters are Sa = 5.42 nm, Sq = 7.91 nm for (a) and Sa = 0.816 nm, Sq = 1.11 nm for (b), indicating that the ridges are the major contributors to surface roughness.

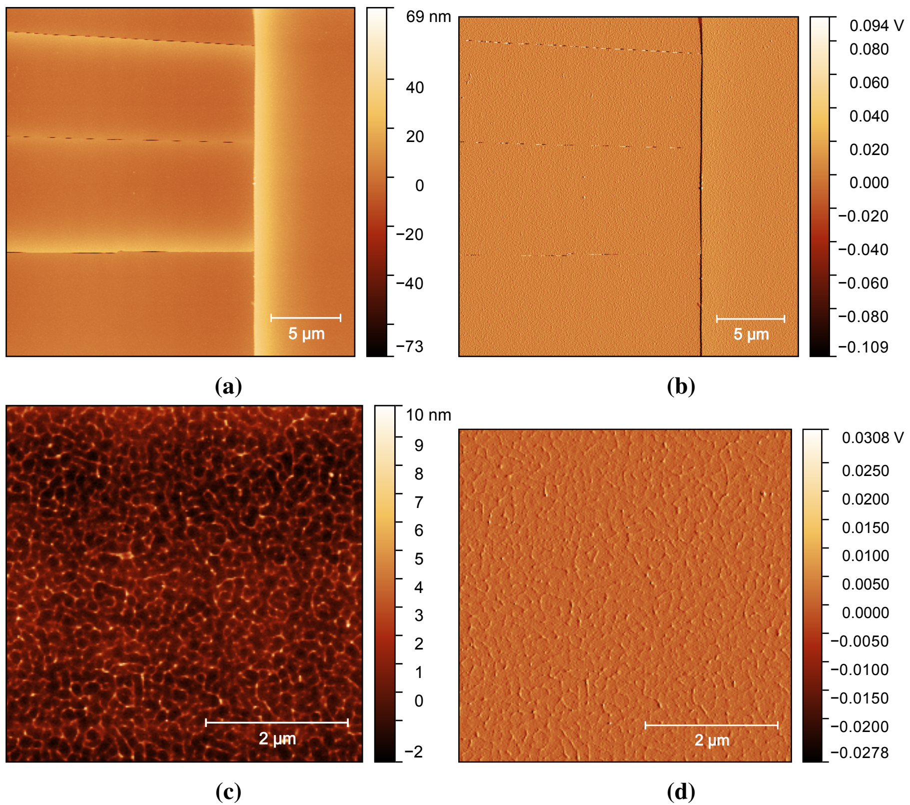


**Figure 4.15:** AFM measurements from the centre of sample W-D0.1-1.8, displaying (a) a height map with (b) accompanying peak force error map, and (c) a higher resolution height map from the centre of (a) with (d) accompanying peak force error map. The scan crosses four apparent ridge lines, arrayed vertically and near-horizontally. Scanning direction is left-to-right.

**Polygons.** AFM measurements from an edge region of sample W-D0.1-F1.8, crossing multiple ridge lines, are presented in figure 4.16 for (a) height map with (b) accompanying peak force error map, and (c) higher resolution height map from the centre of (a) with (d) accompanying peak force error map. In (a), multiple ridge lines of random orientations are visible, with slopes to either sides centred around what appear to be single-pixel cracks at the middle. The contour of the apparent cracks is mirrored in the peak force error map in (b). Studying the zoomed-in scan in (c), the surface structure does not follow any recognisable pattern, with an even distribution of sharp peaks. The same cavity close to the centre is identifiable in both height maps. Obtained roughness parameters are Sa = 4.60 nm, Sq = 6.20 nm for (a) and Sa = 4.15 nm, Sq = 5.60 nm for (c), being again slightly higher when the ridge lines are included in the measurement.

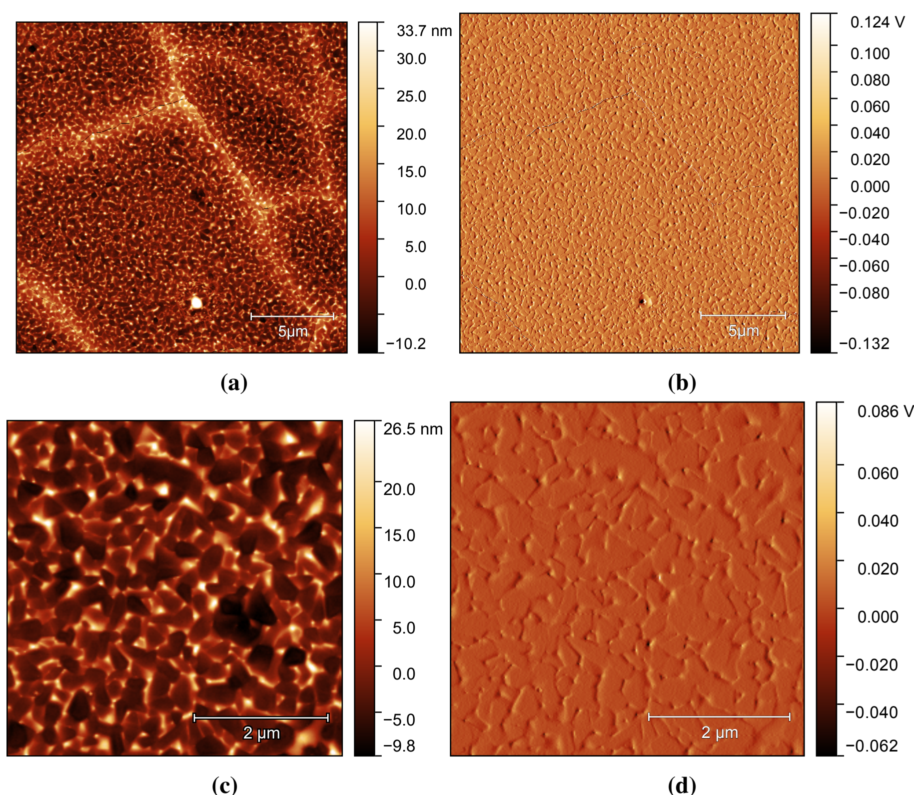


**Figure 4.16:** AFM measurements from edges of sample W-D0.1-F1.8, displaying (a) and (c) height maps of varying resolution from the same spot, with (b) and (d) corresponding peak force error maps. Scanning direction is left-to-right.

### 4.2.4 Scanning Electron Microscopy

SEM investigations were carried out to investigate the roughness in the SIMS sputter craters in the 0.9 J/cm$^2$ samples, and the lines constituting the overall morphology as observed with the optical microscope in section 4.2.1, creating either polygons, rectangles or straight lines.

**Morphology investigations.**

As presented in the optical investigations, the surface morphology close to the centre of 1.8 J/cm$^2$ annealed PLM samples was dominated by straight lines meeting at right angles, while the 0.9 J/cm$^2$ annealed PLM samples had a polygonal morphology. Figure 4.17 shows high magnification micrographs for (a) a meeting of straight lines in sample W-D1-F1.8, and (b) a corner of a polygon in sample W-D2-F0.9. In (a), it appears as if the surface has broken along straight lines, with a continuity in the surface patterning across the dark gap. The width of the crack is estimated to ~52 nm along the horizontal, and ~36 nm along the vertical by comparing line measurements to the scale bar. The surface has apparently also broken up in (b) for the lower fluence sample, with a similar continuity in surface patterning across the gap. The opposing sides appear slightly shifted with regards to one another, as evidenced by the pinching directly to the right of the meeting point of the cracks. The width of this crack is less uniform, and is estimated to vary between 20-35 nm.

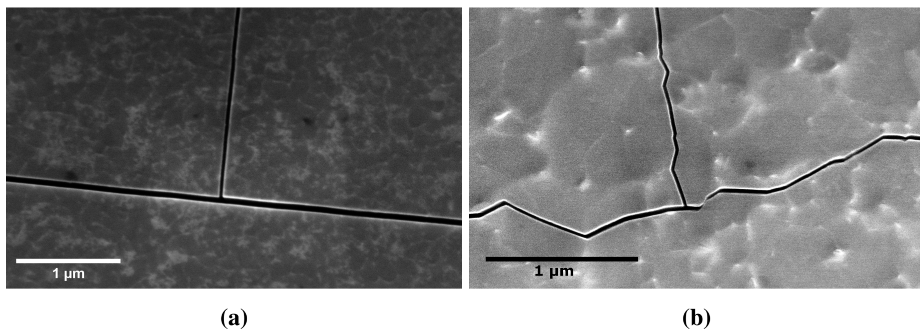


(a) (b)

**Figure 4.17:** SEM micrographs of the features giving rise to the dominant surface morphology in the PLM samples, showing (a) straight lines for sample W-D1-F1.8, and (b) irregular lines for sample W-D2-F0.9. In both cases, the source appears to be sub-100 nm wide cracks.

### SIMS craters

**Fluence 0.9 J/cm$^2$ samples.** SEM micrographs of the (a) shallow and (b) deep SIMS crater bottoms from sample W-D1-F0.9 are shown in figure 4.18. In (a), the crater bottom is mostly smooth, with a crisscross of well-defined trenches. The surface between the trenches is heavily pocked with shallow, triangle-like indentations. In (b), the trenches have become wider and more irregular in shape, and the previously pocked surface is thoroughly roughened to a terrace-like or rippled structure. The structure has a clear directional cohesion, with the thin grooves creating the wavy pattern oriented roughly horizontally in the micrograph.

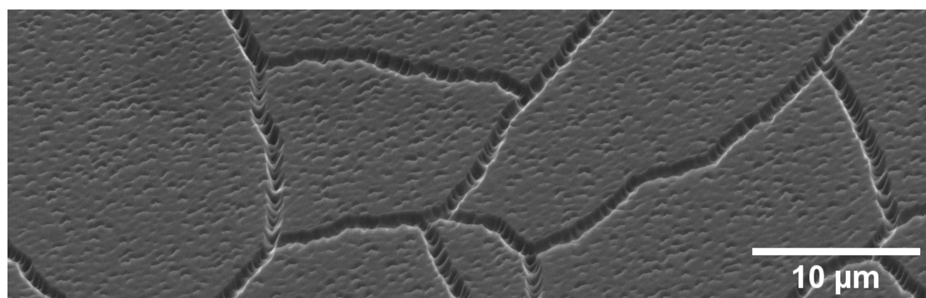


**(a)**

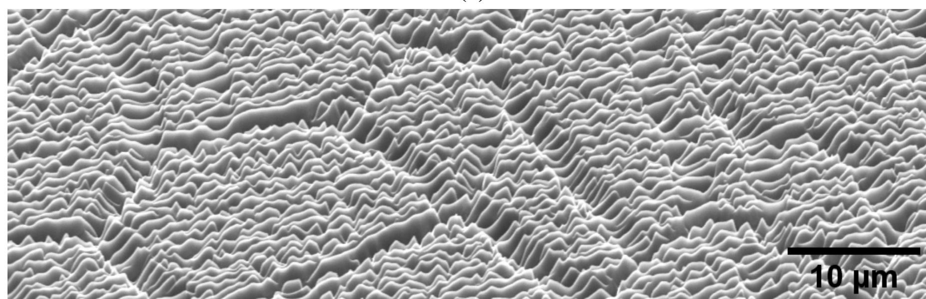


**(b)**

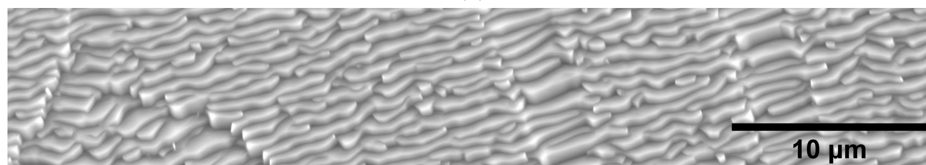


**(c)**

**Figure 4.18:** SEM micrographs of sample W-D1-F0.9 showing the (a) shallow and (b,c) deep sputter craters resulting from SIMS. In the shallow crater (a), the surface is mostly smooth, but crisscrossed with trenches, while in the deep crater (b) there is a directional roughening throughout. (c) shows an alternate angle. (a) and (b) acquired with SE signal at 20 keV and 70° tilt in the Zeiss Ultra 55 LE. (c) acquired with SE at 10 keV in the SEM Apreo.

**Fluence 1.8 J/cm$^2$ samples.** The SIMS crater in sample W-D1-F1.8 is shown in figure 4.19 (a). The holes which were identified with the optical profiler are here shown to be individual manifestations of the triangular structures which created the rippled bottom in sample W-D1-F0.9. Visually, the holes appear as a terraced structure of two triangles, tilted such that one edge of the triangles protrudes from the surface, while the rest is below the surface, creating a cavity. Similar, disjointed ripple formation is observed in figure 4.19 (b) for sample W-D2-F1.8, though the density of surface indentations is much greater for this sample. The entire surface is covered in a fine, wavy pattern, with the pattern coinciding with the edges of the triangular ripple-hole structures, as well as the deeper grooves in the trench. The pattern almost disappears at the top left of the image as the edges of the SIMS crater are reached.

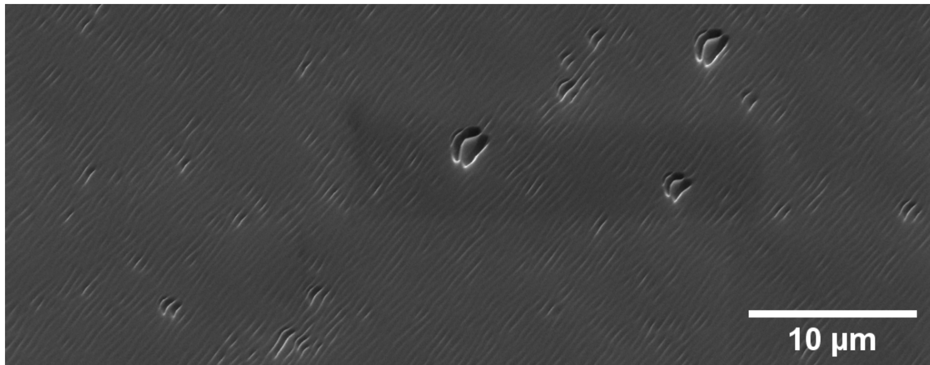


**(a)**

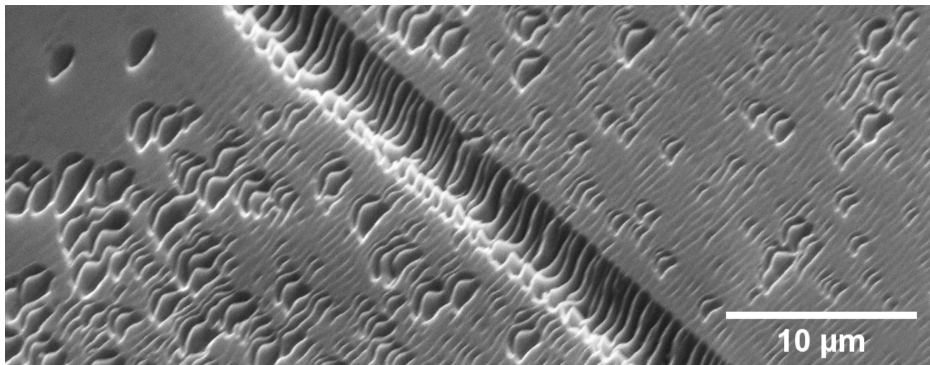


**(b)**

**Figure 4.19:** SEM micrographs of sputter craters from SIMS in samples (a) W-D1-F1.8 and (b) W-D2-F1.8. In both samples, the holes in the surface appear near-identical and aligned with the grooved pattern across the surfaces. Both micrographs acquired with SE signal at 20 keV accelerating voltage with Zeiss Ultra 55 LE at 70° tilt.

# 4.3 Near-surface Properties

## 4.3.1 Electron Backscatter Diffraction

The main purpose of the PLM treatment is to recover a crystal structure in the region amorphised by ion implantation. The PLM may create a single crystal with the same orientation as the underlying Fz-Si, or some form of polycrystallinity, depending on how far into the bulk the silicon melted. In this section only, crystal recovery will be defined as the emergence of a large, continuous area of some coherent crystal direction within the PLM affected volume. The crystal recovery was studied with EBSD, as it is able to detect crystallinity and determine crystal orientation.

This section will first present the data processing method used to obtain crystal orientation maps, after which the orientation maps will be presented for each sample on a per-fluence basis. Results for fluence 1.8 J/cm$^2$ samples will be presented first, and they will also receive the greatest emphasis, both here and in the discussion. Kikuchi patterns from each sample will be presented only in the discussion, to help with interpretation of the presented crystal orientation maps. At the end, a table will summarise whether crystal recovery was achieved or not with regards to the above definition.

**Data processing.** The orientation maps are presented as image composites, where an image quality (IQ) map has been overlaid as a mask on the base crystal orientation map. The computation method for the IQ map is proprietary and differs between software providers, but universally it is intended to serve as an indicator of diffraction pattern quality and confidence of indexing. The IQ map is bright where pattern quality and indexing confidence are high, and dark where they are low. Thus, by combining the orientation maps with corresponding IQ maps, the most accurate picture of the crystallinity is formed. The effects of this data processing are shown in figure 4.20, where high confidence orientations are brightly coloured, while low confidence orientations darken to blackness in the composite crystal orientation map. In inverse pole figure (IPF) key is displayed with the measurements to relate map colour to crystal orientation.

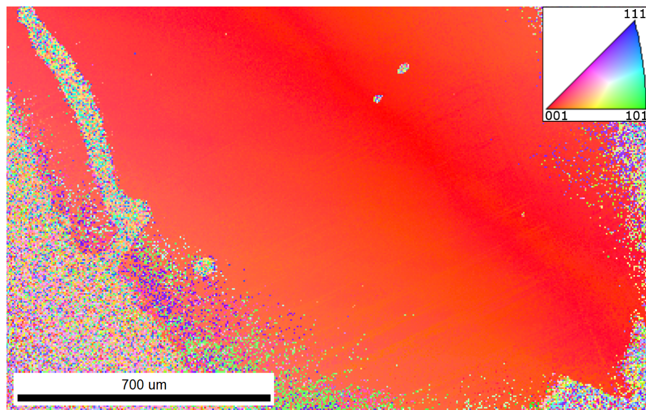


**(a)** Raw crystal orientation map

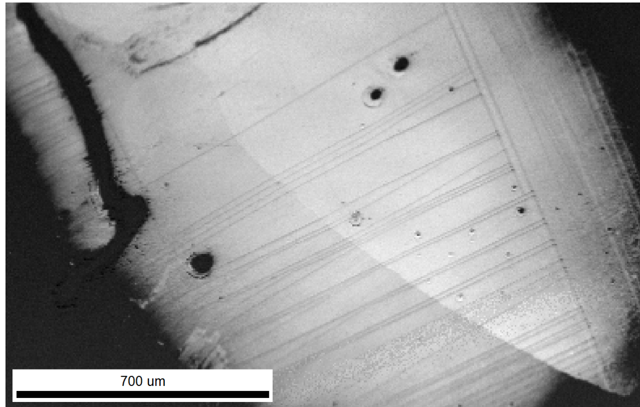


**(b)** Image quality map

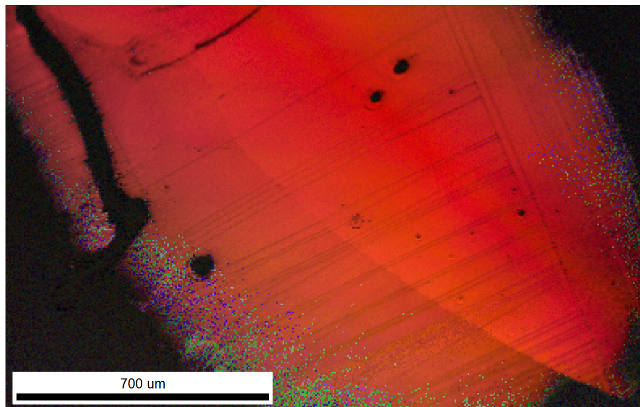


**(c)** Combined map

**Figure 4.20:** Illustration of the effects of combining a (a) crystal orientation map with a (b) image quality map to create a (c) composite crystal orientation map. By taking into account pattern quality and confidence of indexing, a more accurate orientation map is obtained.

**Sample W-D0.1-F1.8.** The crystal orientation map for the W-D0.1-F1.8 sample, and a SEM micrograph with corresponding EBSD collection area are shown in figure 4.21 (b) and (a), respectively. An IPF key for orientation is inset in (f). The crystal orientation of the underlying Fz-Si has been recovered, with the majority of the investigated area being most closely aligned with a $\langle 001 \rangle$-orientation with regards to the sample normal. There appears to be a fault line from the centre-left to the centre-bottom, creating two regions with a small yet distinct orientation mismatch between them. Also within both regions there are small angle variations between grains.

The transition at the edges from $\langle 001 \rangle$-orientation to essentially no pattern is abrupt, with no distinctly polycrystalline region of large, randomly orientated grains is detected. The transition corresponds well with the change in surface morphology, as observed in the SEM micrograph in 4.21 (a).

In the bottom-right region of the map, there is a sparse, irregular distribution of green dots, which would correspond to a $\langle 101 \rangle$-orientation. Section 5.2.2 elaborates on why these are considered erroneously indexed. The same holds for any blue dots signalling $\langle 111 \rangle$-orientation in the majorly red $\langle 001 \rangle$-area.

**Sample W-D1.F1-8.** A SEM micrograph with indicated EBSD collection area and corresponding crystal orientation map are shown in figure 4.21 (c) and (d), respectively, with an IPF for interpretation inset in (f). The results are very similar to the previous sample, with a large, contiguous area of roughly $\langle 001 \rangle$-orientation dominating the map. The transition from $\langle 001 \rangle$-orientation to blackness is abrupt, but there are more blue and green dots close to the edges. Again, these apparent $\langle 101 \rangle$ and $\langle 111 \rangle$ grains are attributed to incorrect indexing rather than measured high-mismatch grains, as per section 5.2.2. For this sample, the edges of the crystalline area correspond well to visible surface features, lining up neatly with the light-dark transition seen in the SEM micrograph.

**Sample W-D2-F1.8.** Last among the 1.8 J/cm$^2$ fluence samples is W-D2-F1.8, for which the SEM micrograph with indicated EBSD collection area and corresponding crystal orientation map with inset IPF key are shown in figure 4.21 (e) and (f), respectively. This sample, too, has successful crystal recovery, albeit in a distinctly smaller area. There is a central, contiguous region with roughly $\langle 001 \rangle$-orientation, excepting a crater in the top left and a square well from FIB sampling in the middle. Unlike the previous 1.8 J/cm$^2$ samples investigated, which had abrupt transitions from $\langle 001 \rangle$ to no detected crystal structure, W-D2-F1.8 appears to have a continuous transition region with orientation(s) in-between $\langle 001 \rangle$ and $\langle 101 \rangle$ on the left side. The edges of the detected crystalline region correspond well to the visible transition between the lighter and darker areas in the SEM image.

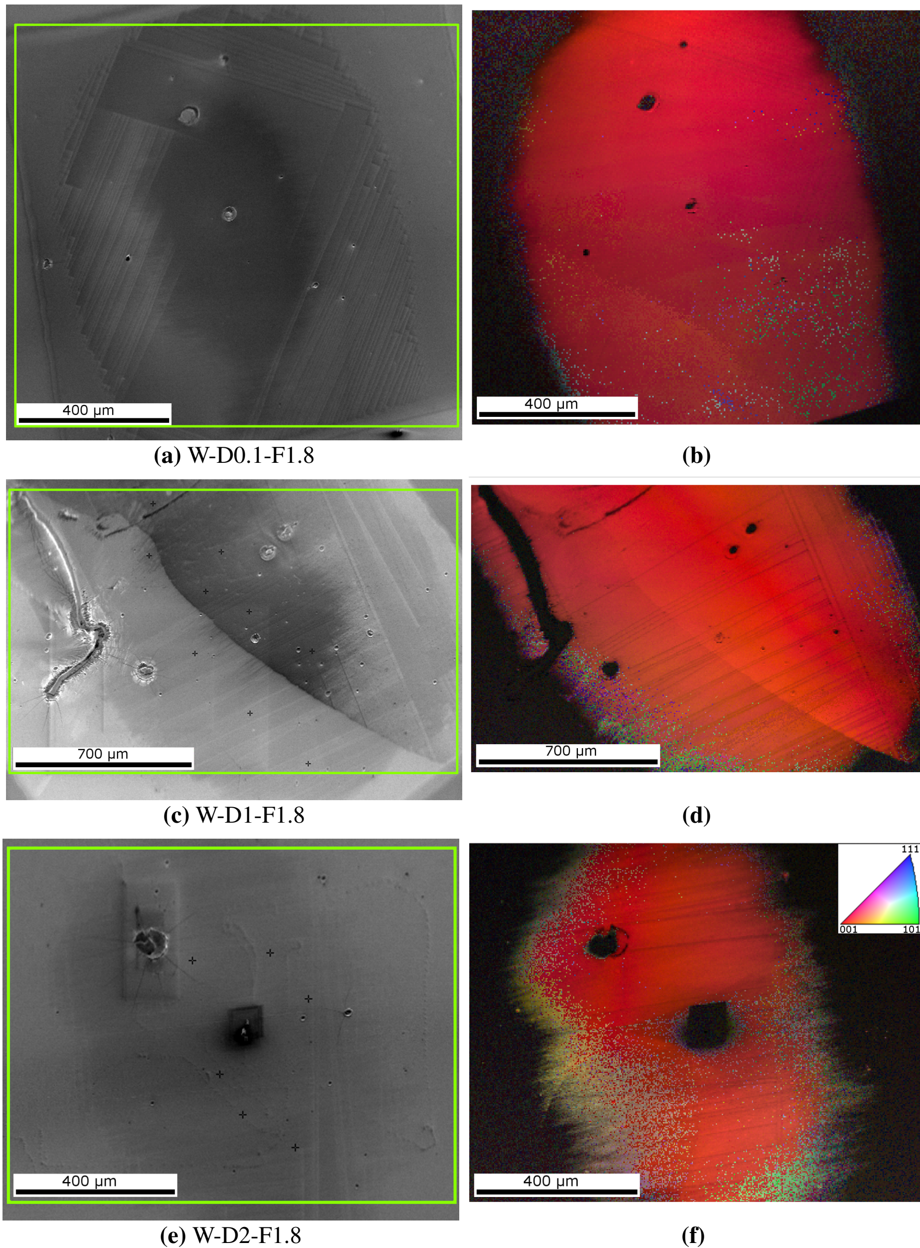


**(a)** W-D0.1-F1.8 **(b)**

**(c)** W-D1-F1.8 **(d)**

**(e)** W-D2-F1.8 **(f)**

**Figure 4.21:** SEM micrographs for samples (a) W-D0.1-F1.8, (c) W-D1-F1.8 and (e) W-D2-F1.8, with EBSD collection areas indicated by green squares. Corresponding IQ-modified crystal orientation maps for samples (b) W-D0.1-F1.8, (d) W-D1-F1.8, and (f) W-D2-F1.8, with an IPF key inset in (f), which is valid for all orientation maps.

**Sample W-D0.1-F1.4.** The crystal orientation map and SEM view with indicated EBSD collection area for sample W-D0.1-F1.4 are shown in figure 4.22 (b) and (a), respectively. A continuous area most closely aligned with a $\langle 001 \rangle$-orientation is detected, with the left hand side of the orientation map showing many data points of $\langle 111 \rangle$-orientation. The data points of $\langle 111 \rangle$-orientation are yet again attributed to incorrect indexing. The transition from detected crystallinity to no detected crystal structure is gradual, corresponding well to the gradual change in surface morphology as seen in the SEM micrograph in (a).

**Sample W-D1-F1.4.** A SEM micrograph with indicated EBSD collection area and crystal orientation map with inset IPF key displayed in figure 4.22 (a) and (b), respectively, for sample W-D1-F1.4. Crystalline recovery was unsuccessful for this sample, with only disconnected pockets showing detected crystallinity. Interestingly, the detected crystallinity, which is of $\langle 001 \rangle$-orientation, aligns physically with holes on the surface, as seen in the SEM image.

**Sample W-D2-F1.4.** No Kikuchi lines were detected anywhere in the PLM affected area for sample W-D2-F1.4, and as a result no EBSP was produced. Crystalline recovery was decidedly unsuccessful.

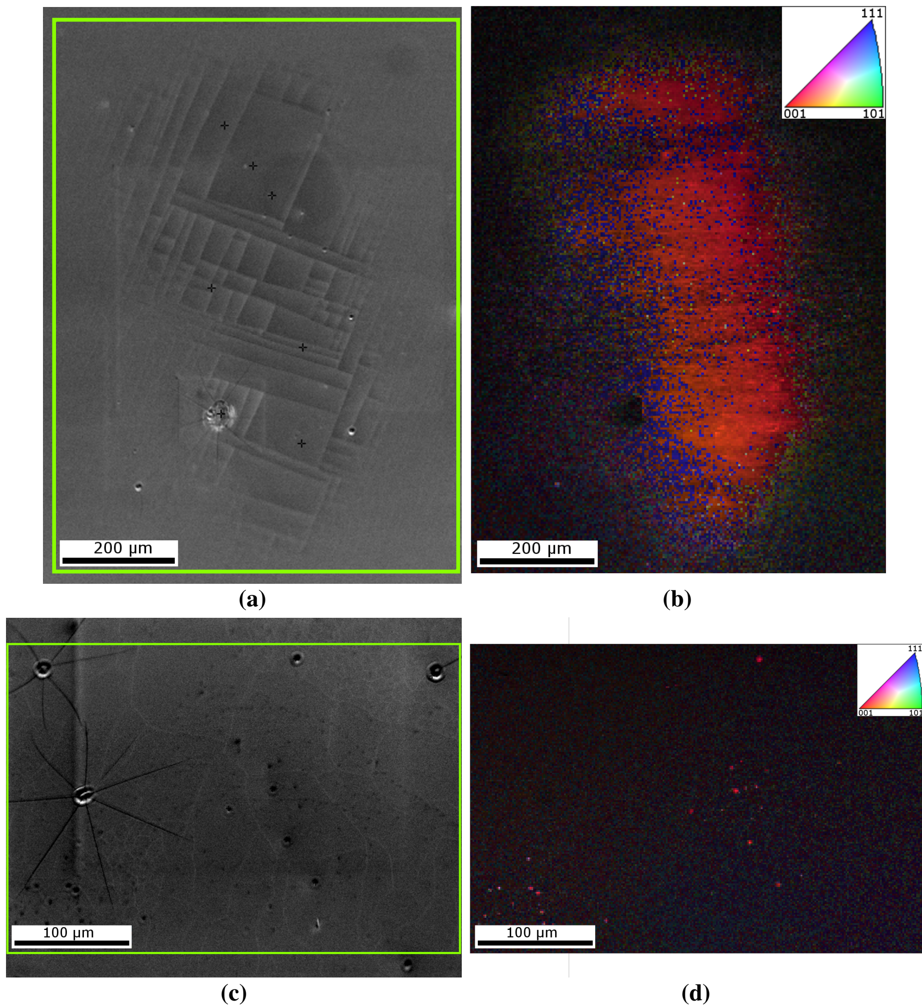


**Figure 4.22:** For sample **W-D0.1-F1.4**, (a) SEM micrograph with EBSD collection area indicated by the green box, and (b) IQ-modified crystal orientation map with inset IPF key. For sample **W-D1-F1.4**, (c) SEM micrograph with EBSD collection area indicated by the green box, and (d) IQ-modified crystal orientation map with inset IPF key.

**Fluence 0.9 J/cm$^2$ PLM samples.** For the sample set with the lowest laser fluence, an EBSP was only obtained from the W-D0.1-F0.9 sample. Its orientation map with inset IPF key and SEM micrograph with indicated EBSD collection area are displayed in figure 4.23 (b) and (a), respectively. It should immediately be noted that this sample differs from the others, in that the laser spot is partially outside the 0.1 at% W-implanted area. The bottom part extends into the accidentally implanted area. In the orientation map, crystallinity is detected in a thin, horizontal strip along the border between the 0.1% W and accidentally implanted regions, as well as a broader, diagonal strip following the edges of the laser spot in the accidentally implanted region. The dominant crystal orientation is closely aligned with $\langle 001 \rangle$. Despite this crystalline area, crystalline recovery as per the stated objective of growth from below has failed.

For the other 0.9 J/cm$^2$ samples, W-D1-F0.9 and W-D2-F0.9, no Kikuchi lines were detected, and thus no EBSPs or orientation maps were produced. For these two samples, crystalline recovery was unsuccessful.

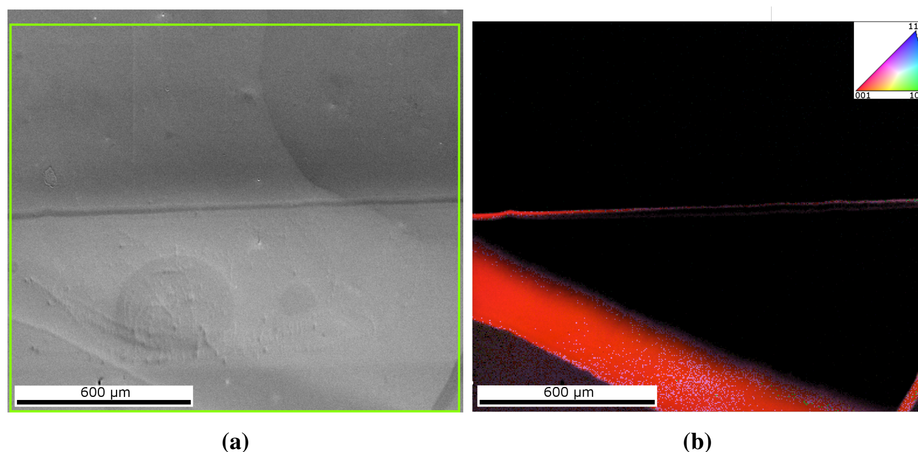


**(a)** **(b)**

**Figure 4.23:** For sample W-D0.1-F0.9, (a) SEM micrograph with EBSD collection area indicated by the green box, and (b) IQ-modified crystal orientation map with inset IPF key.

**Summary.** The findings of the EBSD investigations in this section are summarised in table 4.1. For the highest laser fluence of 1.8 J/cm$^2$, crystalline recovery was attained for all concentrations of W, with the orientation of the detected crystalline area being closely aligned with that of the underlying $\langle 001 \rangle$ Fz-Si. For fluence 0.9 J/cm$^2$ samples, no crystalline recovery was achieved. For the middling laser fluence of 1.4 J/cm$^2$, only the sample with 0.1% W had crystalline recovery, while the sample with 1% W had spots of $\langle 001 \rangle$-orientation.

**Table 4.1:** Summary of EBSD investigations for all W-implanted samples. A tick in the column for crystalline recovery indicates that there exists a continuous area with roughly $\langle 001 \rangle$-orientation within the PLM spot, i.e. the same orientation as the substrate. The recovered area was never equal in size nor shape to the PLM treated area. A tick in the column for EBSP indicates that any crystallinity at all was detected for the sample, allowing pattern collection.

| Sample | EBSP obtained | Crystalline recovery |
|---|---|---|
| W-D0.1-F1.8 | ✓ | ✓ |
| W-D0.1-F1.4 | ✓ | ✓ |
| W-D0.1-F0.9 | ✓ | - |
| W-D1-F1.8 | ✓ | ✓ |
| W-D1-F1.4 | ✓ | - |
| W-D1-F0.9 | - | - |
| W-D2-F1.8 | ✓ | ✓ |
| W-D2-F1.4 | - | - |
| W-D2-F0.9 | - | - |

### 4.3.2 Raman Spectroscopy

In this section, crystallinity, crystal stresses, and the presence of amorphous Si and tungsten compounds will be investigated with Raman spectroscopy. First, a spectrum from a piece of Fz-Si which was not sent to ion implantation will be presented, to act as a baseline for comparison. Next, spectra from intentionally and perceived accidentally ion implanted regions will be presented. Spectra from the fluence 1.8 J/cm$^2$ PLM samples will follow, before a Raman map of sample W-D2-F1.8 ends the section. Line scans across some SIMS crater walls will be presented in appendix F.

For most measurements, the position and width of the Γ-peak of Si is given. The associated uncertainties are the 95 % confidence interval bounds for the numerically computed values.

All spectra display some fine-structure below ~200 cm$^{-1}$. It is due in part to imperfect wavelength separation at the diffraction grating, the breadth of the laser line, and polarisation of atmospheric gases. Thus, only the general shape of the spectra are considered at low wavenumbers.

**Fz-Si.** To establish a reference for further comparisons, a spectrum from Fz-Si was obtained, and is shown in figure 4.24. In the theory, a number of peaks related to phonon modes in a silicon crystal were predicted. These peaks have been indicated and labelled in the figure, with easily distinguishable peaks at 228 cm$^{-1}$, 303 cm$^{-1}$, 435 cm$^{-1}$, 521 cm$^{-1}$, 620 cm$^{-1}$, 670 cm$^{-1}$, 824 cm$^{-1}$ and 962 cm$^{-1}$, with the last peak manifesting as a double-peak of 942 and 978 cm$^{-1}$ Raman shifts. The TA mode at 150 cm is barely distinguishable, but also labelled. In addition to the predicted peaks, there appears to be a small peak at 758 cm$^{-1}$. The dominating, triply degenerate optical Γ-peak at nominally 521.1 cm$^{-1}$ is determined to have a centre of 520.64 $\pm$ 0.05 cm$^{-1}$ and full width at half maximum (FWHM) of 4.50 $\pm$ 0.08 cm$^{-1}$ via Lorentzian curve fitting, as shown in the figure with a dotted line.

The measurement in the figure used a laser power of 50 mW. For a lower laser power of 1 mW at the same measurement spot, a Γ-peak position of 521.13 $\pm$ 0.01 cm$^{-1}$ with FWHM of 3.44 $\pm$ 0.05 cm$^{-1}$ was obtained. Laser powers of 5 mW and 10 mW did not shift the Γ-peak away from 521.1 cm$^{-1}$.

**Amorphous Si.** Figure 4.25 shows Raman spectra from the as-implanted region of each dosage of W, as well as a spectrum from the accidentally implanted region. The as-implanted spectra are virtually identical, with broad bands around 150, 300, 390 and 470 cm$^{-1}$, with lower intensity bands at roughly 600 and 800 cm$^{-1}$, consistent with expectations from the theory. The spectrum from the accidentally implanted region shares these features, however with a sharper peak at 300 cm$^{-1}$, corresponding to the 2TA X-peak of c-Si. The Γ-peak of c-Si is also present, shifted to 513 cm$^{-1}$, as well as

a small and broad 2TO peak around 950 cm$^{-1}$.

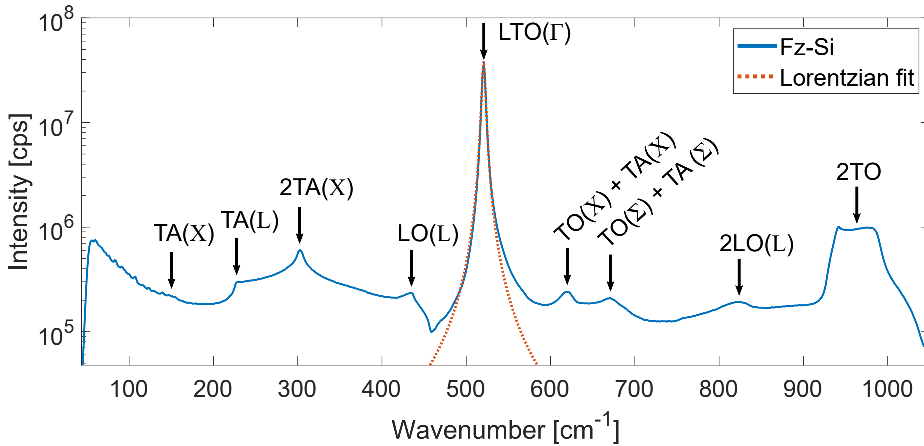


**Figure 4.24:** Raman spectrum from Fz-Si sample, to be used as a comparison reference against implanted samples. Known peaks arising from phonon modes in crystalline Si at 228 cm$^{-1}$, 303 cm$^{-1}$, 435 cm$^{-1}$, 521 cm$^{-1}$, 620 cm$^{-1}$, 670 cm$^{-1}$, 824 cm$^{-1}$ and 962 cm$^{-1}$ are indicated and labelled. Short-hand key: Acoustic (A), optical (O), longitudinal (O), transverse (T). A Lorentzian fit of the Γ-peak is included with a dotted line. Laser power: 50 mW.

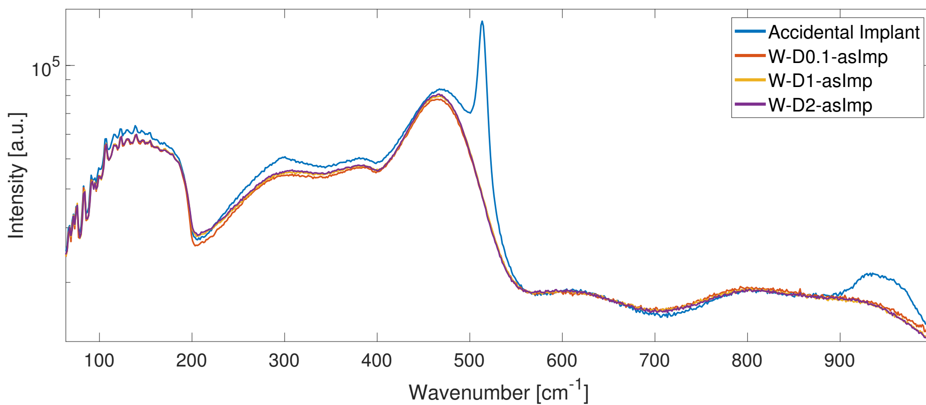


**Figure 4.25:** Raman spectra from the as-implanted regions containing 0.1, 1 and 2 at% W, as well as a spectrum from the accidentally implanted region. The as-implanted spectra are virtually identical, suggesting that the Si is already completely amorphised by the lowest dose. In the accidentally implanted region, some crystallinity remains as evidenced by the c-Si Γ-peak, which has shifted to 513 nm, as well as a low 2TO peak at 950 nm.

**Spectra from "FzSi"** To investigate the effects of eventual stray ions from the ion implantation, a spectrum was obtained from near the edge of the W-D2 wafer piece from a region which should have remained as unaffected Fz-Si. This spectrum is displayed in figure 4.26, with the reference Fz-Si spectrum included with dotted lines for ease of comparison. For the W-D2-spectrum, all previously observed Si-related peaks are present, but in a broadened state, shifted to lower wavenumbers. Of new features, there is a broad peak centred around 150 $cm^{-1}$ and a peak around 470 $cm^{-1}$, manifesting as a shoulder to the Γ-peak of c-Si, which is shifted from 521 $cm^{-1}$ to 509 $cm^{-1}$. The combined TA + TO Σ and X-peaks of c-Si at nominally 620 and 670 $/cm^2$, as well as the 2LO peak at 824 $cm^{-1}$, are still present in sample W-D2-"FzSi", but are lost to broadening on the W-D1 wafer piece.

**Effects of PLM.** In figure 4.27 are presented spectra from the centres of each 1.8 $J/cm^2$ PLM sample, compared to the spectrum from Fz-Si. The inset shows calculated Γ-peak positions from Lorentzian curve fitting. For the PLM samples, expected peaks from c-Si are present at ~230, 300, 430, 520, 620, 670, 820 and 950 $cm^{-1}$, however slightly broadened and shifted to lower wavenumbers compared to the Fz-Si. For the PLM samples, the Γ-peak is shifted to 515.2-517.4 $cm^{-1}$, with increasing concentrations of W giving higher shifts. The exact positions are given in the figure inset. A broad band from a-Si is present below 200 $cm^{-1}$, as well as a contribution around 470 $cm^{-1}$ which manifests as a shoulder to the c-Si Γ-peak. Finally, in the PLM samples there is a new peak present at 598-600 $cm^{-1}$, which increases in magnitude with decreasing W dosage.

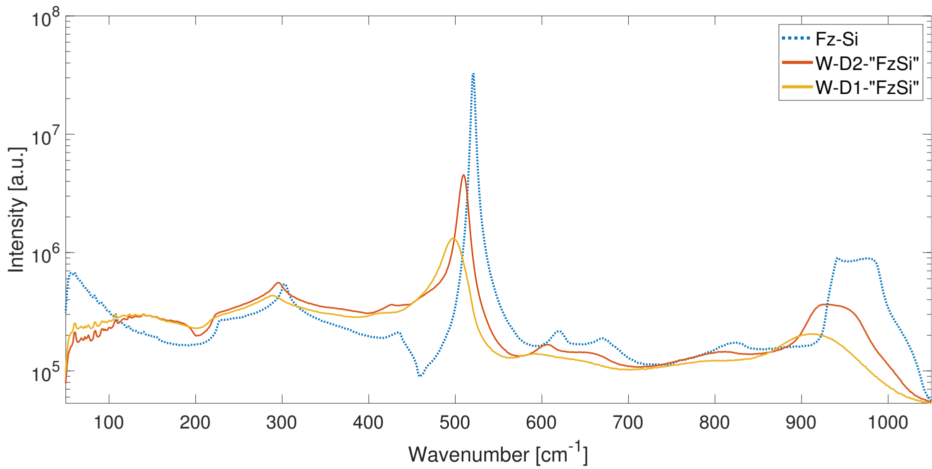


**Figure 4.26:** Raman spectra from presumed Fz-Si regions on the W-D2 and W-D1 wafer pieces, showing the effect of stray ions during implantation. Fz-Si reference spectrum is displayed in a dotted line for ease of comparison. c-Si related peaks experience a broadening, and are shifted to lower wavenumbers, approaching the expected spectrum from a-Si.

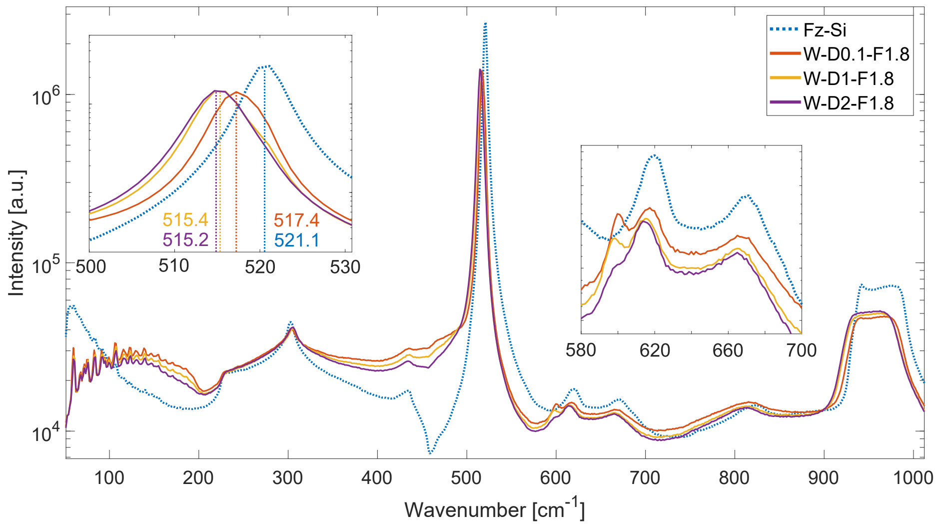


**Figure 4.27:** Raman spectra from PLM samples annealed with 1.8 J/cm$^2$ , compared to Fz-Si. The inset details the shifts in primary peak position, as determined by Lorentzian curve fitting. Spectra were obtained with 50X objective at 50 mW laser power and are normalised for total area.

**Stress mapping.** Due to the surface cracking, it was of interest to investigate the residual stresses in the crystal. To do this, a map of 576 Raman spectra was acquired from sample W-D2-F1.8, and the shift of the main Si peak was investigated. Figure 4.28 shows an optical image of the sample, with indicated mapping area and the size of the focused laser beam (a), and a map showing the absolute magnitude of the Γ-peak shift in each point. The shifts were all towards lower wavenumbers, ranging from $-0.34\,\mathrm{cm}^{-1}$ to $-4.16\,\mathrm{cm}^{-1}$. As seen in the map, the peak shifts are lowest for the data points that align with surface cracks, growing in magnitude as the distance to the nearest crack increases. The magnitude of the shifts is generally higher towards the top of the map than the bottom, that is, towards the centre of the PLM affected area.

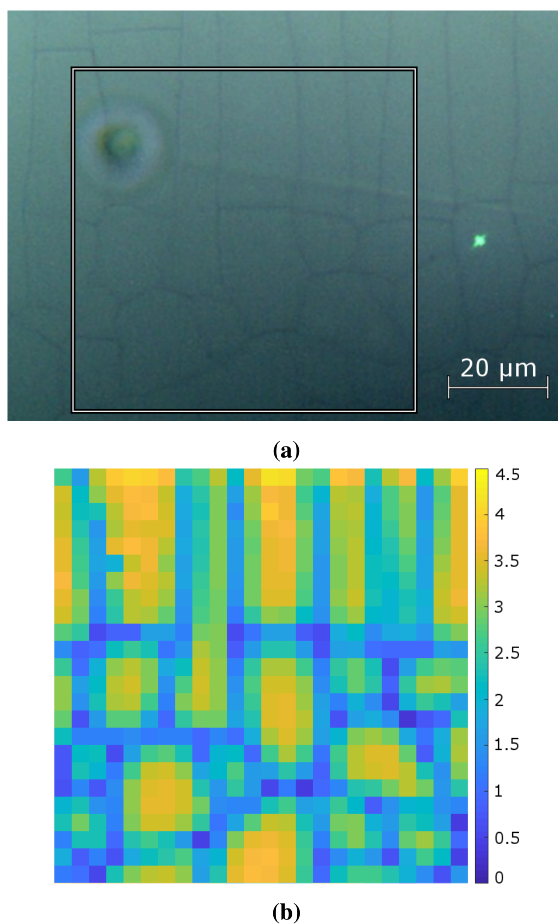


**Figure 4.28:** For sample W-D2-F1.8, (a) an optical image with mapping area indicated by the square and (b) map of position vs shift of the Γ-peak of c-Si in $\mathrm{cm}^{-1}$. The size of the laser dot is visible in (a).

### 4.3.3 Secondary Ion Mass Spectrometry

#### Depth Calibration

As the SIMS sputtering was reported as counts per cycle from the instrument, it was necessary to relate the sputtering cycles to the crater depth to attain actual depth profiles. To do this, the Bruker CountourGT-K Optical Profiler was used to image the SIMS sputter craters with VSI/VXI. In this section, representative measurement of SIMS craters for the as-implanted, fluence 0.9 J/cm$^2$, and fluence 1.8 J/cm$^2$ PLM samples will be shown, with the rest of the measurements included in appendix C. At the end of the section, a table summarising all measured depths and corresponding sputter rates for each sample will be provided. Around the roughly square craters are oval depressions, which uniquely identify the different sputtering craters, and are indicative of beam size during the SIMS measurements.

**As-implanted samples.** A greyscale image (a) and topographic map (b) of the SIMS crater in sample W-D0.1-asImp is shown in figure 4.29. The crater bottom is detected as having an average depth of 2025 nm relative to the surrounding surface by the step detection algorithm. The crater bottom, where no small holes are present, appears as very smooth with well defined walls, as is the case for the SIMS craters in all the as-implanted samples.

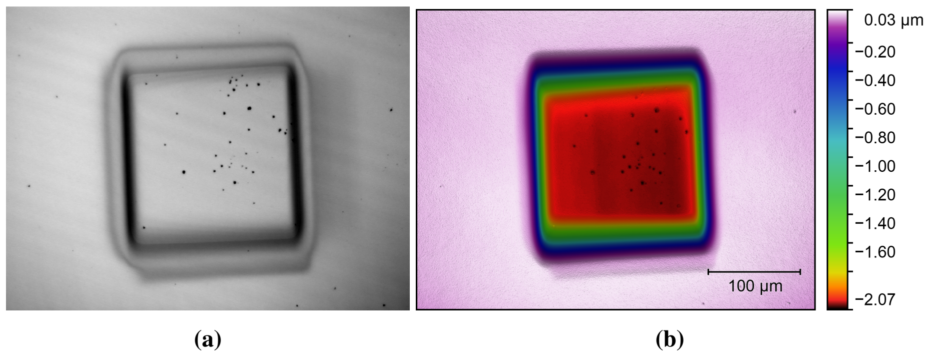


(a) (b)

**Figure 4.29:** For sample W-D0.1-asImp, (a) a greyscale image and (b) a topographic map of the sputter craters formed by SIMS depth profiling.

**Fluence 1.8 J/cm$^2$ samples.** A greyscale image (a) and topographic map (b) of the SIMS crater in sample W-D0.1-F1.8 is presented in figure 4.30. The bottom of the crater has some hole formation. The surface of the sample exhibits a diagonally oriented pattern of waves with ~10 µm spacing which has been retained through the sputtering process and is also seen at the bottom of the crater. The near-parallel cracks that traverse the sample vertically have become wide trenches across the crater bottom. The average depth of the crater bottom is detected as 1892 nm.

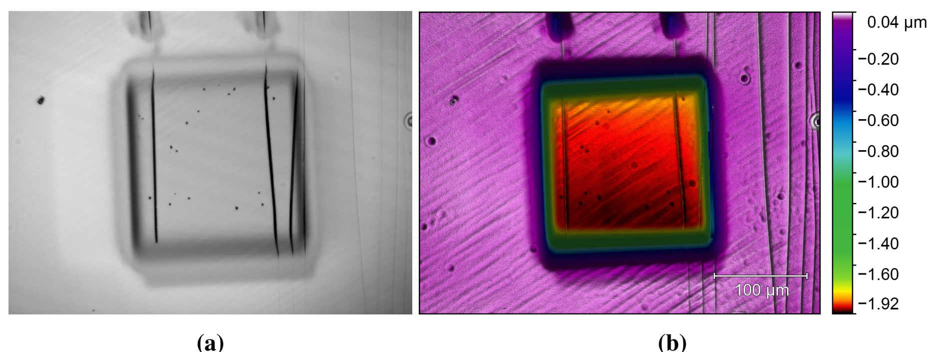


**Figure 4.30:** For sample W-D0.1-F1.8, (a) a greyscale image and (b) a topographic map of the sputter craters formed by SIMS depth profiling.

**Fluence 0.9 J/cm$^2$ samples.** For the PLM samples recrystallised with 0.9 J/cm$^2$, both a shallow and a deep crater was obtained, as the sputter yield of $^{30}Si_2^+$ increased greatly throughout the measurement. Figure 4.31 presents for sample W-D1-F0.9 (a) a greyscale image and (b) topographic map for the shallow crater, and (c) a greyscale image and (d) topographic map of the deep crater.

For the shallow crater, as seen in (a), the cracks in the sample surface have been amplified into trenches by the sputtering. Outside of the trenches, however, the bottom of the crater appears smooth, as was the case for the 1.8 J/cm$^2$ PLM sample. From the topographic map in (b), the average depth of the crater is evaluated to 512 nm.

In the deep crater, the bottom has become overall very rough, as seen in (c). The trenches originating from the surface cracks have become wider, and the surface between the trenches is now rough as well. The bottom was too rough for step detection to function, and the depth of the crater was evaluated to 1940 nm through manual XY profile averaging.

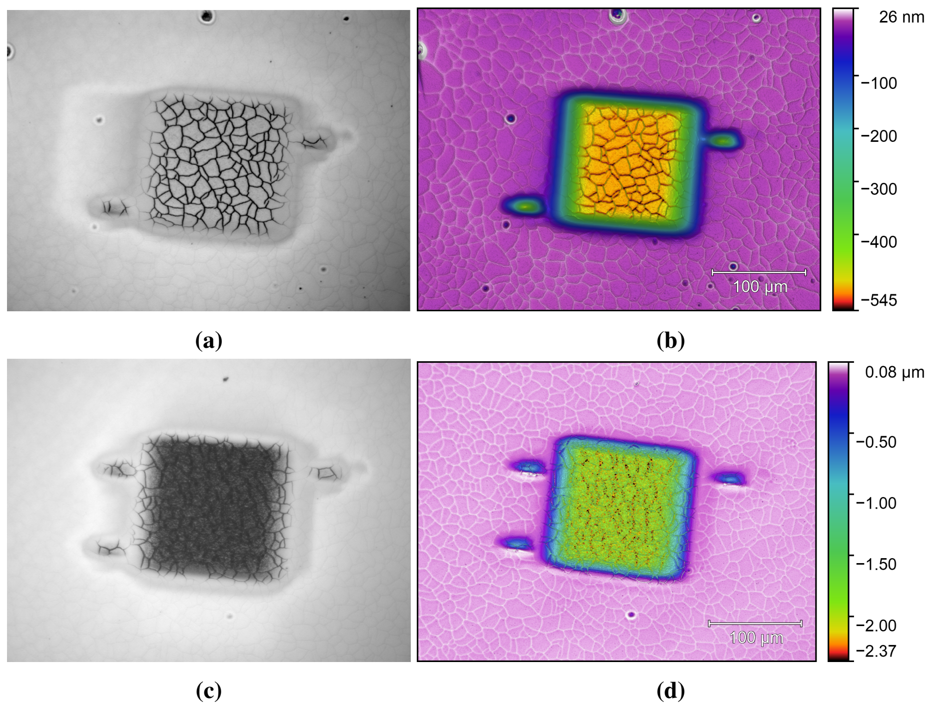


**Figure 4.31:** For sample W-D1-F0.9, a (a) greyscale image and (b) topographic map for the shallow crater, and (c) greyscale image and (d) topographic map for the deep crater, both formed by SIMS depth profiling.

**Crater depth summary.** The presented SIMS craters are representative for the other samples, with as-implanted samples producing smooth crater bottoms with some pitting, and 1.8 J/cm$^2$ PLM samples producing smooth crater bottoms with trench formation from the straight cracks. The other 0.9 J/cm$^2$ PLM samples similarly produced rough bottoms for the deep craters and smooth bottoms for the shallow craters. This was also true for sample W-D0.1-F0.9, which does not have cracks on the surface and thus no trench formation. The obtained depth values for the various samples are given in table 4.2, along with average sputter rates calculated from the measured depths and the active sputtering time as reported by the instrument logs.

**Table 4.2:** Depths of SIMS craters as measured with the Bruker ContourGT-K 3D Optical Profiler using VXI at 11X effective magnification. Based on the depths and total sputtering time, an average sputter rate was calculated for each sample. Note that it is assumed in the rate calculation that the SIMS craters are perfect cubes of raster area x depth, while in reality they are trapezoidal prisms with inward-sloping walls. However, the error is similar between the craters, as the depth is small compared to the area, both for shallow and deep craters.

| Sample | Depth [nm] | Avg. rate [µm$^3$/s] |
| --- | --- | --- |
| W-D0.1-asImp | 2025 | 29.4 |
| W-D0.1-F0.9 | 2002 | 28.6 |
| W-D0.1-F0.9 shallow | 451 | 29.7 |
| W-D0.1-F1.8 | 1892 | 28.0 |
| W-D1-asImp | 1859 | 27.3 |
| W-D1-F0.9 | 1970 | 28.8 |
| W-D1-F0.9 shallow | 512 | 29.7 |
| W-D1-F1.8 | 2265 | 31.0 |
| W-D1-"FzSi" | 536 | 29.1 |
| W-D1 accidental implant | 1294 | 28.5 |
| W-D2-asImp | 2077 | 31.0 |
| W-D2-F0.9 | 2009 | 30.1 |
| W-D2-F0.9 shallow | 524 | 32.1 |
| W-D2-F1.8 | 2039 | 31.0 |

### Depth adjustments for F0.9 samples

As stated under experimental details, the 0.9 J/cm$^2$ PLM samples provided additional challenges relating to depth calibration, because it was observed that the $^{30}Si_2^+$ signal was continuously increasing. The $^{30}Si_2^+$ yields from the different PLM samples are shown in figure 4.32, where 0.9 J/cm$^2$ PLM samples are plotted with a dashed red line, and other samples with a solid black line. The counts per second from the 0.9 J/cm$^2$ PLM samples increase by almost an order of magnitude, while the signals from the other samples are relatively constant.

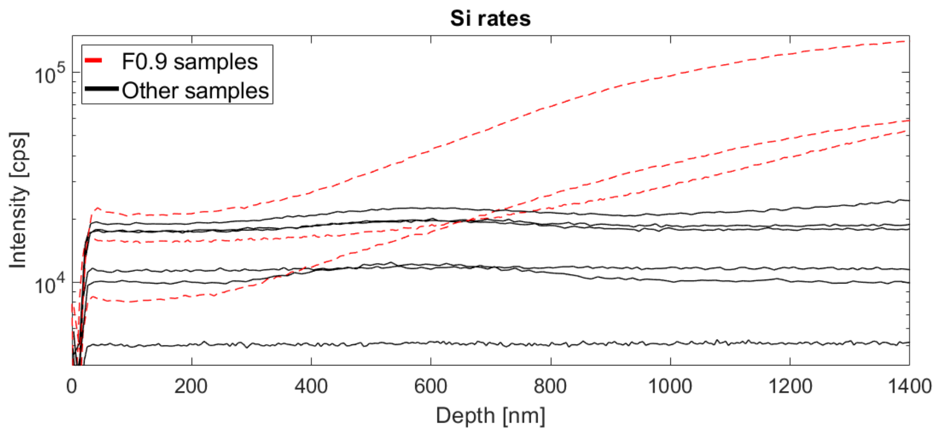


**Figure 4.32:** $^{30}Si_2^+$ yield from as-implanted and PLM samples, as recorded by the instrument. The dashed red line indicates PLM samples of 0.9 J/cm$^2$ laser fluence, while the other samples are drawn with solid black lines.

During the experiment, it was assumed that the signal increase was related to an increase in sputter speed by the ion beam. Therefore, an additional shallow crater was sputtered to more accurately relate depth to the sputtering cycles. It was observed that there was a small dip in the $^{184}$W-signal preceding the main peak. This dip was located in the depth profiles for both the deep and shallow craters, and the data points for the deep crater profiles were linearly stretched/compressed so that the dip would occur at the same depth as it did in the shallow craters. The data endpoints are not affected by the value shift. The effects of the adjustments are displayed visually in figure 4.33, where the location of the aforementioned dip is indicated by a red circle.

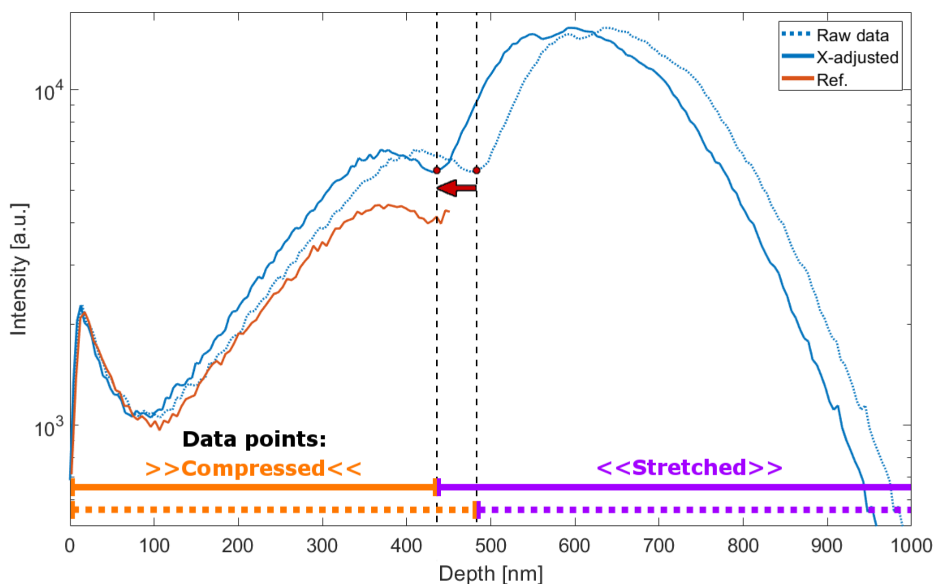


**Figure 4.33:** For sample W-D0.1-F0.9, the graph shows the effect on the data points of the deep SIMS crater when x-values (depth) are adjusted to better match data obtained from the shallow SIMS crater, here termed "Ref" for reference. Data point density increases to the left of the adjusted value, and decreases to the right of it, but the recorded depths of the first and last data points remain unchanged. The inherent volatility of SIMS is also exemplified by these graphs, as the adjusted measurement and ref. measurement obtain different peak counts of $^{184}$W, even though they were performed on the same sample in close temporal succession.

### W depth profiles

SIMS depth profiling was performed to investigate the effects of the PLM on the distribution of W within the bulk. As explained in the theory, a push of dopants towards the surface is expected due to dopant diffusion across the solid-liquid interface while the sample is molten, and it was of interest to study this effect. As a secondary objective, SIMS should be able to detect the species responsible for the presumed accidental ion implantation on the wafer pieces.

**As-implanted samples.** The SIMS profiles for W-concentration from the as-implanted samples are shown in figure 4.34, with (a) showing the raw recorded counts, while (b) shows the W-signal divided by the Si-signal to account for sputter yield variations. The curves are bell-shaped with a trailing tail. By modelling them with a Gaussian fit (not shown), mean depths of 574, 571 and 590 nm are found for the dosages D2, D1 and D0.1, respectively. Additionally, there is a concentration spike close to the surface for each sample in the Si-divided signal, but it is 2-4 orders of magnitude smaller than the peaks of the bell curves. Regarding the peak heights of the curves, if dosage D1 is set to 1, dosages D2 and D0.1 attain heights of 2.45 and 0.0438 for the raw signal, and 4.01 and 0.0729 for the relative signal, respectively.

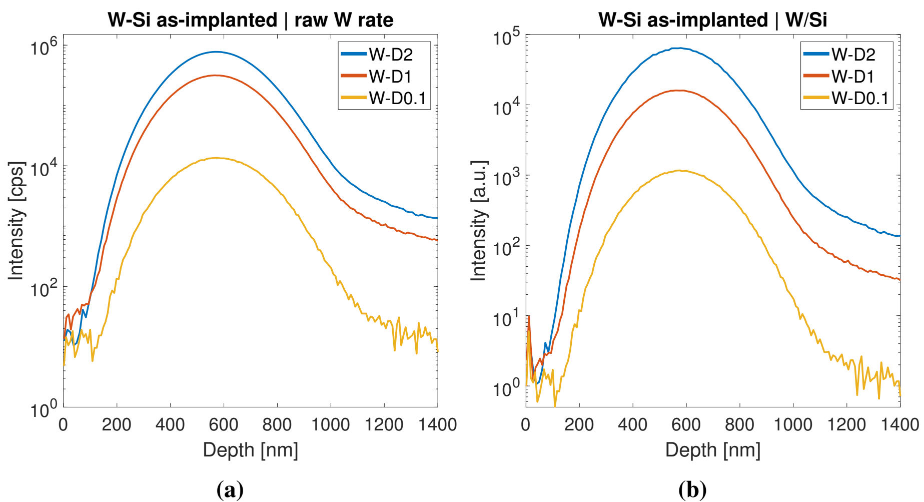


**Figure 4.34:** SIMS depth profiles for as-implanted samples with W concentrations of 0.1, 1 and 2 at.%, showing (a) raw $^{184}W$-signal and (b) $^{184}W$-signal divided by $^{30}Si_2^+$-signal. The curves display characteristic Gaussian profiles resulting from ion implantation.

**0.9 J/cm$^2$ PLM samples.** Displayed in figure 4.35 are the SIMS depth profiles for W-concentration in the PLM samples of fluence 0.9 J/cm$^2$, showing (a) the raw obtained counts for $^{184}$W and (b) the W signal divided by the Si signal. For these samples, a push of W towards the surface is observed. In sample W-D0.1-F0.9, this is manifests as a double peak structure, with the valley between them centred around 435 nm. For samples W-D1-F0.9 and W-D2-F0.9, the overall bell shape is preserved, with the former displaying a dip in the leading edge around 450 nm, and the latter at 490 nm. For dosages D1 and D0.1, there is a local concentration maximum at the very surface, while dosage D2 displays a shoulder in the concentration profile at 90 nm. The surface concentration spike is within 2 orders of magnitude in the raw signal, and one order of magnitude in the Si-divided signal.

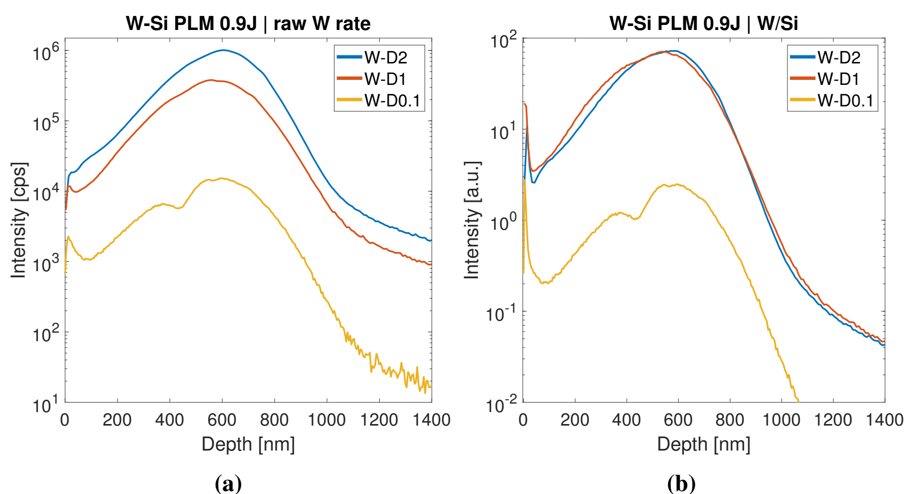


**Figure 4.35:** SIMS depth profiles for 0.9 J/cm$^2$ annealed PLM samples with W concentrations of 0.1, 1 and 2 at.%, showing (a) raw $^{184}$W-signal and (b) $^{184}$W-signal divided by $^{30}Si_2^+$-signal. A push of the implanted W towards the surface is observed.

**1.8 J/cm² PLM samples.** The SIMS depth profiles for W-concentration in the PLM samples annealed with a fluence of 1.8 J/cm² are displayed in figure 4.36, for (a) the raw $^{184}$W-signal and (b) the W signal divided by the Si signal. For dosages D0.1 and D1 a double peak structure is clearly observed, while for D2 the secondary peak manifests itself as a shoulder at the trailing edge of the bell curve. The valley between the peaks has its minima at 840 nm for D0.1 and 920 nm for D1. A similar point exists at 960 nm for D2, which is the middle of the lower-sloping part of the shoulder. The surface concentration spike is prominent for this sample set, surpassing the main peak in amplitude for the Si-divided signal for dosage D0.1, being similar in magnitude for D1, and within an order of magnitude for D2.

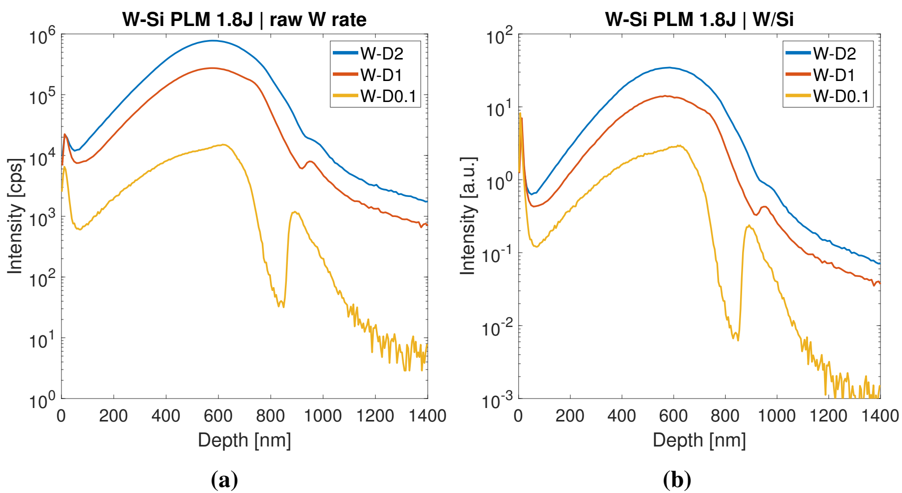


**Figure 4.36:** SIMS depth profiles for fluence 1.8 J/cm² PLM samples with W concentrations of 0.1, 1 and 2 at.%, showing (a) raw $^{184}$W-signal and (b) $^{184}$W-signal divided by $^{30}Si_2^+$-signal. A push of the implanted W towards the surface is observed, manifesting as double peak structures.

**Accidental W implantation.** SIMS profiles were also obtained from areas on the samples, outside the $1 \times 1$ cm as-implanted squares, where ion implantation was suspected. Such profiles tracking $^{183}$W and $^{184}$W are displayed in figure 4.37 (a) from the aptly named "accidentally implanted" region, and in (b) for the nominally unimplanted "FzSi" region on wafer piece W-D1. A bell-shaped distributions akin to those for the as-implanted samples is realised in the accidentally implanted region, with means of $572 \pm 1$ nm and $569 \pm 1$ nm for $^{183}$W and $^{184}$W, respectively. In the "FzSi" region, there is a weak signal for $^{184}$W peaking at 38 cps, and a very weak signal for $^{183}$W at <10 cps.

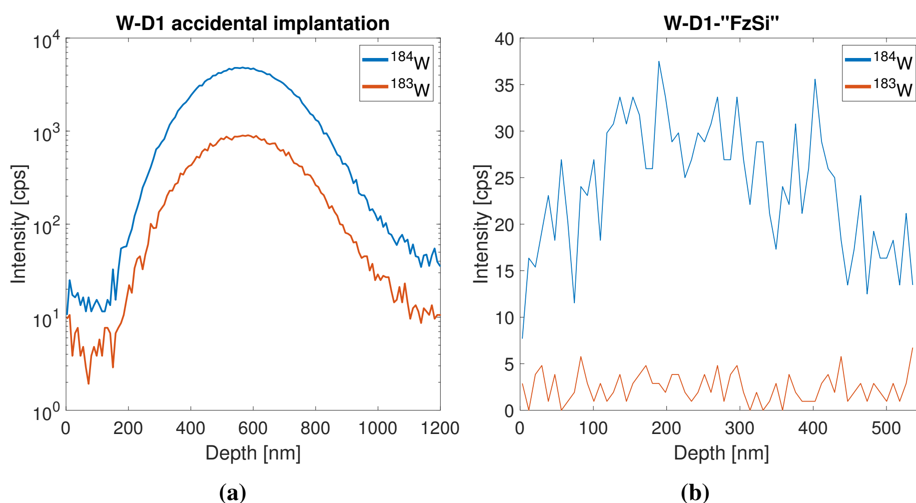


**Figure 4.37:** SIMS profiles for $^{183}$W and $^{184}$W from (a) the accidentally implanted region and (b) the nominally unimplanted region on wafer piece W-D1.

**Count consistency.** To examine the consistency of the results, total $^{184}W$ ion yields until a depth of 1.4 µm for the fluence 0.9 J/cm$^2$ , 1.8 J/cm$^2$ , and as-implanted samples are listed in table 4.3. Regarding first raw W counts, while samples containing 2 at.% W obtain more counts than those of 1 at.% W, which in turn obtain more counts than those of 0.1 at.% W, there is not much consistency. On a per-fluence basis, the ratios are reasonably close to the nominal 2 : 1 : 0.1 values, with W-D2-F0.9 and W-D0.1-asImp as notable outliers with high total counts. Significant differences exist between fluences for any given W dosage. Regarding second the total counts for when the W signal is divided by the Si signal, the consistency did not improve, with greater discrepancies on both a per-fluence and per-dosage basis. The outliers also changed, with sample W-D2-F0.9 going from most to least counts among the 2 at.% W samples, for example, and even measuring fewer counts than the 1 at.% W sample of the same fluence.

**Table 4.3:** Obtained counts of $^{184}W$ until a depth of 1.4 µm from the as-implanted and PLM samples, for the raw W signal and the W signal divided by the Si signal. The ratios have been normalised such that samples with a W dosage of 1 at.% attain a value of 1.

| Signal | Fluence | D2 | D1 | D0.1 | Count Ratio |
|---|---|---|---|---|---|
| W | 0 | $2.25 \times 10^7$ | $1.29 \times 10^7$ | $0.58 \times 10^7$ | 1.74 : 1 : 0.45 |
| | F0.9 | $3.83 \times 10^7$ | $1.62 \times 10^7$ | $0.12 \times 10^7$ | 2.36 : 1 : 0.07 |
| | F1.8 | $3.02 \times 10^7$ | $1.12 \times 10^7$ | $0.10 \times 10^7$ | 2.70 : 1 : 0.09 |
| W / Si | 0 | 1927 | 673 | 49.4 | 2.86 : 1 : 0.07 |
| | F0.9 | 989 | 1072 | 66.8 | 0.92 : 1 : 0.06 |
| | F1.8 | 1396 | 590 | 217 | 2.37 : 1 : 0.37 |

### 4.3.4 Hyperspectral Imaging & photoluminescence

PL spectroscopy was employed to investigate the internal electronic states of the material, as it is an excellent tool for detecting allowed energy states below the band gap. To probe a large area at a time, PL was conducted in the form of hyperspectral imaging, where every pixel of the image contains a full PL spectrum. The results in this section will be presented for each wafer piece at a time, consisting of spectra from regions of interest, and hyperspectral images to spatially locate the band-to-band (BB) and sub-band gap luminescence origins. For the hyperspectral images, the BB signal is integrated over 1.09-1.11 eV, while the sub-band gap signal is integrated over 0.732-0.773 eV. The integrals are adjusted for varying data point density, such that the images are directly comparable.

**Wafer piece W-D2.** Starting with wafer piece W-D2, in figure 4.38 are shown (a) PL spectra from the 1.8 J/cm$^2$ , 1.4 J/cm$^2$ and 0.9 J/cm$^2$ PLM spots, as well as from the as-implanted region, and (b) hyperspectral images of (left) sub-band gap luminescence and (right) BB luminescence. Observing first the hyperspectral images, both BB and sub-band gap luminescence is low in the as-implanted region, and higher in the PLM spots. Both signals seem to increase with increasing PLM laser fluence, though this is most notable in the sub-band gap signal. The large, rectangular region at the top of the wafer piece with medium intensity is the accidentally implanted region. There are high intensity edge effects in both the BB and sub-band gap signals.

In the extracted PL spectra, studying first the BB peak at 1.1 eV, it is non-existent in the highly amorphous as-implanted region, and increases in amplitude with increasing laser fluence for the PLM spots. The peak of F1.8 is clearly tallest, with F0.9 and F1.4 both having about half the height. Regarding next the sub-band gap luminescence, it follows a similar pattern. No signal is emitted from the as-implanted region, while the broad response around 0.75 eV increases with PLM laser fluence. Though the BB and sub-band gap responses are of similar strength, the maximum amplitude for the sub-band gap response is above that of the BB-peak for all laser annealed samples.

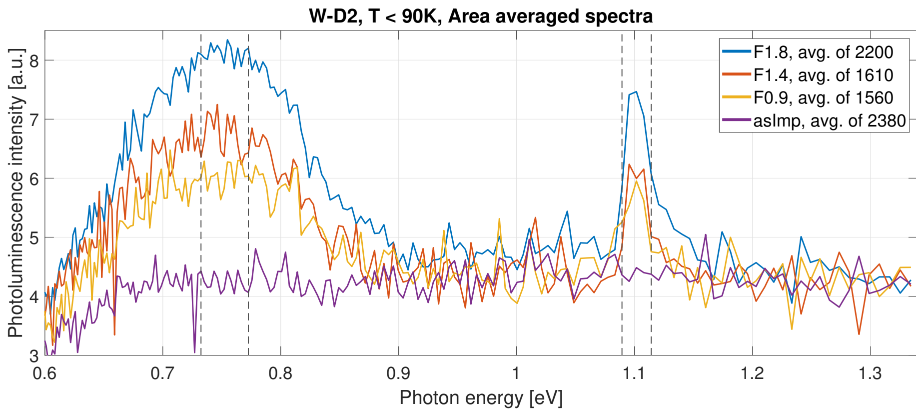


**(a)**

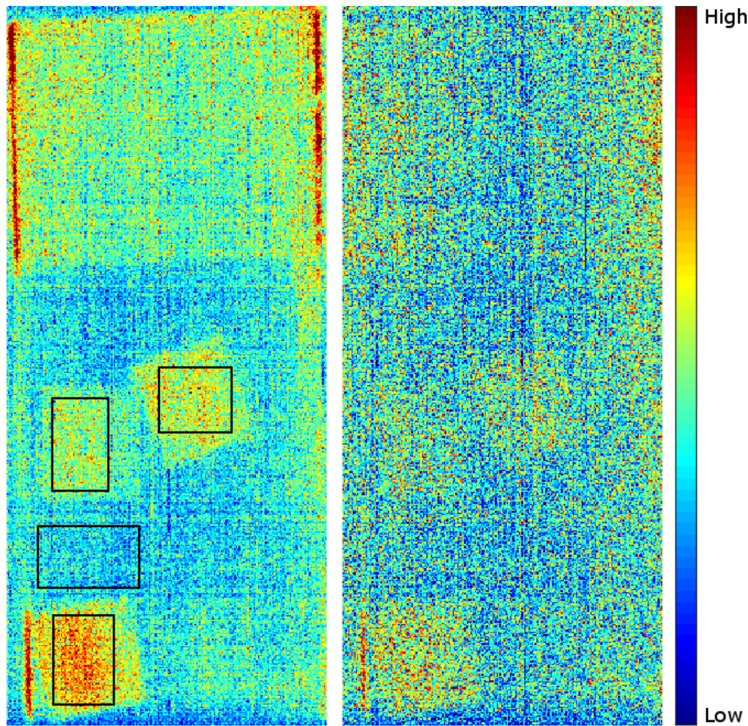


**(b)**

**Figure 4.38:** For wafer piece W-D2, (a) photoluminescence spectra from regions of interest, and (b) hyperspectral images for (left) sub-band gap and (right) band-to-band luminescence. The presented spectra are normalised in intensity with regards to the collection area, shown with overlaid black boxes in (b), and the labels state how many spectra they are an average of. Dashed vertical lines in (a) show the eV integration ranges for the hyperspectral images, which have been normalised in intensity for data point density.

**Wafer piece W-D1.** Moving on to the W-D1 wafer piece, figure 4.39 displays (a) PL spectra from the 1.8 J/cm$^2$ , 1.4 J/cm$^2$ and 0.9 J/cm$^2$ PLM spots, as well as from the as-implanted and "FzSi" regions, and (b) hyperspectral images of (left) sub-band gap luminescence and (right) BB luminescence. Disregarding edge effects, the BB luminescence is most intense at the bottom of the wafer piece in the "FzSi" region, which also has a strong sub-band gap signal. The PLM spots are easily distinguishable from the surrounding as-implanted region for both signals, with the strengths of both signals increasing with increasing laser fluence. Especially for sample W-D1-F1.8, there is a clear variation in sub-band gap signal intensity within the laser spot.

In the PL spectra, the BB-peak at 1.1 eV is highest for Fz-Si and non-existent for the as-implanted region. For the PLM spots, F0.9 is lowest at about a third of the amplitude of the Fz-Si peak, while F1.4 and F1.8 are about equal at half of the intensity, with F1.4 being slightly stronger. All spectra, apart from the as-implanted one, display a broad sub-band gap luminescence centred on approximately 0.75 eV. The peak height increases with increasing PLM fluence. The "FzSi" spectrum also exhibits this broad sub-band gap peak, having an amplitude between F1.4 and F1.8. The maximum intensity of the BB peak is greater than the sub-band gap peak for the "FzSi" spectrum, while the reverse holds true for the PLM spots.

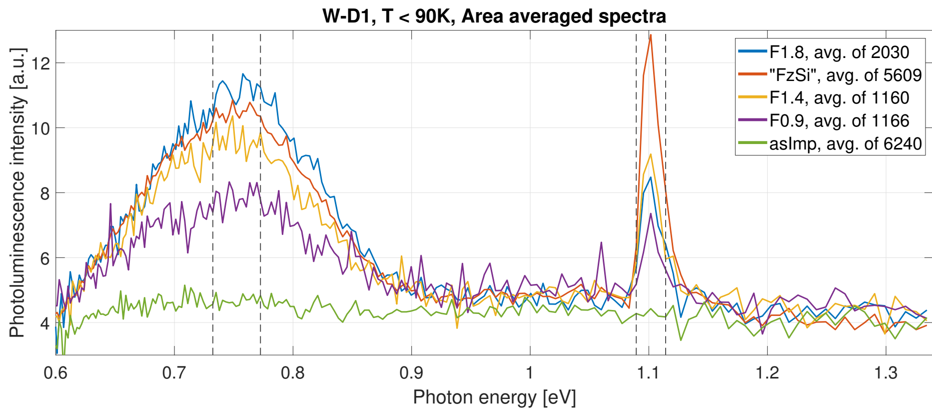


**(a)**

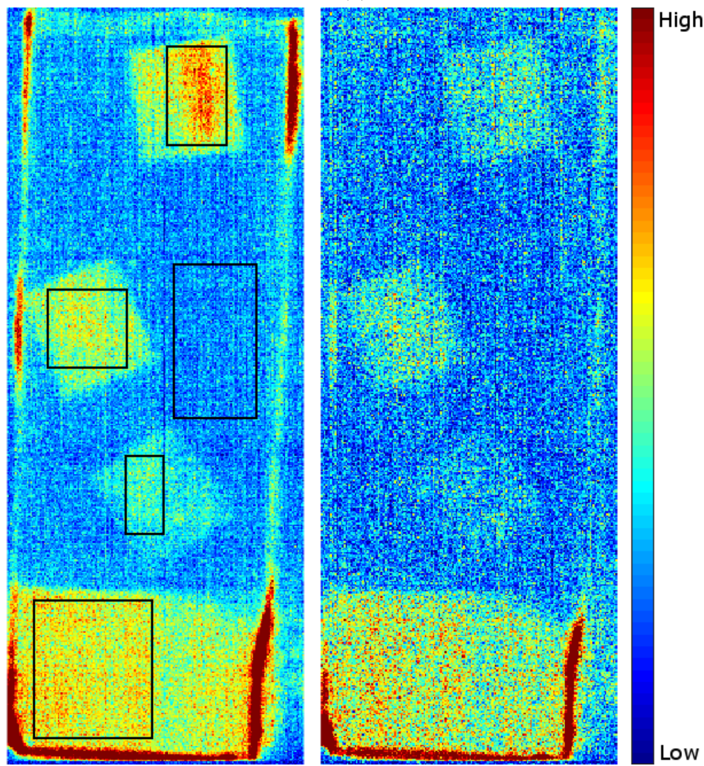


**(b)**

**Figure 4.39:** For wafer piece W-D1, (a) photoluminescence spectra from regions of interest, and (b) hyperspectral images for (left) sub-band gap and (right) band-to-band luminescence. The presented spectra are normalised in intensity with regards to the collection area, shown with overlaid black boxes in (b), and the labels state how many spectra they are an average of. Dashed vertical lines in (a) show the eV integration ranges for the hyperspectral images, which have been normalised in intensity for data point density.

**Wafer piece W-D0.1.** Lastly, for wafer piece W-D0.1 the (a) PL spectra from the 1.8 J/cm$^2$ , 1.4 J/cm$^2$ and 0.9 J/cm$^2$ PLM spots, as well as from the as-implanted region, and (b) hyperspectral images of (left) sub-band gap luminescence and (right) BB luminescence are displayed in figure 4.40. The PLM spots are easily distinguishable from the low intensity of the as-implanted region in both images. Again, the sub-band gap signal offers greater contrast within each PLM spot, but edge effects make the comparisons more difficult for this wafer piece. A large area at the top of the wafer piece consists of the accidentally implanted region, but the contrast between it and the as-implanted region is low in the sub-band gap image, and non-existent in the BB image.

Concerning the PL spectra, the BB peak of 1.1 eV increases with increasing annealing fluence, however the differences between fluences 1.8 J/cm$^2$ and 1.4 J/cm$^2$ are low. The behaviour of the broad sub-band gap peak of 0.75 eV also differs from the previous samples, in that there is a slight response from the as-implanted region. For the PLM spots, F1.8 is again the leader in amplitude, while F1.4 and F0.9 are equal. In relative amplitude between peaks, BB is stronger for F1.8, sub-band gap is weaker for F1.4, and they are equal for F0.9.

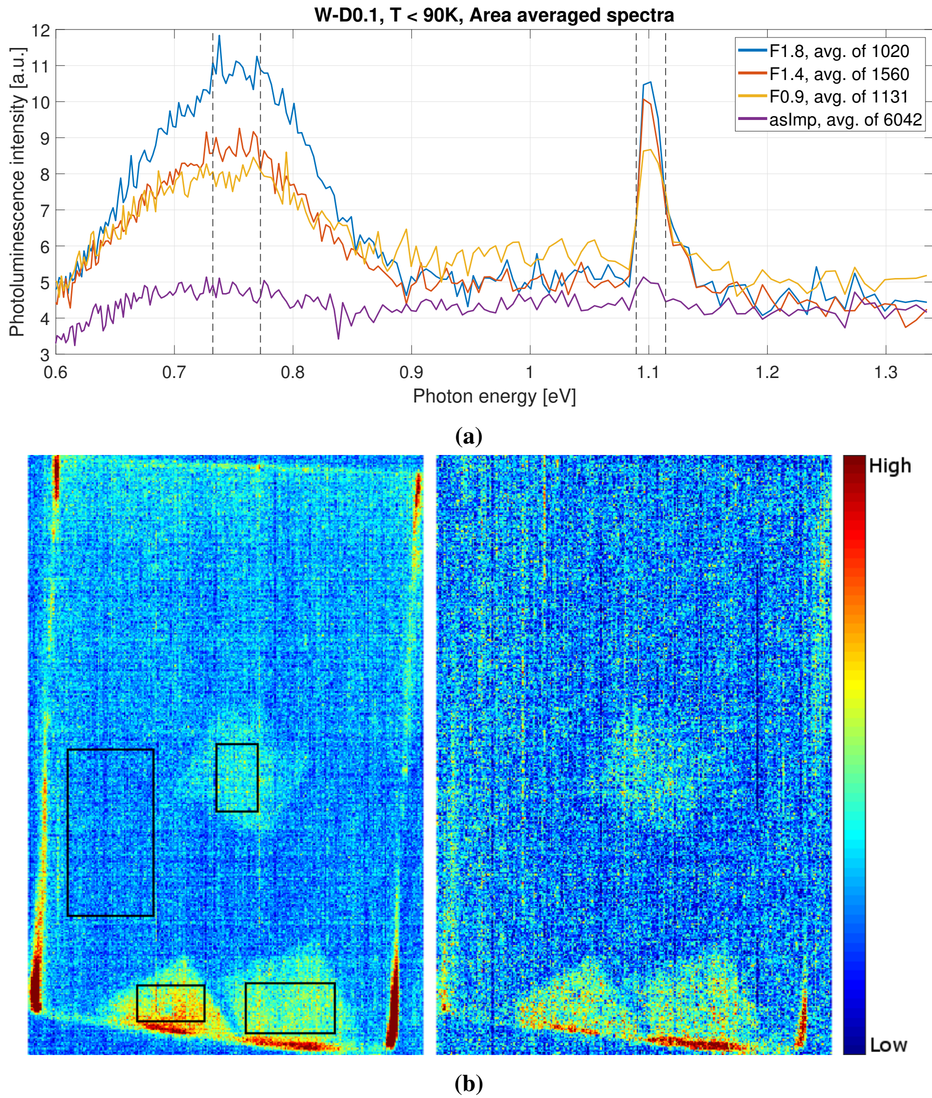


**Figure 4.40:** For wafer piece W-D0.1, (a) photoluminescence spectra from regions of interest, and (b) hyperspectral images for (left) sub-band gap and (right) band-to-band luminescence. The presented spectra are normalised in intensity with regards to the collection area, shown with overlaid black boxes in (b), and the labels state how many spectra they are an average of. Dashed vertical lines in (a) show the eV integration ranges for the hyperspectral images, which have been normalised in intensity for data point density.

*It is the mark of an educated mind to be able to entertain a thought without accepting it.*

Aristotle

# 5 Discussion

In this chapter, the results from the material characterisation will be discussed. Like the preceding chapter, it is divided between surface properties and near-surface properties, but findings from different instruments will be more readily combined here in the discussion. As in the previous chapter, the SIMS craters will be grouped together with the rest of the SIMS discussion, rather than with the other surface features.

Surface morphology is discussed first, followed by a discussion surrounding the technical aspects of the measurements. Next, the crystallinity is discussed based on Raman spectroscopy and EBSD. A look at the SIMS craters and depth profiles follows. The chapter ends with a discussion about the hyperspectral images and photoluminescence spectroscopy.

# 5.1 Surface Properties

## 5.1.1 Surface Morphology

**Overall morphology.** From the optical micrographs in section 4.2.1 it is seen that three distinct surface morphologies were brought forth by the PLM treatment of the W-implanted samples. The first is characterised by large areas (roughly >300 µm) of even surface broken by straight lines, which SEM imaging in section 3.2.1 and AFM scanning in section 4.2.3 have revealed to be cracks. By creating a collage of optical micrographs overlaid on top of the respective PLM spots, it is evident that the straight cracks are aligned with the wafer piece edges. It has been observed that the cleavage planes in crystalline silicon align with high symmetry lattice plane directions [90], and thus it is reasonable to conclude that the straight lines are cracks roughly along the $\langle 110 \rangle$ direction for our samples, as it is the weakest for a (100) plane of crystalline Si [91]. As the cracks are not perfectly parallel, stacking faults or cracking along closely related planes is suggested.

The second distinctive morphology mirrors the first, in that it is comprised of mostly straight, parallel lines which too through AFM and SEM have been revealed as cracks. It differs when it comes to the scale of the features, as the cracks here form rectangles with edges of around 100 µm. Similarly, the cracking is likely to roughly follow lattice planes, though the planes appear more disordered. It is notable that this morphology appeared only for the same samples which had the first morphology as well.

The third and final morphology is a subdivision of the surface into polygons of various sizes with random wall orientation, with these walls, too, having been determined as cracks. The crack propagation which lead to the polygonal morphology is likely to have occurred mainly along grain boundaries in the crystal [92–94], explaining the highly irregular shapes. However, as will be established later in section 5.2.2, the grain sizes of our samples cannot be determined from the available data, so the statement about propagation along grain boundaries is not definitive.

When viewed with the optical profiler, all three morphologies appeared as ridges protruding from the sample surface. The cracks as measured in the SEM are about an order of magnitude smaller than the Abbe diffraction limit of visible light, and are therefore expected to not be visible in the interferograms. The ridges are thus best understood as a curling of the sample surface close to the cracks, which is also in agreement with the data from the AFM measurements in section 4.2.3. As the Raman investigations revealed, the PLM affected volume cracked from tensile stresses, causing the surface close to the cracks to compress, elevating the edges that form the cracks. Though the materials and cracking mechanisms are very different, it is apt to here make a comparison to drying soil, which also cracks from tensile stresses [95]. In figure 5.1 is given a comparison between a heightmap render from a PLM sample and cracked soil, which

also forms cracks with curling edges.

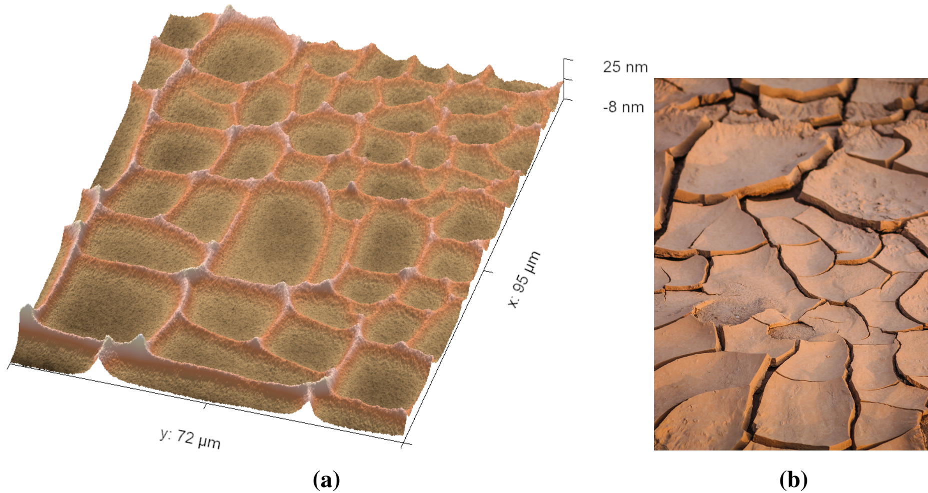


(a) (b)

**Figure 5.1:** **(a)** 3D render of polygonal surface morphology from a PLM sample. **(b)** photograph of clay which has cracked when drying, producing raised edges at the surface close to the cracks. Though the scales are orders of magnitude apart, in both cases tensile fracture leads to similar results. Unknown photographer, acquired from [96].

Regarding the spatial ordering of the three distinct morphologies, in samples where all are present, the trend from the centre to the edges of the PLM spot is always large lines $\rightarrow$ small rectangles $\rightarrow$ polygons of various sizes. The relative areas of the morphologies for any given dose of W are related to the PLM laser fluence, with greater fluences corresponding to larger areas of the first and second morphologies. For the PL samples of fluence 0.9 J/cm$^2$ , the large-scale line morphology was completely absent, while for the fluence of 1.4 J/cm$^2$ , only sample W-D0.1-F1.4 had straight lines and rectangles present. Thus, two implications are brought forth. First, there is a direct relation between the energy of the laser pulse and the obtained surface morphology. Secondly, the intensity distribution of the laser beam for the PLM setup is not uniform, with a greater photon density in the centre, and lower towards the edges. The fluences of 0.9 J/cm$^2$ , 1.4 J/cm$^2$ , and 1.8 J/cm$^2$ are thus to be understood as averages over some spatial distribution.

**Smaller features.** Regarding other surface features, all samples showed the presence of spherical holes of various sizes on the surface. The holes may be explained by explosive boiling, where the laser first melts the surface, and then further superheats the melt as the heating from the laser is greater than thermal dissipation throughout the material. When the melt is superheated above the boiling point, large density fluctuations arise, and vapour bubbles are created and grow due to homogeneous nucleation [97]. A

schematic representation of explosive boiling is provided in figure 5.2. The 25 ns laser pulse forms a high temperature region close to the sample surface. After the pulse, some portion of the transferred energy propagates into the bulk of the material via thermal diffusion, while the excess energy increases the temperature of the melt, superheating it. When 0.9 $T_c$ is reached, where $T_c$ is the thermodynamic critical temperature, the melt abruptly transforms into a mixture of liquid droplets and vapour. The vapour is then ejected from the melt, analogously to boiling water, however bubble nucleation in this case is strictly homogeneous. Heterogeneous bubble nucleation, as would be the case in normally boiling water, is an unlikely mechanism [98]. Where a vapour bubble is passing through the surface as the silicon melt re-solidifies, a hole is formed. This is in agreement with the raised edges of most holes, as was observed with the optical profiler, since the matter from directly atop the bubble must be displaced when the bubble penetrates the surface.

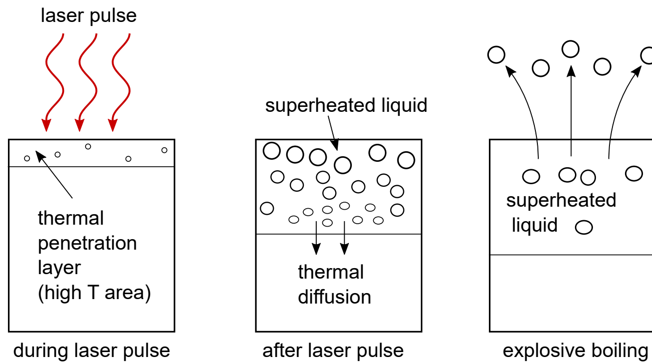


**Figure 5.2:** Schematic representation of laser ablation and explosive boiling. Figure reproduced based on fig. 2 in [99]. Not to scale.

On the surfaces of multiple samples, most notably those of fluence 1.8 J/cm$^2$, ripples or waves were observed. Wave formation on silicon surfaces resulting from nano- or femtosecond laser irradiation is a known phenomenon, both for single and multiple pulses, and fluences both above and below the ablation threshold [100–104].

Every PLM annealed sample had at least one hole with slightly curving, protruding lines. These extending lines were revealed by the optical profiler to be shallow grooves (figure 4.14 page 55). While hole formation and cracking in silicon resulting from laser ablation has been widely studied [90, 97, 105–109], similar structures have not been reported in the literature. The orientation of the grooves appears to have no relation to the orientation of any other feature on the samples, save that they extend radially outwards from holes in the samples. A further investigation of the mechanism underlying their creation is beyond the scope of this thesis.

### 5.1.2 Crack Investigation Technicalities

#### AFM

**Sample W-D0.1-1.8 centre cracks** The scan from the centre of sample W-D0.1-F1.8, as was presented in figure 4.15 (page 57) seemed to indicate that the surface contained straight, raised ridge lines, with cracks located at the centre of the ridges. In the height map, there are virtually parallel and perpendicular ridges with respect to the scanning direction, as well as a ridge at a slightly tilted angle towards the top of the image. In each case, there is a gradual slope on one or both sides of the ridges. The ridge lines may appear suspiciously straight, raising concern about scanning artefacts being interpreted as features [110]. An immediate error source concern is low pass filtering in the software, which causes steps between even surfaces to appear as one sided sloped ridges, as is the appearance of the vertical ridge in the scan. Excessive low pass filtering is unlikely, as the slopes appear in the horizontal and near-horizontal scans as well, where there is no difference in the peak force error compared to the flat areas, signifying that the sloping is indeed real. Among other error sources, there are no apparent contributions from scanner drift, hysteresis, linearity effects, repeating features, creep, sticking surface contamination, vibrations or electronic interference. What is likely is an under-representation of the width and depth of the crack, as the width of the probe prevents it from reaching the bottom. While the bottom horizontal crack may be suspected as a line artefact, as the surface depressions occur on almost a single scan line, the near-horizontal line at the top of the image covers 21 scan lines vertically and too contains the steep depressions. When crossing the ridge and crack, the peak force error instantaneously reaches a highly positive value before gradually changing to a highly negative value and then returning to normal, indicating that the needle is indeed ascending out of some depression, rather than simply falling off a ledge onto a flat surface. Finally, the middle horizontal line displays the depressions with no significant sloping on either side, strengthening the interpretation of the cracks as real features.

**Sample W-D0.1-F1.8 edge** The scan from the edge of sample W-D0.1-F1.8 was displayed in figure 4.16 (page 58), and indicated the presence of more randomly oriented cracks with raised edges, seemingly forming ridges as was the case for the centre of the sample. The orientation of the ridges or cracks with regards to the scanning direction (horizontal left-to-right) does not seem to have any influence on their magnitude or shapes, indicating that they are not scanning artefacts. Other common artefact, as detailed in the previous paragraph, are also not found. At the bottom centre of the scan, there appears to be a raised feature or contaminant particle, with possible scanning artefacts in the immediate vicinity arising from the tip's interaction with soft dust tissue. The effect is local, however, and does not impact the interpretation of data concerning the cracks/ridges. As none of the cracks are near-parallel, covering only 2-4 data points

along each scan line, the changes in peak force error do not explicitly help feature interpretation. However, it is clear that there is some sharp feature present, causing a sudden shift in the position of the probe.

### SEM

As was presented in figure 4.17 (page 59), it appeared as if the surface had split for both samples, forming cracks with a continuity in surface patterns across the gaps. However, as the micrographs were acquired with an Everhart-Thornley detector, the possibility of shadowing from 3D structures must be considered [60, 111]. The detector is mounted on the side of the chamber, which means that tall features between the probed point and the detector may prevent electrons from reaching the detector, creating the appearance of dark shadows. Thus, the dark area could be interpreted as a shadow arising from tall steps, rather than a gap. However, an understanding of the contrast mechanisms of secondary electron imaging makes the interpretation of the black area as a shadow unlikely. As detailed in the theory in section 2.3.2, protruding edges appear bright when imaged with the SE signal, as electrons may escape from a greater fraction of the interaction volume. In the micrographs, the signal from the edges of the surface on both sides of the black area is bright, indicating that the black area is empty space into which additional signal-generating electrons escape. If it were a shadow from a tall step, only one edge would appear bright. Additionally, we know from measurements with the AFM and optical profiler that the opposing surface sections have virtually the same height, so the only electrons blocked from reaching the detector are those from the bottom of the cracks, hence the blackness.

## 5.2 Near-surface Properties

### 5.2.1 Raman Spectroscopy

The Raman spectra from section 4.3.2 are interpreted in this section. The focus will be on oxide and silicide compounds when identifying peaks, because metallic tungsten cannot be detected by Raman spectroscopy. As a conductor, its electron clouds are not sufficiently polarisable by the laser beam to undergo Raman scattering.

**Temperature effects.** A lingering concern in Raman spectroscopy is the possibility of laser-induced heating or damage to the sample, as the beam may be directed on a small area of the sample for hours, or even days, depending on the nature of the measurement. For silicon, the relationship between the Γ-peak position and surface temperature has been studied extensively [112–115]. By comparing the fitted peak values from the Fz-Si sample to experimental findings, the maximal heating of the sample from full 100 mW laser power is unlikely to exceed 30 K, with lower laser power of 50 mW realising temperature increases of at most 23 K. Lower laser powers did not shift the Γ-peak from 521.1 $cm^{-1}$. Thus, heat-related phenomena are unlikely to significantly influence the overall shapes of the spectra, via for instance thermal broadening.

**Fz-Si.** All the expected features in the Raman spectrum from c-Si were identified in our sample. Additionally, there was a single unexpected peak at 759 $cm^{-1}$. This is attributed to being a shoulder of the 2LO-peak at 824 $cm^{-1}$, visible only due to the excellent signal-to-noise ratio attainable on our samples. This conclusion is drawn as no matching peaks arising from carbon or oxygen in the Si matrix is found in the literature. The best documented candidate would be organic contamination from the amino acid tryptophan, whose indole ring produces shifts of 757-760 $cm^{-1}$ [116, 117]. Other Raman shifts associated with the molecule are absent, however, making its presence highly unlikely. Astute readers might question the absence of a peak from boron, as the Fz-Si sample is P-doped. B atoms in the Si matrix are, instead of creating a separate peak, known to cause a Fano-broadening of the Γ-peak [117].

**1.8 PLM.** The expected features from c-Si were identified in the spectra for the 1.8 $J/cm^2$ PLM samples, albeit in a broadened state, shifted to slightly lower wavenumbers. Contributions corresponding to a-Si were also identified, as a broad band at 100-200 $cm^{-1}$, and as a shoulder to the Γ-peak of c-Si around 440-480 $cm^{-1}$. These contributions are interpreted as arising from a high variation in Si-Si bonding angles next to W precipitates and W-rich phases, rather than from incorporated a-Si phases in the bulk. However, the contribution may also result from incorporation of Si into tungsten silicides, which are known to have a Raman band around 450 $cm^{-1}$. [118–120]. For tetragonal $WSi_2$, a band

at ~330 $cm^{-1}$ is expected, however it is not distinguishable in our spectra. It could be lost to broadening, or suggest other configurations of tungsten silicides, such as hexagonal $WSi_2$ or $W_5Si_3$.

Regarding the Γ-peak of c-Si, it is broader and of lesser magnitude than for Fz-Si, indicating greater disorder in the crystal for the PLM samples. The shift of the Γ-peak for the PLM samples to lower wave numbers is interpreted as an increase in tensile stress in the crystal with increasing W concentration, as the peak heights are nearly identical [121]. The significance of the variation in shape of the 440-480 $cm^{-1}$-shoulder with W-concentration is unclear, having its centre point shifted to lower wavenumbers for lower W-doses.

A feature in the spectra from the PLM samples which did not suit known silicon-related peaks was the peak at 597-600 $cm^{-1}$. Though W-doped, recrystallised Si has not been previously studied with Raman spectroscopy to the author's best knowledge, there are studies on other W-containing materials that suggests it may be attributed to some form of tungsten oxide. Castro et al. [122] heated tungsten platforms with different elements to 900 °C and studied the results with Raman spectroscopy. They obtained a peak at 597 $cm^{-1}$ which they attributed to $WO_3$. Harrison et al. [123] studied layered materials containing tungsten and selenium oxides (of the form $M_2(WO_3)_3SeO_3$). They obtained a broad main peak at 638 $cm^{-1}$, which they attributed to a symmetric stretching mode of $WO_6$, with sub-peaks at 598, 678 and 706 $cm^{-1}$ attributed to various $WO_6$-modes. The 678 $cm^{-1}$-peak would overlap with Si-modes in our spectra, while the 638 and 706 $cm^{-1}$-peaks are not present. The two missing peaks at 638 and 706 $cm^{-1}$ are of low intensity in the original work, and are reasonably lost to broadening in our spectra, or they might not be present in the first place due to differences in the materials disallowing certain Raman active modes.

Additionally, peaks from terminal W=O bonds for all configurations of $WO_3$ are expected around 930-960 $cm^{-1}$, with peak shape and location varying greatly with grain size and hydration level [124–127]. Surface W-atoms are active and form $W_6^+$-OH bonds when exposed to an oxidising atmosphere [128]. The entire reported area for the W=O peak coincides with the broad 2TO-mode in c-Si, making it undetectable in our samples.

The relative intensities of the ~600 $cm^{-1}$ peak also suggests a relation to W, as the intensity is greatest for lower doses of W. When there are more W atoms present, W precipitation is more likely to result in metallic phases, which produce no Raman shifts. Increased metallic cluster formation in higher-dose W samples is supported by TEM investigations of the samples by Sørhaug [129].

For the sake of completeness, it must be stated that silicon oxides have a prominent Raman band nearby at 607 $cm^{-1}$ [130, 131]. In the spectra from the 1.8 $J/cm^2$ PLM samples, the Γ-peak of Si was shifted by 3.7-5.7 $cm^{-1}$ relative to Fz-Si, as was the χ-peak at nominally 620 $cm^{-1}$. It is therefore extremely unlikely for the silicate peak

between them to shift by 7-10 $cm^{-1}$, and the peak at 597-600 $cm^{-1}$ in the PLM samples is not interpreted to arise from any known silicon oxide.

**Stress mapping.** The presented map from sample W-D2-F1.8 showed the magnitude of the Γ-peak shift as a function of position in the sample, with values of −0.34 to −4.16 $cm^{-1}$. As crack propagation has occurred in multiple directions, it is reasonable to assume that the stresses are biaxial rather than uniaxial. When working with scalar values rather than the stress tensor, stress in $\langle 001 \rangle$-oriented silicon from the Γ-peak shift is often estimated by

$$\sigma = -250\Delta\omega,$$

where $\sigma$ is the biaxial stress in MPa, and $\Delta\omega$ is the shift of the Γ-peak in $cm^{-1}$ [121]. It is clear from the equation that a negative peak shift results in a stress that is tensile, i.e. pulling the crystal apart. Thus, stresses from 85 MPa near the cracks to ~1 GPa far away from the cracks are obtained. From the gradient of increasing tensile stress away from the cracks it is evident that the lattice strain in the re-grown crystal has exceeded the fracture strength of the silicon, as may be expected from the solidification velocities obtained with nanosecond regime PLM [44].

### 5.2.2 Electron Backscatter Diffraction

To discuss the EBSD orientation maps for the various samples given in section 4.3.1, it is useful to take a closer look at the individual Kikuchi patterns that they are indexed from. As stated in section 3.2.1, the EBSD collection system presented some stability-related challenges which may have impacted the results. First, the quality of the obtained EBSPs will be evaluated and compared, including examples of incorrect map indexing. A discussion of the orientation maps will follow, on a per-fluence basis.

In figure 5.3, a Kikuchi pattern from a piece of Fz-Si which was not sent to W implantation is compared with those from the fluence 1.8 J/cm$^2$ PLM samples. It is evident that there is a difference in pattern quality between the (a) Fz-Si and (b) W-D0.1-F1.8 samples on one hand, and samples (c) W-D1-F1.8 and (d) W-D2-F1.8 on the other hand. Part of the difference may be explained by the gradual variation in intensity across the pattern for the samples with 1 and 2 at.% W. While the system logs state that patterns (c) and (d) are background subtracted, the presence of the intensity gradient and the scratch marks in the lower left corners indicate that background subtraction during pattern acquisition has failed. While this should not majorly impact pattern indexing, as a dynamic background subtraction and division is performed in the process, some negative effect in indexing confidence may be expected.

Background intensity aside, the patterns for PLM samples with 1 and 2 at.% W are blurrier than for Fz-Si and 0.1 at.% W, notably so for sample W-D2-F1.8. A blur or broadening in the pattern may have many causes, but relevant here are surface contamination or roughness, residual crystal stresses, and overlaid patterns from grain boundary crossings [132]. If the electron crosses a grain boundary from one grain to another, and they are both sufficiently large to form a Kikuchi pattern, then overlaid patterns are expected. However, if one of the grains is very small, then a broadening of the Kikuchi pattern from the 1$^{st}$ grain is expected instead [133]. Surface investigations with the optical profiler revealed some variation in surface roughness between the 1.8 J/cm$^2$ PLM samples, originating mainly from the raised edges at the surface cracks. However, RMS-roughness (Sq) remained below 10 nm for all 1.8 J/cm$^2$ PLM samples, and they are considered to be smooth enough that surface conditions should not negatively affect the pattern quality. Regarding crystal stresses, Raman investigations on sample W-D2-F1.8 revealed a variation in the tensile stress in the crystal with a variation in position along the surface, making this a likely cause of pattern broadening in (c) and (d). The crystal stresses are probably a result of W segregation near the surface from cellular breakdown, as is suggested from TEM investigations of this very sample set by Sørhaug [129]. As the segregated W-rich phases were determined to be only a few nm wide, they will blur the Si-related bands, rather than superpose W-related Kikuchi bands [133, 134].

To investigate the presence of bands originating from phases other than c-Si, and the validity of indexations greatly differing from $\langle 001 \rangle$-orientation, the obtained EBSPs

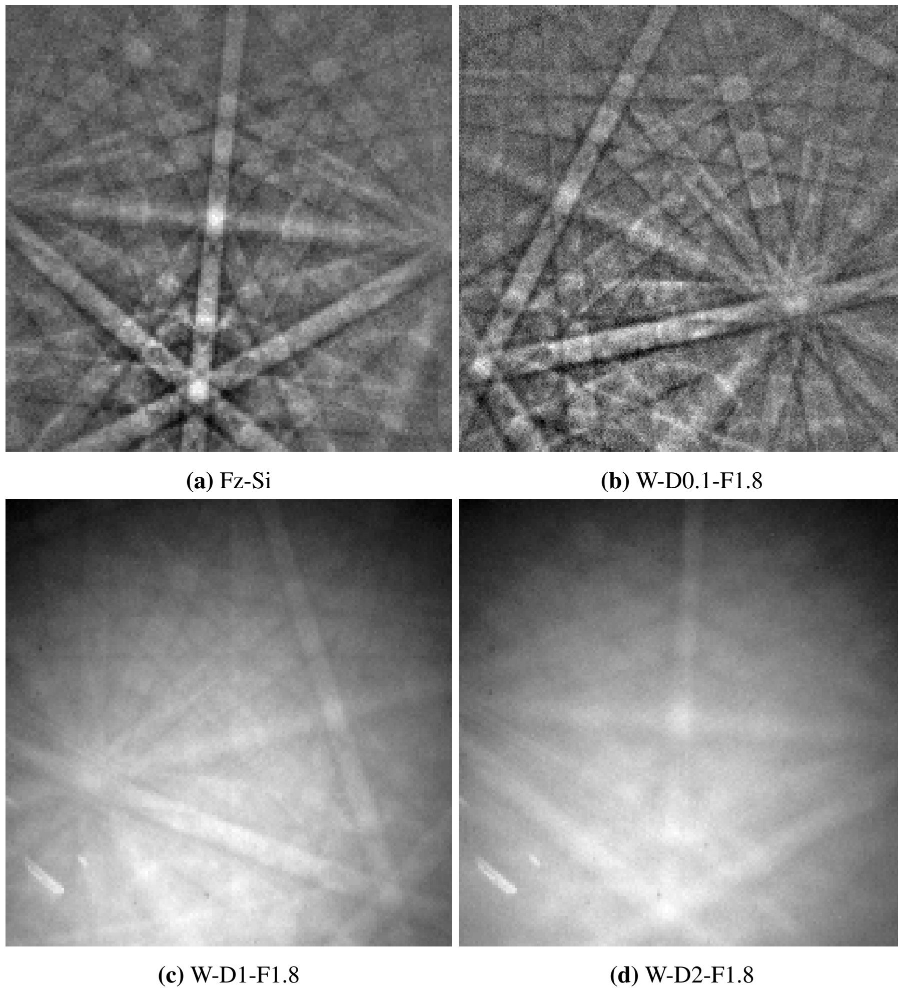

**(a)** Fz-Si

**(b)** W-D0.1-F1.8

**(c)** W-D1-F1.8

**(d)** W-D2-F1.8

**Figure 5.3:** EBSD patterns of the highest quality obtained from (a) Fz-Si and 1.8 J/cm$^2$ PLM samples with W concentrations of (b) 0.1, (c) 1, and (d) 2 at%.

were viewed manually with Nordif EBSD Extraction software. The software allows the user to move the mouse cursor around in the EBSD collection area to view the Kikuchi pattern from each individual sampling point. While this does not allow manual review of every single Kikuchi pattern (of which there are tens of thousands in every orientation map), it allows a cursory investigation of the patterns in any area where incorrect indexing, possibly from additional phases, is suspected [132]. The manual EBSP investigation revealed no additional bands than those expected from Si in the Kikuchi patterns. If there were grains with orientations close to $\langle 101 \rangle$ or $\langle 111 \rangle$, large orientation changes in the Si bands would be expected, however there were not. Only small-angle changes and an increased blurring of the Kikuchi patterns when moving the cursor from the centre to the edges of the PLM spots was detected. While this does not eliminate the possibility of W-related bands or the presence of large grains significantly different from $\langle 001 \rangle$-orientation, as every Kikuchi pattern could not be reviewed manually, it does make it unlikely. It is important to note that the presence of high-angle grain boundaries with grains too small for detection is still possible.

As stated during the presentation of the EBSD orientation maps in section 4.3.1, indexed crystal orientations which differed greatly from $\langle 001 \rangle$ were understood as incorrect indexations by the software. In figures 5.4 and 5.5 are shown a (a) Kikuchi pattern, (b) calibration solution, and (c,d) incorrect indexing results for samples W-D2-F1.8 and W-D1-F1.4, respectively. The cause of the incorrect indexing seems to be erroneous detection of the $[1\bar{2}1]$ zone axis for sample W-D2-F1.8, and the $[0\bar{1}1]$ zone axis for sample W-D1-F1.4. While easily distinguishable by a human, the blurring of the Kikuchi bands greatly broadens their corresponding peak in the Hough transform, causing the software to assign the peak to the individually brightest pixel rather than centre of the peak. The result is an off-centre assignment of the zone axes, as seen in the figures. Due to this incorrect zone axis assignment, supported by the manual review in the previous paragraph, all crystal orientation solutions which differ greatly from $\langle 001 \rangle$ are considered as software errors, and thus invalid. This phenomenon of point-wise misindexing is known in the literature as orientation speckle [132, 135].

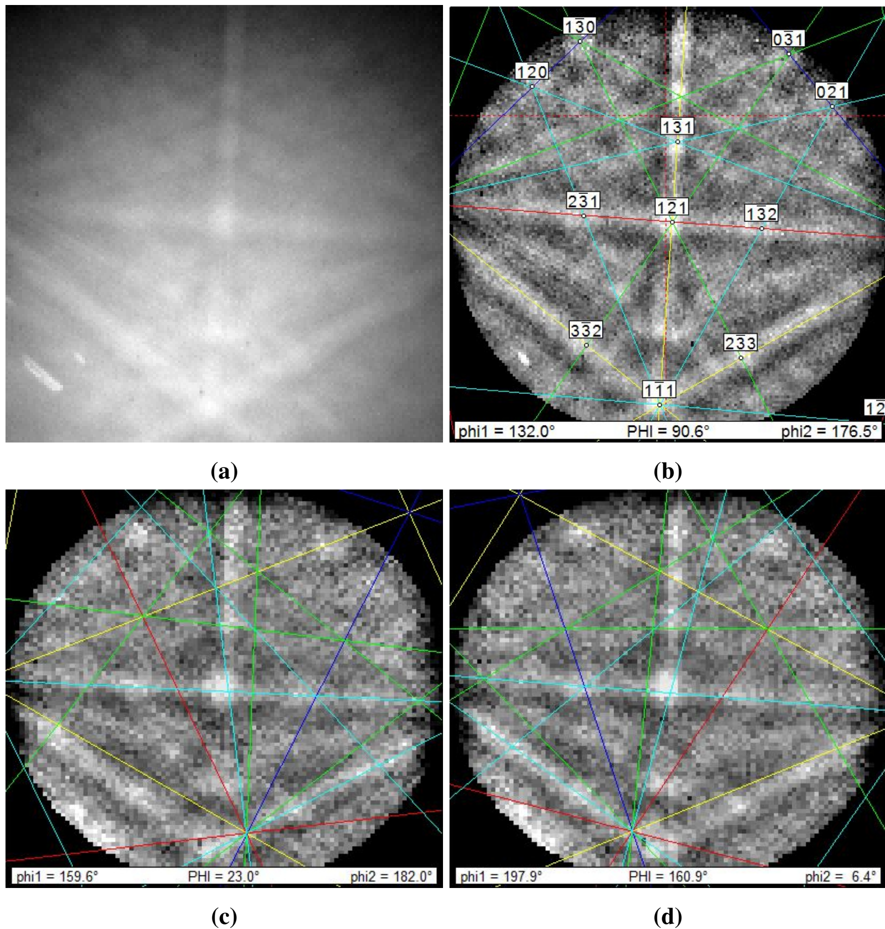


**(a)** **(b)**

**(c)** **(d)**

**Figure 5.4:** For PLM sample W-D2-F1.8 is shown (a) a raw Kikuchi pattern and (b) its calibration for orientation. In (c) and (d) are shown orientation assignment errors during automated indexing. Misassignment of only a few bands as the pattern quality decays towards the edges may greatly affect the orientation solution, leading to incorrect data in the orientation maps.

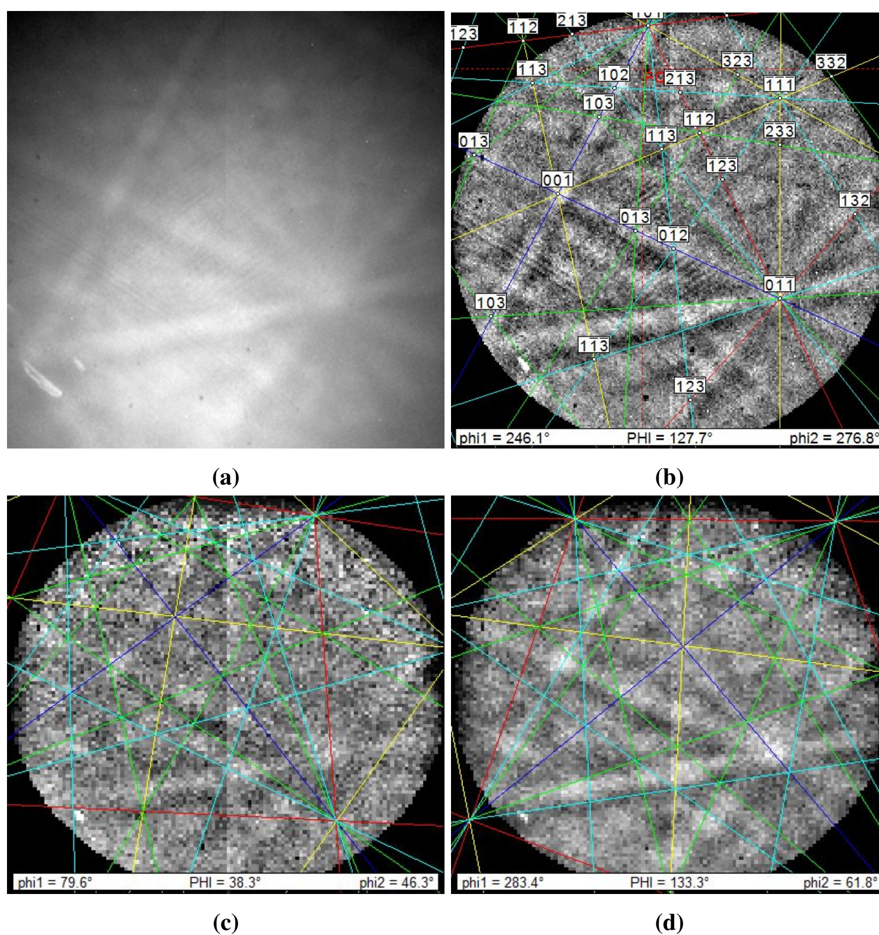


**Figure 5.5:** For PLM sample W-D0.1-F1.4 is shown (a) a raw Kikuchi pattern and (b) its calibration for orientation. In (c) and (d) are shown orientation assignment errors during automated indexing. Misassignment of only a few bands as the pattern quality decays towards the edges may greatly affect the orientation solution, leading to incorrect data in the orientation maps.

**Orientation maps.** For all fluence 1.8 J/cm$^2$ PLM samples, crystalline recovery was successful with a large, continuous area of orientation most closely aligned with $\langle 001 \rangle$, which is the orientation of the Si below the implanted volume. However, regrowth of a single crystal is not implied. The manual Kikuchi pattern investigation revealed small changes in the rotation of the bands at various points within the recovered area, which is reflected in the crystal orientation maps as slight deviations from the $\langle 001 \rangle$-orientation. A polycrystalline material is said to be textured if its grains have a preferred orientation, rather than being fully random [136]. The slight variations in orientation across the samples, while still being most closely aligned with $\langle 001 \rangle$ of the high-symmetry crystal directions, supports the idea of a textured polycrystal resulting from the PLM treatment. TEM investigations of these samples by Sørhaug [129], which show Moiré patterns from overlapping crystal planes, as well as apparent grain boundaries with W segregation, lend credence to the interpretation of the orientation maps as showing a textured polycrystal.

Now that the central region in each orientation map is interpreted as a textured polycrystal, it stands to reason that the outer region, which is mostly black in the orientation maps, is polycrystalline as well. A lack of Kikuchi patterns from the outer regions may be explained by a loss of texture, coupled with grain sizes that are smaller than the interaction volume, meaning that no grain is large enough to produce a visible pattern [133, 134]. If texture was kept, a similar outcome would be expected from a great reduction in grain size, where each electron would cross enough grain boundaries as to become randomly scattered. The determination of grain sizes, and thus the mechanism for signal loss in the outer region, is clearly outside the resolving power of the instrument used. By utilising a system with beam deceleration, it could be possible to reduce the BSE interaction volume sufficiently to achieve a signal from this region [137, 138]. It is also possible to re-configure the detector system to allow for transmission diffraction measurements in the SEM with sufficiently thin samples. This technique, termed transmission Kikuchi diffraction (TKD), has been shown to attain spatial resolutions of 2 nm [139].

Regarding the grain sizes in the indexed central regions, they are also not possible to determine from the available data. Step sizes of 3-4.5 µm were used for the 1.8 J/cm$^2$ samples, and in each case the orientation of the Kikuchi pattern may change slightly from one collection point to the next, indicating that a grain boundary has been crossed. Acquisition of an EBSP over a smaller region with sub-micron step sizes on sample W-D2-F1.8 was attempted, however severe drift from sample charging prevented the system from assigning satisfactory calibration points to allow for pattern collection. Electrical contact between the sample and holder could possibly have been improved by use of a carbon adhesive tape, but was not done to prevent sample contamination. Previous work in my project thesis [140] has shown that minority carrier lifetime measurements are negatively impacted by carbon tape residue, even after multiple rounds of immersion

in organic solvents with applied ultrasonics [140]. Had the measurement succeeded, it would still not be outright reasonable to assume that the grain sizes in the centre should be equal for all dosages of W given the same laser fluence.

Moving on to samples of fluence 1.4 J/cm$^2$, sample W-D0.1-F1.4 was the only one to achieve crystalline recovery. It has a continuous, central region most closely aligned with $\langle 001 \rangle$-orientation, but with many data points of $\langle 111 \rangle$-speckle. In figure 5.5 are shown some incorrect indexations resulting in orientation speckle for this sample. The same argumentation as for the 1.8 J/cm$^2$ samples may be repeated here, including the findings from manual Kikuchi pattern review, and the central region is interpreted as a textured polycrystal.

Sample W-D1-F1.4 did not achieve crystalline recovery, however the EBSD orientation map revealed many disconnected spots of $\langle 001 \rangle$-orientation. Each spot of detected crystallinity corresponded to a small hole in the surface, as seen in the SEM micrograph, but not every hole had detected crystallinity. As the detailed mechanisms in the PLM process are beyond the scope of this thesis, no thorough discussion of the possible reasons for this form of crystal growth will be performed. Nonetheless, an explanation is attempted. In section 5.1.1 it was argued that holes in the surface result from explosive boiling. Assuming that bubble nucleation occurs where the local temperature is the highest, bubble nucleation points should coincide with the points where the melt penetrates deepest locally. Thus, the melt in these points may have just reached the underlying Fz-Si, which acted as a seed for crystal orientation, while the other grains are randomly oriented due to growth from a-Si. This does not explain why a bubble had to be passing through the surface at the time of solidification for the grain to be detectable by EBSD, nor the apparent multi-pixel/micrometre size of the grains.

Of the fluence 0.9 J/cm$^2$ samples, an EBSP was only captured from sample W-D0.1-F0.9. A continuous area with crystal orientation most closely aligned with $\langle 001 \rangle$ was observed, however it was only in the part of the PLM spot which hit the accidentally implanted region on the wafer piece; no crystallinity was detected in the 0.1 at% W-implanted part of the laser spot. The accidentally implanted region has a mixture of amorphous and $\langle 001 \rangle$-oriented Si, as detected in previous EBSD measurements in my project thesis [140], meaning that a $\langle 001 \rangle$-oriented seed will be available irrespective of melt penetration depth. While lateral resolidification with PLM is an intriguing topic that has received some attention [141], its relevancy is low for this thesis.

### 5.2.3 SIMS Craters

As was seen in the SEM micrographs in figures 4.18 and 4.19 (page 60), the bottoms of the SIMS craters are covered by a wave-like pattern. For the fluence 1.8 J/cm$^2$ PLM samples, the bottom is mostly smooth, but with hole formation aligned with the wavy pattern. For the fluence 0.9 J/cm$^2$ sample, the bottom was smooth in the shallow SIMS crater, but very rough in the deep crater, forming a terrace-like structure. The formation of the terraces is known as ion sputter induced rippling, and has been observed in both amorphous and crystalline silicon [142, 143]. The wavy patterning is a less extreme manifestation of rippling, and has received some attention with regards to functional materials research [144, 145]. While a full discussion of ion sputter induced rippling and its mechanisms are well beyond the scope of this thesis, the findings will nonetheless be related to the literature, as they are somewhat unusual.

Since the 1960s, multiple models have been proposed to understand the mechanism of ripple formation, with various linear and non-linear contributions from surface stresses, defects, ion beam angle, voltage, crystal direction and so forth [146–149]. To date, there is no single model able to explain all the experimental findings, as there appears to be a critical condition which dictates whether ripple growth is linear or exponential [150]. Common experimentally investigated parameters are sputter angle [143], energy [151] and depth [152]. Though there are differences in the literature [153], it is generally found that rippling occurs perpendicular to the incident ion beam direction, above some critical angle and energy threshold, and with an exponential growth in amplitude with increasing depth [143, 151, 152, 154].

Vajo et al. [151] sputtered $\langle 100 \rangle$-oriented Si with a 9 keV $O_2^+$-beam, i.e. nearly identical parameters to our experiment, and obtained results nearly identical to some of ours. In figure 5.6 are shown their SEM micrographs of four increasingly deep SIMS craters. In (a), the wavy surface pattern is recognisable, with some triangle formation in (b), as seen in the 1.8 J/cm$^2$ PLM samples. In (c) and (d), they have similar terrace formation to what was observed in the deep craters in the 0.9 J/cm$^2$ PLM samples. As the rippling increased, they observed an increase in the secondary ion yield of Si, similar to our findings plotted in figure 4.32 (page 79). They concluded that, given a sufficiently high keV beam of $O_2^+$, ripple formation would occur with an exponential amplitude-sputter depth relationship.

While the results from the 0.9 J/cm$^2$ PLM samples suit the literature summarised above very well, with a big increase in ripple amplitude from the shallow craters at ~500 nm to the deep ones at ~2000 nm, the as-implanted and 1.8 J/cm$^2$ PLM samples did not share this behaviour. The optical profiler could not detect any surface rippling in the as-implanted and 1.8 J/cm$^2$ PLM samples, while the AFM measurement from the bottom of the SIMS crater in sample W-D1-asImp detected nano-patterned rippling with an RMS roughness (Sq) of only 1.44 nm. As the other SIMS craters were not measured

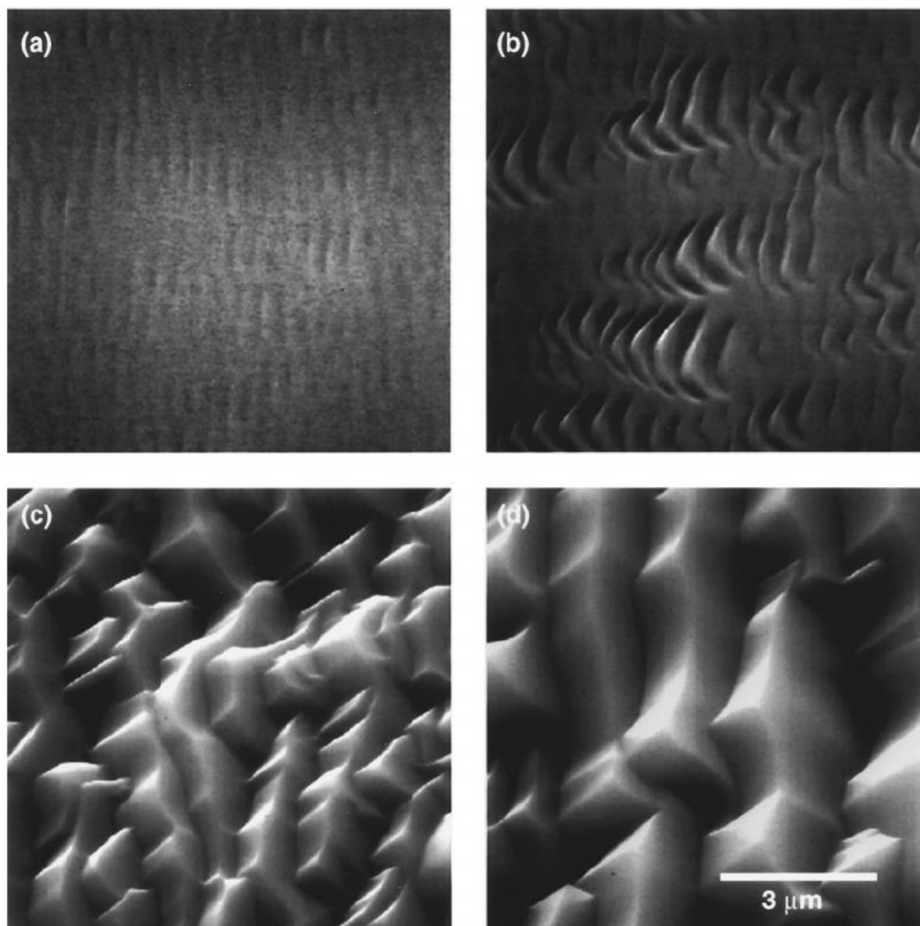


**Figure 5.6:** SEM micrographs of surface rippling caused by sputtering with a 9 keV $O_2^+$-beam at 45° incidence on ⟨100⟩-oriented Si to normalised depths of (a) 0.8, (b) 1, (c) 1.9 and (d) 3.1. A depth of 1 indicates the onset of rapid ripple growth. Results obtained by Vajo et al. in [151].

with the AFM, nothing conclusive may be stated about their surface conditions. It is reasonable to assume, however, that any rippling present would be of the same magnitude as for sample W-D1-asImp, as any significant increase in amplitude (e.g. to 3 nm) would be within the specified resolving power of the optical profiler. Crater depths are all roughly 2 microns since the beam flux and incidence angle were kept constant between measurements. As crystal orientation relative to the beam has been shown to have little effect [152], the discrepancy in crater bottom roughnesses between the samples is unanticipated. Apart from trench creation, pre-sputter surface morphology does not seem to influence the results much. As seen in the surface roughness measurements in section 4.2.2, higher fluence PLM samples tend towards rougher surfaces, but retain relatively smooth SIMS crater bottoms.

By having eliminated the other major variables, it is reasonable to conclude that the exponential growth in ripple amplitude as seen in the 0.9 J/cm$^2$ PLM samples is caused by some transition within the material. This is especially suggested by the fact that, outside of the trenching, the surface of the shallow crater is still quite smooth, though with many indentations. As is covered in the next section, the penetration depth of melting is estimated to around 450-500 nm for the 0.9 J/cm$^2$ PLM samples. At this depth, the material was still amorphous prior to PLM, and the growth was polycrystalline, as determined by EBSD and Raman spectroscopy. Accordingly, a highly-irregular crystalline-amorphous interface due to explosive recrystallisation is expected [46, 155] which may provide the necessary critical roughness required for micro-roughening of the surface to initiate, as proposed in the widely accepted model by Sigmund [156], improved by Bradley-Harper [147] and Cuerno and Barabási [148].

The formation of trenches along the cracks in the sample surfaces is in accordance with literature, as it has been shown that the local material erosion rate is greater in depressions than on elevations [156]. Thus, an increased erosion rate in the cracks relative to the flat surface would cause the cracks to expand. Logically, there would exist a threshold width for which the trench is no longer experienced as a "local" depression by the incident ions, and this effect would be diminished. Such a threshold has likely not been reached in our samples, however, as the trenches continued to widen from the shallow to the deep craters in the 0.9 J/cm$^2$ PLM samples.

The sputter induced surface rippling poses challenges related to the depth measurements of the SIMS craters. For VSI/VXI measurements in particular, which were used to investigate the SIMS craters, steep edges and ledges are known to cause inaccuracies in the reported height values [157, 158]. Protruding corners will appear taller, while sharp depressions will appear deeper, making the surface seem more uneven than it is in reality. However, as the sidewalls of the SIMS craters were all smooth and well within the capabilities of the instrument, the effect of the uneven bottoms in the 0.9 J/cm$^2$ PLM craters is likely reduced. The depth data from said SIMS craters was also not used quantitavively, so there is no impact on any of the conclusions reached.

### 5.2.4 SIMS Depth Profiles

**Implantation profile** Regarding first the depth profiles for the as-implanted samples, the implantation profiles are Gaussian in nature, as is expected from the theory. A comparison between the expected depth profile from TRIM calculations and the achieved profile as measured with SIMS is given in figure 5.7. The TRIM calculations yielded a mean of 500 nm, while the measured mean varies between 570-590 nm for the as-implanted samples. The discrepancy may be due to the limitations of the TRIM calculations, as they do not take into account channelling effects or damage to the sample from previous ions passing through, both effects which may reduce the stopping power of the W ions as they penetrate into the sample [159].

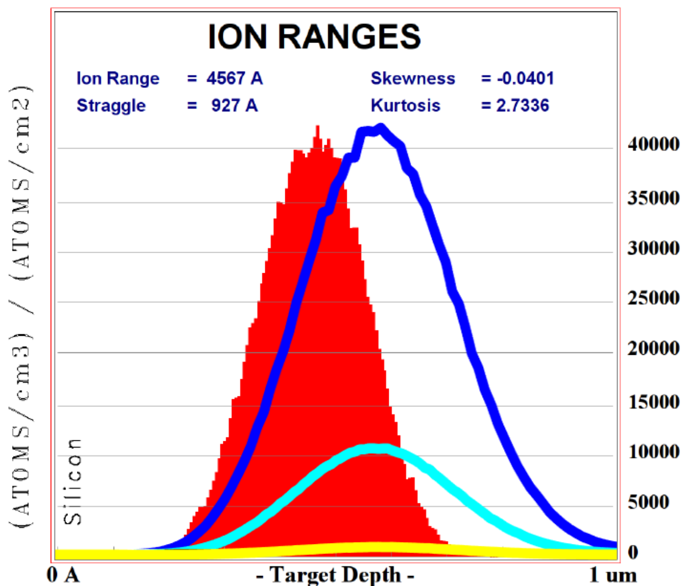


**Figure 5.7:** Comparison between W ion distribution calculated with TRIM, and actual measured distribution with SIMS. As presented in section 4.3.3, the mean of the realised distribution is between 570-590 nm.

It is relevant here to briefly consider whether the discrepancy in mean depth could stem from a temporary variation in sputtering rate. As was seen in figure 4.32 (page 79), the Si-counts for all as-implanted samples experience a moderate increase between ~400-800 nm, which could be interpreted as an increase in sputter rate. While it may not necessarily bear any relevance to the as-implanted samples, it is also noteworthy that the average sputter rate for the 0.9 J/cm$^2$ PLM samples was higher in the shallow craters than in the deep craters, suggesting a faster milling speed in W-rich areas. If there has been a temporary increase in sputter rate prior to reaching the top of the as-implanted peak, the position would actually be reported as more shallow than the true

depth.

**PLM samples.** For the fluence 1.8 J/cm$^2$ PLM samples, as well as the 0.1 at.% W sample of fluence 0.9 J/cm$^2$, a double peak structure can be seen in the depth profiles in figures 4.36 and 4.35. The valley between the peaks indicates the penetration depth of the melt into the material [56]. The valley is located deeper in the material with increasing implantation dose of W, which is in agreement with the findings of Narayan et al., who reported that the silicon melts deeper as the crystallinity decreases [160].

For all PLM samples, a push of the W towards the surface is observed, which is consistent with literature on PLM for other dopants, namely Ti in Si [56, 161–163]. Close to the surface, a local maximum in W-concentration is observed both in raw and relative counts (the exception being raw counts for W-D2-F0.9, where there is a plateau instead). The profile is reminiscent of the SIMS profiles for cellular breakdown of Au in Si found by Recht et al. [52], however the position of the peak is at <50 nm for our samples, while Recht observed it at ~100 nm. Despite the push towards the surface, the majority of the W remains deep in the bulk, with peak concentrations at a depth of ~0.5 µm for all PLM samples. W was chosen as the dopant species because it was hypothesised that it would not be removed from the bulk by the PLM, and the available data demonstrably supports the hypothesis.

Concerning the near-surface peak, it is relatively larger for lower than higher concentrations of W, compared to the peak concentration in the bulk. This may be related to W's unusually complex and slow diffusion mechanism [24]. As detailed in section 2.2.3, the primary mechanism for dopant segregation during PLM is the diffusion of W from the solid into the liquid, across the solid-liquid interface. The W may not, however, diffuse across the interface if it cannot reach it in the first place. Thus, if the process is limited by diffusion speed, relatively more W will cross the solid-liquid-interface for lower concentrations of W.

It is also possible that the near-surface peak is simply an artefact due to preferential sputtering. It has been known since the 1970s that different elements sputter at different rates in a multi-element compound [164]. At the onset of sputtering, a thin layer at the surface will have its elemental composition gradually changed until a steady state is reached, at which point the rates of the different elements will correspond to the stoichiometric composition of the bulk. From the temporary, but abrupt, dip in $^{30}Si_2$ yield close to the surface, one may assume that sputtering of W is preferential to that of Si. The result is an artificial inflation of the W concentration close to the surface. The effects of preferential sputtering may be compensated for by applying the extended mixing-roughness-information depth model [165]. The model requires parameters for surface roughness and atomic mixing in the ion impact induced collisional cascade to be determined, as well as numerical solutions to the instantaneous surface concentration of the analyte species. Its application is beyond the scope of this thesis.

Regarding relative peak heights, they did not follow a 2:1:0.1 ratio for the as-implanted samples, as would have been expected, obtaining instead ratios of ~2.5:1:0.04 and 4:1:0.07 for the raw and relative W-rates, respectively. The total counts of W until 1.4 µm in table 4.3 did also not have the expected ratios. As explained the in theory in section 2.3.4, the secondary ion yield is greatly dependent on the immediate chemical surroundings, termed the matrix effect. Sputter yield has been extensively studied for the $Si_{1-x}Ge_x$-system to experimentally determine the relationship between composition and relative ion yields [166–170]. A non-linear, monotonic relationship is reported, but a complete quantification of the matrix effect has not yet been achieved. By analogy, it is not possible from our SIMS measurements to verify that the ion implantation has produced the desired peak concentrations of W, or whether the peak concentrations in the bulk are still above the Mott limit after PLM. If there had been W doped calibration samples of similar concentrations available, better approximations could have made.

Regarding the increasing $^{30}Si_2$ signal in the fluence 0.9 J/cm$^2$ PLM samples, it is likely to stem from the roughening of the crater bottom, rather than an increase in sputter speed. Sputtering of periodically modulated and terraced surfaces is predicted to produce a greater yield than flat surfaces, according to models by Wittmaack and Barabási et. al. based on Sigmund's framework [147, 148, 156, 171–173]. However, there is also experimental data where sputter ripple formation decreases secondary ion yield [174], directly contradicting said models. The models are also not in agreement with recent Monte Carlo or binary-collision simulations [175, 176]. In sum, the relationship between secondary ion yield and sputter induced rippling is not well understood and is a current research topic, but does seem to account for the signal increase in the 0.9 J/cm$^2$ PLM samples. This interpretation is supported by the average sputter speed being similar across all samples, as seen in table 4.2 (page 78).

**Accidentally implanted W.** Due to the matrix effect, it is also not possible to quantify the W concentrations detected in the accidentally implanted region. With a Gaussian peak centred at ~570 nm, the profile is very similar to those from the as-implanted regions. The strength of the signal at almost $10^4$ cps makes the presence of W irrefutable.

Less certain is the detected W in the nominally unimplanted "FzSi" region on wafer piece W-D1. With only ~30 cps per point in the $^{184}$W signal between 150-400 nm, the intensity is comparable to the low-intensity tails in the other samples. Three things must be kept in mind when interpreting the result. First, when sputtering past the main peak in the high concentration W samples, there will always be a signal from W present. A part of the crater wall will have the peak W-containing layer exposed, and because the ion beam is wide and diffuse, some W will be milled from the walls. Secondly, the background noise level as reported by the instrument was <0.01 cps for all measurements. 30 cps, while much lower than recorded counts for other samples, are still 3 orders of magnitude above the recorded noise floor. Thirdly, Raman investigations showed dam-

age to and slight amorphisation of the Si crystal structure in the "FzSi" region compared to Fz-Si that had not been sent to implantation, which is consistent with effects from ion bombardment. Additionally, it is noteworthy that the signal for $^{184}$W is stronger than for $^{183}$W, which is also the case for the other samples (not shown), with $^{184}$W being the more abundant naturally occurring isotope.

To determine whether the detected W outside the as-implanted regions could stem from diffusion, a counter-example will be given for Ni, which is a fast-diffusing species in silicon. At room temperature, the diffusion front of Ni moves at ~6 nm $h^{-1}$ [24]. Assuming a diffusion time of 2 years, the Ni would have diffused up to ~105 µm, but W was detected more than 1 cm outside the nominally implanted areas. The room temperature diffusion constant of W is estimated to about 17 orders of magnitude lower than that of Ni [24, 177]. Therefore, diffusion cannot explain the presence of W outside the as-implanted squares.

### 5.2.5 Hyperspectral Imaging & photoluminescence

As summarised in the theory in section 2.1.4, W is reported to introduce a wide range of energy levels in the band gap of Si, between 0.22-0.59 eV from the band edges. Expected PL signals from W are therefore in the 0.53-0.90 eV range, though the most commonly reported transitions fall between 0.7 and 0.8 eV. The reported energy levels were all detected with deep level transient spectroscopy; to the best knowledge of the author, PL has never been performed on annealed/recrystallised W doped Si, so there are no results available for direct comparison.

A possible source for luminescence from Si are defects with C or O in interstitial or substitutional lattice sites [178]. In the case of one substitutional and one interstitial C, a peak at 0.969 eV may be observed. Known as the G-centre, it arises from the bond between the C atoms creating an allowed trap state. An interstitial C may also bond with an interstitial O to give a peak at 0.789 eV (C-centre). Emission lines at 0.767, 0.92 and 0.95 eV are also possible from various CO-complexes [179].

The Fz-Si wafer from which the sample set is made is p-type through boron (B) doping, meaning that radiative recombination facilitated by excitons bound to B must be considered. As the PL experiment was conducted at low temperatures (<90 K), electron-hole-pairs are expected to occupy the shallow levels introduced by the dopant. If, for instance, an electron was trapped close to the conduction band in a high temperature semiconductor, it would have a high probability of thermal excitation back into the conduction band instead of recombining with a hole. In low temperature measurements, therefore, emission of photons with energies slightly below the band gap are expected. Luminescence from B-related excitons in Si has been reported at 1.092 and 1.098 eV [180, 181].

A sharp, low-intensity peak at 0.77 eV is expected due to the instrument setup [182]. The low-pass filter used to block the reflected laser light is not perfect, and some of the reflected light will enters the optics of the camera. Upon encountering the diffraction grating in the camera, most of the laser light will become diffracted to spots of no consequence. However, the 2$^{nd}$ order diffraction will hit the CCD chip exactly where the 1$^{st}$ order maximum of light with twice the wavelength is normally recorded. The result is a sharp peak at 1616 nm = 0.77 eV. While the peak coincides well with the increased response below the band gap in the PLM samples, it is not clearly distinguishable in the obtained spectra. The intensity of the laser peak is reportedly low, typically lower than the BB response, and is understandably lost in the large sub band gap response of the PLM samples.

Defects in Si may also act as radiative recombination centres. Damage from ion bombardment may create W-centres, which have a photoemission line at 1.018 eV [179]. Associated with dislocations in Si are multiple luminescent bands, with the main bands conventionally labelled D1-4 with respective energies of 0.807, 0.870, 0.95, and 0.99 eV.

[183–185] While only the D1 line is visible at room temperature, they should all be detectable at ~90 K. Figure 5.8 shows experimentally detected D-lines from a defect rich area in a multicrystalline silicon sample. The intensity of the D-lines is anti-correlated with BB luminescence intensity and minority carrier lifetime [184–186].

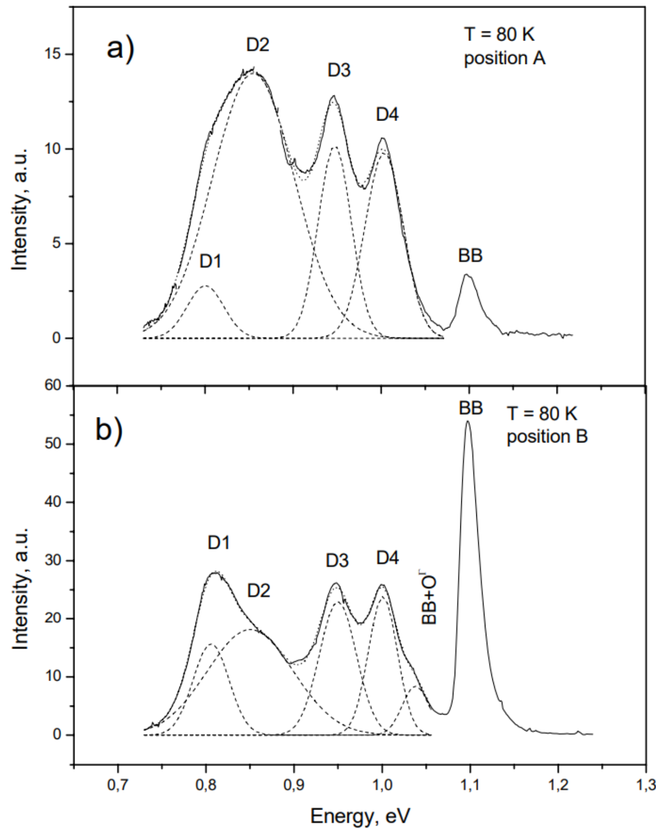


**Figure 5.8:** Deconvolution of D-line peaks from two separate areas on a Si wafer by Arguirov et al. Acquired from figure 4.7 in [185].

Additionally, Burud et. al. [186] and Flø et. al. [187] have reported a 5$^{th}$ dislocation line centred at 0.75 eV in their respective experiments on polycrystalline Si wafers. Spatially, the 0.75 eV-peak was found to originate from small points and clusters distributed across the wafer, with many of the points coinciding with D1 emission sites. As the exact mechanisms behind the main dislocation lines D1-4 are a current research topic, no conclusions were drawn about the mechanisms behind the 0.75 eV-line. However, the authors suggested some form of point defect as the spatial origin, in light of which the peak shall henceforth be referred to as D0.

To relate the known emissions to the PL spectra from the W doped samples, it would

have been useful to perform Multivariate Curve Resolution (MCR) analysis, as is common in hyperspectral imaging [187]. However, the MCR Toolbox is not included in NTNU's MATLAB license, and thus only qualitative comparisons will be possible. As seen in the obtained PL spectra (e.g. fig. 4.38 (a) on page 87), all PLM samples exhibit a broad response around 0.75 eV and the BB response at 1.1 eV.

Regarding first the BB luminescence, it creates an easily distinguishable peak for all PLM samples. The BB-peak is arguably visible in the as-implanted sample of 0.1 at % as well, but not for higher W concentrations. The small peak is likely due to signal from Fz-Si below the implanted volume, as the information depth of 1.1 eV photons is several microns, while the amorphisation only reached a depth of 1 micron per Sørhaug [129]. This interpretation is supported by the lack of any detected crystallinity in the as-implanted regions by Raman spectroscopy. For the PLM samples, the BB peaks appear to have high-energetic tails, most easily visible for sample W-D2-F1.8. The obtained shape is consistent with thermal broadening of the BB luminescence. [188] Due to the available spectral resolution, possible luminescence from excitons is not resolvable from the BB-peak, despite their expected activity at the measured temperatures.

Regarding next the broad sub-band gap response, several of the expected emissions are likely contributors. Luminescence from the C-centre and D1 lines fall within the range of the broad response, but being close to 0.8 eV they are at the edge of the broad peak, and are also not individually resolvable from the noise. More interesting is the 0.75 eV D0 peak reported by Burud and Flø, which coincides with the maximum of the broad luminescence in the PLM samples. Relative intensities should be kept in mind, however, as the D0 peak never reached even half the intensity of the BB peak in their measurements, while the intensities of the BB peak and sub band peak are comparable in the PLM samples. In width the D0 line is a good match, terminating at approximately 0.6 and 0.8 eV, which, coupled with the other contributions around 0.8 eV, would give the correct peak shape.

As luminescence from oxygen precipitates has been reported in the energy range of interest, particularly CO-precipitates at 0.77 eV, other combinations should also be considered. In particular tungsten oxides, as their presence was detected with Raman spectroscopy. The luminescence of $WO_3$ has been measured, both macroscopically and for nanoparticles, and in both cases its emissions lie in the 2.6-3 eV range, making it an unlikely candidate. [189, 190].

Any expected features between the broad response and the BB luminescence are not manually resolvable. This means that contributions from the G-centre or dislocation lines D2-4, while likely present, are lost in the noise. The same holds true for detected signals from multiple CO-complexes in the same energy range.

Finally, states in the band gap introduced by W must be considered. While the other phenomena are able to account for the entire range of observed luminescence above the noise floor, they are generally reported as low-intensity signals. The sub-band gap

response in the PLM samples is not a low intensity feature, being on par or even greater than the BB intensity. What may be seen as a counter-point is the strong sub-band gap response from the nominally unimplanted part of the W-D1 wafer piece, the spectrum for W-D1-"Fzsi" in figure 4.39 (page 89). However, as seen from the SIMS and Raman results, that part of the wafer has very likely received an unknown, low dose of W implantation. As the minimum dose of W required to introduce measurable energy states in the band gap is not known, effects from W cannot be discounted for the "FzSi" sample.

Regarding intensities, they may not necessarily be compared directly between different parts of the wafer pieces. As the PL intensity is generally linear with excitation laser power, inhomogeneities in the illumination across the sample will lead to systematic variations in peak height. The effect may be seen as more or less intense lines along the scan direction, and is present in all of the recorded hyperspectral images presented (thin, vertical lines). For wafer piece W-D1 it is especially obvious that the entire right half of the wafer piece has lower intensity than the left half, which accounts for the lower BB intensity in sample W-D1-F1.8 compared to W-D1-F1.4.

It is also with regards to intensity that the unfortunate experimental conditions come into play. The ice crystals forming on the sample surface are expected to contribute to uneven illumination of the sample, as well as introduce uncertainty as to the true origin of any given photon due to diffraction. If the crystals form with a preferred orientation rather than randomly, an added uncertainty component in spectral information may be expected, due to the stationary position of the camera relative to the measured line.

**Hyperspectral images.** Moving onto the hyperspectral images, the spatial origins of the signals may be studied. It should be noted, though, that for the imaging setup used, the noise is about an order of magnitude greater than the useful signal [182]. Although noise reduction and median filtering have been applied to the data, obvious effects still remain per the previous paragraphs. Care should therefore be taken if comparison of intensities between separate hyperspectral measurements is intended, while comparison between features in images from a single measurement is mostly fine.

In the BB signal, all the PLM spots on each wafer piece are distinguishable. For each wafer piece, the intensity of the BB signal increases with increasing laser fluence in the PLM spots. Higher laser fluences produced larger areas of detected textured crystallinity per EBSD, which should decrease non-radiative recombination at grain boundaries and thus improve PL intensity. Similarly, due to numerous defects from ion bombardment causing non-radiative recombination in the as-implanted regions, there the BB signal remains low on every wafer piece. On wafer piece W-D2 the BB signal is elevated in the accidentally implanted region at the top of the image, which is consistent with Raman spectroscopy finding a damaged, but not completely amorphised, lattice in the region. The BB signal was strongest in the "FzSi" part of wafer piece W-D1, which is in

line with results from Raman, as well as EBSD from the pre-master's project, showing good crystallinity in the region. When the hyperspectral imaging was conducted, it was assumed that this "FzSi" region could serve as a control sample, and a separate Fz-Si piece which had not been sent to implantation was not scanned. Unfortunately the assumption proved wrong, and no spectra for unimplanted Fz-Si exist in our data for feature comparisons.

All of the PLM spots are also distinguishable in the sub-band gap signal, even more so than in the BB signal. The intensities reflect the uneven distribution of laser fluence within each PLM spot, and increase more strongly for increasing laser fluences than the BB signal did. Like for the BB signal, there is increased sub-band gap luminescence in the accidentally implanted and "FzSi" regions in wafer pieces W-D2 and W-D1, respectively. Unfortunately wafer piece W-D0.1 is broken right through the 1.8 J/cm$^2$ PLM spot, as it had the largest detected crystallinity in the EBSD measurements. Sample W-D1-F1.8 appears to show the strongest sub-band gap response, though as stated, comparison between separate hyperspectral images should be done with care. Apart from W-D1-"FzSi", there are no unexpected sources of sub-band gap luminescence on the wafer pieces.

The maximum intensities are recorded at the edges/corners of the wafer pieces for both BB and sub-band gap signals. The camera lens is wider than the imaging area, so the edges of the lens will have an unimpeded view of the sample edge, which should allow more signal to escape from the same volume. Crystalline Si also exhibits some birefringence [191], so the effect may be strengthened if the edges act as waveguides, with a preferred emission direction towards the camera. It is noticeable that the strong edge emission occurs mainly when there are other notable features within the same horizontal line. It is possible for an excited carrier to travel some distance before annihilating, meaning that minority carrier diffusion must be considered. The diffusion distance $L$ of a charge carrier is given by $L = \sqrt{D\tau}$, where $D$ is the diffusivity and $\tau$ the lifetime [37]. $\tau$ was measured to 3.3 µs with µ-PCD at room temperature (Appendix D), and will be roughly halved at 90 K [192]. For a favourable rough estimate, assuming $\tau = 2\,\mu s$ and $D = 33\,cm^2/s$, a value of $L = 81\,\mu m$ is obtained. As the separation between the edges and PLM spots are on the millimetre scale, diffusion of excited carriers is an unlikely contributor to luminescence at the edges. Further possibilities will not be explored as the edge luminescence is not central to this thesis.

**Section Summary.** To summarise the discussion surrounding the hyperspectral imaging, all PLM spots show a strong band-to-band and sub-band gap luminescence. Both luminescence signals are also present in areas on the wafer pieces that have received low, unknown doses of W implantation. The sub-band gap luminescence is broad, and its entire width may be accounted for by previously reported defect related luminescence in silicon. However, the sub-band gap response is similar in strength to the band-to-band

one, and seems to vary in sync with it, while defect related signals tend to anti-correlate with the band-to-band response. While there is no conclusive evidence for energy states introduced by W, the results warrant further investigation. The experiment should be re-run under better experimental conditions.

*Data and data sets are not objective; they are creations of human design. We give numbers their voice, draw inferences from them, and define their meaning through our interpretations.*

Kate Crawford

# 6 Conclusions

In this work, W doped Si has been investigated from the perspective of a potential intermediate band (IB) solar cell material. The samples were manufactured by ion implanting W into single crystalline Si to achieve W concentrations above the equilibrium solubility limit, with nominal W peak concentrations of 0.1, 1 and 2 at.%. Using single 25 ns pules from a KrF excimer laser, parts of the implanted volumes were recrystallised with average laser fluences of $0.918 \pm 0.066$, $1.481 \pm 0.106$ and $1.888 \pm 0.135$ J/cm$^2$. The resulting materials have been characterised with a focus on crystal structure recovery and dopant diffusion.

Surface investigations with optical microscopy revealed that the energy density of the laser is non-uniform, with a complex fluence gradient towards the edges from the centre maximum. Also, the laser beam did not hit the middle of the laser mask. Further investigations with AFM, SEM, and WLI revealed that the surface patterns seen in the optical microscope were surface cracks on the nanometre-scale. The crack edges curved upwards, increasing RMS surface roughness from <1 nm for the as-implanted and Fz-Si samples to up to 10 nm in the PLM samples.

All samples annealed with 1.8 J/cm$^2$ , and 0.1 at.% W annealed with 1.4 J/cm$^2$ , recovered a crystal structure most closely aligned with the orientation of the Fz-Si beneath, as shown by EBSD. The structure was determined to be a highly textured polycrystal, but the grain sizes were too small for determination. There was a clear correlation between cracking morphology and detected crystal orientation. Mostly straight cracks

formed where EBSD detected $\langle 001 \rangle$-orientation; otherwise the cracks formed irregular polygons.

From SIMS, it was found that the majority of the W remained in the bulk following PLM, though there was a push of the dopant towards the surface. As there was no discernible relationship between W ion yield and concentration, the data from SIMS could not be quantified. It is therefore unclear if the Mott limit remained exceeded after PLM. Sputter induced roughening of the 0.9 J/cm$^2$ PLM samples prompted investigation of the SIMS craters with SEM and WLI, and the onset of roughening was correlated to Si melt penetration depth.

Hyperspectral imaging showed significant luminescence below the band gap of Si in a broad energy range centred on 0.75 eV. While the entire width of the luminescence response may be accounted for by reported defect related luminescence, defect luminescence tends to anti-correlate with band-to-band luminescence in c-Si. In the W doped samples, the band-to-band and sub-band gap luminescence varied in sync. Nothing conclusive about the influence of W could be stated. It remains unclear whether the broadness of the sub-band gap luminescence is inherent to the material or a result of the experimental conditions.

A secondary objective in this thesis was to examine an area of presumed accidental ion implantation, as suspected from the pre-master's project work. SIMS confirmed that W implantation outside the intended $1 \times 1$ cm squares had occurred, and Raman spectroscopy detected a-Si in all parts of the wafer pieces which were sent to implantation. The cause for the mislocated W cannot by ascertained from the implantation instrument logs.

*We live in a wonderful world that is full of beauty, charm and adventure. There is no end to the adventures that we can have if only we seek them with our eyes open.*

Jawaharlal Nehru, 1st PM of India

# 7
# Future Work

This section will suggest some further work based on the findings in this thesis. First, some suggestions regarding characterisation techniques on the current samples will be given, with some points repeated from the discussion. Secondly, some ideas for further materials processing will be presented.

Currently, the crystallinity of the material is not completely understood, with questions remaining about grain sizes, boundaries, and the presence of tungsten silicides. If the EBSD were repeated on a system with beam deceleration, a better detector and/or TKD setup, a better understanding could be gained. However, processing required to improve sample conductivity and signal-to-noise ratio could be detrimental to other characterisation methods.

The PL spectroscopy should be repeated under better experimental conditions, as the obtained data was too noisy to draw any conclusions regarding contributions from W. The laboratory at NMBU is currently installing a new hyperspectral camera, which should allow better spatial and spectral resolution. Alternatively, the band structure may be probed by other methods, such as photoemission spectroscopy, UV-vis absorption spectroscopy or FTIR.

As minority carrier lifetime is of utmost importance for an actual solar panel, the μ-PCD measurements should be completed. Techniques such as carrier density imaging and quasi steady state photo conductance are also viable alternatives.

For further materials processing, there should be a focus on preventing fracture of

the silicon during growth, as W has been shown to remain incorporated in the bulk after PLM. By utilising a longer laser pulse, the heating and cooling rates would be slower, resulting in a more gentle temperature gradient and less mechanical stress. The trade-off is a longer time window where W may diffuse across the solid-liquid interface, exacerbating dopant segregation and cellular breakdown at the sample surface.

An even slower alternative is flash lamp annealing (FLA), whereby the sample is heated to a high temperature, close to its melting point, for several milliseconds. As the silicon does not melt in the process, solid phase crystal growth ensues. FLA has been shown to induce crystal growth while suppressing cellular breakdown and mechanical fracture in silicon hyperdoped with titanium. [53] While FLA is many orders of magnitude slower than PLM, the dopant diffusivity is also many orders of magnitude lower in solid than liquid silicon [41, 51], especially for W [24], meaning that net diffusion length should decrease.

# Wafer Shape Investigations

Originally, it was of interest to use WLI to quantify the laser ablation resulting from PLM. However, WLI measurements of the PLM spots always appeared curved with a minimum in the measurement centre. Only by stepping and stitching measurements across the wafer pieces did it become clear that the pieces themselves were bending significantly. For clarity, it must be stated that the wafer pieces in these measurements are much larger than in the overview images in section 4.1, where they have been cleaved further for instrument compatibility reasons.

In figure A.1 (a) is displayed a stitch of VSI measurements on an Fz-Si wafer piece, showing height variations of several microns across the piece. A PSI stitching (not shown) was also performed with similar results, however the incline towards the tip at the top right of the map was too sharp for PSI at the used sample tilt. To verify the obtained height information, multiple line scans with a Veeco Dektak 150 contact stylus profiler were performed on the same wafer piece. Using MATLAB, a surface was interpolated from the line scans, as shown in figure A.1 (b). The surface follows the same general shape as was obtained from the WLI measurements. The contact stylus profiler is limited to a scan length of 5 cm, and the scan lines are plotted in blue in the figure. As the line scans were performed manually, the recorded height of the first data point was always '0', and for simplicity this was not changed in the MATLAB surface interpolation, which does alter the shape of the obtained surface as it is clear from the WLI stitching that the left edge of the wafer piece is not flat and level.

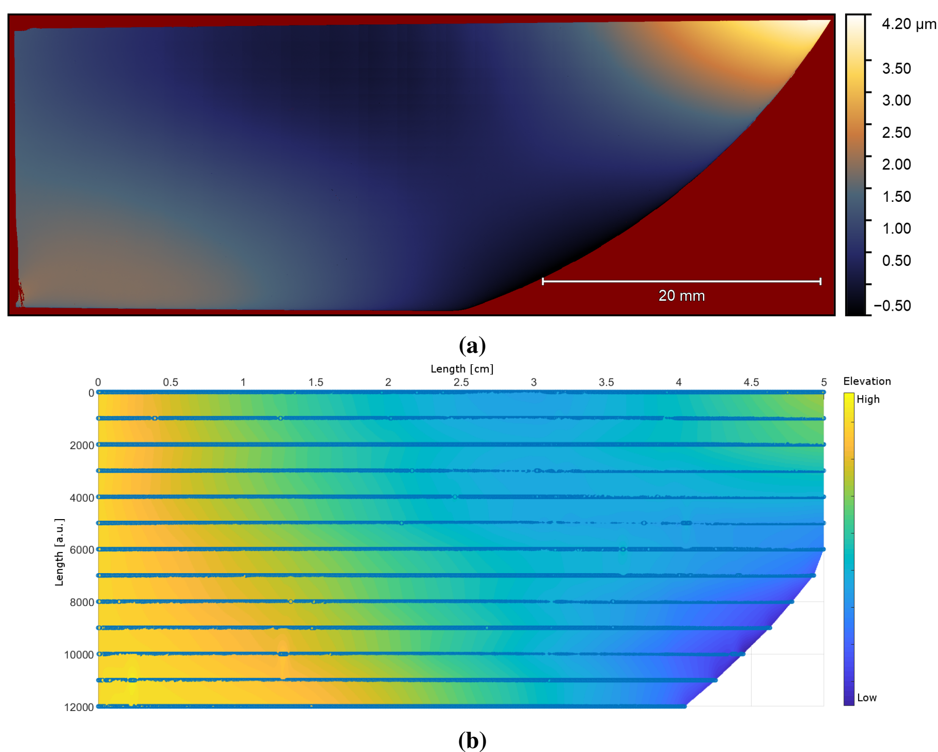


**Figure A.1:** For an Fz-Si wafer piece, **(a)** a stitching of VSI measurements and **(b)** an interpolated surface from contact stylus line scans. In (b), the scans are done from left to right, and each starting point has the same height value, which makes the interpolated surface slightly different from the one acquired with VSI stitching. However, the general curvature of the surface in both measurements is the same.

In figures A.2 and A.3 are displayed PSI measurement stitches from the W doped PLM samples, as well as from a piece of undoped Fz-Si which was shot with 100 laser pulses of ~1.6 J/cm$^2$. The PLM spots have been marked on each heightmap. In the W doped samples, the locations of the PLM spots would be evident even without the markings, as they form depressions in the wafer pieces. However, the depressions are not sharply defined, nor centred in the PLM spots, and are therefore mainly a result of the wafer piece twisting rather than material loss from ablation. As c-Si is about 2 % more dense than a-Si, a reduction in volume at the PLM spot is expected. This interpretation fits well with the data from the laser-shot Fz-Si piece, where the PLM spot is barely visible and does not impact the local curvature.

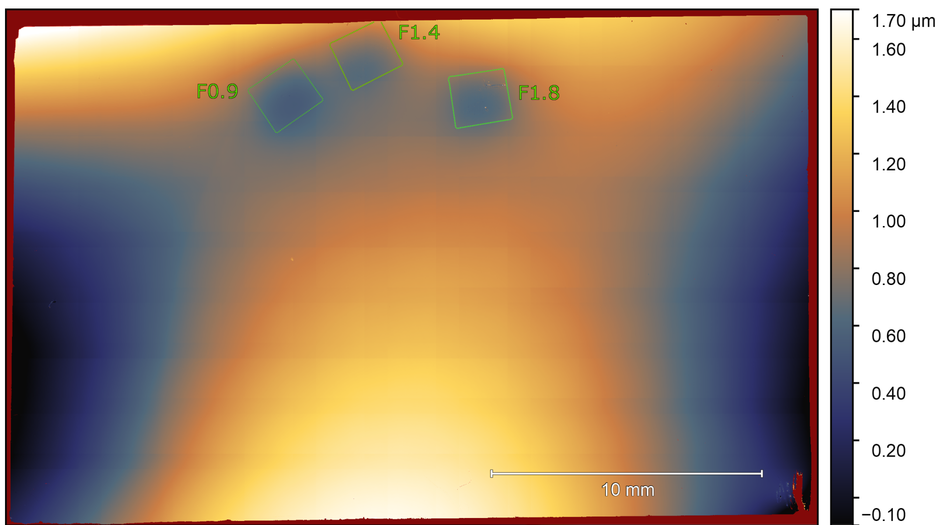


**Figure A.2:** For wafer piece W-D1, a stitching of PSI measurements to map the overall curvature of the sample. The PLM spots are indicated with green squares.

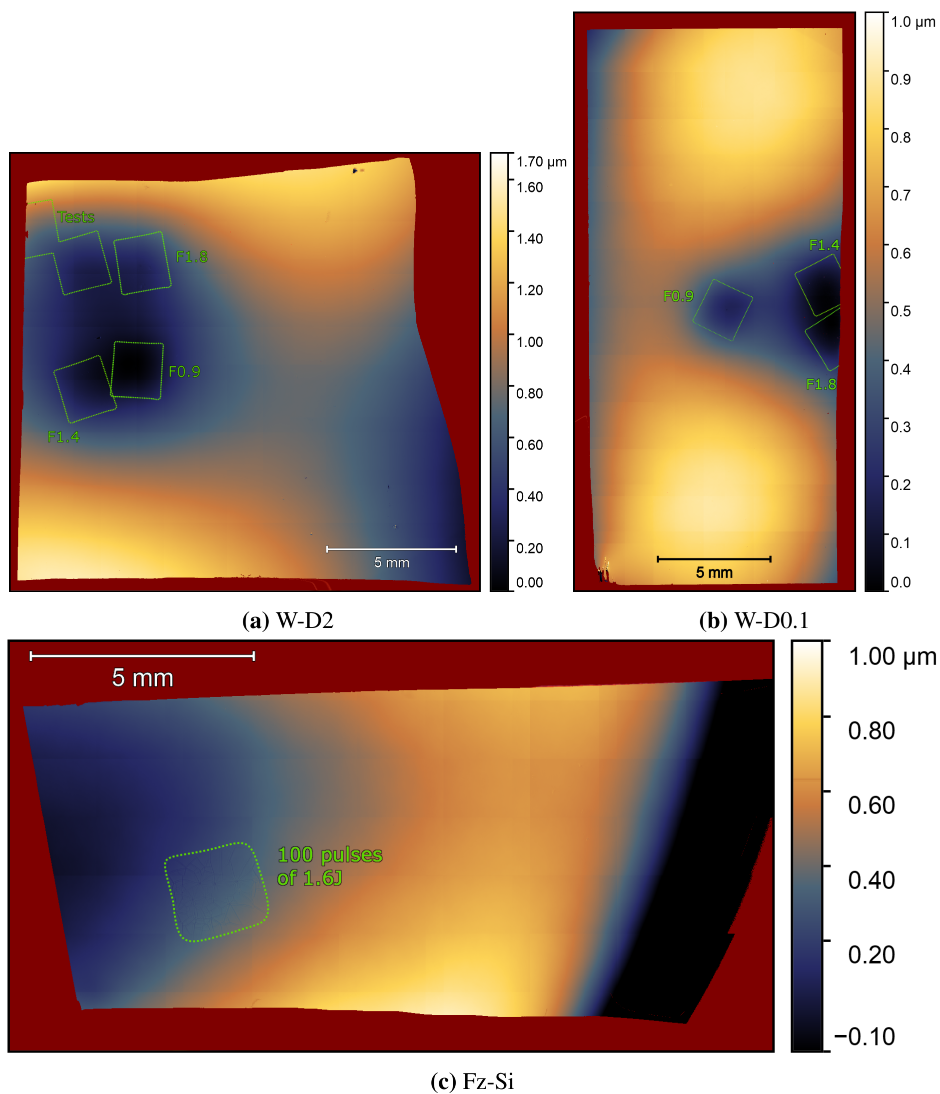


**(a)** W-D2 **(b)** W-D0.1

**(c)** Fz-Si

**Figure A.3:** Stitchings of PSI measurements for wafer pieces **(a)** W-D2, **(b)** W-D0.1, and **(c)** a piece of Fz-Si which was not sent to implantation. PLM spots have their applied laser fluences labelled and are indicated by green squares. In (c), in addition to the indicated spot which was shot with 100 pulses of ~1.6 J/cm$^2$, there exists two PLM spots of single pulses at 0.9 and 1.6 J/cm$^2$ which are indiscernible in the measurements.

# B
# WLI Roughness Measurements

In this appendix are presented the surface roughness measurements for the PLM samples. The obtained three-dimensional roughness parameters are summarised in table B.1. The presented heightmaps in figures B.1, B.2, and B.3 have ~2 % outliers cut off for increased readability. The outlier elimination does not affect the obtained roughness parameters, which were computed by the Bruker ContourGT-K profiler.

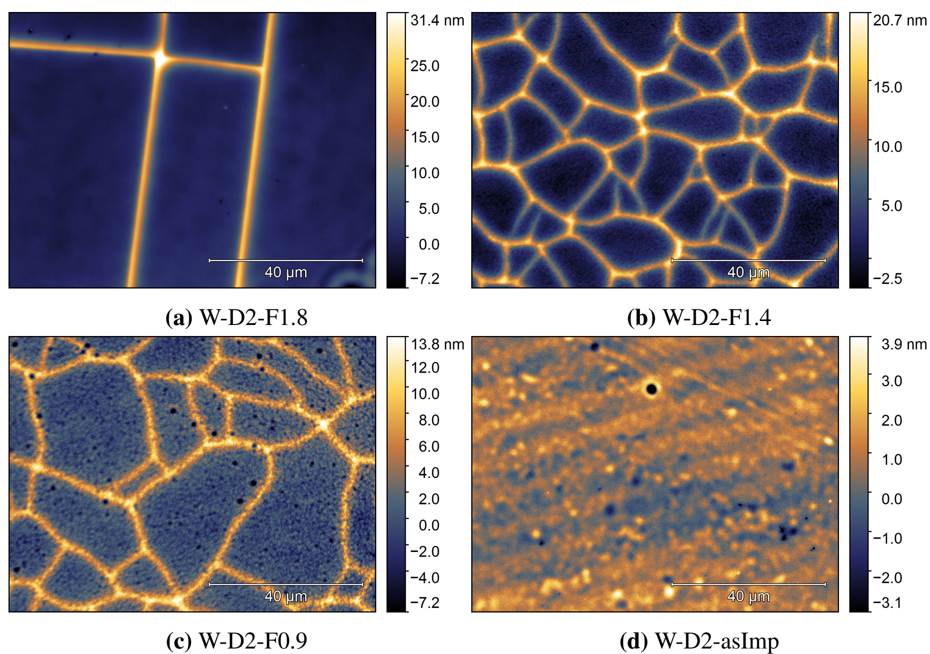


**(a)** W-D2-F1.8 **(b)** W-D2-F1.4

**(c)** W-D2-F0.9 **(d)** W-D2-asImp

**Figure B.1:** WLI measurements of surface roughness for 2 at.% W containing samples. Shown heightmaps are averages of 10 acquisitions. In **(d)**, the surface is so flat that the interference fringes become visible and impact the measurement. The fringes appear as plane waves with the wavefront oriented towards the top left. Acquired with PSI at 50 X magnification.

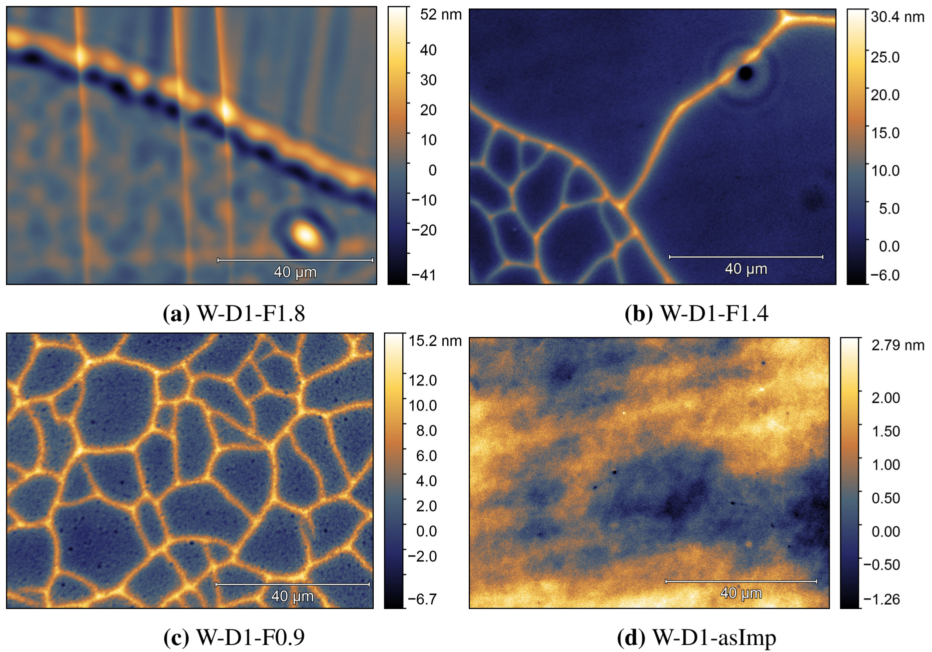


**(a)** W-D1-F1.8

**(b)** W-D1-F1.4

**(c)** W-D1-F0.9

**(d)** W-D1-asImp

**Figure B.2:** WLI measurements of surface roughness for 1 at.% W containing samples. Shown heightmaps are averages of 10 acquisitions. In **(d)**, the surface is so flat that the interference fringes become visible and impact the measurement. The fringes appear as plane waves with the wavefront oriented towards the top left. Acquired with PSI at 50 X magnification.

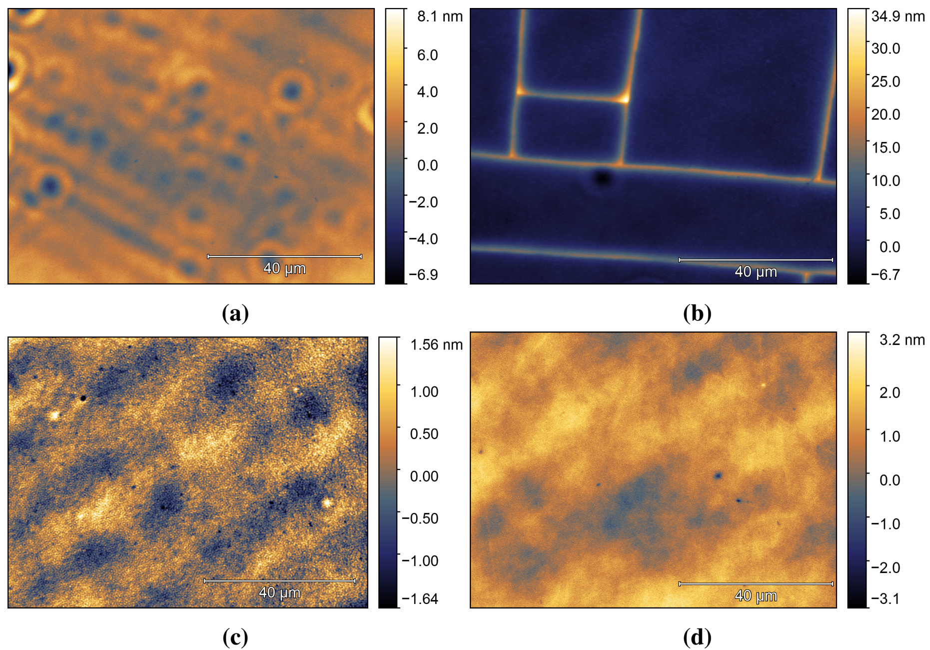


**Figure B.3:** WLI measurements of surface roughness for 0.1 at.% W containing samples. Shown heightmaps are averages of 10 acquisitions. In **(c)** and **(d)**, the surfaces are so flat that the interference fringes become visible and impact the measurement. The fringes appear as plane waves with the wavefront oriented to the top left. The diagonal ridges in **(a)** are not interference fringes, but actual surface features, as observed optically in figure 4.3 on page 45. Acquired with PSI at 50 X magnification.

**Table B.1:** Surface roughness parameters for all samples. Parameters are Sa (arithmetic mean roughness), Sq (root mean squared roughness), Ssk (skewness), Sku (kurtosis) and Sdq (root mean square surface slope). For the PLM samples, the measurements are from the centre of the PLM spot. Measured and analysed with Bruker CountourGT-K 3D Optical Profiler.

| Sample | Sa [nm] | Sq [nm] | Sdq [°] | Sku | Ssk |
|---|---|---|---|---|---|
| W-D0.1-F1.8 | 0.70 | 0.90 | 0.20 | 4.49 | 0.14 |
| W-D0.1-F1.4 | 2.88 | 4.12 | 0.31 | 8.00 | 2.22 |
| W-D0.1-F0.9 | 0.49 | 0.61 | 0.22 | 3.09 | 0.03 |
| W-D0.1-asImp | 0.45 | 0.55 | 0.19 | 2.64 | -0.07 |
| W-D1-F1.8 | 5.93 | 9.17 | 0.42 | 6.99 | 0.44 |
| W-D1-F1.4 | 2.93 | 4.14 | 0.34 | 8.05 | 2.13 |
| W-D1-F0.9 | 2.42 | 2.94 | 0.38 | 2.88 | 0.77 |
| W-D1-asImp | 0.58 | 0.71 | 0.28 | 2.68 | -0.02 |
| W-D2-F1.8 | 3.30 | 5.17 | 0.29 | 10.75 | 2.71 |
| W-D2-F1.4 | 3.58 | 4.32 | 0.39 | 3.08 | 0.91 |
| W-D2-F0.9 | 2.44 | 3.09 | 0.14 | 3.61 | 0.80 |
| W-D2-asImp | 0.50 | 0.68 | 0.30 | 33.03 | -1.64 |
| Fz-Si | 0.92 | 1.21 | 0.25 | 4.78 | 0.90 |

# C
# WLI SIMS Crater Measurements

The WLI measurements of the SIMS craters in W doped samples used for depth calibration will be given here in full. It is meant to serve as a point of easy comparison between samples, and as a catalogue for crater identification, should it be needed in further work on the samples. The measurements will be provided on a per-fluence basis, with optical image and WLI scan side by side. Scans from 1.8 $J/cm^2$ PLM samples are in figure C.1, from deep craters in 0.9 $J/cm^2$ PLM samples in figure C.2 and shallow craters in figure C.3, and from the as-implanted samples in figure C.4.

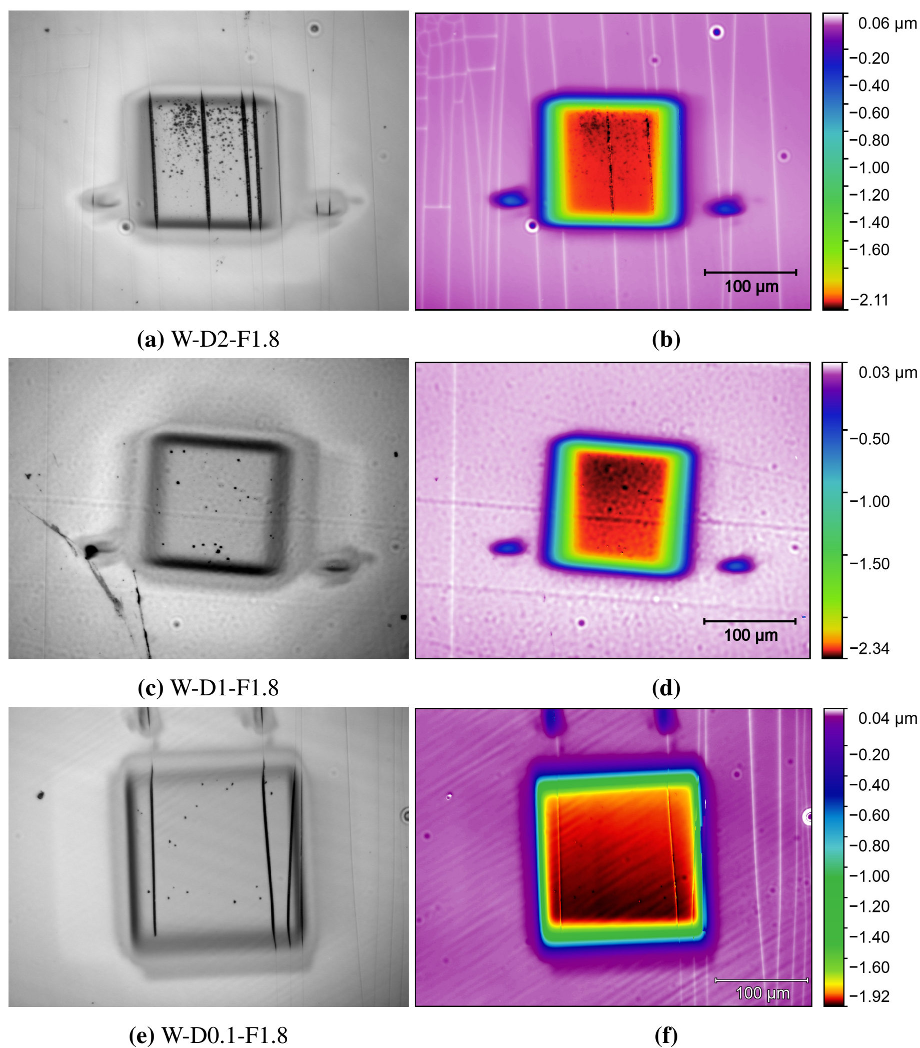


**(a)** W-D2-F1.8 **(b)**

**(c)** W-D1-F1.8 **(d)**

**(e)** W-D0.1-F1.8 **(f)**

**Figure C.1:** WLI measurements and corresponding optical micrographs of SIMS craters in fluence 1.8 J/cm$^2$ PLM samples. Acquired with VSI at 11 X magnification.

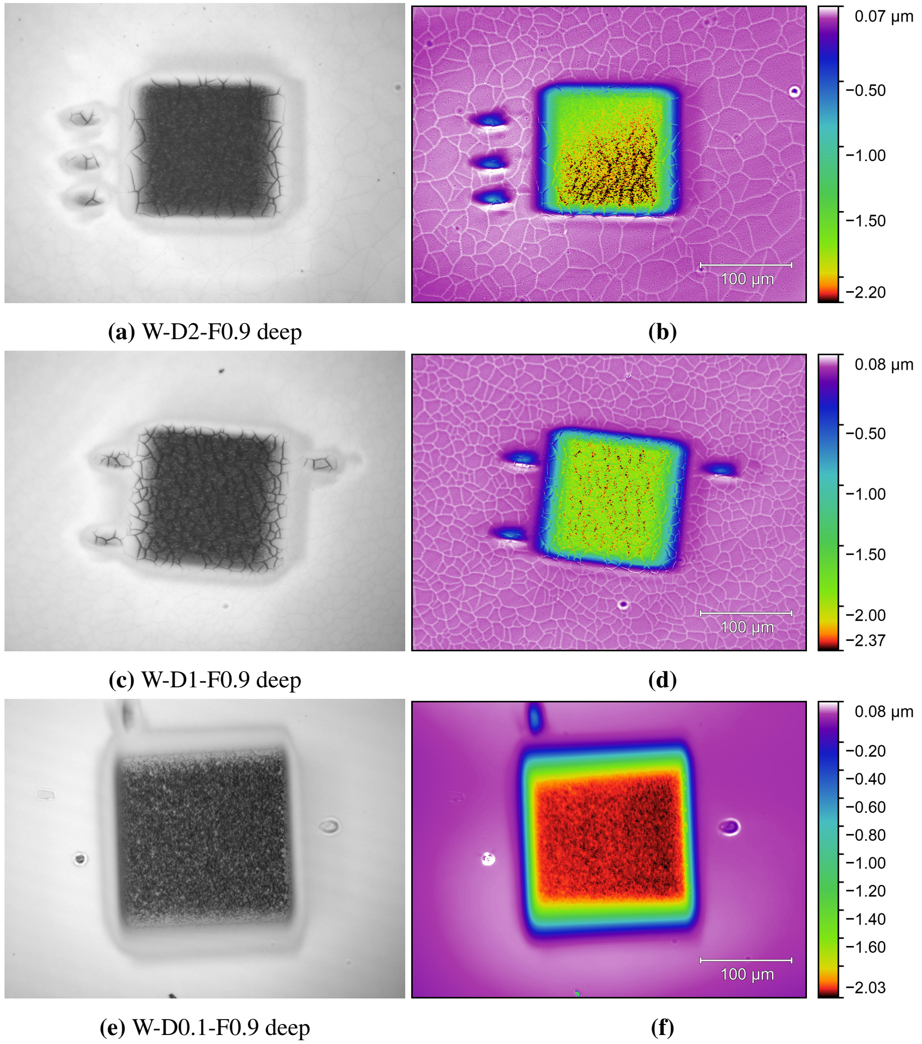


**(a)** W-D2-F0.9 deep

**(b)**

**(c)** W-D1-F0.9 deep

**(d)**

**(e)** W-D0.1-F0.9 deep

**(f)**

**Figure C.2:** WLI measurements and corresponding optical micrographs of deep SIMS craters in fluence 0.9 J/cm$^2$ PLM samples. Acquired with VXI at 11 X magnification.

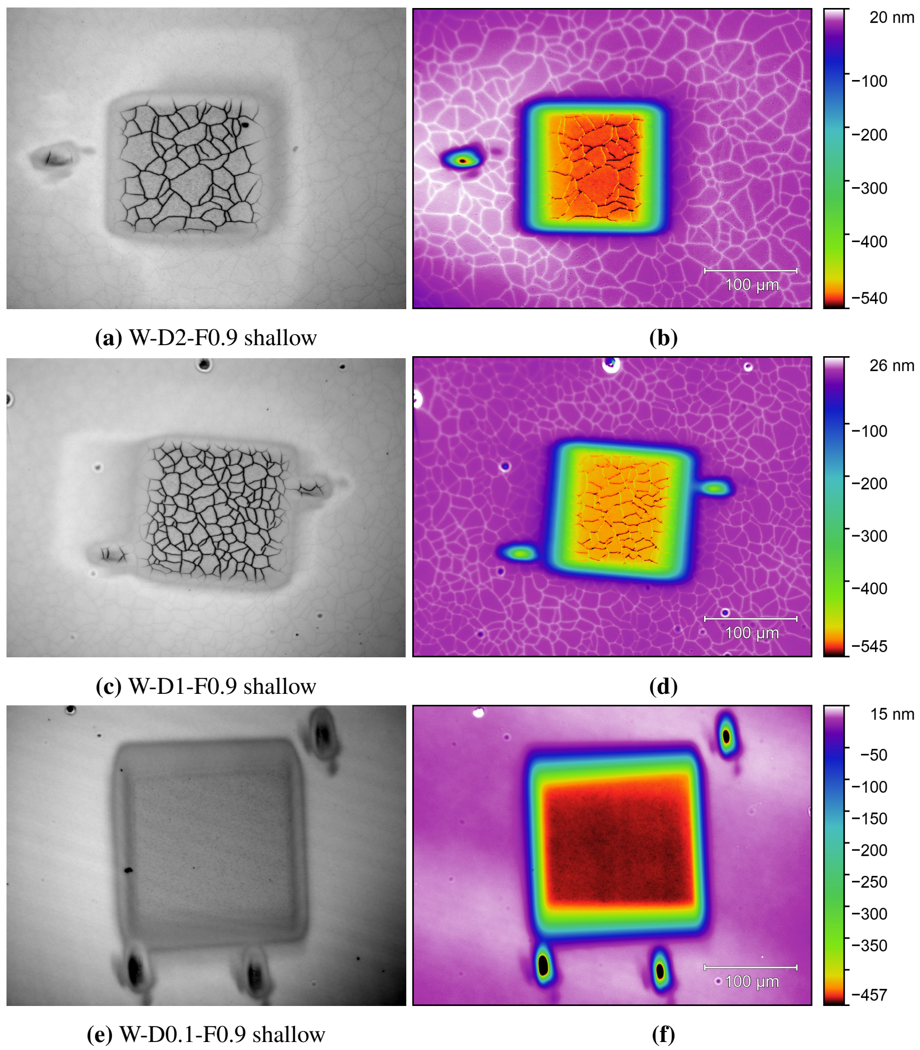


**(a)** W-D2-F0.9 shallow

**(b)**

**(c)** W-D1-F0.9 shallow

**(d)**

**(e)** W-D0.1-F0.9 shallow

**(f)**

**Figure C.3:** WLI measurements and corresponding optical micrographs of shallow SIMS craters in fluence 0.9 J/cm$^2$ PLM samples. Acquired with VSI at 11 X magnification.

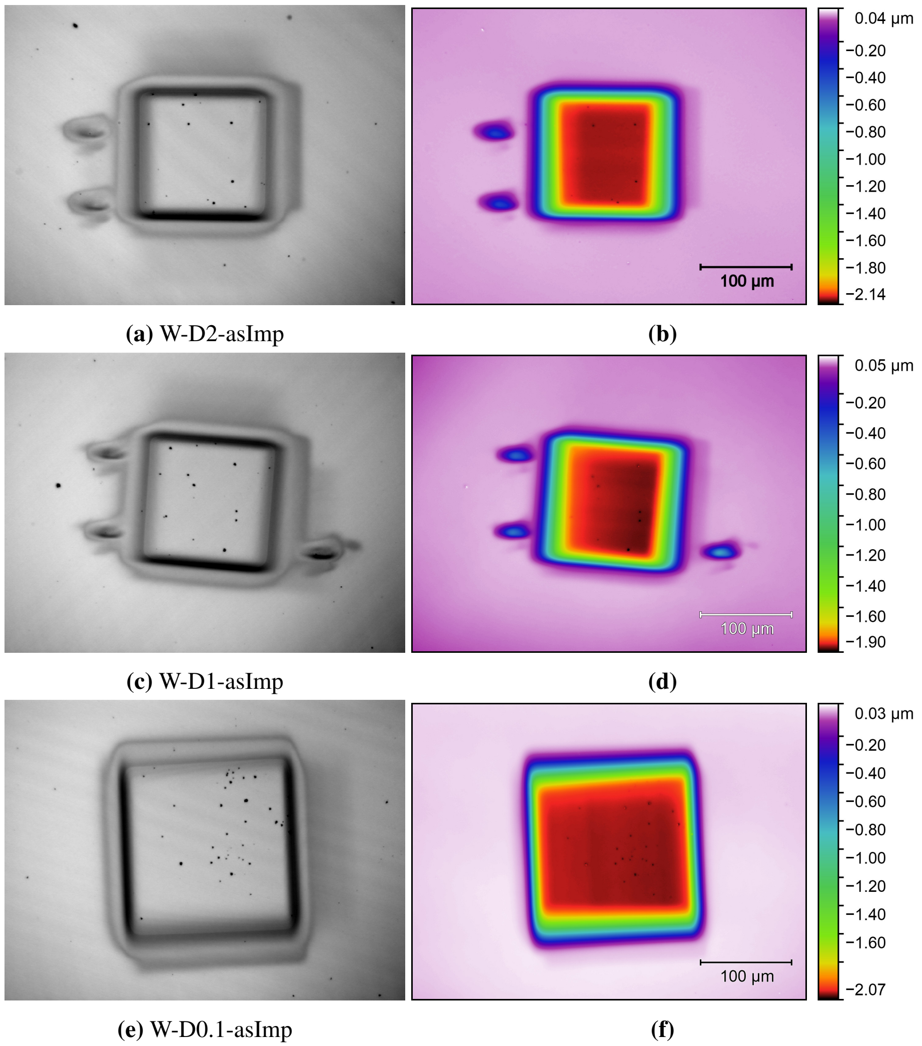


**(a)** W-D2-asImp **(b)**

**(c)** W-D1-asImp **(d)**

**(e)** W-D0.1-asImp **(f)**

**Figure C.4:** WLI measurements and corresponding optical micrographs of SIMS craters from the as-implanted samples. Acquired with VSI at 11 X magnification.

# D
# μ-PCD of W-D1

Minority carrier lifetime is an important metric for real-world performance in solar cells. Investigations of the minority carrier lifetime in the PLM samples with μ-PCD was planned, however the instrument setup was unexpectedly disassembled for relocation to a new lab. Only one sample has therefore been scanned. The μ-PCD mapping from wafer piece W-D1 is presented in figure D.1, for scans both before and after recrystallisation. The PLM spots are clearly visible in the map, having improved lifetime compared to the surrounding as-implanted region. The as-implanted region has lifetimes around 2.7 μs, while the PLM spots attain up to ~3.4 μs. The lifetime in parts of the PLM spots is comparable to that of the accidentally implanted area on the right. From earlier work it is known that the lifetime of the accidentally implanted region in the area measured here is very close to that of unimplanted Fz-Si, though that is not generally true. The instrument has some inconsistencies between runs, as can be seen in the ~0.3 μs lifetime difference in the accidentally implanted region between the measurements in (a) and (b). In any case, recrystallisation with PLM has succeeded in minority carrier lifetime recovery.

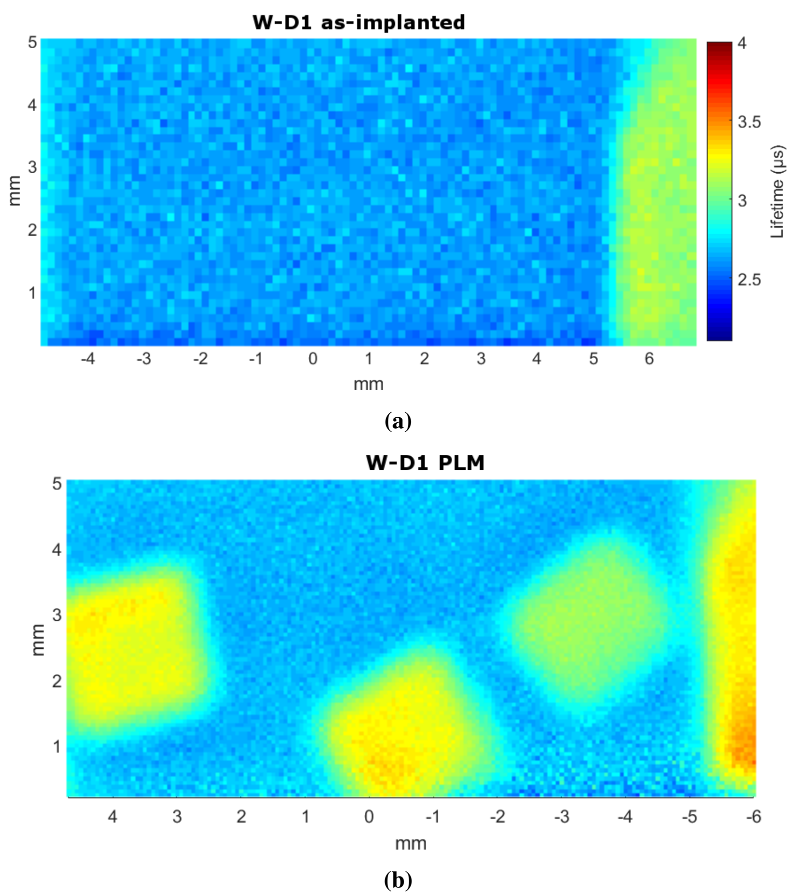


**Figure D.1:** For wafer piece W-D1, μ-PCD minority carrier lifetime maps **(a)** before PLM and **(b)** after PLM. The PLM spots are easily distinguishable from the surrounding as-implanted region by virtue of their increased lifetime. Measurements performed with a Semilab WT-2000.

# E

# More AFM of PLM Samples

In this appendix are presented additional AFM measurements from the W-D1 wafer piece. A scan from the bottom of the SIMS crater in sample W-D1-asImp is shown in figure E.1. There is nanoscale surface rippling present across the measured area, and by extension the entire crater bottom. Scans across cracks in the PLM spots are shown in figure E.2, with fluence 0.9 J/cm$^2$ at the top, 1.4 J/cm$^2$ in the middle, and 1.8 J/cm$^2$ at the bottom. In all samples are observed raised edges next to the cracks.

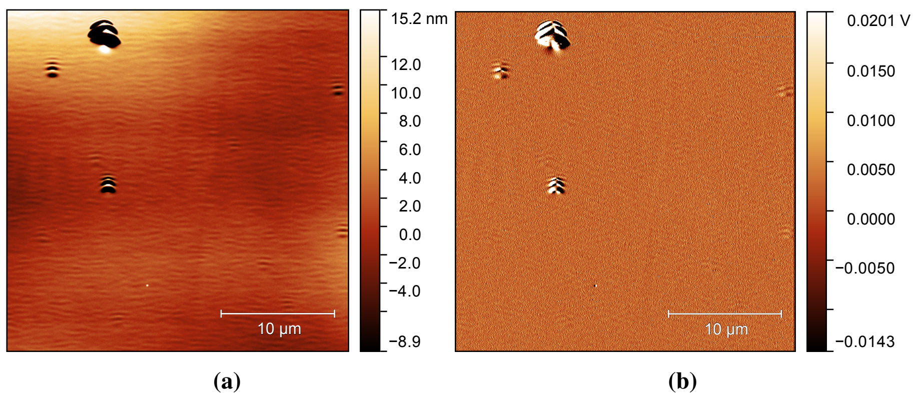


**Figure E.1:** For sample W-D1-asImp, AFM measurement from the bottom of the SIMS crater, with (a) heightmap and (b) peak force error. Nanoscale surface rippling is observed.

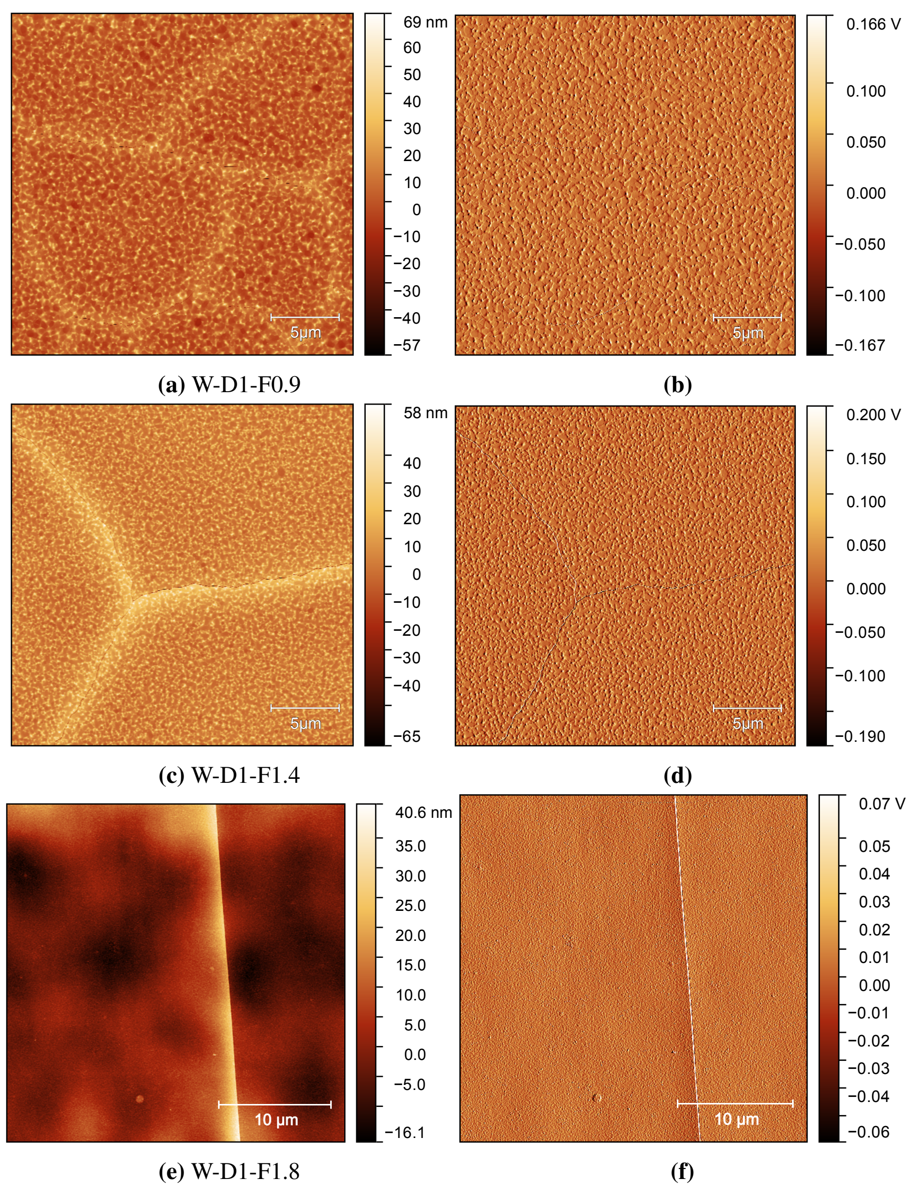


**(a)** W-D1-F0.9 **(b)**

**(c)** W-D1-F1.4 **(d)**

**(e)** W-D1-F1.8 **(f)**

**Figure E.2:** AFM measurements from the centres of the PLM samples on wafer piece W-D1, with fluences in ascending order. Heightmaps are on the left, while peak force error maps are on the right. The density of cracks is greater for lower laser fluences.

# F

# Raman of W-D2-F0.9

An extended Raman spectrum obtained from the centre of sample W-D2-F0.9 is presented in figure F.1, with the spectrum from Fz-Si plotted with dashed lines for comparison. The spectrum was obtained at a low laser power of 1 mW so that temperature effects can be definitively neglected. All expected features from c-Si are present, as are contributions from a-Si and oxides as was the case for the fluence 1.8 J/cm$^2$ PLM samples. The sample is definitively crystalline, despite not being detectable by EBSD. The Γ-peak of c-Si is determined to be at $520.7 \pm 0.2$ cm$^{-1}$, compared to 521.1 cm$^{-1}$ for Fz-Si. Peaks past ~1100 cm$^{-1}$ do not stem from properties of the sample, but rather from contaminants and atmospheric gases. Peaks have been identified for $O_2$ gas at 1556 cm$^{-1}$ [193], the carbonyl group at 1662 cm$^{-1}$ (e.g. acetone) [194], $CO_2$ gas at 2310 cm$^{-1}$ [195], $N_2$ gas at 2331 cm$^{-1}$ [196], and carbon compounds at 2724 cm$^{-1}$ [197].

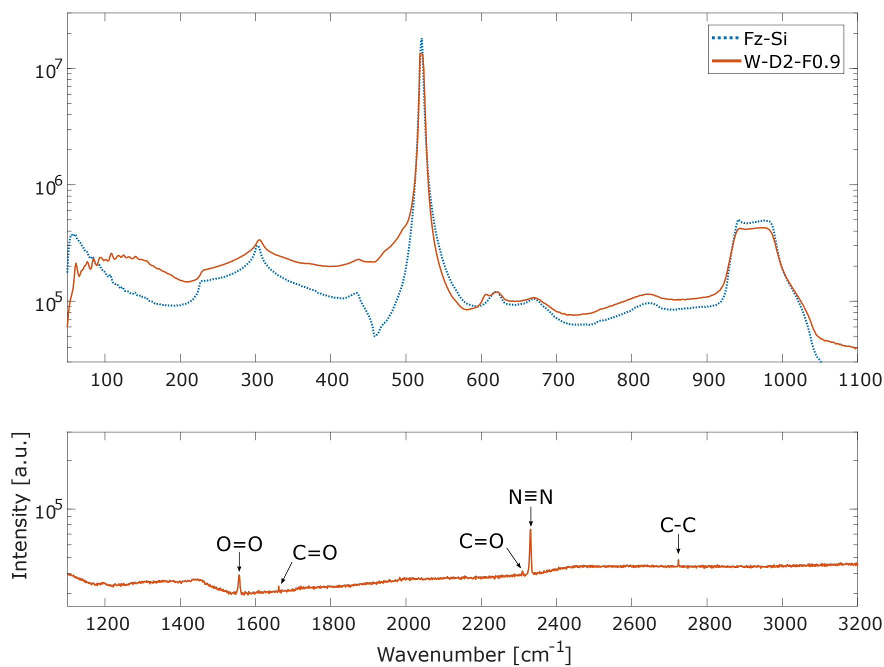


**Figure F.1:** Extended Raman spectrum from sample **W-D2-F0.9**, with the spectrum from Fz-Si plotted with dashed lines for comparison. The sample is quite clearly crystalline, but has contributions from a-Si and oxides, as was the case for the fluence 1.8 J/$cm^2$ PLM samples. Peaks from contaminants/gasses have been labelled.

# G
# MATLAB Code

In this appendix, the code related to the SIMS data adjustment and plotting is given. The script has been minimally cleaned, and might require some changes in commenting with regards to the plots. It is provided 'as is', with reservations for typing errors and other slips. Curve fitting was done interactively with the Curve Fitting Toolbox for the SIMS samples. While it was automated for the Raman, that particular piece of code is generic.

**Listing G.1:** SIMS-plot-W.m

```
1  clc;
2  close all;
3  %%
4  % Depth constants in nm from 3D profiler
5  depA = 2025;
6  depBC = 2002;
7  depD = 1892;
8  depE = 2265;
9  depF = 1859;
10 depG = 1970;
11 depH = 511.6;
12 depI = 535.8;
13 depJ = 1294;
```

```matlab
depK = 451.2;
depL = 2039;
depM = 2008.7;
depN = 523.7;
depO = 2077;

%%
% W-D0.1
A = dlmread('190603a.txt','',15,0);  % A = W-D0.1-asImp
B = dlmread('190603b.txt','',15,0);  % B + C = W-D0.1-F0.9
C = dlmread('190603c.txt','',15,0);
D = dlmread('190603d.txt','',15,0);  % D = W-D0.1-F1.8
K = dlmread('190603k.txt','',15,0);  % K = W-D0.1-F0.9-toDip

Ax = A(:,1)*depA/A(end,1);  % A = W-D0.1-asImp
Ay1 = A(:,2);   % 30 Si
Ay2 = A(:,6);   % 183 W
Ay3 = A(:,8);   % 184 W
Dx = D(:,1)*depD/D(end,1);  % D = W-D0.1-F1.8
Dy1 = D(:,2);   % 30 Si
Dy2 = D(:,4);   % 183 W
Dy3 = D(:,6);   % 184 W
Kx = K(:,1)*depK/K(end,1);  % K = W-D0.1-F0.9-toDip
Ky1 = K(:,2);   % 30 Si
Ky2 = K(:,4);   % 183 W
Ky3 = K(:,6);   % 184 W

% Merging
Bx = B(:,1);    % BC = W-D0.1-F0.9
Cx = C(:,1)+B(end,1);
BCx = cat(1,Bx,Cx);
for i=1:412
    BCx(i)=0+2002/411*(i-1);
end

BCy1 = cat(1,B(:,2),C(:,2));
BCy2 = cat(1,B(:,4),C(:,4));
BCy3 = cat(1,B(:,6),C(:,6));

%%
```

```
% W—D1
E = dlmread('190603e.txt','',15,0);  % E = W—D1—F1.8
F = dlmread('190603f.txt','',15,0);  % F = W—D1—asImp
G = dlmread('190603g.txt','',15,0);  % G = W—D1—F0.9
H = dlmread('190603h.txt','',15,0);  % H = W—D1—F0.9—toPeak
I = dlmread('190603i.txt','',15,0);  % I = W—D1—FzSi
J = dlmread('190603j.txt','',15,0);  % I = W—D1—accImp

Ex = E(:,1)*depE/E(end,1);  % E = W—D1—F1.8
Ey1 = E(:,2);   % 30 Si
Ey2 = E(:,4);   % 183 W
Ey3 = E(:,6);   % 184 W

Fx = F(:,1)*depF/F(end,1);  % F = W—D1—asImp
Fy1 = F(:,2);   % 30 Si
Fy2 = F(:,4);   % 183 W
Fy3 = F(:,6);   % 184 W

Gx = G(:,1)*depG/G(end,1);  % G = W—D1—F0.9
Gy1 = G(:,2);   % 30 Si
Gy2 = G(:,4);   % 183 W
Gy3 = G(:,6);   % 184 W

Hx = H(:,1)*depH/H(end,1);  % H = W—D1—F0.9—toPeak
Hy1 = H(:,2);   % 30 Si
Hy2 = H(:,4);   % 183 W
Hy3 = H(:,6);   % 184 W

Ix = I(:,1)*depI/I(end,1);  % I = W—D1—FzSi
Iy1 = I(:,2);   % 30 Si
Iy2 = I(:,4);   % 183 W
Iy3 = I(:,6);   % 184 W

Jx = J(:,1)*depJ/J(end,1);  % J = W—D1—accImp
Jy1 = J(:,2);   % 30 Si
Jy2 = J(:,4);   % 183 W
Jy3 = J(:,6);   % 184 W

%%
% W—D2
```

```
94  L = dlmread('190603l.txt','',15,0);  % L = W—D2—F1.8
95  M = dlmread('190603m.txt','',15,0);  % M = W—D2—F0.9
96  N = dlmread('190603n.txt','',15,0);  % N = W—D2—F0.9—toDip
97  O = dlmread('190603o.txt','',15,0);  % O = W—D2—asImp
98
99  Lx = L(:,1)*depL/L(end,1); % L = W—D2—F1.8
100 % Lx = Lx*depL/Lx(end);
101 Ly1 = L(:,2);   % 30 Si
102 Ly2 = L(:,4);   % 183 W
103 Ly3 = L(:,6);   % 184 W
104
105 Mx = M(:,1)*depM/M(end,1); % M = W—D2—F0.9
106 My1 = M(:,2);   % 30 Si
107 My2 = M(:,4);   % 183 W
108 My3 = M(:,6);   % 184 W
109
110 Nx = N(:,1)*depN/N(end,1);  % N = W—D2—F0.9—toDip
111 Ny1 = N(:,2);   % 30 Si
112 Ny2 = N(:,4);   % 183 W
113 Ny3 = N(:,6);   % 184 W
114
115 Ox = O(:,1)*depO/O(end,1);  % O = W—D2—asImp
116 Oy1 = O(:,2);   % 30 Si
117 Oy3 = O(:,8);   % 184 W
118
119 %%
120 % X—Axis Adjustments
121
122 % Point indices
123 %%%% D0.1:
124 dpBC = 100;
125 dpK = 84;
126 d01dx = Kx(dpK)—BCx(dpBC);
127
128 for i = 2:1:dpBC
129         BCx(i)=BCx(i)+i*(d01dx)/dpBC;
130 end
131
132 for i = dpBC+1:1:length(BCx)
133     BCx(i) = BCx(i) + d01dx + (i—dpBC)*(d01dx)/—(length(BCx)—dpBC);
```

```
134 end
135
136 %%%% D1:
137 dpG = 56; % x = 4766
138 dpH = 50; % x = 448;
139 d1dx = Hx(dpH)-Gx(dpG);
140
141 for i = 2:1:dpG
142         Gx(i)=Gx(i)+i*(d1dx)/dpG;
143 end
144
145 for i = dpG+1:1:length(Gx)
146     Gx(i) = Gx(i) + d1dx + (i-dpG)*(d1dx)/-(length(Gx)-dpG);
147 end
148
149 %%%% D2:
150 dpM = 45; % x = 352
151 dpN = 45; % x = 435;
152 d2dx = Nx(dpN)-Mx(dpM);
153
154 for i = 2:1:dpM
155         Mx(i)=Mx(i)+i*(d2dx)/dpM;
156 end
157
158 for i = dpM+1:1:length(Mx)
159     Mx(i) = Mx(i) + d2dx + (i-dpM)*(d2dx)/-(length(Mx)-dpM);
160 end
161
162
163 %%
164 % % % 184W/30Si2 All-asImp
165 figure; hold on; box on;
166 pO = plot(Ox,Oy3./Oy1,'LineWidth',2,'DisplayName','W-D2');  % max =
        64.25
167 pF = plot(Fx,Fy3./Fy1,'LineWidth',2,'DisplayName','W-D1');  % max =
        15.9990
168 pA = plot(Ax,Ay3./Ay1,'LineWidth',2,'DisplayName','W-D0.1'); % max =
         1.1661
169 title('W-Si as-implanted | W/Si');
170
```

```
171 % All F1.8 184W/30Si
172 figure; hold on; box on;
173 pL = plot(Lx,Ly3./Ly1,'LineWidth',2,'DisplayName','W-D2');
174 pE = plot(Ex,Ey3./Ey1,'LineWidth',2,'DisplayName','W-D1');
175 pD = plot(Dx,Dy3./Dy1,'LineWidth',2,'DisplayName','W-D0.1');
176 title('W-Si PLM 1.8J | W/Si');
177 
178 % All F0.9 184W/30Si
179 figure; hold on; box on;
180 pM = plot(Mx,My3./My1*3,'LineWidth',2,'DisplayName','W-D2');
181 pG = plot(Gx,Gy3./Gy1*3,'LineWidth',2,'DisplayName','W-D1');
182 pBC = plot(BCx,BCy3./BCy1*3,'LineWidth',2,'DisplayName','W-D0.1');
183 title('W-Si PLM 0.9J | W/Si')
184 
185 % % %Raw W not divided by Si
186 % %as-imp
187 figure; hold on; box on;
188 pO = plot(Ox,Oy3,'LineWidth',2,'DisplayName','W-D2');  % max =
        775138
189 %  % O(1:123) = 2.2496e+07 MOD: 1927
190 pF = plot(Fx,Fy3,'LineWidth',2,'DisplayName','W-D1');  % max =
        316081
191 % % F(1:170) = 1.2886e+07 mod:  673.1574
192 pA = plot(Ax,Ay3,'LineWidth',2,'DisplayName','W-D0.1');   % max =
        13539
193 % % A(1:172) = 5.7740e+05 mod: 49.3812
194 title('W-Si as-implanted | raw W rate')
195 
196 % % All F0.9
197 figure; hold on; box on;
198 pM = plot(Mx,My3,'LineWidth',2,'DisplayName','W-D2');
199 % %M(1:167) = 3.8293e+07 MOD: 989.0885
200 pG = plot(Gx,Gy3,'LineWidth',2,'DisplayName','W-D1');
201 % % G(1:165) = 1.6154e+07 MOD: 1072.4
202 pBC = plot(BCx,BCy3,'LineWidth',2,'DisplayName','W-D0.1');
203 % % BC(1:293) = 1.1888e+06 MOD: 66.7898
204 title('W-Si PLM 0.9J | raw W rate')
205 
206 % % All F1.8
207 figure; hold on; box on;
```

```
208 pL = plot(Lx,Ly3,'LineWidth',2,'DisplayName','W-D2'); % L(1:150) = 3.0171e+07 MOD: 1395.5
209 pE = plot(Ex,Ey3,'LineWidth',2,'DisplayName','W-D1');   % E(1:155) = 1.1153e+07 MOD: 589.6
210 pD = plot(Dx,Dy3,'LineWidth',2,'DisplayName','W-D0.1'); % D(1:295) = 1.0098e+06 MOD: 216.6
211 title('W-Si PLM 1.8J | raw W rate')
212 
213 % %  W in D1-FzSi
214 figure; hold on; box on;
215 % pI0 = plot(Ix,Iy1,'LineWidth',2,'DisplayName','^3^0Si_2^+');
216 pI1 = plot(Ix,Iy3,'LineWidth',2,'DisplayName','^1^8^4W');
217 pI2 = plot(Ix,Iy2,'LineWidth',2,'DisplayName','^1^8^3W');
218 title('W-D1-FzSi')
219 
220 %  W in D1-accImp
221 figure; hold on; box on;
222 pJ1 = plot(Jx,Jy3,'LineWidth',2,'DisplayName','^1^8^4W'); % cent = 596 nm
223 pJ2 = plot(Jx,Jy2,'LineWidth',2,'DisplayName','^1^8^3W');
224 title('W-D1 accidental implantation')
225 
226 % % Si rates
227 figure; hold on; box on;
228 pb = plot(BCx,BCy1,'r--','LineWidth',1,'DisplayName','B + C = W-D0.1-F0.9');
229 pa = plot(Ax,Ay1,'k','LineWidth',1,'DisplayName','A = W-D0.1-asImp');
230 pd = plot(Dx,Dy1,'k','LineWidth',1,'DisplayName','D = W-D0.1-F1.8');
231 pe = plot(Ex,Ey1,'k','LineWidth',1,'DisplayName',' E = W-D1-F1.8');
232 pf = plot(Fx,Fy1,'k','LineWidth',1,'DisplayName','F = W-D1-asImp');
233 pg = plot(Gx,Gy1,'r--','LineWidth',1,'DisplayName','G = W-D1-F0.9');
234 % ph = plot(Hx,Hy1,'b--','LineWidth',1,'DisplayName','H = W-D1-F0.9-toPeak');
235 % pi = plot(Ix,Iy1,'b*','LineWidth',1,'DisplayName','I = W-D1-FzSi');
236 % pj = plot(Jx,Jy1,'LineWidth',1,'DisplayName','');
237 % pk = plot(Kx,Ky1,'c--','LineWidth',1,'DisplayName','K = W-D0.1-F0.9-toDip');
238 pl = plot(Lx,Ly1,'k','LineWidth',1,'DisplayName','L = W-D2-F1.8');
```

```
239 pm = plot(Mx,My1,'r--','LineWidth',1,'DisplayName','M = W-D2-F0.9');
240 % pn = plot(Nx,Ny1,'r--','LineWidth',1,'DisplayName','N = W-D2-F0.9-
        toDip');
241 po = plot(Ox,Oy1,'k','LineWidth',1,'DisplayName','O = W-D2-asImp');
242 
243 hold off;
244 set(gca,'XScale','lin','YScale','log')
245 ax = gca;
246 ax.FontSize = 20.6;
247 xlabel('Depth [nm]')
248 ylabel('Intensity [cps]')
249 % ylabel('Intensity [a.u.]')
250 xlim([0 550])
251 % ylim([0.01  100])
252 [~, hobj, ~, ~] = legend({},'Fontsize',20,'Location','northeast');
253 hl = findobj(hobj,'type','line');
254 set(hl,'LineWidth',4);
255 ht = findobj(hobj,'type','text');
256 set(ht,'FontSize',20);
257 set(gcf, 'Position',  [100, 100, 1280, 720])
```

# Bibliography


[1] Spencer Dale and BP. BP Statistical Review of World Energy 2019. Technical report, 2019.

[2] V. Masson-Delmotte, P. Zhai, H. O. Pörtner, D. Roberts, J. Skea, P. R. Shukla, A. Pirani, W. Moufouma-Okia, C. Péan, R. Pidcock, S. Connors, J. B. R. Matthews, Y. Chen, X. Zhou, M. J. Gomis, E. Lonnoy, I. Maycock, M. Tignor, and Waterfield (eds.) T. Global warming of 1.5°C. An IPCC Special Report on the impacts of global warming of 1.5°C above pre-industrial levels and related global greenhouse gas emission pathways, in the context of strengthening the global response to the threat of climate change, sustainable development, and efforts to eradicate poverty. Technical report, IPCC, Geneva, 2018. URL https://www.ipcc.ch/sr15/.

[3] Gavin Conibeer. Third-generation photovoltaics. *Materials Today*, 10(11): 42–50, 11 2007. ISSN 1369-7021. doi: 10.1016/S1369-7021(07)70278-X. URL https://www.sciencedirect.com/science/article/pii/S136970210770278X?via%3Dihub.

[4] Martin A. Green, Yoshihiro Hishikawa, Ewan D. Dunlop, Dean H. Levi, Jochen Hohl-Ebinger, Masahiro Yoshita, and Anita W.Y. Ho-Baillie. Solar cell efficiency tables (Version 53). *Progress in Photovoltaics: Research and Applications*, 27(1): 3–12, 1 2019. ISSN 10627995. doi: 10.1002/pip.3102. URL http://doi.wiley.com/10.1002/pip.3102.

[5] Simon Philipps and Werner Warmuth. Photovoltaics Report. Technical report, Fraunhofer Institute for Solar Energy Systems, Freiburg, 2019. URL https://www.ise.fraunhofer.de/content/dam/ise/de/documents/publications/studies/Photovoltaics-Report.pdf.

[6] Andy Extance. The reality behind solar power's next star material. *Nature*, 570 (7762):429–432, 6 2019. ISSN 14764687. doi: 10.1038/d41586-019-01985-y.

[7] Antonio Luque, Antonio Martí, and Colin Stanley. Understanding intermediate-band solar cells. *Nature Photonics*, 6(3):146–152, 3 2012. ISSN 1749-4885. doi:

10.1038/nphoton.2012.1. URL http://www.nature.com/articles/nphoton.2012.1.

[8] Tomohiro Nozawa and Yasuhiko Arakawa. Detailed balance limit of the efficiency of multilevel intermediate band solar cells. *Applied Physics Letters*, 98(17):171108, 4 2011. ISSN 0003-6951. doi: 10.1063/1.3583587. URL http://aip.scitation.org/doi/10.1063/1.3583587.

[9] Christie B. Simmons, Austin J. Akey, Jonathan P. Mailoa, Daniel Recht, Michael J. Aziz, and Tonio Buonassisi. Enhancing the Infrared Photoresponse of Silicon by Controlling the Fermi Level Location within an Impurity Band. *Advanced Functional Materials*, 24(19):2852–2858, 5 2014. ISSN 1616301X. doi: 10.1002/adfm.201303820. URL http://doi.wiley.com/10.1002/adfm.201303820.

[10] I. Ramiro, E. Antolin, M. J. Steer, P. G. Linares, E. Hernandez, I. Artacho, E. Lopez, T. Ben, J. M. Ripalda, S. I. Molina, F. Briones, C. R. Stanley, A. Marti, and A. Luque. InAs/AlGaAs quantum dot intermediate band solar cells with enlarged sub-bandgaps. In *2012 38th IEEE Photovoltaic Specialists Conference*, pages 000652–000656. IEEE, 6 2012. ISBN 978-1-4673-0066-7. doi: 10.1109/PVSC.2012.6317694. URL http://ieeexplore.ieee.org/document/6317694/.

[11] Tooru Tanaka, Kin M. Yu, Alejandro X. Levander, Oscar D. Dubon, Lothar A. Reichertz, Nair Lopez, Mitsuhiro Nishio, and Wladek Walukiewicz. Demonstration of ZnTe$_{1-x}$O$_{x}$ Intermediate Band Solar Cell. *Japanese Journal of Applied Physics*, 50(8):082304, 8 2011. ISSN 0021-4922. doi: 10.1143/JJAP.50.082304. URL http://stacks.iop.org/1347-4065/50/082304.

[12] Heidi Sæverud Hauge. *Fabrication and Characterization of an Intermediate Band Material based on Ion Implantation and Pulsed Laser Melting of Ag in Fz-Si*. Msc thesis, NTNU, 2015. URL https://ntnuopen.ntnu.no/ntnu-xmlui/handle/11250/2615743.

[13] Hogne Lysne. *3D TEM characterization of silver implanted silicon for intermediate band solar cells*. Msc thesis, NTNU, 2017. URL https://ntnuopen.ntnu.no/ntnu-xmlui/handle/11250/2615579.

[14] Germán González Díaz, Eric García Hemme, Rodrigo García Hernansanz, Javier Olea Ariza, Daniel Pastor, Álvaro del Prado Millán, Ignacio Plaza, and Perla Wahnón Benarroch. Intermediate band solar cells. The transition metal supersaturated Silicon approach, 2013. URL https://www.semanticscholar.

org/paper/Intermediate-band-solar-cells.
-The-transition-metal-D%C3%ADaz-Hemme/
5829bc34ef4b41e856cefcb30f98521719007818.

[15] Antonio Luque, Antonio Martí, Elisa Antolín, and César Tablero. Intermediate bands versus levels in non-radiative recombination. *Physica B: Condensed Matter*, 382(1-2):320–327, 6 2006. ISSN 09214526. doi: 10.1016/j.physb.2006.03.006. URL https://linkinghub.elsevier.com/retrieve/pii/S0921452606006946.

[16] Wenjie Yang, Jay Mathews, and J.S. Williams. Hyperdoping of Si by ion implantation and pulsed laser melting. *Materials Science in Semiconductor Processing*, 62:103–114, 5 2017. ISSN 1369-8001. doi: 10.1016/J.MSSP.2016.11.005. URL https://www.sciencedirect.com/science/article/pii/S1369800116305029?via%3Dihub#f0040.

[17] A. Martí, C.R. Stanley, and A. Luque. Intermediate Band Solar Cells (IBSC) Using Nanotechnology. *Nanostructured Materials for Solar Energy Conversion*, pages 539–566, 1 2006. doi: 10.1016/B978-044452844-5/50018-4. URL https://www.sciencedirect.com/science/article/pii/B9780444528445500184.

[18] Antonio Luque and Antonio Martí. A metallic intermediate band high efficiency solar cell. *Progress in Photovoltaics: Research and Applications*, 9(2):73–86, 3 2001. ISSN 10627995. doi: 10.1002/pip.354. URL http://doi.wiley.com/10.1002/pip.354.

[19] T NAVRUZ and M SARITAS. Efficiency variation of the intermediate band solar cell due to the overlap between absorption coefficients. *Solar Energy Materials and Solar Cells*, 92(3):273–282, 3 2008. ISSN 09270248. doi: 10.1016/j.solmat.2007.08.012. URL https://linkinghub.elsevier.com/retrieve/pii/S0927024807003431.

[20] Frederick K. Lutgens and Edward J. Tarbuck. *Essentials of geology*. Prentice Hall, 2000. ISBN 0130145440.

[21] Gøran Bye and Bruno Ceccaroli. Solar grade silicon: Technology status and industrial trends. *Solar Energy Materials and Solar Cells*, 130: 634–646, 11 2014. ISSN 09270248. doi: 10.1016/j.solmat.2014.06.019. URL https://linkinghub.elsevier.com/retrieve/pii/S0927024814003286.

[22] R. Merget, T. Bauer, H. Küpper, S. Philippou, H. Bauer, R. Breitstadt, and T. Bruening. Health hazards due to the inhalation of

amorphous silica. *Archives of Toxicology*, 75(11-12):625–634, 1 2002. ISSN 0340-5761. doi: 10.1007/s002040100266. URL http://www.ncbi.nlm.nih.gov/pubmed/11876495http://link.springer.com/10.1007/s002040100266.

[23] A. Borghesi and G. Guizzetti. *Handbook of Optical Constants of Solids*. Number C. Academic Press, New York, 1991. ISBN 0125444222.

[24] A. De Luca, A. Portavoce, M. Texier, C. Grosjean, N. Burle, V. Oison, and B. Pichaud. Tungsten diffusion in silicon. *Journal of Applied Physics*, 115 (1):013501, 1 2014. ISSN 0021-8979. doi: 10.1063/1.4859455. URL http://aip.scitation.org/doi/10.1063/1.4859455.

[25] A De Luca, A Portavoce, M Texier, N Burle, and B Pichaud. Dynamic segregation of metallic impurities at SiO <sub>2</sub> /Si interfaces. *Journal of Physics: Conference Series*, 471(1):012029, 11 2013. ISSN 1742-6588. doi: 10.1088/1742-6596/471/1/012029. URL http://stacks.iop.org/1742-6596/471/i=1/a=012029?key=crossref.36533d31cc090f83ca3f49da61048ca0.

[26] Periodic Table of Elements: Los Alamos National Laboratory. URL https://periodic.lanl.gov/list.shtml.

[27] Michael Gasik, editor. *Handbook of Ferroalloys*. Butterworth-Heinemann, 1st ed. edition, 2013. ISBN 9780080977539.

[28] S. Boughaba and D. Mathiot. Deep level transient spectroscopy characterization of tungstenrelated deep levels in silicon. *Journal of Applied Physics*, 69(1):278–283, 1 1991. ISSN 0021-8979. doi: 10.1063/1.347708. URL http://aip.scitation.org/doi/10.1063/1.347708.

[29] Yu A Zibuts, L G Paritskii, S M Ryvkin, and Zh G Dokholyan. Photoelectric Properties of Silicon Doped with Copper, Tungsten and Platinum. *SOVIET PHYS SOLID STATE*, 8(9):2041–2047, 1967.

[30] H. Pettersson, H. G. Grimmeiss, L. Tilly, K. Schmalz, K. Tittelbach, and H. Kerkow. Electrical and optical properties of molybdenum and tungsten related defects in silicon. *Semiconductor Science and Technology*, 6(4):237–242, 1991. ISSN 02681242. doi: 10.1088/0268-1242/6/4/002.

[31] Yoshihisa Fujisaki, Toshio Ando, Hirotsugu Kozuka, and Yukio Takano. Characterization of tungstenrelated deep levels in bulk silicon crystal. *Journal of Applied Physics*, 63(7):2304–2306, 4 1988. ISSN 0021-8979. doi: 10.1063/1.341045. URL http://aip.scitation.org/doi/10.1063/1.341045.

[32] Toshio Ando, Seiichi Isomae, Chusuke Munakata, and Takao Abe. Deeplevel transient spectroscopy on <i>p</i> type silicon crystals containing tungsten impurities. *Journal of Applied Physics*, 70(10):5401–5403, 11 1991. ISSN 0021-8979. doi: 10.1063/1.350196. URL http://aip.scitation.org/doi/10.1063/1.350196.

[33] Gennady Gildenblat, Barbara A. Heath, and William Katz. Interface states induced in silicon by tungsten as a result of reactive ion beam etching. *Journal of Applied Physics*, 54(4):1855–1859, 1983. ISSN 00218979. doi: 10.1063/1.332236.

[34] S. I. Rasmagin. Effect of tungsten coating on the properties of high-resistivity gold-doped silicon. *Inorganic Materials*, 50(11):1075–1077, 2014. ISSN 16083172. doi: 10.1134/S0020168514110144.

[35] H. H. Busta and H. A. Waggener. Precipitation-Induced Currents and Generation-Recombination Currents in Intentionally Contaminated Silicon P+N Junctions. *Journal of the Electrochemical Society*, 124(9):1424–1429, 1977. ISSN 19457111. doi: 10.1149/1.2133667.

[36] Alain Portavoce, Anthony de Luca, Nelly Burle, and Michaël Texier. Redistribution of Metallic Impurities in Si during Annealing and Oxidation: W and Fe. *Defect and Diffusion Forum*, 383:17–22, 2 2018. ISSN 1662-9507. doi: 10.4028/www.scientific.net/DDF.383.17. URL https://www.scientific.net/DDF.383.17.

[37] Gary S. May and S. M. Sze. *Fundamentals of semiconductor fabrication*. Wiley, 2004. ISBN 9780471232797. URL https://www.wiley.com/en-us/Fundamentals+of+Semiconductor+Fabrication-p-9780471232797.

[38] V. Castaldo. High Resolution Scanning Ion Microscopy, 2011. URL https://repository.tudelft.nl/islandora/object/uuid%3A011a479f-9c7c-40bc-b542-6d27b97b1301?collection=research.

[39] Channeling. In *Ion Implantation and Synthesis of Materials*, pages 93–106. Springer Berlin Heidelberg, Berlin, Heidelberg, 2006. doi: 10.1007/978-3-540-45298-0{_}8. URL http://link.springer.com/10.1007/978-3-540-45298-0_8.

[40] Alain Claverie, Larbi Laânab, Caroline Bonafos, Christian Bergaud, Augustin Martinez, and Daniel Mathiot. On the relation between dopant anomalous

diffusion in Si and end-of-range defects. *Nuclear Instruments and Methods in Physics Research Section B: Beam Interactions with Materials and Atoms*, 96(1-2):202–209, 3 1995. ISSN 0168583X. doi: 10.1016/0168-583X(94)00483-8. URL https://linkinghub.elsevier.com/retrieve/pii/0168583X94004838.

[41] Michael Nastasi and James W. Mayer. *Ion Implantation and Synthesis of Materials*. Springer Berlin Heidelberg, Berlin, Heidelberg, 2006. ISBN 978-3-540-23674-0. doi: 10.1007/978-3-540-45298-0. URL http://link.springer.com/10.1007/978-3-540-45298-0.

[42] Taeseok Kim, Manoj R. Pillai, Michael J. Aziz, Michael A. Scarpulla, Oscar D. Dubon, Kin M. Yu, Jeffrey W. Beeman, and Mark C. Ridgway. Heat flow model for pulsed laser melting and rapid solidification of ion implanted GaAs. *Journal of Applied Physics*, 108(1):013508, 7 2010. ISSN 0021-8979. doi: 10.1063/1.3457106. URL http://aip.scitation.org/doi/10.1063/1.3457106.

[43] Michael J Aziz and Theodore Kaplan. Continuous growth model for interface motion during alloy solidification. *Acta Metallurgica*, 36(8):2335–2347, 8 1988. ISSN 0001-6160. doi: 10.1016/0001-6160(88)90333-1. URL https://www.sciencedirect.com/science/article/pii/0001616088903331?via%3Dihub.

[44] P. Baeri and E. Rimini. Laser annealing of silicon. *Materials Chemistry and Physics*, 46(2-3):169–177, 11 1996. ISSN 02540584. doi: 10.1016/S0254-0584(97)80010-7. URL https://linkinghub.elsevier.com/retrieve/pii/S0254058497800107.

[45] J S Williams. Materials modification with ion beams. *Reports on Progress in Physics*, 49(5):491–587, 5 1986. ISSN 0034-4885. doi: 10.1088/0034-4885/49/5/001. URL http://stacks.iop.org/0034-4885/49/i=5/a=001?key=crossref.e27720ea6d043c3c040ba330fd0db1ba.

[46] F. C. Voogt, R. Ishihara, and F. D. Tichelaar. Melting and crystallization behavior of low-pressure chemical-vapor-deposition amorphous Si films during excimer-laser annealing. *Journal of Applied Physics*, 95(5):2873–2879, 3 2004. ISSN 0021-8979. doi: 10.1063/1.1642286. URL http://aip.scitation.org/doi/10.1063/1.1642286.

[47] Michael O. Thompson, G. J. Galvin, J. W. Mayer, P. S. Peercy, J. M. Poate, D. C. Jacobson, A. G. Cullis, and N. G. Chew. Melting Temperature and Explosive Crystallization of Amorphous Silicon during Pulsed Laser Irradiation.

*Physical Review Letters*, 52(26):2360–2363, 6 1984. ISSN 0031-9007. doi: 10.1103/PhysRevLett.52.2360. URL https://link.aps.org/doi/10.1103/PhysRevLett.52.2360.

[48] Jeffrey M. Warrender, Jay Mathews, Daniel Recht, Matthew Smith, Silvija Gradečak, and Michael J. Aziz. Morphological stability during solidification of silicon incorporating metallic impurities. *Journal of Applied Physics*, 115 (16):163516, 4 2014. ISSN 0021-8979. doi: 10.1063/1.4871809. URL http://aip.scitation.org/doi/10.1063/1.4871809.

[49] Jay Mathews, Austin J. Akey, Daniel Recht, Girish Malladi, Harry Efstathiadis, Michael J. Aziz, and Jeffrey M. Warrender. On the limits to Ti incorporation into Si using pulsed laser melting. *Applied Physics Letters*, 104(11):112102, 3 2014. ISSN 0003-6951. doi: 10.1063/1.4868724. URL http://aip.scitation.org/doi/10.1063/1.4868724.

[50] J Olea, E López, E Antolín, A Martí, A Luque, E García-Hemme, D Pastor, R García-Hernansanz, A del Prado, and G González-Díaz. Room temperature photo-response of titanium supersaturated silicon at energies over the bandgap. *Journal of Physics D: Applied Physics*, 49 (5):055103, 2 2016. ISSN 0022-3727. doi: 10.1088/0022-3727/49/5/055103. URL http://stacks.iop.org/0022-3727/49/i=5/a=055103?key=crossref.14af42c17891d324442b7c36abf57e20.

[51] Lars Rebohle, Slawomir Prucnal, and Wolfgang Skorupa. A review of thermal processing in the subsecond range: semiconductors and beyond. *Semiconductor Science and Technology*, 31(10):103001, 10 2016. ISSN 0268-1242. doi: 10.1088/0268-1242/31/10/103001. URL http://stacks.iop.org/0268-1242/31/i=10/a=103001?key=crossref.6c2fe760cfd567835bae64cb068c1992.

[52] Daniel Recht, Matthew J. Smith, Supakit Charnvanichborikarn, Joseph T. Sullivan, Mark T. Winkler, Jay Mathews, Jeffrey M. Warrender, Tonio Buonassisi, James S. Williams, Silvija Gradečak, and Michael J. Aziz. Supersaturating silicon with transition metals by ion implantation and pulsed laser melting. *Journal of Applied Physics*, 114(12):124903, 9 2013. ISSN 0021-8979. doi: 10.1063/1.4821240. URL http://aip.scitation.org/doi/10.1063/1.4821240.

[53] S Prucnal1 R Hübner1 Ye Yuan1 2 W Skorupa1 M Helm1 2 Fang Liu1, 2 and and Shengqiang Zhou1. Suppressing the cellular breakdown in silicon supersaturated with titanium. 2016. doi: 10.1088/0022-3727/49/24/

245104. URL https://iopscience.iop.org/article/10.1088/0022-3727/49/24/245104/pdf.

[54] Austin J. Akey, Daniel Recht, James S. Williams, Michael J. Aziz, and Tonio Buonassisi. Single-Phase Filamentary Cellular Breakdown Via Laser-Induced Solute Segregation. *Advanced Functional Materials*, 25(29):4642–4649, 8 2015. ISSN 1616301X. doi: 10.1002/adfm.201501450. URL http://doi.wiley.com/10.1002/adfm.201501450.

[55] Yiwen Ma and Mathis Plapp. Phase-field simulations and geometrical characterization of cellular solidification fronts. *Journal of Crystal Growth*, 385:140–147, 1 2014. ISSN 00220248. doi: 10.1016/j.jcrysgro.2013.03.027. URL https://linkinghub.elsevier.com/retrieve/pii/S0022024813002145.

[56] J. Olea, M. Toledano-Luque, D. Pastor, E. San-Andrés, I. Mártil, and G. González-Díaz. High quality Ti-implanted Si layers above the Mott limit. *Journal of Applied Physics*, 107(10):103524, 5 2010. ISSN 0021-8979. doi: 10.1063/1.3391274. URL http://aip.scitation.org/doi/10.1063/1.3391274.

[57] S.F. Lombardo, S. Boninelli, F. Cristiano, G. Fisicaro, G. Fortunato, M.G. Grimaldi, G. Impellizzeri, M. Italia, A. Marino, R. Milazzo, E. Napolitani, V. Privitera, and A. La Magna. Laser annealing in Si and Ge: Anomalous physical aspects and modeling approaches. *Materials Science in Semiconductor Processing*, 62:80–91, 5 2017. ISSN 1369-8001. doi: 10.1016/J.MSSP.2016.10.047. URL https://www.sciencedirect.com/science/article/pii/S1369800116304899.

[58] C. Hock, S. Straßburg, H. Haberland, B. v. Issendorff, A. Aguado, and M. Schmidt. Melting-Point Depression by Insoluble Impurities: A Finite Size Effect. *Physical Review Letters*, 101(2):023401, 7 2008. ISSN 0031-9007. doi: 10.1103/PhysRevLett.101.023401. URL http://www.ncbi.nlm.nih.gov/pubmed/18764180https://link.aps.org/doi/10.1103/PhysRevLett.101.023401.

[59] A. Di Gianfrancesco. Technologies for chemical analyses, microstructural and inspection investigations. *Materials for Ultra-Supercritical and Advanced Ultra-Supercritical Power Plants*, pages 197–245, 1 2017. doi: 10.1016/B978-0-08-100552-1.00008-7. URL https://www.sciencedirect.com/science/article/pii/B9780081005521000087.

[60] Weilie Zhou and Zhong Lin Wang, editors. *Scanning Microscopy for Nanotech-*

*nology*. Springer New York, New York, NY, 2007. ISBN 978-0-387-33325-0. doi: 10.1007/978-0-387-39620-0. URL http://link.springer.com/10.1007/978-0-387-39620-0.

[61] Demetrios Voreades. Secondary electron emission from thin carbon films. *Surface Science*, 60(2):325–348, 11 1976. ISSN 00396028. doi: 10.1016/0039-6028(76)90320-4. URL https://linkinghub.elsevier.com/retrieve/pii/0039602876903204.

[62] Jason T. Kite. Secondary electron production and transport mechanisms by measurement of angle -energy resolved cross sections of secondary and backscattered electron emission from gold, 2006. URL https://www.semanticscholar.org/paper/Secondary-electron-production-and-transport-by-of-Kite/2f3681588210de7b749970bc90a34804f4a60265.

[63] Robert A. Schwarzer, David P. Field, Brent L. Adams, Mukul Kumar, and Adam J. Schwartz. Present State of Electron Backscatter Diffraction and Prospective Developments. In *Electron Backscatter Diffraction in Materials Science*, pages 1–20. Springer US, Boston, MA, 2009. doi: 10.1007/978-0-387-88136-2{_}1. URL http://link.springer.com/10.1007/978-0-387-88136-2_1.

[64] EBSD Oxford Instruments - EBSD Explained. URL http://www.ebsd.com/ebsd-explained/10-ebsd-explained.

[65] D. J. Dingley and V. Randle. Microtexture determination by electron back-scatter diffraction. *Journal of Materials Science*, 27(17):4545–4566, 1992. ISSN 0022-2461. doi: 10.1007/BF01165988. URL http://link.springer.com/10.1007/BF01165988.

[66] Michael Bauer. *Raman spectroscopy of laser induced material alterations*. 2010.

[67] Derek J. Gardiner and P. R. (Pierre R.) Graves. *Practical Raman Spectroscopy*. Springer Berlin Heidelberg, 1989. ISBN 9783642740404.

[68] David Tuschel. The Effect of Microscope Objectives on the Raman Spectra of Crystals. URL http://www.spectroscopyonline.com/effect-microscope-objectives-raman-spectra-crystals.

[69] My Nhung, Thi Tran, Magnus Rønning, and Samuel K Regli. In situ characterization of industrial catalysts with Raman spectroscopy. Technical report.

[70] M Grimsditch, A Polian, and R Vogelgesang. The phonon density of states

in amorphous materials. *Journal of Physics: Condensed Matter*, 15(31): S2335–S2341, 8 2003. ISSN 0953-8984. doi: 10.1088/0953-8984/15/31/309. URL http://stacks.iop.org/0953-8984/15/i=31/a=309?key=crossref.05502023b7feb4f9f0723f88761bd6de.

[71] J. E. Smith, M. H. Brodsky, B. L. Crowder, M. I. Nathan, and A. Pinczuk. Raman Spectra of Amorphous Si and Related Tetrahedrally Bonded Semiconductors. *Physical Review Letters*, 26(11):642–646, 3 1971. ISSN 0031-9007. doi: 10.1103/PhysRevLett.26.642. URL https://link.aps.org/doi/10.1103/PhysRevLett.26.642.

[72] R. L. C. Vink, G. T. Barkema, and W. F. van der Weg. Raman spectra and structure of amorphous Si. *Physical Review B*, 63(11):115210, 3 2001. ISSN 0163-1829. doi: 10.1103/PhysRevB.63.115210. URL https://link.aps.org/doi/10.1103/PhysRevB.63.115210.

[73] W. F. van der Weg, A. J. M. Berntsen, F. W. Saris, and A. Polman. Ion implantation into amorphous solids. *Materials Chemistry and Physics*, 46:140–146, 1996. URL http://www.erbium.nl/wp-content/uploads/2016/08/Ion_implantation_in_amorphous_solids_-_Mat_Chem_Phys_1996.pdf.

[74] Igor Iatsunskyi, Stefan Jurga, Valentyn Smyntyna, Mykolai Pavlenko, Valeriy Myndrul, and Anastasia Zaleska. Raman spectroscopy of nanostructured silicon fabricated by metal-assisted chemical etching. page 913217, 5 2014. doi: 10.1117/12.2051489. URL http://proceedings.spiedigitallibrary.org/proceeding.aspx?doi=10.1117/12.2051489.

[75] Kai F. Dombrowski. *Micro-Raman Investigation of Mechanical Stress in Si Device Structures and Phonons in SiGe*. PhD thesis, Technische Universität Cottbus, 2000. URL https://core.ac.uk/download/pdf/33427606.pdf.

[76] S.A. Schwarz. Secondary Ion Mass Spectroscopy. In *Encyclopedia of Materials: Science and Technology*, pages 8283–8290. Elsevier, 2001. doi: 10.1016/B0-08-043152-6/01482-0. URL https://linkinghub.elsevier.com/retrieve/pii/B0080431526014820.

[77] Lasse Vines. Secondary ion mass spectrometry (SIMS), Lecture notes MENA3100. page 2, 2009.

[78] Scientific Image - Atomic Force Microscope Illustration | NISE Network. URL https://www.nisenet.org/catalog/scientific-image-atomic-force-microscope-illustration.

[79] Bruker Nano Surfaces Division. Interferometry Basics, User Training Slides. Technical report, 2016.

[80] Bruker Nano Surfaces Division. Phase Shifting Interferometry, User Training Slides. pages 1–18, 2016.

[81] Bruker Nano Surfaces Division. Vertical Scanning Interferometry, User Training Slides. pages 1–9, 2016.

[82] L M Manojlović, M B Živanov, M P Slankamenac, D Z Stupar, and J S Bajić. Resolution limit of the white-light interferometric sensor for absolute position measurement based on central fringe maximum identification. *Physica Scripta*, T162(T162):014052, 9 2014. ISSN 0031-8949. doi: 10.1088/0031-8949/2014/T162/014052. URL `http://stacks.iop.org/1402-4896/2014/i=T162/a=014052?key=crossref.104c436ddd5d7af6c598d8c58dfc2554`.

[83] White Light Interferometry - Nanoscience Instruments. URL `https://www.nanoscience.com/techniques/optical-profilometry/white-light-interferometry/`.

[84] Ivan Pelant and Jan Valenta. Luminescence of excitons. In *Luminescence Spectroscopy of Semiconductors*, pages 161–204. Oxford University Press, 2 2012. doi: 10.1093/acprof:oso/9780199588336.003.0007. URL `http://www.oxfordscholarship.com/view/10.1093/acprof:oso/9780199588336.001.0001/acprof-9780199588336-chapter-7`.

[85] Dieter K. Schroder. *Semiconductor material and device characterization*. IEEE Press, 2006. ISBN 9780471739067. URL `https://www.wiley.com/en-us/Semiconductor+Material+and+Device+Characterization%2C+3rd+Edition-p-9780471739067`.

[86] P. J. Dean, W. F. Flood, and G. Kaminsky. Absorption due to Bound Excitons in Silicon. *Physical Review*, 163(3):721–725, 11 1967. ISSN 0031-899X. doi: 10.1103/PhysRev.163.721. URL `https://link.aps.org/doi/10.1103/PhysRev.163.721`.

[87] FEI Quantitative BioImaging Laboratory. FEI Lab | Hyperspectral Imaging. URL `https://fei-lab.org/hyperspectral-imaging/`.

[88] Hogne Lysne. Tungsten doped silicon for intermediate band solar cells.

[89] MunEm M Hossain and Masud H Chowdhury. Heat transfer simulations for pulsed laser annealing of silicon thin film. In *2013 IEEE 56th International Midwest Symposium on Circuits and Systems (MWSCAS)*, pages 732–735. IEEE, 8

2013. ISBN 978-1-4799-0066-4. doi: 10.1109/MWSCAS.2013.6674753. URL http://ieeexplore.ieee.org/document/6674753/.

[90] Sungho Choi and Kyung-Young Jhang. Thermal damages on the surface of a silicon wafer induced by a near-infrared laser. *Optical Engineering*, 53(1):017103, 1 2014. ISSN 0091-3286. doi: 10.1117/1.OE.53.1.017103. URL http://opticalengineering.spiedigitallibrary.org/article.aspx?doi=10.1117/1.OE.53.1.017103.

[91] R. F. Cook. Strength and sharp contact fracture of silicon. *Journal of Materials Science*, 41(3):841–872, 2 2006. ISSN 0022-2461. doi: 10.1007/s10853-006-6567-y. URL http://link.springer.com/10.1007/s10853-006-6567-y.

[92] I. Adlakha, M. A. Tschopp, and K. N. Solanki. The role of grain boundary structure and crystal orientation on crack growth asymmetry in aluminum. *Materials Science and Engineering A*, 618:345–354, 11 2014. ISSN 09215093. doi: 10.1016/j.msea.2014.08.083.

[93] J. Shi and M. A. Zikry. Grain-boundary interactions and orientation effects on crack behavior in polycrystalline aggregates. *International Journal of Solids and Structures*, 46(21):3914–3925, 10 2009. ISSN 00207683. doi: 10.1016/j.ijsolstr.2009.07.019.

[94] Weiyi Lu, Srinivas S. Chakravarthula, Jin Chen, and Yu Qiao. Propagation of a cleavage crack front across a field of persistent grain boundaries. *International Journal of Solids and Structures*, 49(3-4):584–589, 2 2012. ISSN 00207683. doi: 10.1016/j.ijsolstr.2011.11.003.

[95] Jayantha Kodikara and Susanga Costa. Desiccation cracking in clayey soils: Mechanisms and modelling. *Springer Series in Geomechanics and Geoengineering*, 3:21–32, 2013. ISSN 18668755. doi: 10.1007/978-3-642-32492-5{_}2.

[96] Cracked earth, cracked soil, texture dry cracking earth | icon0.com - Free images for personal, commercial and noncommercial use. Attribution is not required. URL https://www.flickr.com/photos/icon0/33194572758/sizes/l.

[97] J. H. Yoo, S. H. Jeong, R. Greif, and R. E. Russo. Explosive change in crater properties during high power nanosecond laser ablation of silicon. *Journal of Applied Physics*, 88(3):1638–1649, 8 2000. ISSN 0021-8979. doi: 10.1063/1.373865. URL http://aip.scitation.org/doi/10.1063/1.373865.

[98] Roger Kelly and Antonio Miotello. Does normal boiling exist due to laser-pulse or ion bombardment? *Journal of Applied Physics*, 87(6):3177–3179, 3 2000. ISSN 0021-8979. doi: 10.1063/1.372319. URL http://aip.scitation.org/doi/10.1063/1.372319.

[99] Quanming Lu, Samuel S. Mao, Xianglei Mao, and Richard E. Russo. Delayed phase explosion during high-power nanosecond laser ablation of silicon. *Applied Physics Letters*, 80(17):3072–3074, 4 2002. ISSN 0003-6951. doi: 10.1063/1.1473862. URL http://aip.scitation.org/doi/10.1063/1.1473862.

[100] S. Lugomer, A. Maksimović, Z. Geretovszky, and T. Szörényi. Nonlinear waves generated on liquid silicon layer by femtosecond laser pulses. *Applied Surface Science*, 285:588–599, 11 2013. ISSN 0169-4332. doi: 10.1016/J.APSUSC.2013.08.098. URL https://www.sciencedirect.com/science/article/pii/S0169433213015894.

[101] A. J. Pedraza, Y. F. Guan, J. D. Fowlkes, and D. A. Smith. Nanostructures produced by ultraviolet laser irradiation of silicon. I. Rippled structures. *Journal of Vacuum Science and Technology B: Microelectronics and Nanometer Structures*, 22(6):2823–2835, 11 2004. ISSN 10711023. doi: 10.1116/1.1821575.

[102] G D Tsibidis, M Barberoglou, P A Loukakos, E Stratakis, and C Fotakis. Dynamics of ripple formation on silicon surfaces by ultrashort laser pulses in subablation conditions. Technical report.

[103] Jiangmin Xu, Chao Chen, Tengfei Zhang, and Zhenchun Han. A study of polycrystalline silicon damage features based on nanosecond pulse laser irradiation with different wavelength effects. *Materials*, 10(3), 2017. ISSN 19961944. doi: 10.3390/ma10030260.

[104] Felice Gesuele, Jijil JJ Nivas, Rosalba Fittipaldi, Carlo Altucci, Riccardo Bruzzese, Pasqualino Maddalena, and Salvatore Amoruso. Analysis of nascent silicon phase-change gratings induced by femtosecond laser irradiation in vacuum. *Scientific Reports*, 8(1), 12 2018. ISSN 20452322. doi: 10.1038/s41598-018-30269-0.

[105] V. Craciun, N. Bassim, R.K. Singh, D. Craciun, J. Hermann, and C. Boulmer-Leborgne. Laser-induced explosive boiling during nanosecond laser ablation of silicon. *Applied Surface Science*, 186(1-4):288–292, 1 2002. ISSN 0169-4332. doi: 10.1016/S0169-4332(01)00766-8. URL https://www.sciencedirect.com/science/article/pii/S0169433201007668.

[106] J.Y. Xu, H. Hu, and Y.L. Lei. Morphological features of silicon substrate by using different frequency laser ablation in air and water. *Applied Surface Science*, 317:666–671, 10 2014. ISSN 0169-4332. doi: 10.1016/J.APSUSC.2014.08.038. URL https://www.sciencedirect.com/science/article/pii/S0169433214017723.

[107] Stefan Tatra, Rodrigo Gómez Vázquez, Christian Stiglbrunner, and Andreas Otto. Numerical Simulation of Laser Ablation with Short and Ultrashort Pulses for Metals and Semiconductors. *Physics Procedia*, 83:1339–1346, 1 2016. ISSN 1875-3892. doi: 10.1016/J.PHPRO.2016.08.141. URL https://www.sciencedirect.com/science/article/pii/S1875389216302486.

[108] D.M. Karnakis. High power single-shot laser ablation of silicon with nanosecond 355ănm. *Applied Surface Science*, 252(22):7823–7825, 9 2006. ISSN 0169-4332. doi: 10.1016/J.APSUSC.2005.09.040. URL https://www.sciencedirect.com/science/article/pii/S016943320501322X.

[109] J. Bonse, S. Baudach, J. Krüger, W. Kautek, and M. Lenzner. Femtosecond laser ablation of siliconmodification thresholds and morphology. *Applied Physics A*, 74(1):19–25, 1 2002. ISSN 0947-8396. doi: 10.1007/s003390100893. URL http://link.springer.com/10.1007/s003390100893.

[110] Claudio Canale, Bruno Torre, Davide Ricci, and Pier Carlo Braga. Recognizing and avoiding artifacts in atomic force microscopy imaging. *Methods in molecular biology (Clifton, N.J.)*, 736:31–43, 2011. ISSN 1940-6029. doi: 10.1007/978-1-61779-105-5{_}3. URL http://www.ncbi.nlm.nih.gov/pubmed/21660719.

[111] W. Polkowski, N. Sobczak, A. Polkowska, J. Kalarus, and M. Warmuzek. A comparison of various imaging modes in scanning electron microscopy during evaluation of selected Si/refractory sessile drop couples after wettability tests at ultra-high temperature. *Prace Instytutu Odlewnictwa*, 57(4):337–344, 2017. ISSN 1899-2439. doi: 10.7356/iod.2017.35.

[112] Christopher B. Saltonstall, Justin Serrano, Pamela M. Norris, Patrick E. Hopkins, and Thomas E. Beechem. Single element Raman thermometry. *Review of Scientific Instruments*, 84(6), 6 2013. ISSN 00346748. doi: 10.1063/1.4810850.

[113] Matej Par, Ozren Gamulin, Nika Spanovic, Ruza Bjelovucic, and Zrinka Tarle. The effect of excitation laser power in Raman spectroscopic measurements of the degree of conversion of resin composites. *Dental Materials*, 35(9):

1227–1237, 9 2019. ISSN 0109-5641. doi: 10.1016/J.DENTAL.2019.05.018. URL https://www.sciencedirect.com/science/article/abs/pii/S0109564119300855.

[114] T. R. Hart, R. L. Aggarwal, and Benjamin Lax. Temperature dependence of raman scattering in silicon. *Physical Review B*, 1(2):638–642, 1970. ISSN 01631829. doi: 10.1103/PhysRevB.1.638.

[115] Junjie Niu, Jian Sha, and Deren Yang. Temperature dependence of the first-order Raman scattering in silicon nanowires. *Scripta Materialia*, 55(2):183–186, 7 2006. ISSN 13596462. doi: 10.1016/j.scriptamat.2006.03.060.

[116] Yao Chen, Jianhua Dai, Xueqian Zhou, Yunjie Liu, Wei Zhang, and Guiyong Peng. Raman spectroscopy analysis of the biochemical characteristics of molecules associated with the malignant transformation of gastric mucosa. *PLoS ONE*, 9(4), 4 2014. ISSN 19326203. doi: 10.1371/journal.pone.0093906.

[117] Challa S.S.R. Kumar. *Raman spectroscopy for nanomaterials characterization*, volume 9783642206207. Springer-Verlag Berlin Heidelberg, 3 2012. ISBN 9783642206207. doi: 10.1007/978-3-642-20620-7.

[118] Peter J. Codella, Fran Adar, and Yung S. Liu. Raman microprobe analysis of tungsten silicide. *Applied Physics Letters*, 46(11):1076–1078, 1985. ISSN 00036951. doi: 10.1063/1.95766.

[119] Rama Vuppuladhadium, Howard E. Jackson, and Joseph T. Boyd. Raman study of the formation of tungsten silicide thin films. *Journal of Applied Physics*, 73 (11):7887–7893, 1993. ISSN 00218979. doi: 10.1063/1.353940.

[120] Sandeep Kumar, Samhita Dasgupta, Howard E. Jackson, and Joseph T. Boyd. Raman scattering from rapid thermally annealed tungsten silicide. *Applied Physics Letters*, 50(6):323–325, 1987. ISSN 00036951. doi: 10.1063/1.98188.

[121] G. Sarau, M. Becker, G. Andrä, and S. Christiansen. Residual stress measurements in multicrystalline silicon bulk and thin film solar cells using micro-Raman spectroscopy. pages 1–6, 2008. URL https://www.researchgate.net/publication/228922442_Residual_stress_measurements_in_multicrystalline_silicon_bulk_and_thin_film_solar_cells_using_micro-Raman_spectroscopy.

[122] M. A. Castro, A. J. Aller, K. Faulds, and D. Littlejohn. Characterization of condensed phase beryllium species in the presence of aluminium and silicon matrices during electrothermal heating on graphite and tungsten platforms. *Journal of Analytical Atomic Spectrometry*, 26(9):1722–1732, 9 2011. ISSN 02679477. doi: 10.1039/c1ja10017c.

[123] William T.A. Harrison, Laurie L. Dussack, Thomas Vogt, and Allan J. Jacobson. Syntheses, crystal structures, and properties of new layered tungsten(VI)-containing materials based on the hexagonal-WO3 structure: M2(WO3)3SeO3 (M = NH4, Rb, Cs). *Journal of Solid State Chemistry*, 120(1):112–120, 11 1995. ISSN 1095726X. doi: 10.1006/jssc.1995.1385.

[124] J. A. Horsley, I. E. Wachs, J. M. Brown, G. H. Via, and F. D. Hardcastle. Structure of surface tungsten oxide species in the WO3/Al2O3supported oxide system from X-ray absorption near-edge spectroscopy and Raman spectroscopy. *Journal of Physical Chemistry*, 91(15):4014–4020, 1987. ISSN 00223654. doi: 10.1021/j100299a018.

[125] J. Engweiler, J. Harf, and A. Baiker. WOx/TiO2 catalysts prepared by grafting of tungsten alkoxides: Morphological properties and catalytic behavior in the selective reduction of NO by NH3. *Journal of Catalysis*, 159(2):259–269, 1996. ISSN 00219517. doi: 10.1006/jcat.1996.0087.

[126] M. Boulova, A. Gaskov, and G. Lucazeau. Tungsten oxide reactivity versus CH4, CO and NO2 molecules studied by Raman spectroscopy. *Sensors and Actuators, B: Chemical*, 2001. ISSN 09254005. doi: 10.1016/S0925-4005(01)00938-8.

[127] G. M. Ramāns, J. V. Gabrusenoks, and A. A. Veispāls. Structure of Tungstic Acids and Amorphous and Crystalline WO3 Thin Films. *physica status solidi (a)*, 74(1):K41–K44, 1982. ISSN 1521396X. doi: 10.1002/pssa.2210740153.

[128] E. Cazzanelli, C. Vinegoni, G. Mariotto, A. Kuzmin, and J. Purans. Low-Temperature Polymorphism in Tungsten Trioxide Powders and Its Dependence on Mechanical Treatments. *Journal of Solid State Chemistry*, 143(1):24–32, 2 1999. ISSN 00224596. doi: 10.1006/jssc.1998.8061.

[129] Jørgen Sørhaug. *TEM characterization of tungsten-implanted silicon - A study of a potential intermediate band solar cell material*. Msc thesis, NTNU, 2019. URL `http://hdl.handle.net/11250/2625257`.

[130] D. R. Tallant, B. C. Bunker, C. J. Brinker, and C. A. Balfe. RAMAN SPECTRA OF RINGS IN SILICATE MATERIALS. In *Materials Research Society Symposia Proceedings*, volume 73, pages 261–267. Materials Research Soc, 1986. ISBN 0931837391. doi: 10.1557/proc-73-261.

[131] P. Yuan, H. P. He, D. Q. Wu, D. Q. Wang, and L. J. Chen. Characterization of diatomaceous silica by Raman spectroscopy. *Spectrochimica Acta - Part A: Molecular and Biomolecular Spectroscopy*, 60(12):2941–2945, 10 2004. ISSN 13861425. doi: 10.1016/j.saa.2004.02.005.

[132] Robert A. Schwarzer and Jarle Hjelen. High-Speed Orientation Microscopy with Offline Solving Sequences of EBSD Patterns. *Solid State Phenomena*, 160:295–300, 2 2010. ISSN 1662-9779. doi: 10.4028/www.scientific.net/SSP.160.295. URL https://www.scientific.net/SSP.160.295.

[133] Aimo Winkelmann, T Ben Britton, and Gert Nolze. Constraints on the Effective Electron Energy Spectrum in Backscatter Kikuchi Diffraction. Technical report, 2018. URL https://arxiv.org/pdf/1810.09525.pdf.

[134] N. BRODUSCH, H. DEMERS, and R. GAUVIN. Nanometres-resolution Kikuchi patterns from materials science specimens with transmission electron forward scatter diffraction in the scanning electron microscope. *Journal of Microscopy*, 250(1):1–14, 4 2013. ISSN 00222720. doi: 10.1111/jmi.12007. URL http://www.ncbi.nlm.nih.gov/pubmed/23346885http://doi.wiley.com/10.1111/jmi.12007.

[135] Marie-Agathe Charpagne, Florian Strub, and Tresa M. Pollock. Accurate reconstruction of EBSD datasets by a multimodal data approach using an evolutionary algorithm. 3 2019. doi: 10.1016/j.matchar.2019.01.033. URL http://arxiv.org/abs/1903.02988http://dx.doi.org/10.1016/j.matchar.2019.01.033.

[136] H-R Wenk and P Van Houtte. Texture and anisotropy. *Reports on Progress in Physics*, 67(8):1367–1428, 8 2004. ISSN 0034-4885. doi: 10.1088/0034-4885/67/8/R02. URL http://stacks.iop.org/0034-4885/67/i=8/a=R02?key=crossref.d67071618fd36c904cd5b849f70e5e0a.

[137] James C Bouwer, Thomas J Deerinck, Eric Bushong, Vadim Astakhov, Ranjan Ramachandra, Steven T Peltier, and Mark H Ellisman. Deceleration of probe beam by stage bias potential improves resolution of serial block-face scanning electron microscopic images. *Advanced structural and chemical imaging*, 2(1):11, 2017. ISSN 2198-0926. doi: 10.1186/s40679-016-0025-y. URL http://www.ncbi.nlm.nih.gov/pubmed/27695667http://www.pubmedcentral.nih.gov/articlerender.fcgi?artid=PMC5025511.

[138] D. Phifer, L. Tuma, T. Vystavel, P. Wandrol, and R.J. Young. Improving SEM Imaging Performance Using Beam Deceleration. *Microscopy Today*, 17(4):40–49, 7 2009. ISSN 1551-9295. doi: 10.1017/S1551929509000170. URL https://www.cambridge.org/core/product/identifier/S1551929509000170/type/journal_article.

[139] Gwénaëlle Proust, Patrick Trimby, Sandra Piazolo, and Delphine Retraint. Char-

acterization of ultra-fine grained and nanocrystalline materials using transmission kikuchi diffraction. *Journal of Visualized Experiments*, 2017(122), 4 2017. ISSN 1940087X. doi: 10.3791/55506.

[140] Markus J. B. Ristola. *Initial characterisation of W-implanted Si - For use in high-effciency intermediate band solar cells*. Project work, NTNU, 2019.

[141] Julia Eizenkop, Ivan Avrutsky, Daniel G. Georgiev, and Vipin Chaudchary. Single-pulse excimer laser nanostructuring of silicon: A heat transfer problem and surface morphology. *Journal of Applied Physics*, 103(9):094311, 5 2008. ISSN 0021-8979. doi: 10.1063/1.2910196. URL `http://aip.scitation.org/doi/10.1063/1.2910196`.

[142] P.A.W. van der Heide, M.S. Lim, S.S. Perry, and J. Bennett. A systematic study of the surface roughening and sputter rate variations occurring during SIMS ultra-shallow depth profile analysis of Si with Cs+. *Nuclear Instruments and Methods in Physics Research Section B: Beam Interactions with Materials and Atoms*, 201 (2):413–425, 2 2003. ISSN 0168-583X. doi: 10.1016/S0168-583X(02)01647-6. URL `https://www.sciencedirect.com/science/article/pii/S0168583X02016476?via%3Dihub#FIG5`.

[143] K. Wittmaack. Apparent and real transient effects in SIMS depth profiling using oxygen bombardment. *Applied Surface Science*, 203-204: 20–26, 1 2003. ISSN 01694332. doi: 10.1016/S0169-4332(02) 00640-2. URL `https://linkinghub.elsevier.com/retrieve/pii/S0169433202006402`.

[144] Adrian Keller and Stefan Facsko. Ion-Induced Nanoscale Ripple Patterns on Si Surfaces: Theory and Experiment. *Materials (Basel, Switzerland)*, 3(10):4811–4841, 10 2010. ISSN 1996-1944. doi: 10.3390/ma3104811. URL `http://www.ncbi.nlm.nih.gov/pubmed/28883355http://www.pubmedcentral.nih.gov/articlerender.fcgi?artid=PMC5445787`.

[145] Javier Muñoz-García, Mario Castro, and Rodolfo Cuerno. Nonlinear Ripple Dynamics on Amorphous Surfaces Patterned by Ion Beam Sputtering. *Physical Review Letters*, 96(8):086101, 2 2006. ISSN 0031-9007. doi: 10.1103/PhysRevLett.96.086101. URL `https://link.aps.org/doi/10.1103/PhysRevLett.96.086101`.

[146] G. Carter, M. J. Nobes, F. Paton, J. S. Williams, and J. L. Whitton. Ion bombardment induced ripple topography on amorphous solids. *Radiation Effects*, 33(2):65–73, 1 1977. ISSN 0033-7579. doi: 10.1080/

00337577708237469. URL http://www.tandfonline.com/doi/abs/10.1080/00337577708237469.

[147] R. Mark Bradley and James M. E. Harper. Theory of ripple topography induced by ion bombardment. *Journal of Vacuum Science & Technology A: Vacuum, Surfaces, and Films*, 6(4):2390–2395, 7 1988. ISSN 0734-2101. doi: 10.1116/1.575561. URL http://avs.scitation.org/doi/10.1116/1.575561.

[148] Rodolfo Cuerno and Albert-László Barabási. Dynamic Scaling of Ion-Sputtered Surfaces. *Physical Review Letters*, 74(23):4746–4749, 6 1995. ISSN 0031-9007. doi: 10.1103/PhysRevLett.74.4746. URL https://link.aps.org/doi/10.1103/PhysRevLett.74.4746.

[149] Mario Castro, Rodolfo Cuerno, Luis Vázquez, and Raúl Gago. Self-Organized Ordering of Nanostructures Produced by Ion-Beam Sputtering. *Physical Review Letters*, 94(1):016102, 1 2005. ISSN 0031-9007. doi: 10.1103/PhysRevLett.94.016102. URL https://link.aps.org/doi/10.1103/PhysRevLett.94.016102.

[150] M. Castro, R. Gago, L. Vazquez, J. Munoz-Garcia, and R. Cuerno. Energy dependence of the ripple wavelength for ion-beam sputtering of silicon: Experiments and theory. In *AIP Conference Proceedings*, volume 1525, pages 380–385. American Institute of Physics, 4 2013. doi: 10.1063/1.4802355. URL http://aip.scitation.org/doi/abs/10.1063/1.4802355.

[151] John J. Vajo, Robert E. Doty, and EunHee Cirlin. Influence of O <sup>+</sup> <sub>2</sub> energy, flux, and fluence on the formation and growth of sputteringinduced ripple topography on silicon. *Journal of Vacuum Science & Technology A: Vacuum, Surfaces, and Films*, 14(5):2709–2720, 9 1996. ISSN 0734-2101. doi: 10.1116/1.580192. URL http://avs.scitation.org/doi/10.1116/1.580192.

[152] B. Fares, B. Gautier, N. Baboux, G. Prudon, P. Holliger, and J.C. Dupuy. Influence of surface orientation on the formation of sputtering-induced ripple topography in silicon. *Applied Surface Science*, 231-232:678–683, 6 2004. ISSN 0169-4332. doi: 10.1016/J.APSUSC.2004.03.178. URL https://www.sciencedirect.com/science/article/pii/S0169433204004179?via%3Dihub.

[153] Roger Smith. Ripple structures on ion bombarded surfaces arising from the sputter yield dependence on incidence angle. *Nuclear Instruments and Methods in Physics Research Section B: Beam Interactions with Materials and Atoms*,

352:213–216, 6 2015. ISSN 0168-583X. doi: 10.1016/J.NIMB.2014.11.104. URL https://www.sciencedirect.com/science/article/pii/S0168583X14010052?via%3Dihub.

[154] K. Zhang, H. Hofsäss, F. Rotter, M. Uhrmacher, C. Ronning, and J. Krauser. Morphology of Si surfaces sputter-eroded by low-energy Xe-ions at glancing incident angle. *Surface and Coatings Technology*, 203(17-18):2395–2398, 6 2009. ISSN 0257-8972. doi: 10.1016/J.SURFCOAT.2009.02.105. URL https://www.sciencedirect.com/science/article/pii/S0257897209001224?via%3Dihub.

[155] W.C. Sinke, A. Polman, S. Roorda, and P.A. Stolk. Explosive crystallization of amorphous silicon: triggering and propagation. *Applied Surface Science*, 43(1-4):128–135, 12 1989. ISSN 0169-4332. doi: 10.1016/0169-4332(89)90201-8. URL https://www.sciencedirect.com/science/article/pii/0169433289902018?via%3Dihub.

[156] Peter Sigmund. A mechanism of surface micro-roughening by ion bombardment. *Journal of Materials Science*, 8(11):1545–1553, 11 1973. ISSN 0022-2461. doi: 10.1007/BF00754888. URL http://link.springer.com/10.1007/BF00754888.

[157] Peter Lehmann, Stanislav Tereschenko, and Weichang Xie. Fundamental aspects of resolution and precision in vertical scanning white-light interferometry. *Surface Topography: Metrology and Properties*, 4(2), 6 2016. ISSN 2051672X. doi: 10.1088/2051-672X/4/2/024004.

[158] Abraham Mario Tapilouw, Yi-Wei Chang, Long-Yo Yu, and Hau-Wei Wang. Reduction of batwing effect in white light interferometry for measurement of patterned sapphire substrates (PSS) wafer. page 996006, 8 2016. doi: 10.1117/12.2236874. URL http://proceedings.spiedigitallibrary.org/proceeding.aspx?doi=10.1117/12.2236874.

[159] James F. Ziegler, M.D. Ziegler, and J.P. Biersack. SRIM The stopping and range of ions in matter (2010). *Nuclear Instruments and Methods in Physics Research Section B: Beam Interactions with Materials and Atoms*, 268(11-12):1818–1823, 6 2010. ISSN 0168-583X. doi: 10.1016/J.NIMB.2010.02.091. URL https://www.sciencedirect.com/science/article/pii/S0168583X10001862.

[160] J. Narayan, C. W. White, M. J. Aziz, B. Stritzker, and A. Walthuis. Pulsed excimer (KrF) laser melting of amorphous and crystalline silicon layers. *Journal of Applied Physics*, 57(2):564–567, 1 1985. ISSN 0021-8979. doi: 10.1063/1.334738. URL http://aip.scitation.org/doi/10.1063/1.334738.

[161] D. Pastor, J. Olea, A. Muñoz-Martín, A. Climent-Font, I. Mártil, and G. González-Díaz. Interstitial Ti for intermediate band formation in Ti-supersaturated silicon. *Journal of Applied Physics*, 112(11):113514, 12 2012. ISSN 0021-8979. doi: 10.1063/1.4768274. URL `http://aip.scitation.org/doi/10.1063/1.4768274`.

[162] D. Pastor, J. Olea, A. del Prado, E. García-Hemme, R. García-Hernansanz, and G. González-Díaz. Insulator to metallic transition due to intermediate band formation in Ti-implanted silicon. *Solar Energy Materials and Solar Cells*, 104:159–164, 9 2012. ISSN 09270248. doi: 10.1016/j.solmat.2012.04.049. URL `https://linkinghub.elsevier.com/retrieve/pii/S0927024812002280`.

[163] J. Olea, D. Pastor, I. Mártil, and G. González-Díaz. Thermal stability of intermediate band behavior in Ti implanted Si. *Solar Energy Materials and Solar Cells*, 94(11):1907–1911, 11 2010. ISSN 09270248. doi: 10.1016/j.solmat.2010.06.045. URL `https://linkinghub.elsevier.com/retrieve/pii/S0927024810004137`.

[164] E. Zinner. Depth profiling by secondary ion mass spectrometry. *Scanning*, 3 (2):57–78, 1980. ISSN 01610457. doi: 10.1002/sca.4950030202. URL `http://doi.wiley.com/10.1002/sca.4950030202`.

[165] S. Hofmann, S. Y. Lian, Y. S. Han, Q. R. Deng, and J. Y. Wang. Correlation of depth resolution and preferential sputtering in depth profiles of thin layers by Secondary Ion Mass Spectrometry (SIMS). *Thin Solid Films*, 662:165–167, 9 2018. ISSN 00406090. doi: 10.1016/j.tsf.2018.07.045.

[166] R. J. H. Morris and M. G. Dowsett. Ion yields and erosion rates for Si1xGex(0x1) ultralow energy O2+ secondary ion mass spectrometry in the energy range of 0.251 keV. *Journal of Applied Physics*, 105(11):114316, 6 2009. ISSN 0021-8979. doi: 10.1063/1.3139279. URL `http://aip.scitation.org/doi/10.1063/1.3139279`.

[167] Gui Dong, Cha Liangzhen, Liu Rong, and A. T. S. Wee. SIMS quantification of Si1?xGex alloys using polyatomic secondary ions. *Surface and Interface Analysis*, 32(1):171–174, 8 2001. ISSN 0142-2421. doi: 10.1002/sia.1030. URL `http://doi.wiley.com/10.1002/sia.1030`.

[168] Mathieu Gavelle, Emmanuel Scheid, Fuccio Cristiano, Claude Armand, Jean-Michel Hartmann, Yves Campidelli, Aomar Halimaoui, Pier-Francesco Fazzini, and Olivier Marcelot. Detection of Cs2Ge+ clusters for the quantification of germanium atoms by secondary ion mass spectrometry: Application to

the characterization of Si1xGex layers (0x1) and germanium diffusion in silicon. *Journal of Applied Physics*, 102(7):074904, 10 2007. ISSN 0021-8979. doi: 10.1063/1.2786037. URL http://aip.scitation.org/doi/10.1063/1.2786037.

[169] M.G. Dowsett, R. Morris, Pei-Fen Chou, S.F. Corcoran, H. Kheyrandish, G.A. Cooke, J.L. Maul, and S.B. Patel. Charge compensation using optical conductivity enhancement and simple analytical protocols for SIMS of resistive Si1xGex alloy layers. *Applied Surface Science*, 203-204:500–503, 1 2003. ISSN 0169-4332. doi: 10.1016/S0169-4332(02)00765-1. URL https://www.sciencedirect.com/science/article/pii/S0169433202007651?via%3Dihub.

[170] A. Mikami, T. Okazawa, K. Saito, and Y. Kido. Positive secondary Ion emission from Si1xGex bombarded by O2+. *Applied Surface Science*, 253(3): 1620–1625, 11 2006. ISSN 0169-4332. doi: 10.1016/J.APSUSC.2006.02.052. URL https://www.sciencedirect.com/science/article/pii/S0169433206002406?via%3Dihub.

[171] K. Wittmaack. Effect of surface roughening on secondary ion yields and erosion rates of silicon subject to oblique oxygen bombardment. *Journal of Vacuum Science & Technology A: Vacuum, Surfaces, and Films*, 8(3):2246–2250, 5 1990. ISSN 0734-2101. doi: 10.1116/1.576744.

[172] Maxim A. Makeev and Albert László Barabási. Secondary ion yield changes on rippled interfaces. *Applied Physics Letters*, 72(8):906–908, 1998. ISSN 00036951. doi: 10.1063/1.120932.

[173] Maxim A. Makeev and Albert László Barabási. Effect of surface morphology on the sputtering yields. II. Ion sputtering from rippled surfaces. *Nuclear Instruments and Methods in Physics Research, Section B: Beam Interactions with Materials and Atoms*, 222(3-4):335–354, 8 2004. ISSN 0168583X. doi: 10.1016/j.nimb.2004.02.028.

[174] D. P. Adams, T. M. Mayer, M. J. Vasile, and K. Archuleta. Effects of evolving surface morphology on yield during focused ion beam milling of carbon. *Applied Surface Science*, 252(6):2432–2444, 1 2006. ISSN 01694332. doi: 10.1016/j.apsusc.2005.06.013.

[175] Gerhard Hobler, R. Mark Bradley, and Herbert M. Urbassek. Probing the limitations of Sigmund's model of spatially resolved sputtering using Monte Carlo simulations. *Physical Review B*, 93(20), 5 2016. ISSN 24699969. doi: 10.1103/PhysRevB.93.205443.

[176] V. I. Shulga. Sputter yield of rippled surfaces: A simulation study. *Nuclear Instruments and Methods in Physics Research, Section B: Beam Interactions with Materials and Atoms*, 412:207–213, 12 2017. ISSN 0168583X. doi: 10.1016/j.nimb.2017.09.015.

[177] J. Lindroos, D. P. Fenning, D. J. Backlund, E. Verlage, A. Gorgulla, S. K. Estreicher, H. Savin, and T. Buonassisi. Nickel: A very fast diffuser in silicon. *Journal of Applied Physics*, 113(20), 2013. ISSN 00218979. doi: 10.1063/1.4807799.

[178] Gordon Davies. The optical properties of luminescence centres in silicon, 1989. ISSN 03701573.

[179] Dilla Duryha Berhanuddin. Generation and characterisation of the carbon G-centre in silicon. Technical report, 2015.

[180] S Charnvanichborikarn, B J Villis, B C Johnson, J Wong-Leung, J C Mccallum, J S Williams, and C Jagadish. Effect of boron on interstitial-related luminescence centers in silicon. *Citation: Applied Physics Letters*, 96:123707, 2010. doi: 10.1063/1.3300836. URL `http://dx.doi.org/10.1063/1.3300836http://scitation.aip.org/content/aip/journal/apl/96/5?ver=pdfcov`.

[181] P J Dzan, J R Havnes, and Ann W F Floon Bel. SEPTEMSER New Radiative Recombination Processes Involving Neutral Donors and Acceytors in Silicon and Germanium. Technical report.

[182] Guro Marie Wyller, Florian Schindler, Wolfram Kwapil, Jonas Schon, Espen Olsen, Halvard Haug, Stephan Riepe, and Martin C. Schubert. Correlation of defect luminescence and recombination in multicrystalline silicon. *IEEE Journal of Photovoltaics*, 9(1):55–63, 1 2019. ISSN 21563381. doi: 10.1109/JPHOTOV.2018.2875209.

[183] S. Pizzini, M. Guzzi, E. Grillit, and G. Borionetti. Photoluminescence emission in the 0.7-0.9 eV range from oxygen precipitates, thermal donors and dislocations in silicon. *Journal of Physics Condensed Matter*, 12(49):10131–10143, 12 2000. ISSN 09538984. doi: 10.1088/0953-8984/12/49/312.

[184] S Ostapenko, I Tarasov, J P Kalejs, C Haessler, and E-U Reisner. Defect monitoring using scanning photoluminescence spectroscopy in multicrystalline silicon wafers. Technical report, 2000.

[185] Tzanimir Vladimirov Arguirov. *Electro-optical properties of dislocations in silicon and their possible application for light emitters*. PhD thesis, Brandenburgischen Technischen Universität Cottbus, 2008. URL `https://opus4.kobv.de/opus4-btu/frontdoor/index/index/docId/450`.

[186] I. Burud, A. S. Flø, and E. Olsen. On the origin of inter band gap radiative emission in crystalline silicon. *AIP Advances*, 2(4), 2012. ISSN 21583226. doi: 10.1063/1.4766588.

[187] A. Flø, I. Burud, K. Kvaal, R. Søndenå, and E. Olsen. Distribution of radiative crystal imperfections through a silicon ingot. *AIP Advances*, 3(11), 11 2013. ISSN 21583226. doi: 10.1063/1.4834155.

[188] Woo Sik Yoo, Kitaek Kang, Gota Murai, and Masahiro Yoshimoto. Temperature Dependence of Photoluminescence Spectra from Crystalline Silicon. *ECS Journal of Solid State Science and Technology*, 4(12):456–461, 2015. doi: 10.1149/2.0251512jss.

[189] V. Madhavi, P. Kondaiah, O. M. Hussain, and S. Uthanna. Structural, Optical, and Luminescence Properties of Reactive Magnetron Sputtered Tungsten Oxide Thin Films. *ISRN Optics*, 2012:1–8, 2012. ISSN 2090-7826. doi: 10.5402/2012/801468.

[190] I. S. Burkhanov, L. L. Chaikov, N. A. Bulychev, M. A. Kazaryan, and V. I. Krasovskii. Nanoscale metal oxide particles produced in the plasma discharge in the liquid phase upon exposure to ultrasonic cavitation. 2. Sizes and stability. Dynamic light scattering study. *Bulletin of the Lebedev Physics Institute*, 41(10): 297–304, 2014. ISSN 1934838X. doi: 10.3103/S1068335614100054.

[191] Christoph Krüger, Daniel Heinert, Alexander Khalaidovski, Jessica Steinlechner, Ronny Nawrodt, Roman Schnabel, and Harald Lück. Birefringence Measurements on Crystalline Silicon. 4 2015. doi: 10.1088/0264-9381/33/1/015012. URL `http://arxiv.org/abs/1504.06503http://dx.doi.org/10.1088/0264-9381/33/1/015012`.

[192] Masaya Ichimura, Hirotaka Tajiri, Tomonao Ito, and Eisuke Arai. Temperature dependence of carrier recombination lifetime in Si wafers. *Journal of the Electrochemical Society*, 145(9):3265–3271, 1998. ISSN 00134651. doi: 10.1149/1.1838796.

[193] Lena Bressel, Dominique de Ligny, Eugene G. Gamaly, Andrei V. Rode, and Saulius Juodkazis. Observation of O_2 inside voids formed in GeO_2 glass by tightly-focused fs-laser pulses. *Optical Materials Express*, 1(6):1150, 10 2011. ISSN 2159-3930. doi: 10.1364/ome.1.001150.

[194] Ying-Te Lee. Hydrogen Bond Effect on the Raman Shift of theCarbonyl Stretching Mode of Various Amide Solutions. *Journal of Raman Spectroscopy*, 28(1):45–51, 1 1997. ISSN 0377-0486. doi:

10.1002/(SICI)1097-4555(199701)28:1<45::AID-JRS79>3.0.CO;2-C. URL http://doi.wiley.com/10.1002/%28SICI%291097-4555%28199701%2928%3A1%3C45%3A%3AAID-JRS79%3E3.0.CO%3B2-C.

[195] Supplementary Information 1. Curing of RMF resin. Technical report, 2016.

[196] Vincenz Sandfort, Barbara Trabold, Amir Abdolvand, Carsten Bolwien, Philip Russell, Jürgen Wöllenstein, and Stefan Palzer. Monitoring the Wobbe Index of Natural Gas Using Fiber-Enhanced Raman Spectroscopy. *Sensors*, 17(12):2714, 11 2017. ISSN 1424-8220. doi: 10.3390/s17122714. URL http://www.mdpi.com/1424-8220/17/12/2714.

[197] Joshua A Robinson, Maxwell Wetherington, Joseph L Tedesco, Paul M Campbell, Xiaojun Weng, Joseph Stitt, Mark A Fanton, Eric Frantz, David Snyder, Brenda L Vanmil, Glenn G Jernigan, Rachael L Myers-Ward, Charles R Eddy, and D Kurt Gaskill. Correlating Raman Spectral Signatures with Carrier Mobility in Epitaxial Graphene: A Guide to Achieving High Mobility on the Wafer Scale. Technical report.

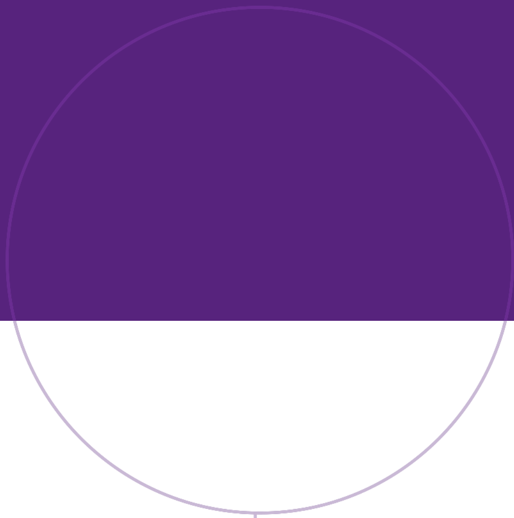

Markus J. B. Ristola

Characterisation of tungsten-doped silicon

NTNU

Kunnskap for en bedre verden